

CONTRAST-ENHANCED ULTRASOUND FOR THE ASSESSMENT OF RESPONSE TO
THERAPY

Juan D. Rojas

A dissertation submitted to the faculty at the University of North Carolina at Chapel Hill in partial fulfillment of the requirements for the degree of Doctor of Philosophy in the Department of Biomedical Engineering.

Chapel Hill
2018

Approved by:

Paul A. Dayton

Richard Goldberg

Yueh Z. Lee

Gianmarco Pinton

W. Kimryn Rathmell

© 2018
Juan D. Rojas
ALL RIGHTS RESERVED

ABSTRACT

Juan D. Rojas: Contrast-Enhanced Ultrasound for the Assessment of Treatment Response to Therapy
(Under the direction of Paul A. Dayton)

Accurate assessment of cancer response to therapy is important for effective treatment outcome and limiting unnecessary therapeutics. The clinical gold standard for evaluating response to therapy consists of tracking changes in volume, which works well for cytotoxic treatments such as radio or chemo therapies, which directly induce cancer cell death. However, tumor volume is ineffective for tracking response to treatments such as antiangiogenic therapies, which target the formation of new blood vessels, and often lags behind the real effect of the drugs.

Studies have shown that techniques such as dynamic contrast-enhanced magnetic resonance imaging, computed tomography, and positron emission tomography perform better at predicting and assessing response to therapy than changes in volume. However, these imaging modalities are expensive, cumbersome, expose patients to ionizing radiation, and use contrast agents that can often be harmful to patients.

Contrast-enhanced ultrasound (CEUS) is an imaging modality that is inexpensive, real-time, and uses microbubble contrast agents that are safe and can be used to obtain quantitative measurements of blood perfusion and levels of endothelial biomarker expression. Moreover, CEUS has been shown to assess response to therapy more accurately than tumor volume in rodent tumor models.

The first hypothesis of this dissertation is that CEUS can evaluate and track response to therapies more accurately than changes in tumor volume. The results show that CEUS can assess response to therapies that are disruptive to tumor vessel formation earlier than tumor volume.

Specifically, the techniques discussed here include perfusion imaging, ultrasound molecular imaging of angiogenesis biomarkers, and acoustic angiography, which can provide metrics about microvessel morphology and density.

The second hypothesis is that CEUS can be performed using phase-change contrast agents (PCCAs). PCCAs have better circulation times than conventional microbubbles and can be small enough to escape the vasculature for extravascular diagnostic imaging, and thus, may provide multiple advantages for the assessment of response to therapy. The development of techniques to perform perfusion and molecular imaging using PCCAs is described. The results show that PCCAs can be used for intravascular molecular imaging, but major modifications to the formulation are required to obtain meaningful measurements of perfusion.

To my parents. I am where I am today because of your effort and dedication.

ACKNOWLEDGEMENTS

I would first like to thank my adviser, Paul Dayton, for giving me a chance in his lab and providing constant guidance and support. I would also like to thank the members of my committee for their direction and advice. To past and present Dayton lab members: I could not have done this without you. Through my hardest research days, you kept me cheerful and motivated. Thank you for the countless discussions about ultrasound and life, bad ultrasound jokes, and hangout sessions.

I would also like to thank my friends and family for your unwavering support, and for listening to me talk about ultrasound and pretending to be interested. Most importantly, I would like to thank my parents; you taught me the meaning of hard work and perseverance, and it is only through your immense sacrifice and effort that I have the life and opportunities that I have.

TABLE OF CONTENTS

LIST OF TABLES.....	XIV
LIST OF FIGURES.....	XV
LIST OF ABBREVIATIONS.....	XX
CHAPTER 1 INTRODUCTION TO CONTRAST-ENHANCED ULTRASOUND	1
1.1 MOTIVATION	1
1.2 LIMITATIONS OF CURRENT CLINICAL DIAGNOSTIC TECHNIQUES	1
1.3 BIOMEDICAL IMAGING FOR ASSESSMENT OF RESPONSE TO THERAPY	1
1.4 CONTRAST-ENHANCED ULTRASOUND AND MICROBUBBLE CONTRAST AGENTS.....	2
1.5 PULSE SEQUENCES FOR CONTRAST-ENHANCED ULTRASOUND.....	4
1.6 ULTRASOUND MOLECULAR IMAGING	5
1.7 DYNAMIC CONTRAST-ENHANCED ULTRASOUND	7
1.8 ACOUSTIC ANGIOGRAPHY	9
1.9 OVERVIEW OF PRE-CLINICAL CEUS FOR THE ASSESSMENT OF RESPONSE TO THERAPY ...	11
CHAPTER 2 PHASE-CHANGE CONTRAST AGENTS	13
2.1 INTRODUCTION TO PHASE-CHANGE CONTRAST AGENTS	13
2.2 PCCAS FOR THERAPY	13
2.3 PCCAS FOR DIAGNOSIS.....	14
2.4 STABILITY OF PCCAS AT ROOM AND BODY TEMPERATURE	14
2.5 LOW BOILING POINT PCCAS.....	15
2.6 VAPORIZATION SIGNAL OF LOW BOILING-POINT PCCAS	16
2.7 POSSIBLE ADVANTAGES OF PCCAS FOR DIAGNOSTIC IMAGING.....	17
CHAPTER 3 ASSESSMENT OF TUMOR RESPONSE TO THERAPY USING MICROBUBBLE CONTRAST AGENTS	19

3.1	INTRODUCTION	19
3.2	METHODS.....	21
3.2.1	<i>Microbubble Contrast Agents</i>	21
3.2.2	<i>Xenograft and Treatment Protocol</i>	21
3.2.3	<i>Animal Protocol and Contrast Administration</i>	22
3.2.4	<i>Imaging and Analysis Protocols</i>	23
3.2.4.1	USMI.....	23
3.2.4.2	DCE-US	26
3.2.4.3	AA- Morphology.....	27
3.2.4.4	AA- Vascular Density	28
3.2.5	<i>CD31 Immunohistochemistry</i>	29
3.2.6	<i>Statistical Analysis</i>	29
3.2.7	<i>Organization of Data</i>	30
3.3	RESULTS	31
3.3.1	<i>USMI</i>	31
3.3.2	<i>DCE-US</i>	39
3.3.3	<i>AA- Morphology</i>	41
3.3.4	<i>AA- Vascular Density</i>	44
3.4	DISCUSSION	48
3.4.1	<i>USMI</i>	49
3.4.2	<i>DCE-US</i>	54
3.4.3	<i>AA- Morphology</i>	55
3.4.4	<i>AA- Vascular Density</i>	56
3.5	CONCLUSIONS.....	57

CHAPTER 4	PULSE SEQUENCES FOR THE USE OF LOW BOILING- POINT PHASE-CHANGE CONTRAST AGENTS FOR CONTRAST ENHANCED ULTRASOUND	59
4.1	INTRODUCTION	59
4.2	METHODS.....	61
4.2.1	<i>Phase-Change Contrast Agent Fabrication</i>	61
4.2.2	<i>Droplet Imaging and Activation Pulse Sequences</i>	61
4.2.3	<i>Animal Protocols</i>	64
4.2.4	<i>Development of Pulse Sequences for The Use of PCCAs</i>	65
4.2.4.1	Data Analysis	68
4.2.5	<i>Optimization of Activation Parameters</i>	70
4.2.5.1	<i>In Vitro</i> Protocols	73
4.2.5.2	<i>In Vivo</i> Imaging.....	74
4.2.6	<i>Vaporization Detection Imaging</i>	76
4.2.6.1	Activation Signal Detection	76
4.2.6.2	Imaging of Phase-Change Contrast Agents.....	78
4.2.6.3	<i>In Vivo</i> Imaging	80
4.2.6.4	Imaging at Depth.....	81
4.2.6.5	Statistical Analysis	82
4.3	RESULTS	82
4.3.1	<i>Contrast Agent Sizing and Concentration</i>	82
4.3.2	<i>Development of Pulse Sequences for the Use of PCCAs</i>	84
4.3.2.1	<i>In Vitro</i> Verification	84
4.3.2.2	<i>In Vivo</i> Acoustic Parameters	85
4.3.2.3	Contrast Enhancement Measurements	87
4.3.2.4	Half-life Measurements.....	91
4.3.3	<i>Optimization of Activation Parameters</i>	92

4.3.4	<i>Vaporization Detection Imaging</i>	97
4.3.4.1	Activation Signal Detection	97
4.3.4.2	<i>In Vivo</i> Imaging	102
4.3.4.3	Activation at Depth	104
4.4	DISCUSSION	105
4.4.1	<i>Development of Pulse Sequences for The Use of PCCAs</i>	105
4.4.2	<i>Optimization of Activation Parameters</i>	107
4.4.3	<i>Vaporization Detection Imaging</i>	109
4.5	CONCLUSIONS.....	112
CHAPTER 5	EFFECT OF HYDROSTATIC PRESSURE, BOUNDARY CONSTRAINTS, AND VISCOSITY ON THE VAPORIZATION THRESHOLD OF LOW BOILING-POINT PHASE-CHANGE CONTRAST AGENTS	114
5.1	INTRODUCTION	114
5.2	MATERIALS AND METHODS.....	116
5.2.1	<i>Phase-Change Contrast Agent Fabrication</i>	116
5.2.2	<i>Microtubes</i>	117
5.2.3	<i>Pressurized Chamber</i>	117
5.2.4	<i>Blood-Mimicking Fluid</i>	118
5.2.5	<i>Phase-Change Contrast Agent Activation</i>	119
5.2.6	<i>Measurement of Activation- Ultrasound Imaging</i>	119
5.2.7	<i>Measurement of Activation- Optical Microscopy</i>	119
5.2.8	<i>Measurement of Activation- Vaporization signal detection</i>	120
5.2.9	<i>In Vivo Droplet Activation</i>	121
5.2.10	<i>Data Analysis</i>	122
5.2.11	<i>Statistical Analysis</i>	123
5.3	RESULTS	123

5.3.1	<i>Effect of Boundary Constraints on Droplet Activation Threshold</i>	123
5.3.2	<i>Effect of Hydrostatic Pressure on Droplet Activation Threshold</i>	127
5.3.3	<i>Effect of Viscosity on Droplet Activation Threshold</i>	127
5.3.4	<i>In Vivo Droplet Activation</i>	128
5.4	DISCUSSION	129
5.4.1	<i>Effect of Boundary Constraints on Droplet Activation Threshold</i>	129
5.4.2	<i>Effect of Hydrostatic Pressure on Droplet Activation Threshold</i>	132
5.4.3	<i>Effect of Viscosity on Droplet Activation Threshold</i>	133
5.4.4	<i>In Vivo Droplet Activation</i>	134
5.4.5	<i>Limitations</i>	134
5.4.6	<i>Implications for In vivo Imaging</i>	135
5.5	CONCLUSIONS.....	136
CHAPTER 6	MOLECULAR IMAGING USING LOW BOILING-POINT PHASE-CHANGE CONTRAST AGENTS	137
6.1	INTRODUCTION	137
6.2	METHODS.....	138
6.2.1	<i>Agent Formulation</i>	138
6.2.2	<i>Size Selection</i>	138
6.2.3	<i>Condensation</i>	139
6.2.4	<i>Agent Sizing</i>	139
6.2.5	<i>Tumor Model and Animal Protocols</i>	139
6.2.6	<i>Pulse Sequences</i>	140
6.2.7	<i>Imaging Protocol</i>	141
6.2.8	<i>Data Analysis</i>	144
6.2.9	<i>Statistical Analysis</i>	146
6.3	RESULTS	146

6.4	DISCUSSION	151
6.5	CONCLUSION	157
CHAPTER 7	PROTOCOLS FOR PERFUSION IMAGING USING PCCAS.....	159
7.1	INTRODUCTION	159
7.2	METHODS.....	160
7.2.1	<i>Animal Protocol</i>	<i>160</i>
7.2.2	<i>PCCA and MCA formulations.....</i>	<i>160</i>
7.2.3	<i>MCA sizing</i>	<i>161</i>
7.2.4	<i>Imaging Protocols.....</i>	<i>161</i>
7.2.5	<i>Data Analysis</i>	<i>161</i>
7.2.6	<i>MCA Perfusion Imaging.....</i>	<i>162</i>
7.2.7	<i>Effect of PCCA Size.....</i>	<i>162</i>
7.2.8	<i>Effect of Concentration and Vaporization Pressure.....</i>	<i>163</i>
7.2.9	<i>Effect of Pulse Length.....</i>	<i>163</i>
7.2.10	<i>Effect of PEG Chain Length.....</i>	<i>163</i>
7.2.11	<i>Effect of Acyl Chain Length.....</i>	<i>164</i>
7.2.12	<i>PCCA Perfusion Imaging.....</i>	<i>164</i>
7.2.13	<i>Statistical Analysis</i>	<i>164</i>
7.3	RESULTS	165
7.3.1	<i>MCA Perfusion Imaging.....</i>	<i>165</i>
7.3.2	<i>Effect of PCCA Size.....</i>	<i>165</i>
7.3.3	<i>Effect of Concentration and Vaporization Pressure.....</i>	<i>166</i>
7.3.4	<i>Effect of Pulse Length.....</i>	<i>167</i>
7.3.5	<i>Effect of PEG Chain Length.....</i>	<i>168</i>
7.3.6	<i>Effect of Acyl Chain Length.....</i>	<i>169</i>
7.3.7	<i>PCCA Perfusion Imaging.....</i>	<i>171</i>

7.4	DISCUSSION	171
7.5	CONCLUSION	173
CHAPTER 8	DISCUSSION AND CONCLUSIONS.....	174
8.1	ASSESSMENT OF RESPONSE TO THERAPY USING MICROBUBBLE CONTRAST AGENTS	174
8.2	PHASE-CHANGE CONTRAST AGENTS FOR THE ASSESSMENT OF RESPONSE TO THERAPY	175
BIBLIOGRAPHY	177

LIST OF TABLES

Table 3.1. Sensitivity and specificity of the USMI metrics targeting intensity, percent anechoic, and tumor volume over the first 3 weeks of treatment.	39
Table 3.2. Number of animals imaged for each treatment week.	45
Table 4.1. Summary of imaging and activation design parameters.	66
Table 4.2. <i>In vivo</i> pressure estimations based on a simple tissue attenuation model.	87
Table 4.3. Vaporization Threshold for the different pulse lengths and dilutions.	98
Table 4.4. Vaporization Threshold used for comparing DFB and OFP.	101
Table 4.5. 80% vaporization threshold.	102

LIST OF FIGURES

Figure 1.1. Pulse inversion pulse sequence.	4
Figure 1.2. Amplitude modulation pulse sequence.	5
Figure 1.3. Cadence contrast pulse sequencing.	5
Figure 1.4. Example USMI protocol. B-mode is used for anatomical reference.	6
Figure 1.5. Time-intensity Curves for DCE-US.	8
Figure 1.6. Parametric perfusion maps overlaid on the corresponding B-mode images.	8
Figure 1.7. Overview of Acoustic Angiography.	10
Figure 2.1. Vaporization and expansion of low boiling-point PCCAs.	17
Figure 3.1. Summary of USMI imaging protocol.	24
Figure 3.2. Method for obtaining anechoic regions in a peak intensity image.	25
Figure 3.3. Example of individual response to the treatment.	26
Figure 3.4. Example USMI images of different treatment groups taken 7 min after injection.	32
Figure 3.5. Targeting intensity for the different treatment groups and timepoints.	33
Figure 3.6. Peak intensity for the different treatment groups and timepoints.	34
Figure 3.7. Percent Anechoic metric.	34
Figure 3.8. Tumor volume for the different treatment groups and timepoints.	36
Figure 3.9. Representative images of CD31 immunohistochemistry from USMI experiment.	37
Figure 3.10. Examples of individual responses of SU and Switch.	38
Figure 3.11. Representative perfusion maps overlaid on B-mode images for each treatment group. ...	40
Figure 3.12. Plots of volumetric perfusion times and tumor volume.	41
Figure 3.13. Representative maximum intensity projections of acoustic angiography images for the different treatment groups.	42
Figure 3.14. Results for the distance metric and sum of angles metric.	43
Figure 3.15. Representative vessel density images from the different treatment groups.	44

Figure 3.16. Tumor volume and blood vessel density for the different imaging weeks.	45
Figure 3.17. Plot of blood vessel density vs volume for all datapoints.	46
Figure 3.18. Representative CD31 staining images of the different treatment groups and Stained Area results.	47
Figure 3.19. Correlation plot of image derived blood vessel density vs CD31 stained neovasculature.....	47
Figure 3.20. Linear regression model used to calculate predicted tumor volume and ROC curve for predicted tumor volume as a classifier.....	48
Figure 4.1. Imaging and activation sequence.	64
Figure 4.2. Transducer output pressure and activation clouds at different depths.	70
Figure 4.3. Example PWM pulse code and generated pulse.	72
Figure 4.4. Example APM parameters for <i>in-vitro</i> activation.	73
Figure 4.5. Pressure map with distance after accounting for attenuation using a rat kidney attenuation model.	75
Figure 4.6. Illustration of the analysis for the activation signal detection section.	78
Figure 4.7. Reconstruction technique for making VDI images.	79
Figure 4.8. ROI drawn on b-mode image and activation locations.	80
Figure 4.9. Example CI image, and mask for analysis.	81
Figure 4.10. Representative distributions of contrast agents used in this study.	83
Figure 4.11. <i>In vitro</i> activation of DFB droplets.	84
Figure 4.12. Example overlays of B-mode ultrasound scans and contrast-specific pulse-inversion scans for each contrast agent tested.	88
Figure 4.13. Examples of contrast measurements taken for individual animals administered DFB and OFP droplets.	89
Figure 4.14. Maximum dB enhancement relative to the mean of the agent-free baseline for microbubbles after injection and droplets after application of a vaporization sequence.	90
Figure 4.15. Maximum contrast enhancement over the mean of the agent-free baseline normalized to the maximum value produced by each animal for microbubbles and droplets.....	92
Figure 4.16. Difference between using APM and a single voltage without PWM on bubble cloud size.	93

Figure 4.17. Intensity profiles were generated by averaging imaged data from activation lines separated by a range of distances between 0.25 and 1 mm.	94
Figure 4.18. APM and optimized spacing creates a region of uniform contrast.	95
Figure 4.19. OFP droplet activation in a rat kidney using APM and optimized spacing.	95
Figure 4.20. Contrast enhancement over the baseline case for each time point, and normalized to the one-minute time-point.	96
Figure 4.21. Example voltage traces from droplet vaporization detection.	97
Figure 4.22. AUC of tube signals after different filters.	98
Figure 4.23. AUC results of DFB and OFP for the different dilutions	99
Figure 4.24. Mean Frequency results of DFB and OFP for the different dilutions.	100
Figure 4.25. AUC comparison between DFB and OFP for the different dilutions using the 25% threshold.	101
Figure 4.26. CE of <i>in vivo</i> data using different filters for both DFB and OFP.	102
Figure 4.27. Example <i>in vivo</i> VDI images from DFB and OFP.	103
Figure 4.28. Example <i>in vivo</i> CI images of DFB and OFP before PCCA injection and at each activation pressure.	103
Figure 4.29. CE of VDI vs CI images for DFB and OFP.	104
Figure 4.30. CE of VDI and CI images of activation at depth in the 2 and 3 cm tubes before and after the introduction of droplets.	104
Figure 4.31. CE of VDI and CI images from droplet activation in the microtubes at 2 and 3 cm.	105
Figure 5.1. Schematic of the pressurized chamber system used for part 2 of the <i>in vitro</i> experiments; testing the effect of hydrostatic pressure on droplet activation.	118
Figure 5.2. Example of activation scheme for US imaging measurement of activation in the 50 μm microtube and in a rat kidney.	122
Figure 5.3. Example fast Fourier transform of the received signal from the 1 MHz piston transducer.	123
Figure 5.4. Post-activation images of the different tubes and pressures.	124
Figure 5.5. Results from the 3 different techniques for measuring droplet vaporization in microtubes of different diameters: US imaging, optical microscopy, and droplet activation detection.	125

Figure 5.6. Microscope images of droplet activation.	126
Figure 5.7. Contrast enhancement generated by droplet activation inside the pressure chamber increased with peak-negative pressure under different hydrostatic pressures.	127
Figure 5.8. Contrast enhancement generated by droplet activation increased with pressure.	128
Figure 5.9. Example images of droplet vaporization in a rat kidney resulting from activation pulses of different pressures.	128
Figure 5.10. Example microscope image of droplet activation in 50 μm tube at 32X magnification.	130
Figure 5.11. AUC measurements from the 105 μm acrylic and 320 μm FEP tubes with a concentration of droplets matching the number of droplets in the 12.5 μm tube.	131
Figure 6.1. Summary of imaging protocol.	142
Figure 6.2. Summary of all experimental trials performed in each animal.	143
Figure 6.3. Illustration of the mask making process.	145
Figure 6.4. Example of data acquired by imaging protocol at the three different timepoints with example clearance curve and example wash-out curve with mean intensity data captured with CSS imaging droplet vaporization.	145
Figure 6.5. Size distributions of MCAs and PCCAs using the Accusizer and NanoSight.	146
Figure 6.6. Example post-activation CSS, VDI, and MCA CSS images.	147
Figure 6.7. Targeting intensity for post-activation CSS and VDI at the different wait times.	148
Figure 6.8. Clearance rate b of control and targeted PCCAs.	148
Figure 6.9. Comparison of VDI and post-activation CSS for all wait times and doses.	149
Figure 6.10. Comparison of PCCAs and MCAs.	149
Figure 6.11. Targeting intensity for the different wait times.	150
Figure 6.12. Wash-out rate, b_{wo} , for control and targeted PCCAs at all wait times.	151
Figure 6.13. Perfusion maps of MCA wash-in, control and targeted PCCA wash-out, overlaid over Bmode images.	155
Figure 7.1. Plots of MCA wash-in rate and curves in rat kidneys before and after administration of dopamine.	165

Figure 7.2. Size distributions for native and size-selected MCAs and the averaged wash-out curves for size-selected PCCAs.	166
Figure 7.3. Plots of wash-out rate and maximum contrast enhancement for different size-selected OFP PCCAs doses and vaporization pressures.	167
Figure 7.4. Example microscopy image of vaporized PCCAs and plot of bubble sizes for each number of cycles group.	168
Figure 7.5. Size distributions of size-selected DFB and OFB bubbles before condensation and after vaporization for PEG2000 and PEG5000.	169
Figure 7.6. Example wash-out curves for size-selected OFP droplets with C:18 and C:20 acyl chain lengths.	170
Figure 7.7 Wash-out rate and maximum contrast enhancement of vaporized size-selected OFP droplets in the kidneys of rats before and after the administration of dopamine.	170
Figure 7.8. Perfusion and standard deviation maps.	172

LIST OF ABBREVIATIONS

AA	Acoustic angiography
ADV	Acoustic droplet vaporization
ANOVA	Analysis of variance
APM	Activation pressure matching
AUC	Area under the curve
BVD	Blood vessel density
ccRCC	Clear-cell renal cell carcinoma
CD31	Cluster of differentiation 31
CE	Contrast enhancement
CEUS	Contrast-enhanced ultrasound
CI	Contrast imaging
CPS	Cadence contrast pulse sequencing
CSS	Contrast-specific pulse sequence
CT	Computed tomography
CTR	Contrast-to-tissue ratio
DBPC	1,2-diarachidoyl-sn-glycero-3-phosphocholine
DCE-US	Dynamic contrast-enhanced ultrasound
DFB	Decafluorobutane
DLL4	Delta-like ligand 4
DM	Distance metric
DSPC	1,2-distearoyl-sn-glycero-3-phosphocholine
DSPE	1,2-distearoyl-sn-glycero-3-phosphoethanolamine
ECM	Extracellular matrix

FEP	Fluorinated Ethylene Propylene
FOV	Field of view
FSA	Fibrosarcoma
GSI	Gamma secretase inhibitor
HER2	Human epidermal growth factor receptor 2
MCA	Microbubble contrast agent
MI	Mechanical index
MRI	Magnetic resonance imaging
MTT	Mean transit time
NSG	NOD/scid/gamma
OFP	Octafluoropropane
PA	Percent anechoic
PBS	Phosphate-buffered saline
PCCA	Phase-change contrast agent
PE	Peak enhancement
PEG	Polyethylene-glycol
PET	Positron emission tomography
PFC	Perfluorocarbon
PI	Peak intensity
PNP	Peak-negative pressure
PWM	Pulse-width modulation
RAD	Cyclo-Arg-Ala-Asp-D-Tyr-Cys
RCC	Renal cell carcinoma
RECIST	Response evaluation criteria in solid tumors
RGD	Cyclo-Arg-Gly-Asp-D-Tyr-Cys
ROI	Region of interest

SOAM	Sum of angles metric
STD	Standard deviation
SU	Sunitinib malate
TI	Targeting intensity
US	Ultrasound
USMI	Ultrasound molecular imaging
VDI	Vaporization detection imaging
VEGF	Vascular endothelial growth factor
VEGFR-2	Vascular endothelial growth factor 2
VHL	Von Hippel-Lindau
VPT	Volumetric perfusion time

CHAPTER 1

INTRODUCTION TO CONTRAST-ENHANCED ULTRASOUND

1.1 Motivation

Cancer is the second leading cause of death in the United States behind cardiovascular disease, and will claim the lives of over 600,000 Americans in the coming year [1]. Because of the lethality of the disease, proper staging and accurate assessment of response to different therapies is critical to optimize therapy and correctly assess prognosis. Assessing the initial response is important for survival outcome, but tumors can develop resistance to different therapeutic regimens and show progression even if the disease seems to be controlled initially [2,3]. Therefore, it is equally important to accurately track the progression of the disease throughout treatment in order to better tailor therapy and enhance efficacy. For example, it has been shown that resistance to therapy can cause a rebound effect where the tumor becomes more aggressive, and this rebound can be worse in cases that showed a better initial response [2]. As such, it is very important to closely track the disease to provide effective treatments and avoid harmful outcomes.

1.2 Limitations of Current Clinical Diagnostic Techniques

The clinical gold standard for noninvasively assessing tumor response to therapy is measuring changes in tumor volume via the Response Evaluation Criteria in Solid Tumors (RECIST) [4]. However, a statistical simulation study showed that RECIST will often delay the identification of progression [5]. Furthermore, functional and molecular changes can occur before any measurable change in tumor size [6], and RECIST often does not appropriately demonstrate these effects of therapy [7–11]. As RECIST relies on changes in volume, it is appropriate for assessing response to cytotoxic

therapies such as radio and chemotherapies that directly kill cancer cells but not for therapies such as antiangiogenic drugs that attack the tumor vasculature [3,12]. These therapies often do not cause tumor shrinkage and are thus incorrectly categorized using tumor size criteria [13,14]. Studies have found that RECIST severely underestimated the response of antiangiogenic therapies in renal cell carcinoma (RCC) and could identify progression-free survival in less than 20% of patients [3,12].

1.3 Biomedical Imaging for Assessment of Response to Therapy

To overcome the limitations of RECIST, there has been a great deal of work in the field of biomedical imaging to create modalities that are sensitive to physiological changes and can accurately track and predict response to therapy. Anatomical imaging modalities such as computed tomography (CT) and magnetic resonance imaging (MRI) are used to provide size measurements for RECIST, but contrast agents can also be used to quantify molecular and functional characteristics of the disease. Contrast-enhanced MRI, contrast-enhanced CT, and positron emission tomography (PET) can predict and track tumor response earlier and more accurately than RECIST [7,15–20]. Contrast-enhanced CT has been shown to outperform RECIST in both RCC [12] and gastrointestinal stromal tumors [7,10], finding that CT density values can more accurately measure the response of the tumors to different therapies. PET has also been proven to be very sensitive at assessing early response to therapy [16,18] and has been shown to be especially effective when combined with CT [19]. However, these imaging modalities are cumbersome, expensive, and expose patients to ionizing radiation in the case of CT and PET. A study tracking the development of cancer in patients who were repeatedly imaged using CT showed that cumulative radiation exposure from CT imaging increases baseline cancer risk [21] and so, to limit exposure and to optimally capture the response to treatment, imaging is usually limited to once every several weeks or months [22]. However, more frequent monitoring is desirable for precise tracking of disease state and response to therapy. Furthermore, iodinated contrast agents for CT may be harmful for patients with compromised kidneys [23], and gadodiamide contrast agents for MRI may

cause nephrogenic systemic fibrosis (fibrosis in skin and lungs and then heart, liver, kidneys) for patients with advanced chronic kidney disease, which can lead to death [24,25].

1.4 Contrast-Enhanced Ultrasound and Microbubble Contrast Agents

In comparison to the imaging modalities discussed in the previous section, contrast-enhanced ultrasound (CEUS) imaging is inexpensive, portable for bed-side diagnostics, widely available, and does not involve any ionizing radiation. CEUS uses contrast agents that are safe for clinical use [26,27], range in size between 1 and 5 μm and thus can freely traverse the vasculature, and have been used for molecular and perfusion imaging of disease [28–31]. Therefore, CEUS can be a powerful tool for serial monitoring of disease and assessment of early response to therapy. Conventional microbubble contrast agents (MCAs) are typically composed of a phospholipid shell to prevent dissolution and coalescence [32] and have cores with gases, such as sulfur hexafluoride or perfluorocarbons (PFCs), which have high molecular weight and low solubility in blood to decrease dissolution and enhance circulation time. Adding polyethylene glycol (PEG) to the shell of nanoparticles has been common practice for decades in the field of drug delivery, as PEG provides a steric shield that prevents immune cell recognition and dramatically decreases particle clearance by the mononuclear phagocytic system, also known as the reticuloendothelial system [33–35]. Hence, PEG is commonly conjugated to the lipid shell to reduce MCA coalescence and recognition by the immune system [36,37] and to attach targeting ligands for molecular imaging [38,39].

Ultrasound (US) uses high frequency pressure waves (in the MHz range) to differentiate tissues based on density. Contrast between tissues arises from mismatches in acoustic impedance, so MCAs provide high US contrast because the density of their cores is much lower than that of blood or tissue. Moreover, microbubbles are highly compressible and generate pressure waves when interrogated with US with frequencies in the clinical range (1-15 MHz). The response of MCAs to US is much different than that of tissue, so contrast-specific pulse sequences can be used to isolate MCA signals from those of tissue.

1.5 Pulse Sequences for Contrast-Enhanced Ultrasound

Contrast-specific sequences separate MCA signals from tissue signals based on their non-linear frequency and amplitude response. Specifically, tissue response to transmitted ultrasound waves is predominantly linear, producing echoes having a frequency content dominated by the excitation frequency and an amplitude linearly proportional to that of the incident pressure wave. Conversely, the frequency content of signals produced by MCAs encompasses the excitation frequency as well as significant energy at higher harmonics [40], and the resulting signal amplitude is not linearly proportional to the excitation pressure [41]. Techniques such as pulse inversion [42] (Figure 1.1) and amplitude modulation [41] (Figure 1.2) take advantage of the non-linear response of MCAs to reduce tissue signal and produce images with a high contrast-to-tissue ratio (CTR). Cadence™ contrast pulse sequencing (CPS) from Siemens Medical Solutions, Inc. (Issaquah, WA, USA) incorporates pulse inversion and amplitude modulation to produce an US sequence that reduces tissue signal and is more sensitive to MCA signal than either pulse inversion or amplitude modulation alone [43] (Figure 1.3).

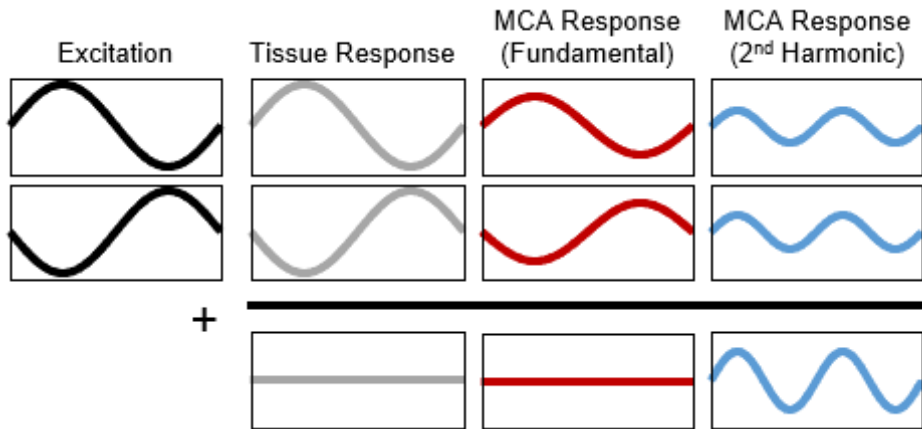


Figure 1.1. Pulse inversion pulse sequence. This scheme uses two pulses that are 180 degrees out of phase to eliminate fundamental frequency content from both tissue and MCAs, so that only the second harmonic component of MCAs remains.

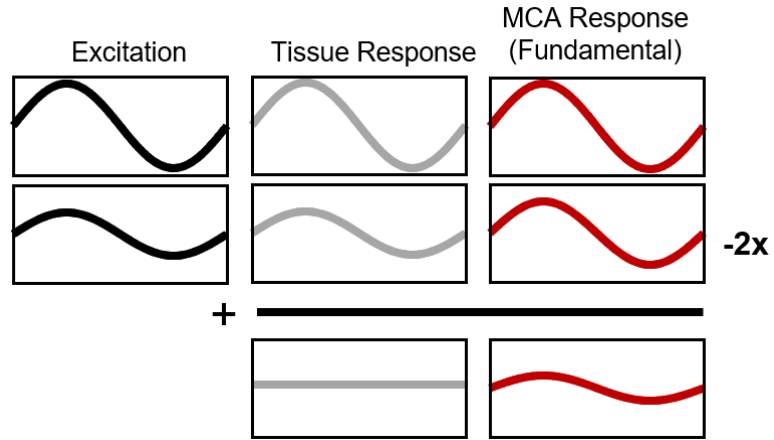


Figure 1.2. Amplitude modulation pulse sequence. This approach consists of subtracting twice a half-amplitude pulse from a full-amplitude pulse to eliminate fundamental tissue signals.

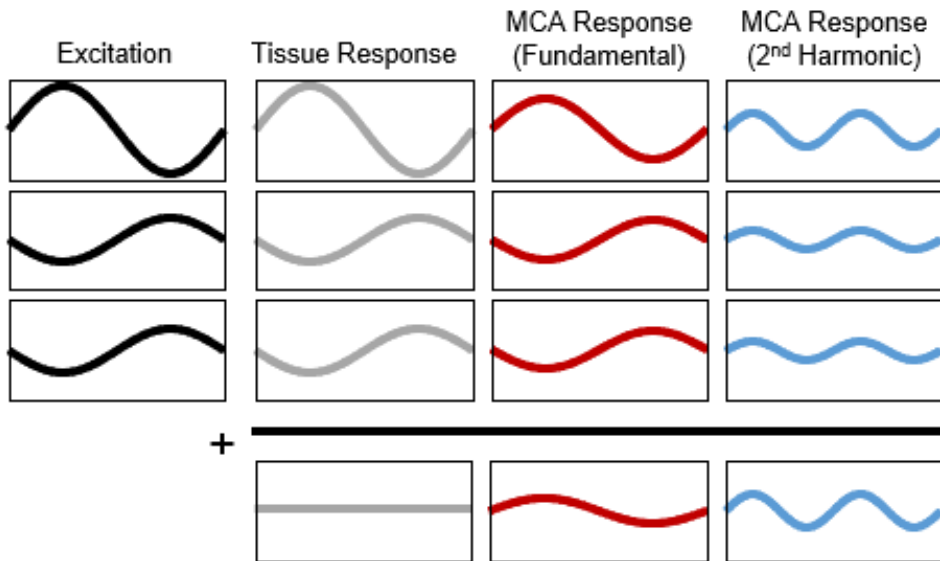


Figure 1.3. Cadence contrast pulse sequencing. Pulse inversion and amplitude modulation are combined to eliminate tissue signal and isolate fundamental and second harmonic frequency components from MCAs. A full-amplitude pulse is followed by 2 inverted and half-amplitude pulses.

1.6 Ultrasound Molecular Imaging

By incorporating targeting ligands such as antibodies or peptides to the microbubble shell, ultrasound molecular imaging (USMI) can be performed, thereby enabling imaging of pathology otherwise difficult to distinguish from normal tissue with the use of conventional US (B-mode) [44]. USMI has been evaluated to assess expression of different molecular biomarkers associated with

cardiovascular disease [44–46], inflammatory disorders [47,48], and angiogenesis [49–51]. Typically, biomarkers expressed on the vascular endothelium such as $\alpha_v\beta_3$ integrin and the Vascular Endothelial Growth Factor receptor (VEGFR-2) are targeted [49,52–55] because available markers are partially limited by the confinement of the microbubbles to the microvasculature due to their size.

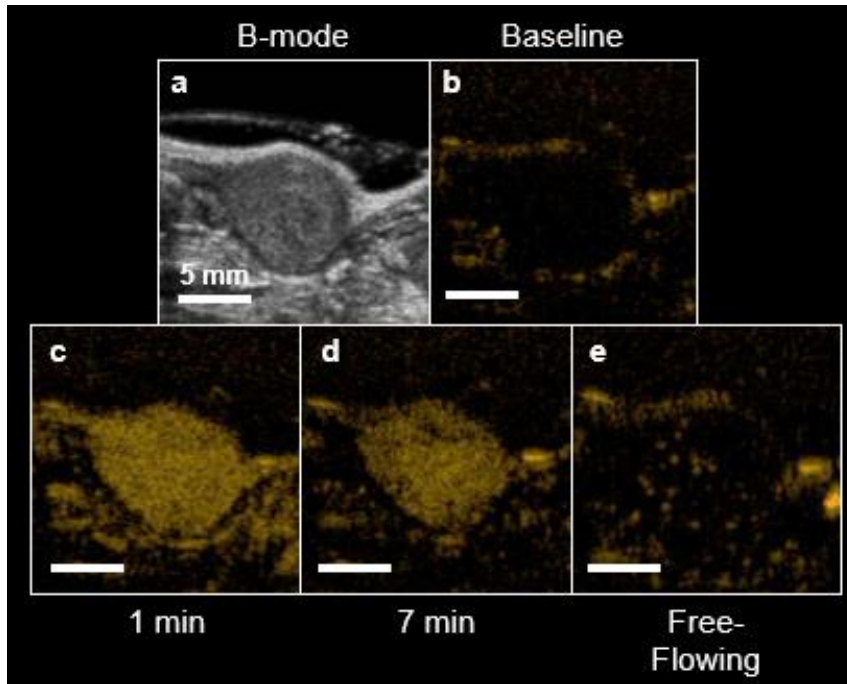


Figure 1.4. Example USMI protocol. B-mode is used for anatomical reference (a). Contrast-specific sequences greatly reduce the tissue signal (b). MCAs are injected and perfuse the entire tissue (c). MCAs are allowed to bind for several minutes while freely-flowing agents are cleared from circulation (d). A destructive flash clears bound MCA from the tumor, so that the level of freely-flowing signal can be captured (e). The USMI signal is calculated by subtracting (e) from (d).

Typically, targeted MCAs are injected into the vasculature and allowed to circulate and bind to endothelial markers. A waiting period of 4-15 minutes is required after injection in order to allow the microbubbles to bind to the targets and for the free-flowing agents to be cleared from circulation. An increased concentration of MCAs enhances target binding, but free-flowing contrast will take longer to clear. A frequently used approach consists of waiting several minutes for binding to occur, then capturing the signal in the tumor before and after a destructive US pulse clears the field of view from both bound and freely-flowing MCAs, so that the molecular imaging signal is the difference between

the two scans [49] (Figure 1.4). This approach reduces the imaging time because it is not needed to wait until all of the freely-flowing MCAs have been cleared from circulation by the liver and lungs.

1.7 Dynamic Contrast-Enhanced Ultrasound

Since MCAs are constrained to the vasculature, CEUS can image characteristics of blood such as perfusion rate, by monitoring the transit time of MCAs leaving or arriving into a target or measuring how long they remain in the tissue. Dynamic contrast-enhanced ultrasound (DCE-US) can produce a quantitative measurement of perfusion that can be used to evaluate functional changes, something that is difficult to do with other US techniques such as Doppler. DCE-US has been shown to measure tissue characteristics such as blood perfusion [56–58] for cardiology [59,60], evaluation and treatment of ischemic stroke [61–63], and cancer assessment and management [64,65] in animal models of disease.

One strategy that is commonly employed in DCE-US is obtaining a time-intensity curve of the contrast signal by delivering a bolus of MCAs and monitoring the signal in the tissue as the agents are cleared from circulation [66] (Figure 1.5). For the time-intensity curve, parameters such as mean transit time (MTT), peak enhancement (PE), and area under the curve (AUC) can be calculated to quantify the perfusion in the tissue. This technique can be subject to error from difference in bolus injection rate and tissue motion over time. Additionally, creating a time-intensity curve of MCA washout can only be performed in one plane unless a 2D transducer is used, and there is evidence demonstrating that tumors have very heterogeneous physiological characteristics, making a 3D scan more appropriate for accurately assessing the state of the disease [67]. In comparison, a method referred to as Flash Replenishment or Destruction Reperfusion can be performed in 3D by sweeping a conventional US transducer across the tissue to obtain perfusion measurements of the entire region of interest (ROI) [58]. Typically, a continuous infusion of MCAs is used so that tissue is saturated with contrast, a flash consisting of destructive pulses clears the ROI of microbubbles, and the intensity inside the ROI is monitored as MCAs flow back in (Figure 1.5). The produced intensity curve can be fitted to a simple exponential equation, and the perfusion coefficient α can be calculated to quantify perfusion.

Additionally, the time for the intensity inside the ROI to reach 20% (20% is common, but any percentage can be used) of the value before the destructive flash can be used as a metric of perfusion.

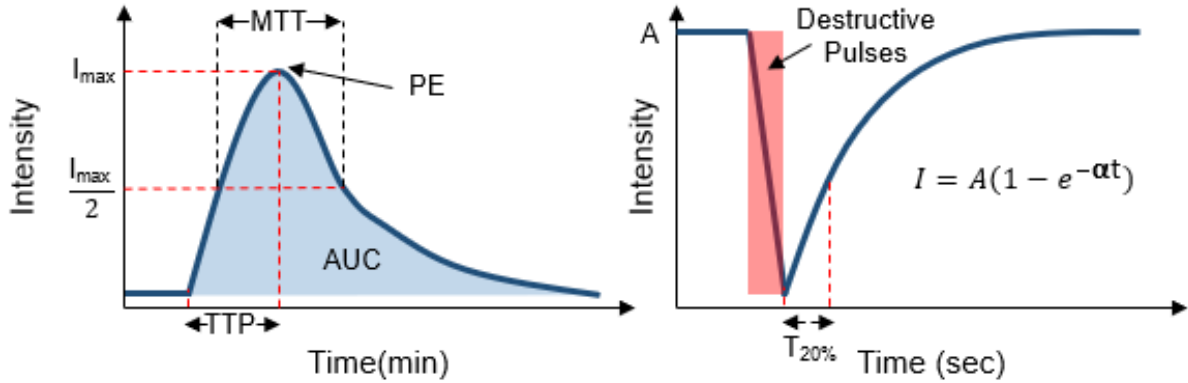


Figure 1.5. Time-intensity Curves for DCE-US. A bolus of MCAs is introduced and the signal is monitored until the agents are cleared from circulation (left). Perfusion metrics such as mean transit time (MTT), peak enhancement (PE), and area under the curve (AUC) can be calculated. The Destruction Reperfusion protocol (right) involves measuring the intensity after a destructive flash clears MCAs from the field of view. A perfusion coefficient α and a time to 20% of baseline can be calculated to quantify perfusion.

Using a similar protocol to Destruction Reperfusion, the same perfusion metrics can be calculated for each pixel in the image to create parametric perfusion maps that allow for quantification of specific areas in the ROI [56,58,68] (Figure 1.6).

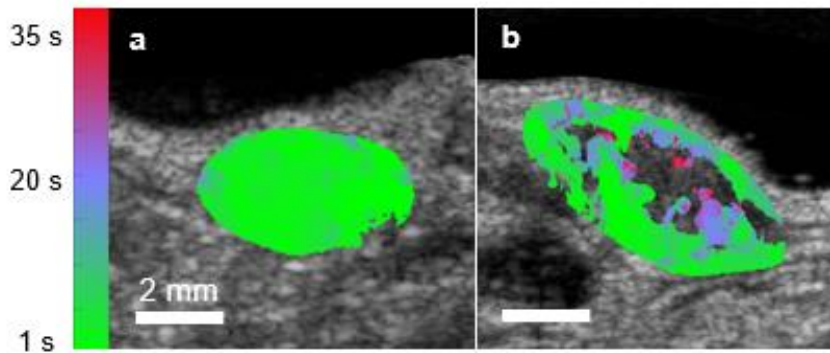


Figure 1.6. Parametric perfusion maps overlaid on the corresponding B-mode images. The figure shows a tumor before treatment (a) and after several weeks of treatment (b). The color of each pixel represents the time it took that pixel to return to 20% of its value before the destructive flash.

1.8 Acoustic Angiography

Acoustic angiography (AA) is another CEUS technique which uses the super-harmonic signals from MCAs to produce high resolution maps of vasculature [40,69]. Specifically, tissue response to transmitted ultrasound waves is predominately linear, producing echoes having the same frequency content dominated by the excitation frequency. Conversely, the frequency content of signals produced by MCAs encompasses the excitation frequency as well as significant energy at higher harmonics [40]. The potential of superharmonic imaging was first demonstrated by Bouakaz et al. [70] and Kruse and Ferrara [71], where it was observed that broadband energy exceeding 45MHz was produced when microbubbles were excited with short 2.5 MHz pulses. Therefore, AA consists of exciting microbubbles at their resonant frequency (typically less than 10 MHz), and receiving at a high frequency (10-30 MHz) to capture their higher harmonic content response, and thus eliminating the fundamental frequency content of tissue (Figure 1.7a). The microbubble harmonics can be detected at several fold of the fundamental frequency, resulting in images with substantially higher resolution and higher CTR than obtained with existing technology [69].

AA is a destructive CEUS technique because MCAs have to be driven with high pressures that cause fragmentation and destruction in order to produce the required higher harmonic content. By changing imaging parameters, such as the frame rate and the amount of frame averaging (or whether or not to average frames), different types of images can be obtained. For example, if a frame rate around 5 Hz with frame averaging is used, AA will produce high resolution images where individual vessels down to 150 μm can be resolved (Figure 1.7b). Large vessels will re-perfuse between frames, but sub-resolution vasculature with slow perfusion will not, so averaging the frames eliminates sub-resolution signal and isolates signal from large, resolvable vessels. This type of image can be used to evaluate vessel morphology in tumors for early detection and monitoring of early development of disease [72,73] and can potentially be used to assess the response of tumor vasculature to different therapies. In comparison, if a slow frame rate of 1 Hz is used without any frame averaging, AA will produce

“cloudy” images containing MCA signal from both sub-resolution and resolvable vessels (Figure 1.7c) that can provide a quantitative measure of microvascular density [74]. Furthermore, a measure of perfusion can be obtained by adjusting imaging parameters, since the main difference between the two types of AA images discussed above is the length of time allowed for re-perfusion between frames [75].

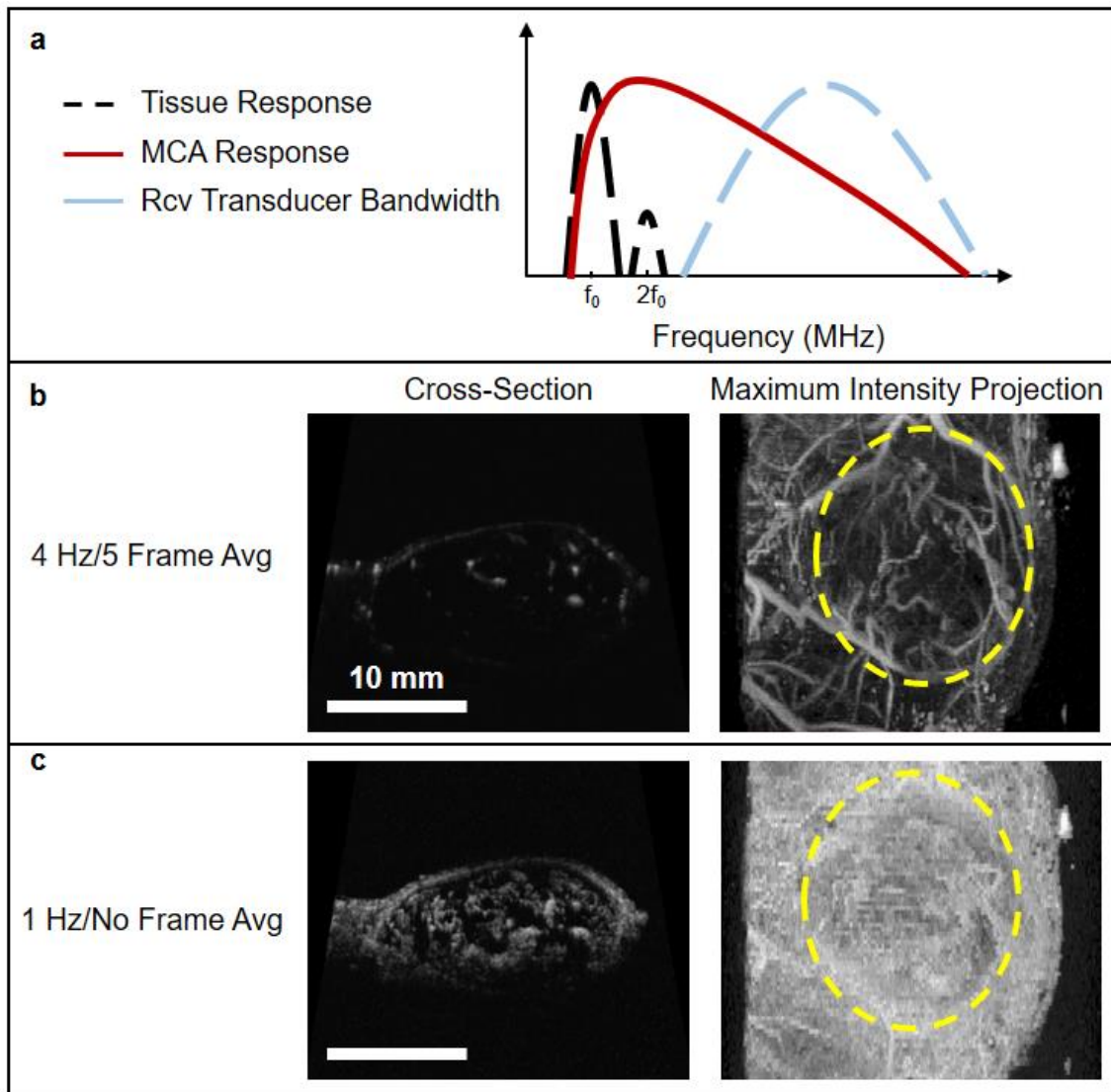


Figure 1.7. Overview of Acoustic Angiography. In (a), a transmit pulse with a frequency of f_0 will produce a tissue response (black dashed line) around f_0 and with some content at $2f_0$, but MCAs (red line) will have a response that extends to several harmonics. A receive transducer with a bandwidth that does not overlap with the tissue response (blue dashed line) can be used to produce images free of tissue with high CTR. Using a high frame rate and frame averaging will produce images with resolvable vessels (b). A slow frame rate and no frame averaging will include signal from both resolvable and sub-resolution vasculature (c). The yellow dashed lines denote the tumor area.

Cancer is characterized by extensive angiogenesis, or the formation of new vasculature [76]. As tumors grow, they use different signaling pathways such as the vascular endothelial growth factor (VEGF) and Notch signaling pathways to recruit new vasculature and feed the rapidly growing number of cells [76,77]. However, angiogenesis in cancer is different than that of normal physiological processes, in that it results in abnormal vasculature that is often disorganized and tortuous due to an excess in signaling [78]. It has been shown that vascular remodeling in cancer can start when the tumor is as small as 100 cells [79], and morphological changes in the vasculature can be detected using AA before the tumor is palpable, or around 2-3 mm [72]. Therefore, AA might be an ideal technique for tracking and assessing the response of cancer to different therapies.

1.9 Overview of Pre-Clinical CEUS for the Assessment of Response to Therapy

Over recent years, researchers have started exploring the potential of CEUS to assess the response of disease to different therapies in rodents. Within the last 3 years, many studies have demonstrated the ability of USMI to target VEGFR-2 in different cancer models and provide imaging results that correlate with histology [80–85]. In line with these findings, some studies have shown that USMI of VEGFR-2 can be used to predict response to antiangiogenic therapy earlier than tumor volume [81–83]. Furthermore, Wang et. al showed that the effects of antiangiogenic therapy can be observed with USMI and DCE-US as early as 24 h after treatment [86]. Streeter et al. found that USMI of $\alpha_v\beta_3$ integrin is capable of differentiating between patient-derived xenografts that respond to aurora-A kinase inhibition and non-responders earlier than tumor volume as an indicator [87], and Sirsi et al. demonstrated that USMI can predict response of antiangiogenic therapy earlier than volume measurements [88].

Although most work on the assessment of response to therapy using CEUS has been focused on USMI, a few studies have shown the ability of US to evaluate response to therapy using DCE-US and AA. Zhou et al. recently demonstrated that both PE and AUC can be used to show response to antiangiogenic treatment before changes in tumor volume [89], and Kasoji et al. used a metric of

vascular density from AA to differentiate between responders and non-responders in tumors treated with radiation [74].

It is worth noting that there have been a handful of clinical studies that use DCE-US to assess early response to antiangiogenic therapy in renal, hepatic, and gastrointestinal cancers [20,90–93] and have shown promising results. However, even though targeted agents for USMI have recently been approved for patient use, there are not studies, to my knowledge, that have used USMI for the assessment of response to therapy in human patients.

To my knowledge, all previous pre-clinical work has used group statistics to show the effectiveness of CEUS to track disease progression, and while measuring differences in response to therapy between populations can provide valuable information for the overall treatment of disease, tracking and predicting response in individuals is more relevant for clinical translation.

CHAPTER 2

PHASE-CHANGE CONTRAST AGENTS

2.1 Introduction to Phase-Change Contrast Agents

Phase-change contrast agents (PCCAs) were introduced almost two decades ago for therapeutic applications, such as occlusion therapy [94–96], cavitation enhancement for tumor ablation [97–100], and aberration correction for diagnosis [94,101,102]. PCCAs conventionally have liquid cores composed of a perfluorocarbon (PFC) with a boiling point around body temperature, which can be vaporized, or activated, into microbubbles using ultrasound in an event termed acoustic droplet vaporization (ADV) by Kripfgans et. al [101]. ADV has been studied extensively over the years [103–110], and it has been found that acoustic vaporization of the liquid core is initiated by superharmonic focusing; high frequencies that can have wavelengths around the size of the agent are created by non-linear propagation and focused because of the difference in speed of sound between the PFC core and media around the agent [109,111]. Because ADV produces bubbles many times the size of the precursor PCCAs, these agents could be used in the occlusion of vessels for starving cancerous tissue or providing point targets for aberration correction.

2.2 PCCAs for Therapy

In the presence of gas bubbles, high-amplitude pressure waves can produce cavitation, which causes a violent collapse of the bubbles [112]. The collapse can cause local increases in temperature of 6500°C for a few microseconds due to the surrounding liquid rushing in to fill the void left by the bubble, as well as high amplitude shock-waves. Cavitation can increase tissue temperature beyond 55°C, which causes irreversible protein denaturing and cell death [113] for tumor ablation [114], but

offsite effects are common due to the high acoustic pressures used [115]. Using MCAs allows localization of the therapeutic effect to the target by providing cavitation nuclei but can cause skin lesions when the concentration of agents is too high [116]. Since PCCAs require acoustic pressures that exceed a certain threshold to become microbubbles, cavitation will only occur around the focus of the US pulse where that threshold is achieved, which helps to precisely control the location of the treatment [98–100]. Furthermore, PCCAs have been used for MR-guided tumor ablation [117,118], and cavitation of microbubbles created by ADV has been used for sonoporation in cells [119].

PCCAs can be manufactured to have a size of 100-400 nm, which may allow them to escape the vasculature in cancerous regions which have disorganized and “leaky” endothelial structures that allow nanoparticle diffusion into the tissue [120–122]. As such, PCCAs can be loaded with drugs and allowed to extravasate and accumulate in the tumor tissue for highly localized delivery [123–125].

2.3 PCCAs for Diagnosis

Although used mainly for therapy, PCCAs have characteristics that can overcome limitations associated with microbubble contrast agents, namely, short circulation time *in vivo* and the inability to extravasate, due to their size, to provide contrast for diagnosis or deliver therapeutic agents into the interstitium. Furthermore, the liquid core greatly reduces dissolution of the PFC into the blood and expiration through the lungs. Because of these advantages and the fact that PCCAs can be vaporized to form echogenic microbubbles capable of providing contrast, droplets have great potential for diagnostic applications, such as molecular and perfusion imaging [126,127].

2.4 Stability of PCCAs at Room and Body Temperature

It was believed that PCCAs remain in the liquid form due to increased Laplace pressure from the small curvature of the agent [128–130], but recent evidence suggests that the stability of droplets is due to the metastability of the pure PFC against vapor nucleation [131,132]. Regardless of the mechanism, PCCAs remain in the liquid form until an acoustic or thermal threshold is exceeded, which

precipitates nucleation of vapor embryos and subsequent vaporization of the entire droplet [107,108,130,131,133]. However, PCCAs have historically been composed of PFCs that are liquid at room or body temperature, such as perfluoropentane or perfluorohexane. Vaporization of these “liquid” PFCs in nano-sized PCCAs requires more energy than micron-sized droplets, so the high acoustic pressures required for activation exceed the Food and Drug Administration limit for diagnostic imaging.

2.5 Low Boiling-Point PCCAs

High boiling-point PCCAs may be desired for therapeutic applications because of enhanced stability *in vivo* and resistance against spontaneous vaporization. Additionally, their stability allows for spatial and temporal control of activation, since vaporization occurs only in areas targeted by acoustic energy and once a high acoustic pressure threshold is achieved. However, there has also been an interest in PCCAs that can be vaporized at low acoustic pressures well within the diagnostic ultrasound regime. Sheeran et al. developed sub-micron PCCAs using low-boiling PFCs that are stable at body temperature and can be vaporized using imaging acoustic pressures [128,129,134]. These low-boiling point droplets are typically composed of either decafluorobutane (DFB, -2°C boiling-point), octafluoropropane (OFP, -37°C boiling-point), or mixtures of these perfluorocarbons. Mixing the PFCs allows for tailoring of the vaporization threshold, so low boiling-point PCCAs have been used *in vitro* as temperature probes [135].

Low boiling-point PCCAs have been characterized extensively *in vitro*. The vaporization threshold has an inverse relationship with agent size and ambient temperature, and as expected, the more volatile PFC (OFP) has a lower acoustic [134] and thermal [131] threshold than DFB. Furthermore, it was found that PCCAs with a 1:1 mixture of DFB and OFP had vaporization thresholds in between those of DFB and OFP, suggesting that low boiling-point PCCAs can be tuned for different applications [134]. However, Mountford et. al showed that OFP preferentially leaks out of PCCAs with a mixture PFC core in environments that are not saturated with the mixture [135], such as *in vivo*, so more work is required to produce tunable PCCAs. Sheeran et. al showed that low-boiling point PCCAs

can be activated using short pulses (< 10 cycles) like those found in clinical scanners, using diagnostically relevant pressures, and that the microbubbles resulting from ADV have sizes similar to those of conventional MCAs or the precursor microbubbles that were condensed to make the PCCAs [130,134]. It is worth noting, however, that the resulting microbubble size after vaporization is often larger than the precursor bubble due to gasses in the environment diffusing in for several seconds after activation [128]. It has been observed that the lipid shell is conserved after condensation [134] and vaporization [136] by fluorescently labelling the shell, so it is not clear why the resulting microbubble is more permeable to gases in the environment. Furthermore, targeting ligands can be attached to the lipid shell since it is retained through condensation and vaporization, and molecular imaging has been demonstrated *in vitro* [126].

2.6 Vaporization Signal of Low Boiling-Point PCCAs

In addition to producing highly echogenic microbubbles, the vaporization event of low-boiling point PCCAs produces very specific acoustic signatures [137]. As the droplet is vaporized, it over-expands and oscillates down to its final size, producing acoustic signals between 0.25 and 2.5 MHz regardless of the excitation frequency (Figure 2.1). Furthermore, the vaporization signals have large amplitudes compared to those resulting from exciting microbubbles with the same pressures, and so, isolating droplet activation signatures may produce images that are specific to PCCAs and eliminate tissue or microbubble signal. Moreover, the low frequency of activation signals may provide better depth of penetration than conventional contrast ultrasound.

Since vaporization signals from droplets ranging between 100 and 400 nm in size have frequencies around 1.5 MHz, a transmit high/listen low strategy has been employed *in vitro* to produce images with high CTRs by transmitting around 8 MHz and receiving around 1 MHz using 2 piezoelectric pistons or a single capacitive micromachined ultrasound transducer [138,139]. However, this approach has not been extended to *in vivo* imaging.

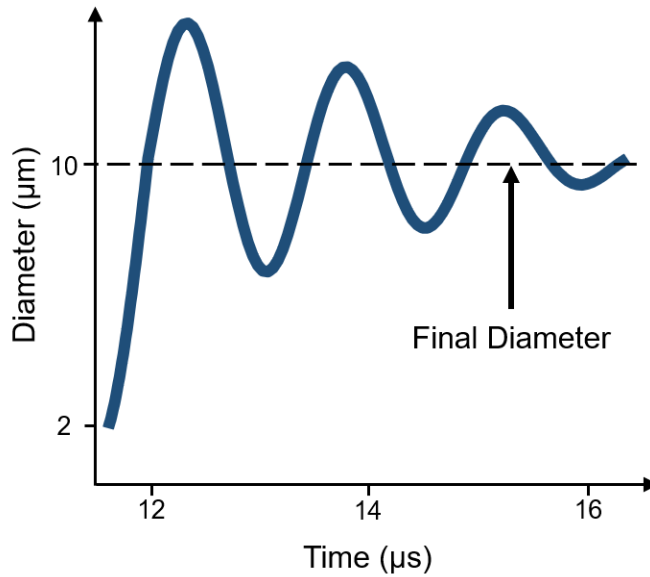


Figure 2.1. Vaporization and expansion of low boiling-point PCCAs. The agent overexpands and oscillates down to its final diameter. The resulting bubbles are around 5 times larger than the PCCAs.

In addition to the work mentioned previously, there have been *in vitro* studies on the condensation of PCCAs [140], the stability of the bubbles produced by PCCA vaporization [104,141], the effect of channel confinement on the contrast provided by PCCA activation [142], and characterization of vaporization using frequencies above 20 MHz [143], but few studies outside the work presented in this thesis have used PCCAs, either high or low-boiling point, for *in vivo* diagnostic imaging [143–145]. It is worth noting that in one of these studies, Nyankima et. al demonstrated that low boiling-point PCCAs can be safely used *in vivo* without causing bioeffects [145].

2.7 Possible Advantages of PCCAs for Diagnostic Imaging

Low boiling-point PCCAs offer advantages over MCAs that might enhance USMI and DCE-US for the assessment of disease and response to therapy. Namely, PCCAs can be manufactured small enough to extravasate, circulate longer *in vivo*, and provide spatial and temporal control of contrast generation. The ability to extravasate might allow PCCAs to target extracellular markers that are not expressed in the endothelium, which may enable the tailoring of treatment to specific patients and cancers; therapies may be more efficacious if changes in the expression of cancer-specific markers can

be detected, instead of changes in markers such as VEGFR-2 that are general to all cancers. For example, increased expression of human epidermal growth factor receptor 2 (HER2) in 25% to 30% of breast cancers correlates with poor disease-free and overall survival [146,147]. Additionally, anti-HER2 antibodies such as trastuzumab have been shown to have significant anti-tumor capabilities and to enhance the efficacy of treatment when used in conjunction with chemotherapy but only in tumors overexpressing HER2 [146,148,149]. Therefore, imaging HER2 can be important to identify aggressive breast cancers with overexpression of HER2 that may not respond well to chemotherapy and to determine if drugs, such as trastuzumab, are viable treatment options.

PCCAs may extravasate due to the enhanced permeability and retention (EPR) effect [120] and bind to markers expressed by cancer cells. In theory, the unbound PCCAs would then be cleared by the lymphatic system, leaving only bound droplets which could be vaporized to obtain USMI signal.

The enhanced circulation time of PCCAs may provide better binding per dose than MCAs, since the agents have more opportunities to bind; thus, smaller doses may be used to reduce the imaging time. Furthermore, PCCAs are only detectable with US after they have been converted to microbubbles, so there is no need to wait until most of the free-flowing agents are cleared from circulation; Vaporization pulses can theoretically be delivered at any point after injection, and after the free-flowing agents wash out of the plane of imaging following activation, the only remaining signal should be that of bound agents. Lastly, since vaporization can be carefully controlled by US, droplets provide excellent temporal and spatial control of contrast generation, so they can be used to measure perfusion in specific areas of the tissue of interest.

CHAPTER 3

ASSESSMENT OF TUMOR RESPONSE TO THERAPY USING MICROBUBBLE CONTRAST AGENTS^{1,2}

3.1 Introduction

In this chapter, the ability of CEUS to assess tumor response to therapy is demonstrated. The chosen model is a clear-cell renal cell carcinoma (ccRCC) xenograft that was evaluated using USMI, DCE-US, and AA.

Metastatic clear-cell renal cell carcinoma results in over 14,000 deaths annually in the US, and over 60,000 new cases are expected to be diagnosed this year [1]. This type of cancer is characterized by increased angiogenesis due to gene mutations in the von Hippel-Lindau gene (VHL), which upregulates various pro-angiogenic factors [150,151]. A common clinical therapeutic strategy for the treatment of ccRCC is antiangiogenic treatment [9,152–155]. Drugs such as Sunitinib, a small molecule multi-kinase inhibitor, reduces the signaling of the vascular endothelial growth factor (VEGF) pathway via its receptor VEGFR-2 [9,152–155]. The VEGF pathway plays a key role in tumor angiogenesis, such that inhibition reduces new vessel formation and starves the tumor. Antiangiogenic therapy is initially effective against ccRCC, which is characterized by increased angiogenesis [150,151], although

¹ © 2018 Ivyspring International Publisher. Reprinted, with permission, from JD Rojas, F Lin, YC Chiang, A Chytil, DC Chong, VL Bautch, WK Rathmell, PA Dayton, “Ultrasound Molecular Imaging of VEGFR-2 in Clear-Cell Renal Cell Carcinoma Tracks Disease Response to Antiangiogenic and Notch-Inhibition Therapy”, *Theranostics*, 2018; 8(1): 141-155.

² © 2018 IEEE. Reprinted, with permission, from JD Rojas, V Papadopoulou, TJ Czernuszewicz, RM Rajamahendiran, A Chytil, YC Chiang, DC Chong, VL Bautch, WK Rathmell, S Aylward, RC Gessner, PA Dayton, “Ultrasound Measurement of Vascular Density to Evaluate Response to Anti-Angiogenic Therapy in Renal Cell Carcinoma”, *IEEE Transactions on Biomedical Engineering*, 2018. In Review.

resistance to anti-angiogenic therapy is almost universally developed after several months of therapy [156–158].

Inhibition of the Notch signaling pathway is an alternative strategy to antiangiogenic therapy that also impairs angiogenesis. Notch signaling promotes vessel growth while suppressing excessive sprouting by down regulating VEGFR-2 on endothelial cells of the growing stalk [159–161]. Endothelial tip cells induce adjacent stalk cells to pattern new vessels [160–162]. Binding between Notch ligands such as Dll4 (Delta-like ligand 4) on tip cells and Notch receptors on stalk cells regulates the specialization of endothelial cells and limits sprout numbers [160,161]. This signaling pathway can be inhibited using gamma secretase inhibitors, which inhibit the activation of Notch via cleavage induced by ligand binding. Therefore, inhibiting Notch signaling yields a disproportionate number of tip cells, resulting in excessive sprouting and immature vasculature, which has been shown to inhibit tumor growth, likely due to inefficient perfusion [160,163–166]. These complementing inhibitory pathways provide an opportunity for parallel angiogenic blockade, and moreover, the additional expression of VEGFR-2 caused by the inhibition of Notch might cause ccRCC undergoing Notch inhibition to re-sensitize to the effects of VEGF receptor targeting. This proposed interaction has the potential to be a mechanism for overcoming resistance to conventional antiangiogenic therapy in ways that may be challenging to monitor with conventional imaging.

In this work, the ability of CEUS to track the response of subcutaneous ccRCC tumors to two kinds of therapy was explored. Mice were treated with an antiangiogenic VEGF receptor targeting, an inhibitor of Notch pathway activation, or a combination of the 2. USMI was used because both types of therapies affect the expression of VEGFR-2 on endothelial cells, so monitoring the levels of this biomarker might elucidate the effects on the tumor. Furthermore, the treatment strategies used here attack the vasculature and lead to inefficient perfusion, which can be quantified with DCE-US, and using AA to quantify vascular density might demonstrate the effect that the therapies are having on the

vasculature. Furthermore, since Notch inhibition produces excess sprouting, the enhanced tortuosity might be captured using AA and could be a good indicator of response.

3.2 Methods

3.2.1 Microbubble Contrast Agents

The contrast agents used for the USMI part of the study were VEGFR-2 targeted perfluorocarbon microbubbles (Visistar VEGFR2, Targeson, San Diego, CA, USA) with a mean diameter of $2.23 \pm 0.02 \mu\text{m}$. Competitive binding experiments show that Targeson VEGFR-2 bubbles produce significantly higher retention in tumors than similar control bubbles bearing isotype-matched antibodies [49], inactivated antibodies [167], or naked microbubbles without targeting antibodies [168].

The lipid-encapsulated perfluorocarbon MCAs used in the rest of this work were manufactured in-house and were similar to commercial lipid-shelled contrast agents. The lipids 1,2-distearoyl-sn-glycero-3-phosphocholine and 1,2-distearoyl-sn-glycero-3-phosphoethanolamine-N-methoxy (polyethylene-glycol)-2000 (DSPE-PEG2000) in a 9:1 M ratio and a total lipid concentration of 1.0 mg/mL were dissolved in a solution of phosphate-buffered saline, propylene glycol, and glycerol (16:3:1). Then, 1.5 mL of the solution was added to a 3-mL glass vial and the head space was gas-exchanged with decafluorobutane gas. Microbubbles (1 μm mean diameter and a 1×10^{10} #/mL concentration) were produced by using an agitation technique.

3.2.2 Xenograft and Treatment Protocol

NSG (NOD/scid/gamma) female mice (*Mus musculus*) were injected subcutaneously in the flank with 8×10^6 786-O human renal cell adenocarcinoma cells, which were obtained from Dr. William Kim at the University of North Carolina [169]. For the tortuosity experiment only, Nude (Nu/Nu) female mice (*Mus Musculus*) were injected with 1×10^6 VHL (R16Q) cells [170] in the flank. These cells have a mutation in the VHL tumor suppressor gene that often leads to RCC and are characterized with high vascular density and excessive sprouting.

Treatment started when the tumors reached 200 mm³ (caliper measurement) and continued for 5 weeks. The drugs used were a Notch pathway inhibitor GSI (Gamma secretase inhibitor, PF-03084014, Pfizer, New York, NY, USA) at a daily dose of 90 mg/kg, and VEGF inhibitor SU (Sunitinib malate, Selleckchem, TX, USA) at a daily dose of 50 mg/kg. The therapies were delivered by oral gavage.

For the USMI experiment a total of 32 mice were placed into 4 treatment groups: GSI, SU, a Switch group (SU to GSI), and Control (100 µL of saline). In the case of the Switch group, the mice were treated with SU for 3 weeks before switching to GSI.

For the DCE-US portion of this work, the mice were treated daily with GSI, SU, a combination of the two drugs, or saline. There were 4 mice per group, except for the GSI group, which had 3 animals.

The AA experiment contained 2 sections: vascular morphology (tortuosity) and vascular density analysis. For the morphology portion, 9 mice were divided into 3 groups: GSI, a combination of GSI and SU, and a Control (saline). The number of animals in each group for the density experiment were 8, 16, and 8 for the Control, SU, and Combo groups, respectively.

3.2.3 Animal Protocol and Contrast Administration

All imaging was performed using methods approved by the UNC Institutional Animal Care and Use Committee. An initial pre-treatment scan was acquired when the tumors reached 150 mm³, and the mice were imaged once per week until the end of treatment or until the tumor exceeded 2 cm (long axis), at which time they were euthanized in accordance with guidelines of the UNC Institutional Animal Care and Use Committee requirement. During each imaging session, the mice were anesthetized with 1.5% isoflurane and body temperature (37°C) was maintained using a heated imaging platform. The area of imaging was cleared of fur using an electric razor and further depilated using a chemical hair remover, and the tissue was coupled to the imaging transducer using water-based ultrasound gel. A 27G catheter was inserted into the tail-vein for the introduction of MCAs.

For the USMI experiment, a bolus of 2×10^6 of the Targeson microbubbles diluted in 100 μL of sterile saline was injected, followed by a 100 μL saline flush to clear the catheter and ensure the entire dose was delivered. An Accusizer 780 A (Particle Sizing Systems, Santa Barbara, CA, USA) was used to size the bubbles before every imaging session to ensure a precise dose was injected for all experiments. In-house MCAs were continuously infused at a rate of 6×10^7 bubbles/min for the DCE-US portion, and at a rate of 1.5×10^8 bubbles/min for both sections of the AA experiment.

3.2.4 Imaging and Analysis Protocols

3.2.4.1 USMI

All imaging was performed using an Acuson Sequoia 512 (Mountain View, CA, USA) driving a 15L8 linear array transducer. The imaging protocol utilized was a standard protocol for ultrasound molecular imaging, as previously described [49], and is summarized in Figure 3.1. A b-mode scan (14 MHz, 0.63 Mechanical Index) was obtained before the introduction of contrast agents for anatomical reference using the system's compounding mode. Next, a contrast baseline scan was acquired using cadence pulse sequencing (CPS), the imaging system's contrast-specific imaging mode. Contrast imaging parameters were: 7 MHz, -7 dB gain, and a Mechanical Index of 0.18, and were found to be non-destructive in preliminary work. A scan to capture the peak contrast enhancement was obtained 1 min after injection, and the bubbles were allowed to circulate for 7 min in order to allow for most of the freely-flowing contrast to be cleared from circulation. Preliminary studies showed that most of the free-flowing contrast was cleared from circulation by 7 min. Next, a second contrast imaging scan was captured, followed by a destructive b-mode scan (14 MHz, 1.9 Mechanical Index) in which the transducer was quickly swept over the tumor volume to remove bound bubbles. Lastly, the level of freely-circulating contrast was measured with a final contrast imaging scan 1 min after the destructive scan. All the imaging scans were captured in 3D by sweeping the transducer in the elevational direction over the tissue, as previously reported [58,67], using a step-size of 400 μm , and capturing a single contrast frame at each step.

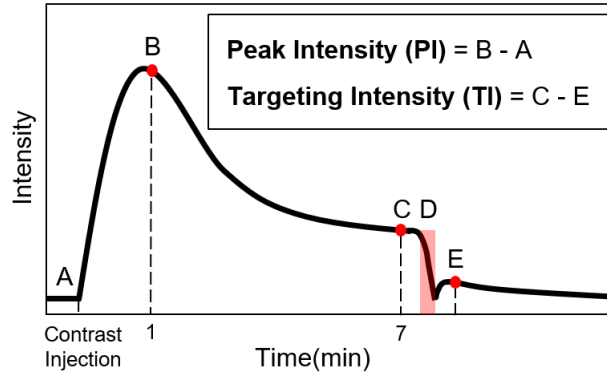


Figure 3.1. Summary of USMI imaging protocol. A baseline contrast scan was captured prior to the microbubble injection (A). A scan to capture the maximum peak intensity was taken 1 min after the introduction of contrast (B). The bubbles were allowed to circulate and bind for 7 min, at which time a contrast scan was taken (C). Destructive pulses clear the tumor of both bound and freely-flowing bubbles (D), and the level of freely-flowing contrast was obtained 1 min after destruction to allow bubbles to reperfuse the tissue (E). Note: data was only collected at B, C, and E and the solid black line is only an estimate of the intensity over time.

The scans were saved as JPEG-compressed DICOM files and were taken from the scanner for analysis. All analysis was performed using custom MATLAB scripts (The MathWorks, Inc., Natick, MA, USA). The volumetric b-mode scan was used to define a 3D region of interest (ROI) encompassing the entire tumor volume, and the mean intensity was calculated for each of the 3 CPS scans by averaging the intensity value of all the pixels inside the ROI. Furthermore, the number of pixels inside the ROI was used, in addition to the step size, to calculate the volume of the tumors. The targeting intensity (TI), a quantitative measure of the level of biomarker expression as indicated by the retention of targeted contrast in the sample volume, was calculated by subtracting the mean intensity of the post-destruction CPS scan (Figure 3.1E) from the contrast scan that was taken 7 min after injection (Figure 3.1C). Peak intensity (PI) was calculated by subtracting the intensity of the contrast baseline scan from that of the 1 min scan. This time point was chosen based on preliminary results, which show that microbubbles have perfused the entire tissue after 1 min, and the intensity in this scan is close to the maximum enhancement for the tumor model being used in this study and treated with the same therapies. Aside from finding the peak intensity, the PI scan was also used to find regions that did not become perfused within 1 min after injection. Based on the blood volume, cardiac output, and cardiac frequency in mice,

microbubbles spread throughout the body and circulate the vasculature several times in one minute and therefore, anechoic regions that have not been perfused by that time do not have patent vasculature and should be excluded from analysis. Since our intent is to compare biomarker presence within the vasculature, inclusion of regions without perfusion would bias this result.

Anechoic regions appear dark in the contrast images, but due to the nature of speckle, an area that is completely perfused will also contain small dark regions. Eliminating pixels that have intensities lower than a certain threshold would thus eliminate regions that are perfused in addition to regions that are anechoic. Therefore, the images were blurred using a Gaussian filter in order to eliminate small dark regions in areas that are full of contrast, in essence eliminating the speckle (Figure 3.2). Next, the regions of the image that were inside the analysis ROI and had an intensity lower than a predefined threshold were removed from the analysis region for the calculation of all metrics. The threshold was defined using preliminary data, and the same value was used for all animals at every time point. Furthermore, the different treatments affect functional characteristics of the tumor, such as perfusion, so the volume of the anechoic areas was used to calculate a “percent anechoic” (PA) metric to assess the response of the disease to the treatment over time. This metric is related to the amount of patent vasculature in the tumor volume, or lack thereof, due to necrosis or other factors.

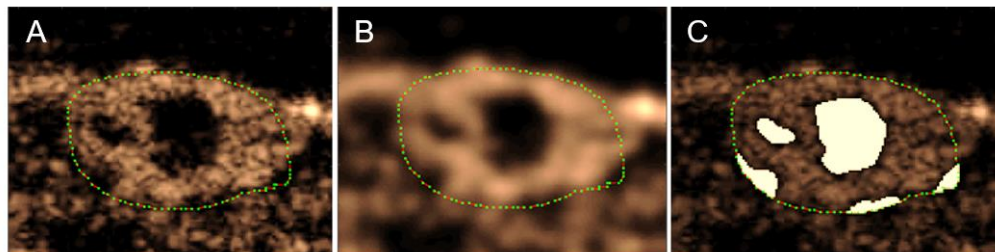


Figure 3.2. Method for obtaining anechoic regions in a peak intensity image (A). The green dots outline the tumor. The image is blurred using a Gaussian filter to eliminate dark areas in speckle (B). The regions below a predetermined intensity threshold are selected as anechoic (C). Note: these are single frames in a 3D volume, so the process will be performed for each slice in the volume.

The response of individual mice to the treatments was compared to the group TI, PA, and volume of the Control mice (Figure 3). A threshold was found for each of the metrics so that any values

above (or below) the threshold for individual mice at the different time points represented response to the treatment. For example, the individual volume (solid black line) in Figure 3.3 becomes smaller than the volume threshold (dashed black line) 3 weeks after the start of treatment, so it can be said that response was detected in the tumor volume at this time. The threshold value at each time point was calculated as the first quadrant of the grouped Control data at each time point for the TI and volume and the third quadrant for the PA. Finally, the percentage of mice in the SU and Switch groups that showed response (sensitivity) to the therapy using each metric was calculated for the first 3 weeks of treatment. The process was repeated for the control mice using the same threshold as with the treated mice to find percentage of animals that were correctly identified as untreated (specificity).

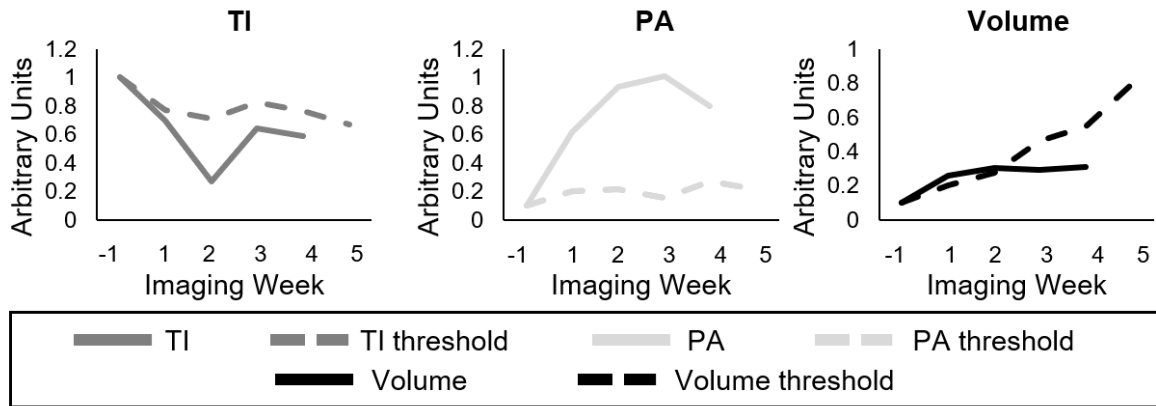


Figure 3.3. Example of individual response to the treatment. The solid lines represent either the TI (dark gray), PA (light gray), and the volume (black) for a single animal, while the dashed lines represent the threshold for each metric calculated using the Control group data. Each metric was determined to show resistance if the individual value (solid) was lower, for the TI and Volume, or higher, for the PA, than its threshold (dashed). The data for each metric were normalized to the pretreatment value, and by an additional factor in order to display the curves in the same scale.

3.2.4.2 DCE-US

All imaging was performed using an Acuson Sequoia 512 driving a 15L8 transducer. MCAs were allowed to circulate for 1 min before the start of imaging to allow for the bubble concentration in the blood to reach a steady-state level. The largest cross-section of the tumors was found using B-mode imaging, and the DCE-US imaging sequence consisted of 1 s of CPS imaging to obtain baseline frames, 1 s of destructive pulses to clear the microbubbles from the imaging plane, and 40 s of CPS imaging to

capture the reperfusion of bubbles back into the FOV. It has been shown that blood flow characteristics can be very heterogeneous in tumors [58], so the imaging sequence was repeated for five different cross-sections to capture the 3D perfusion of the tumor by scanning the transducer in the elevation direction using a computer-controlled motion stage [58]. Since the number of imaging cross-sections was set to five for all experiments, the spacing between imaging locations varied depending on the size of the tumor. A maximum of five planes were imaged because of infusion volume limitations.

For each imaging plane, a parametric perfusion map was generated by calculating the amount of time it took each pixel to reach 80% of the mean intensity from its baseline CPS frames, which is similar to what has been previously reported [56,58]. Pixels that did not reach the threshold in 40 s were left blank and will be referred to as anechoic areas. The mean value of the area inside the ROI of each perfusion map was calculated and averaged to obtain a volumetric perfusion time (VPT) for the entire tumor. The tumor volume was calculated by multiplying the total number of voxels inside the 3D ROI by the size of the voxels.

3.2.4.3 AA- Morphology

To acquire AA images, a Vevo 770 ultrasound system (VisualSonics, Toronto, Canada) was used to control a prototype transducer that allows for transmission at 4 MHz and reception of MCA super harmonic signals around 30 MHz [171]. Two co-aligned, single-elements were mechanically swept and one element was used only for transmit and the other only for receive. The low-frequency element was excited with a single-cycle sinusoid and produced a signal with a peak-negative pressure of 1.2 MPa [72]. In order to explore the changes in morphology resulting from the different therapies, a frame rate of 4 Hz with 5-frame averaging was used to isolate resolvable vessels and eliminate sub-resolution information, as was explained in Chapter 1. Additionally, the transducer was translated elevationally in steps of 100 μm to acquire 3D vascular images.

3D coordinates of individual vessels from the AA images were obtained using a computerized algorithm relying on height ridge traversal for centerline extraction [172]. Using the vessel coordinates,

the tortuosity, or “bendiness”, of the vessels was computed using different metrics previously described by Bullitt et al. [173], and used to characterize tumor vasculature from AA [40,72]. The metrics used were the distance metric (DM) and the sum of angles metric (SOAM). The DM was computed by dividing the length of the vessel by the Euclidian distance between start and end points, and the SOAM is found by calculating the integral of the curvature and normalizing by the vessel length, where the curvature is found by adding the angles between successive groups of 3 points along the vessel. While the DM is appropriate for vessels that loop or arc, the SOAM is effective for vessels that have high-frequency changes in curvature over short distances. Both types of vessels are found in tumors, but it has been found that the SOAM is a better metric for quantifying the tortuosity of cancer vasculature and separating between tumor and normal vessels [40,72]. Nevertheless, both metrics were used to evaluate the response of the tumors to the different therapies.

3.2.4.4 AA- Vascular Density

The imaging system used for this section was a VegaTM platform (SonoVol, Inc., Research Triangle Park, NC), which allows for automated 3D ultrasound image acquisition from mice. The system was used in both high-frequency/high-resolution B-mode for anatomical reference and AA mode for microvascular analysis.

A 3D B-mode “scout scan” with an elevational resolution of 200 μm of was used to locate the tumor. Next, AA images were captured around the tumor location 30 seconds after the start of the MCA infusion. AA imaging consisted of a continuous sweep acquisition, which produced images of vasculature with an elevational resolution of around 500 μm . The tumor was scanned 16 times, allowing MCAs to reperfuse into the tissue for 10 seconds between each scan, and a final AA image was computed by averaging all the acquisitions.

Tumor ROIs were manually segmented using SonoEQTM (SonoVol, Inc., Research Triangle Park, NC) analysis software from B-mode anatomical reference images. Blood vessel density (BVD), or the percentage of the tumor that had measurable perfusion, was computed from the AA

microvasculature images by dividing the number of voxels with intensity values higher than a fixed, predetermined threshold by the total number of voxels in the ROI. The tumor volume was calculated by summing the number of voxels inside the ROI and multiplying by the spatial dimensions of a voxel.

For calculating the BVD, a threshold that separates MCA signal from noise was first found. The threshold selected for all time-points was the value that provided the highest correlation coefficient (ρ) between the imaging results from the last imaging time-point and the results from histological analysis (described in the following section). The correlation coefficient was calculated using a right-tailed Spearman test and was used to evaluate how well the BVD results from imaging correspond to real physiologic characteristics of the tissue.

3.2.5 CD31 Immunohistochemistry

CD31 immunohistochemistry was performed to serve as a gold standard for comparison against imaging results. Tumors were harvested after the last imaging time point or earlier if the size limit was exceeded, or due to poor health. Three tumors from each treatment group of the USMI and vascular density experiments were used for the histological analysis, except for the SU group in the vascular density portion, from which 6 tumors were used. Immunohistochemistry was performed on paraffin-embedded tumor sections on a Leica Bond Max autostainer using anti-CD31 from Novocastra (cat # NCL-CD31-1A10). Following heat-induced epitope retrieval in EDTA for 20 min, the antibody was incubated on the tissue for 1 h at a dilution of 1:100 then visualized with diaminobenzidine (DAB). Thirty stained sections from each treatment group were captured by an Olympus DP 72 or an Infinity2 camera at 200x, and the percentage of positively stained area was determined using NIH ImageJ [174]. A separate cohort of animals was treated with SU and their tumors were harvested after 3 weeks of treatment to obtain a pre-switch measurement of patent vasculature for the USMI experiment.

3.2.6 Statistical Analysis

Kruskal-Wallis analysis was performed for each time point and metric in order to determine if there was a significant difference between any of the groups, and a Tukey range test was used to find

significance between each of the groups. Statistical analysis was performed on all mice available at each time point, regardless of whether the animal survived through the end of the study. ANOVA analysis was used to find any significance between the groups for histology and vessel morphology instead of the Kruskal-Wallis method. Significance was set at $p < 0.05$.

A right-tailed Spearman test was used to assess the correlation between the last imaging BVD timepoint (vascular density analysis section) and histology for different threshold values in order to select the most appropriate threshold.

Furthermore, the BVD at early time points was used to predict response to treatment (treated vs untreated, inferred from the tumor volume at later time points). The BVD around day 7 (day 6 to 10) after the start of treatment was plotted against the corresponding tumor volume measurements from around day 21 (day 17 to 24). A linear regression model was used to fit the data, so that a predicted tumor volume (PTV) for each animal could be calculated from the BVD around day 7. Next, PTV values above and below a threshold were classified as untreated or treated, respectively, for a range of thresholds. Using receiver-operator curve (ROC) analysis, the PTV threshold that produced the best sensitivity (true positive) and specificity (true negative) at separating treated and untreated was calculated.

3.2.7 Organization of Data

The mice started treatment at different days, since the dosing began once the tumors reached 200 mm^3 , so that imaging time points for different animals correspond to different days before/after the start of treatment. Therefore, the imaging time points that were captured before the start of treatment were binned into a baseline (-1) week, those that occurred between 1 and 7 days after the start of treatment were binned into week 1 of imaging, 8-14 days into week 2, 15-21 days into week 3, and 22-28 days after the start of treatment into week 4 of imaging.

3.3 Results

3.3.1 USMI

Example USMI images, taken 7 min after injection (Figure 3.1C), of a single mouse for each group are shown in Figure 3.4. The Control and GSI mice looked very similar throughout the study, but the effect of SU was apparent; for both the SU and Switch mice, the ultrasound intensity decreased after treatment, and the tumors became increasingly anechoic, suggesting necrosis. However, the size of the anechoic region decreased and the intensity increased immediately after the switch to GSI for the Switch group. Many mice in the GSI and Switch groups were euthanized before the fifth imaging session after treatment due to tumor size, and some of the SU-treated mice were euthanized prior to the end of the experiment due to morbidity. This left 1, 5, 3, and 5 mice in the GSI, SU, Switch, and Control groups, respectively, for the final time point. The data for the remaining mouse in the GSI group is not shown. The same mice were imaged for the duration of the study, and each group contained at least 6 mice at each time point. Results were not obtained for all the mice at each of the time points due to a technical problem saving the data on the Sequoia or due to lack of patent tail vein access on some animals late in the study.

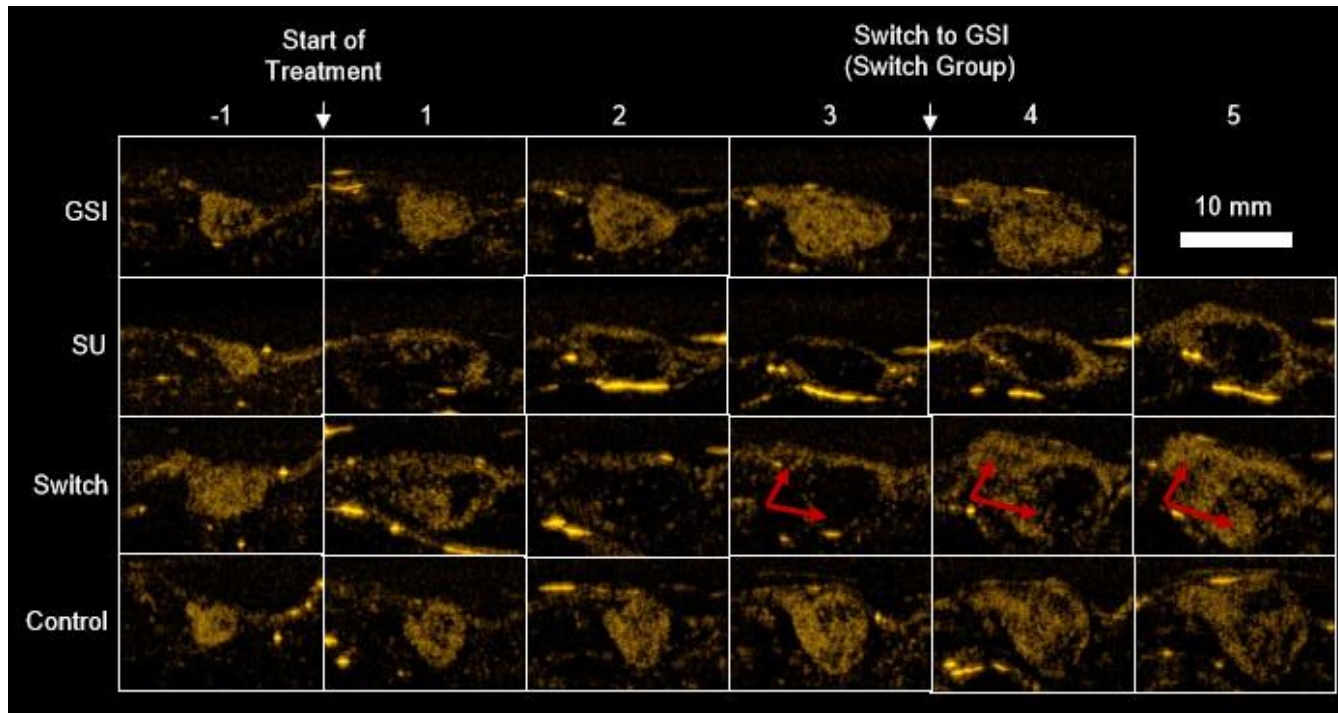


Figure 3.4. Example USMI images of different treatment groups taken 7 min after injection. GSI and Control groups remained similar throughout the study. TI for the SU and Switch groups decreased after the start of treatment, and the tumors became more anechoic. PA and TI increased for the Switch group after the treatment was changed to GSI, indicated by the red arrows. The strong reflections in the images are artifacts and were excluded from the analysis.

A significant difference in targeting intensity (TI), a measure of VEGFR-2 expression, can be seen 2 weeks following the start of treatment (Figure 3.5). TI for SU became, and remained, significantly lower than that of the Control group after the first week ($p < 0.05$ for all time points after the first week of treatment), while the TI of the GSI group remained non-significant from the Control group for the duration of the experiment. TI for the Switch group mimicked that of the SU group for the first 3 weeks after the start of treatment, but it increased after the switch to GSI and became non-significant from the GSI and Control groups 1 week after the switch. It is important to note that when the SU and Switch groups are combined, the TI was significant ($p < 0.05$) from that of the Control group 1 week after the start of treatment. Additionally, a subset of the SU and Switch groups was imaged 2 days after the start of treatment and there was a significant difference ($p < 0.05$) in the TI between this early time point and the baseline scan. USMI was able to closely track changes of VEGFR-2 expression as the result of the two types of therapy.

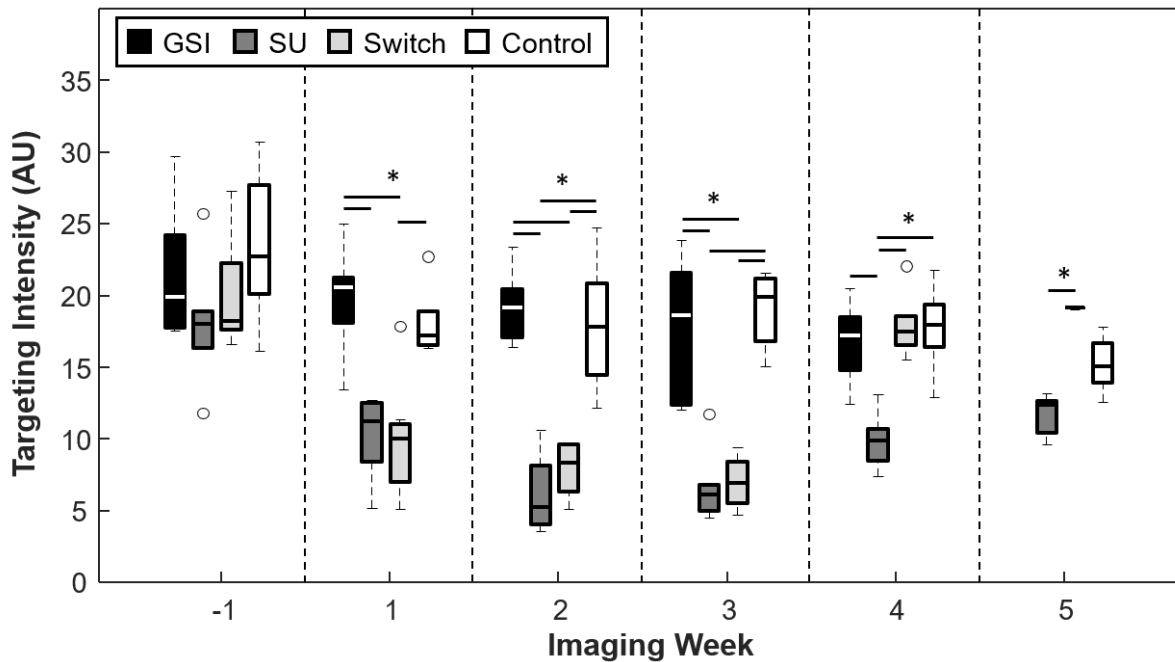


Figure 3.5. Targeting intensity (TI) for the different treatment groups and timepoints. The TI for the GSI and Control groups remained high throughout the study, while it remained low for the SU and Switch groups. However, TI increased in the Switch group after the change to GSI. Asterisks represent significance ($p < 0.05$).

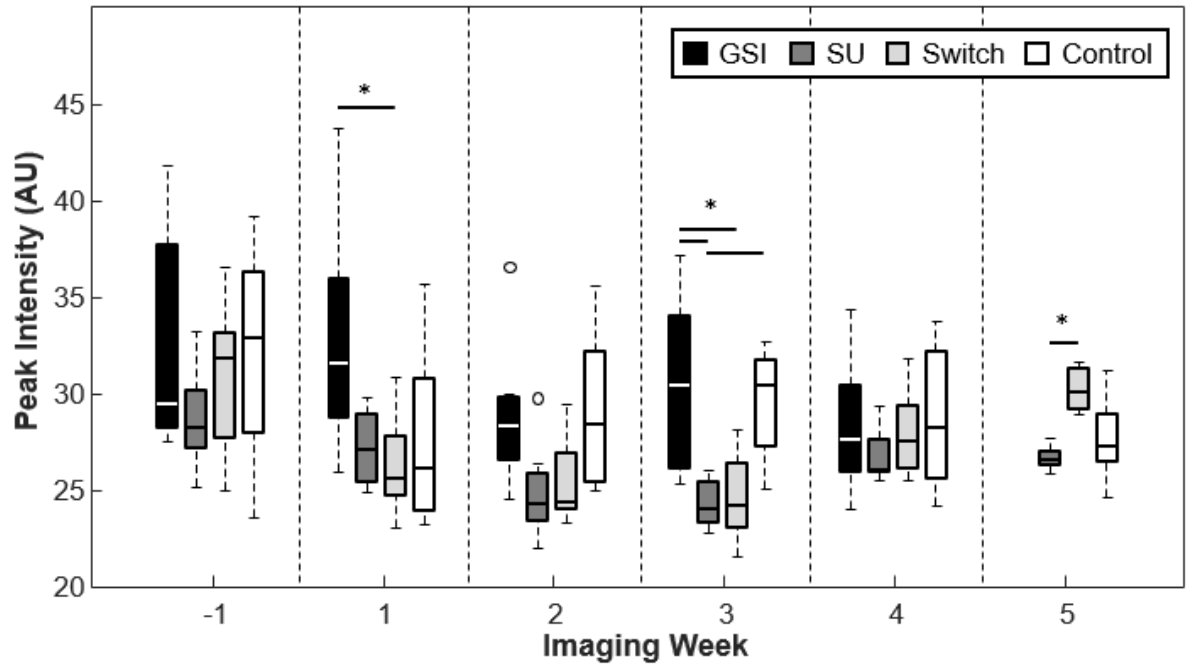


Figure 3.6. Peak intensity (PI) for the different treatment groups and timepoints. PI was typically lower for the groups treated with SU but this relationship was only significant 3 weeks after the start of treatment. PI increased for the Switch group once the mice were treated with GSI and became significant from SU 2 weeks after the switch.

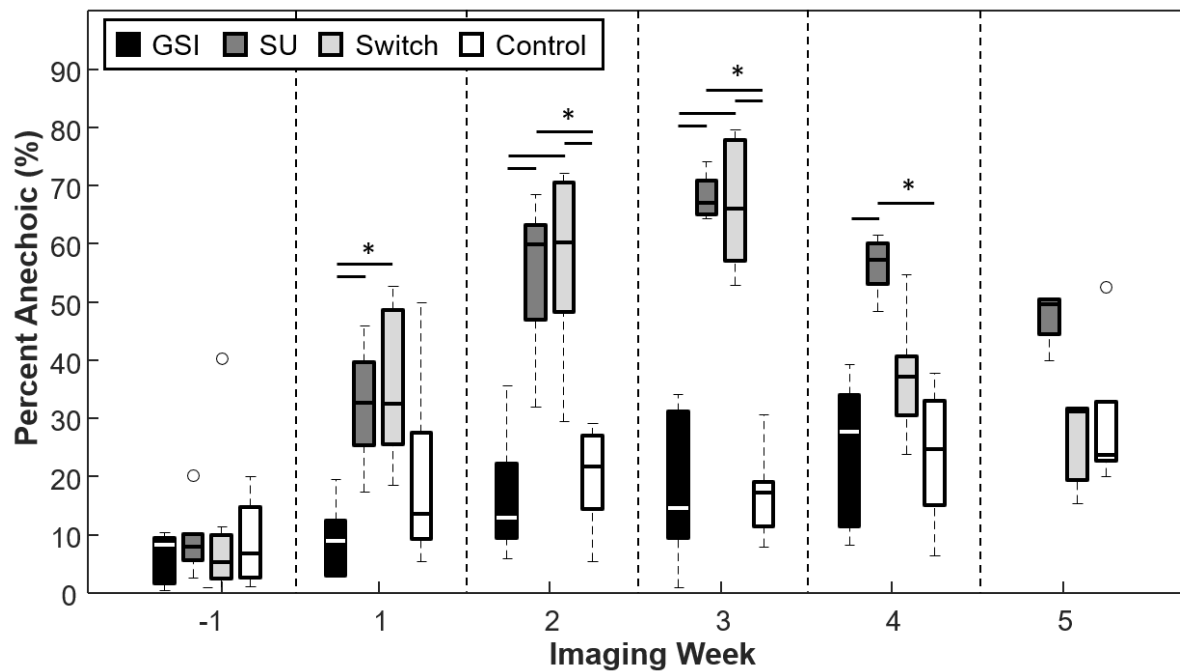


Figure 3.7. Percent Anechoic (PA) metric. Groups treated with SU displayed increased percentages of anechoic regions. The Switch group returned to levels similar to those of the Control group after the switch to GSI. The size of anechoic regions remained low for the GSI and Control groups.

The peak intensity signal (PI), captured 1 min after the injection of contrast, was reduced for the SU and Switch groups in comparison to the Control and GSI groups, but the results were only statistically significant ($p < 0.05$) 3 weeks after the start of treatment (Figure 3.6). The Switch group PI became significant from that of the SU group 5 weeks after the start of treatment. The PI did not provide any significant trends or differences between groups that indicate the ability to track response to therapy.

The groups that were treated with SU showed increased percentages of anechoic regions (PA) as the treatment progressed (Figure 3.7). The SU and Switch group became significantly higher ($p < 0.05$) than the Control 2 weeks after the start of treatment and 1 week after the start of treatment compared to the GSI group. The SU group remained significantly higher than the Control and GSI groups for the remainder of the study, except on the last time point, while the Switch group decreased after the switch to GSI and became non-significant from the Control and GSI groups and significant from the SU group ($p < 0.05$) the week following the switch. The PA for the GSI and Control groups steadily rose throughout the study but remained smaller and non-significant from the SU group. PA provided a useful measure of how the therapy was affecting the amount of patent microvasculature in the tumor throughout the treatment, and the results agreed with the reported effect of the drugs.

GSI enhanced tumor growth ($p < 0.05$) 1 week after the start of treatment and was significantly higher than the Control throughout the study except 2 weeks after the start of treatment (Figure 3.8). The groups treated with SU displayed reduced tumor growth throughout the study. The SU group became statistically lower ($p < 0.05$) than the GSI and Control groups 2 and 5 weeks after the start of treatment, respectively. The volume for the Switch group was similar to that of SU initially, but the change to GSI produced an enhancement in the tumor growth, as was the case with the GSI group, so that the tumor volume grew to be significant from the SU group ($p < 0.05$) one week after the switch. The change in volume eventually demonstrated a response to SU, but it was much later than USMI results.

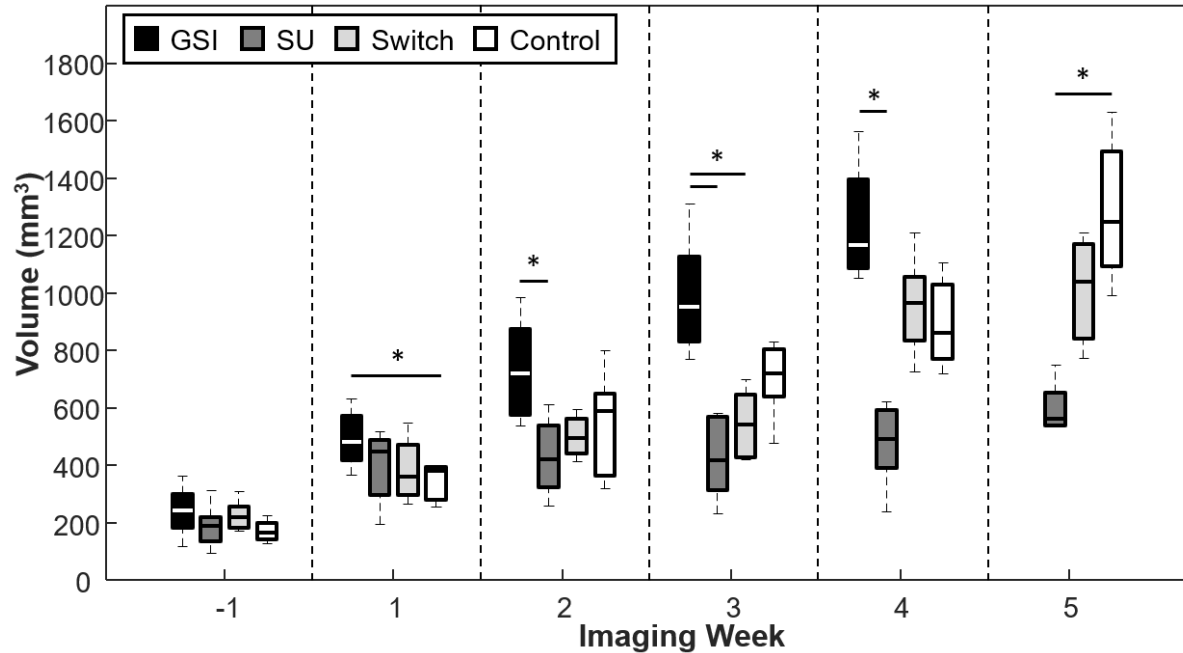


Figure 3.8. Tumor volume for the different treatment groups and timepoints. A reduction in tumor growth was displayed by the groups treated with SU, while an enhancement in tumor growth was observed for the GSI treatment group but was only significant at the 1-week point. The volume for the SU group became significant from GSI 2 weeks after the start of treatment, and after 5 weeks from the controls. The p-value between the SU and Control groups on week 4 was 0.069.

Immunohistochemistry was performed to examine the amount of patent vasculature, and, consequently, the amount of vasculature expressing VEGFR-2 in the tissues of treated xenograft tumors collected at the end of the study. Representative images of the different groups are shown in Figure 3.9. The stained area (SA) was calculated, and the results show that the SU group had a value that is significantly lower, while the Switch group was significantly higher, from all other groups. The GSI and Control groups were not significantly different in this model. Furthermore, the Pre-Switch group was significant from the Switch group. Overall, these findings corresponded closely with the *in vivo* assessments using ultrasound imaging.

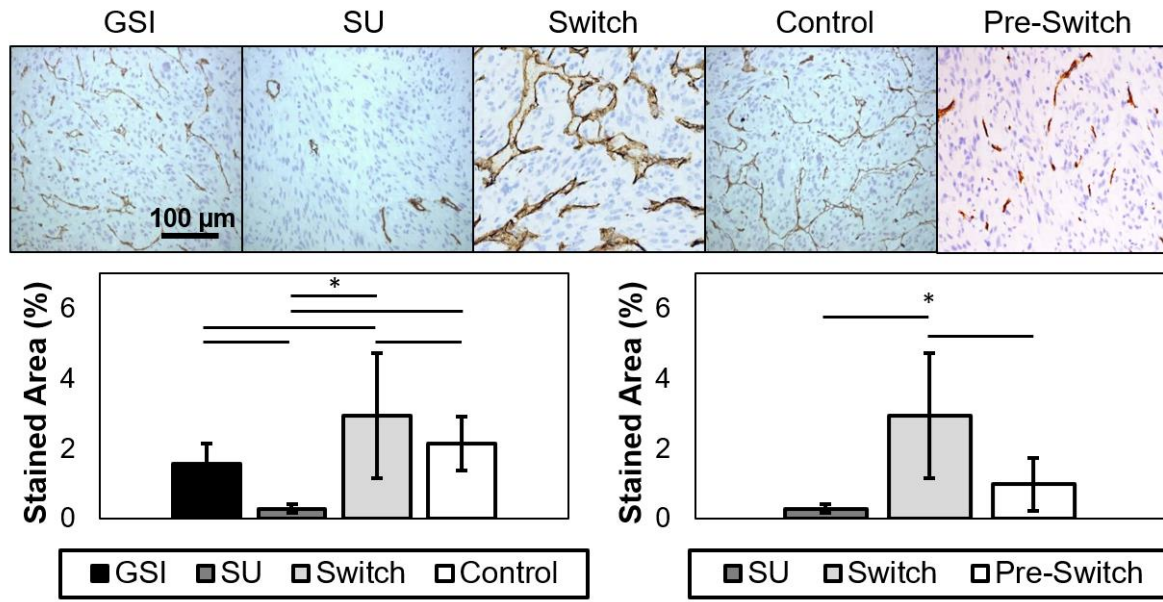


Figure 3.9. Representative images of CD31 immunohistochemistry (top) from USMI experiment. The dark brown stains represent expression of CD31 in endothelial cells. SA results from CD31 staining (bottom). The plot on the left displays the SA of the different treatment groups, while the plot on the right only shows the SU, Switch, and the Pre-Switch cohorts. The SU group has significantly lower values from the other groups, while the Switch group showed significantly higher levels of patent vasculature. The Pre-Switch cohort is significant from the Switch group.

Figure 3.10a-b shows examples of individual responses in the SU group for the TI, PA, and volume metrics, and Figure 3.10c-d gives examples of the Switch group. Analysis of individual responses shows that there were cases in both the SU and Switch groups in which the tumor volume showed response to the treatment at the same time as the other metrics. In both b and d, the individual volume value is smaller than the volume threshold 1 week after the start of treatment. However, the percentage of mice that showed response for each of the metrics over the first 3 weeks of treatment was calculated (Table 3.1), and the TI, PA, and volume detected response in 92.3%, 76.9%, and 40.0%, respectively, of the mice after the first week of treatment. These percentages increased to 100%, 92.3%, and 56.25% for the second week and to 100%, 100%, and 93% for the third week. Interestingly, volume was very sensitive to the change of treatment in the Switch group, and all tumors grew at a faster rate than that of the SU group after week 3 (Figure 3.10c-d). However, the change in TI and PA after the switch was much more abrupt, especially for TI, where 85% of individual values became larger than

the threshold after the switch. Furthermore, the specificity values, correctly identified untreated animals, were 83.3%, 83.3%, and 75% for TI, PA and volume, respectively, for week 1. The values remained similar at 80%, 83.3%, and 75% for week 2, and 66.7%, 66.7%, and 75% for week 3. The results demonstrate TI and PA were able to detect response to therapy earlier than tumor volume in individual cases with high sensitivity and specificity.

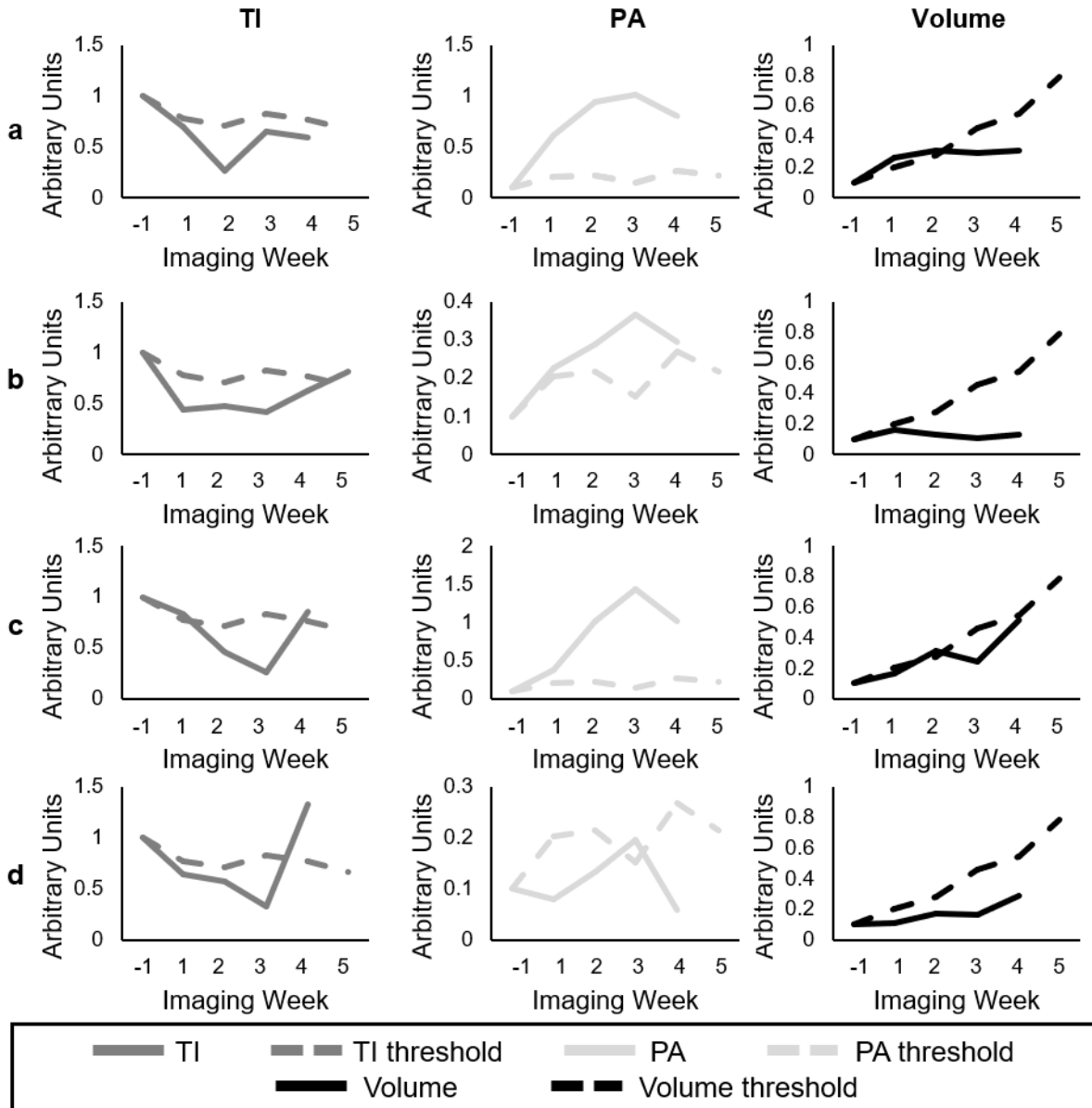


Figure 3.10. Examples of individual responses of SU (rows a and b) and Switch (rows c and d). The solid lines represent the individual values of TI (dark gray), PA (light gray), and volume (black) at each time point, while the dashed lines represent the group threshold for each metric, which was obtained from the Control data.

Imaging Week After Start of Treatment						
	Sensitivity			Specificity		
	1	2	3	1	2	3
TI	92.3	100	100	83.3	80	66.7
PA	76.9	92.3	100	83.3	83	66.7
Volume	40	62.5	100	75	75	75

Table 3.1. Sensitivity (true positive) and specificity (true negative) of the USMI metrics targeting intensity (TI), percent anechoic (PA), and tumor volume over the first 3 weeks of treatment.

3.3.2 DCE-US

Representative images of the perfusion maps for the different treatment groups are shown in Figure 3.11. The maps for the GSI and control groups were similar; the perfusion remained faster (green) than the SU and Combo groups after the start of treatment, but the anechoic regions increased significantly after 3 weeks of treatment. Conversely, large areas of poor perfusion (red) were seen in the SU and Combo groups immediately after the start of treatment and remained present for the duration of the study.

The VPT and volume results can be seen in Figure 3.12. Groups that had very different median values were not statistically significant ($p < 0.05$) because of the small number of animals in each group, so a lower significance level ($p < 0.1$) was also used to illustrate differences between groups. The VPT of the Combo group became significant from that of the Controls a week earlier than tumor volume measurements for those groups. The VPT or volume of the GSI and SU groups did not become significant from the Control group at any point in the study.

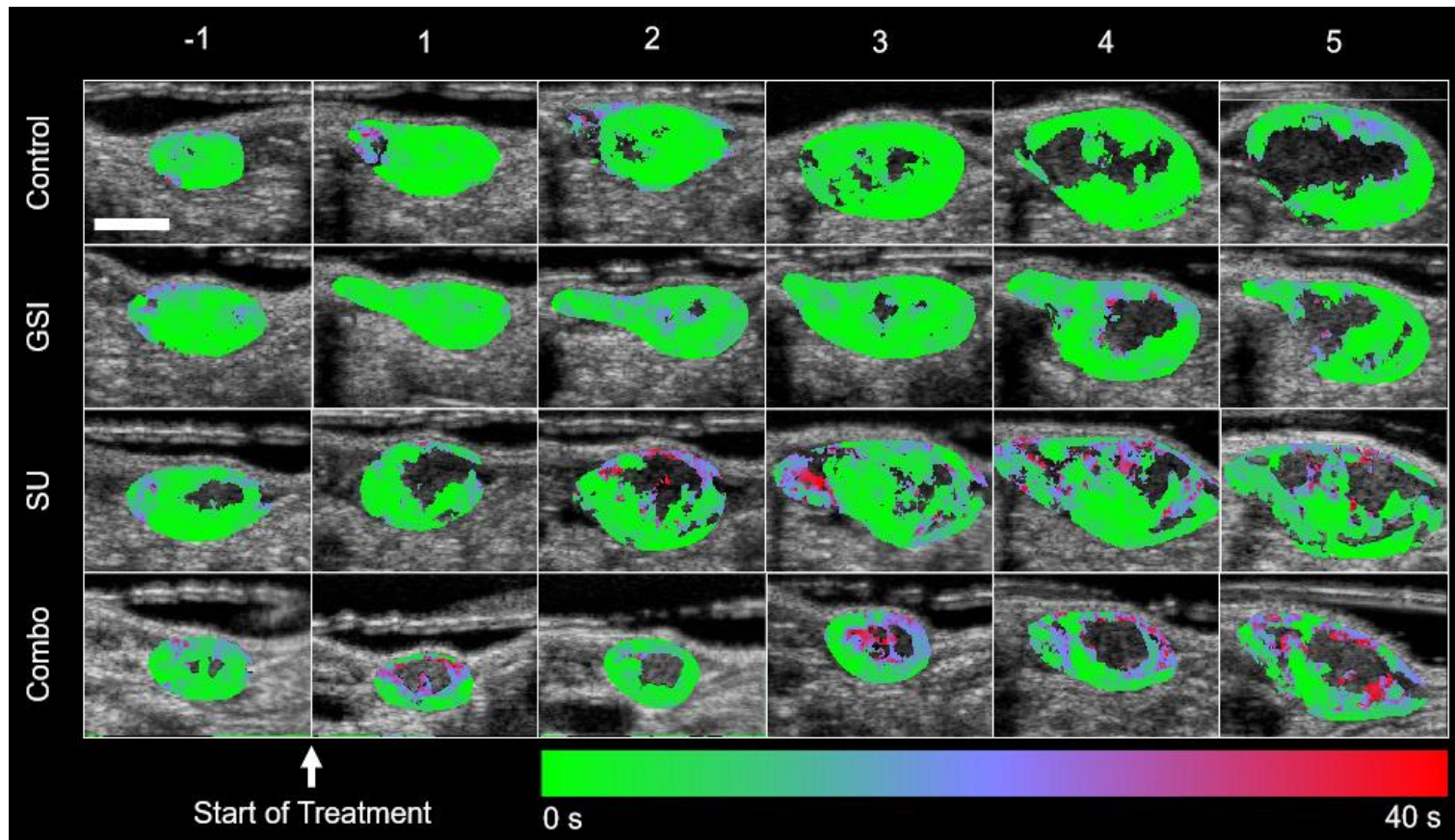


Figure 3.11. Representative perfusion maps overlaid on B-mode images for each treatment group. Treatment started after the first imaging time-point (-1), and the red and green color represents slow and fast perfusion, respectively. Scale bar represents 5mm.

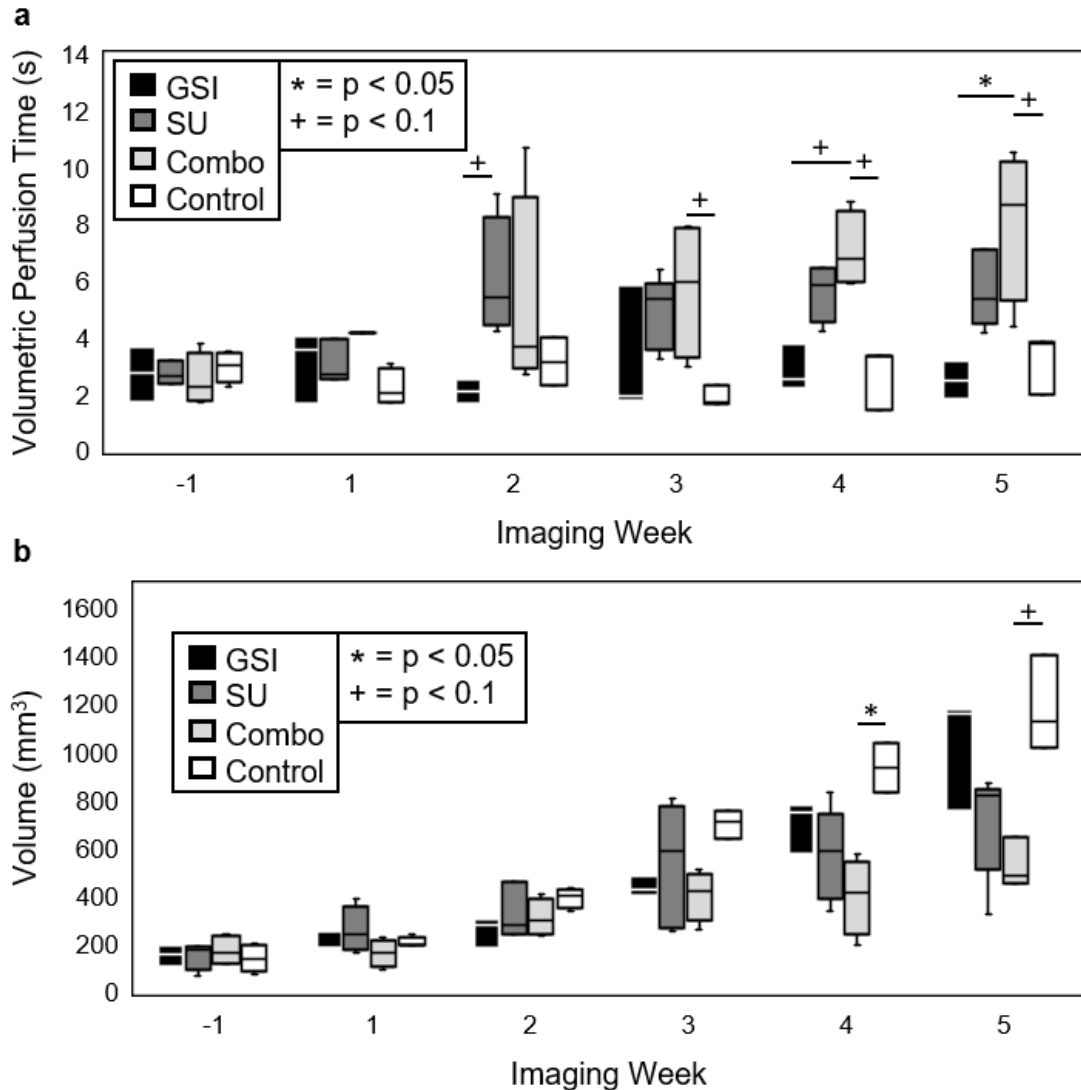


Figure 3.12. Plots of volumetric perfusion times (VPT) and tumor volume. Two levels of significance are displayed: $p < 0.05$ (*) and $p < 0.1$ (+). The Combo group became significant (+) from the control group 3 weeks after the start of treatment, while it took 4 weeks of treatment to produce significant (*) difference in tumor volume.

3.3.3 AA- Morphology

Figure 3.13 shows representative maximum intensity projections of AA images from the different treatment groups. Tumors from all groups have highly tortuous vessels (red arrows) in and around the tumor, and AA allowed for tracking of individual vessels where the tortuosity increased over time (blue arrow).

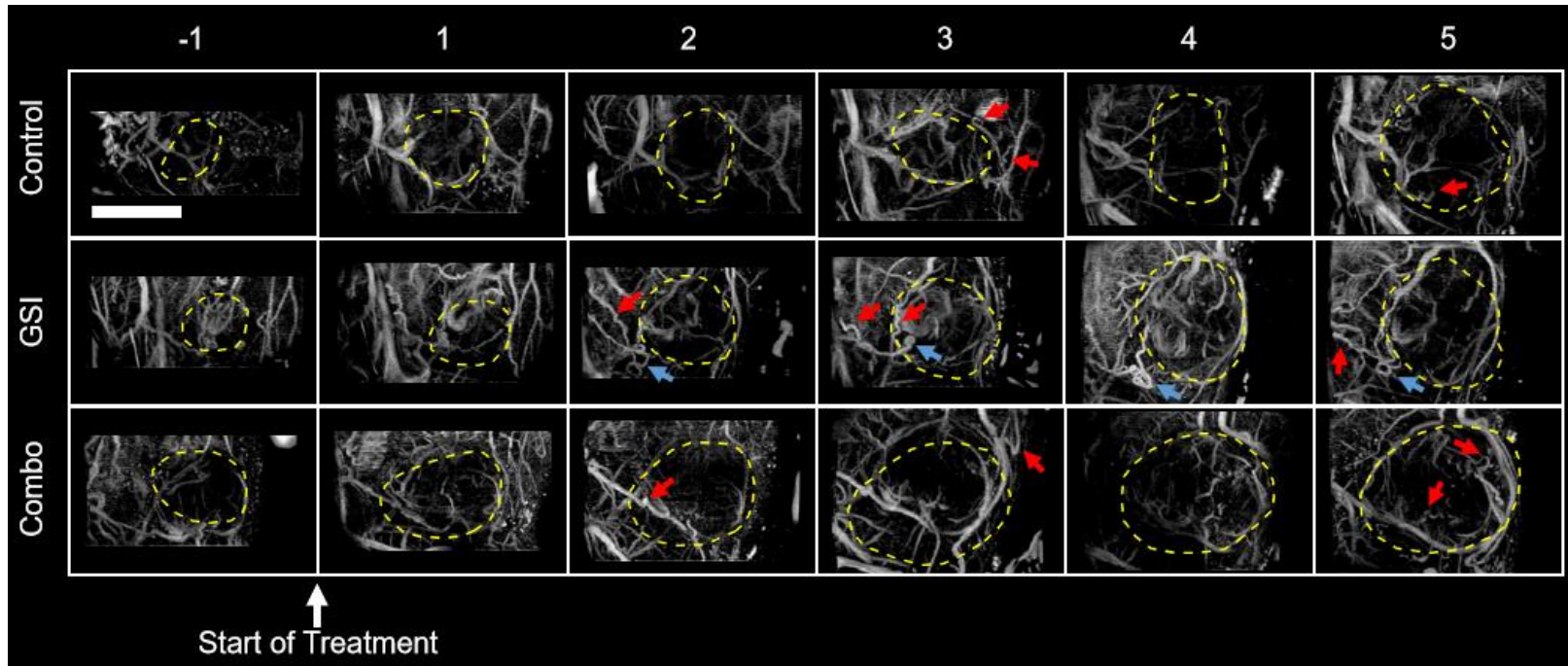


Figure 3.13. Representative maximum intensity projections of acoustic angiography images for the different treatment groups. The tumor is outlined by the yellow dotted lines and the scale bar represents 1 cm. The red arrows point to tortuous vessels, and the blue arrows point towards a vessels that was monitored as its tortuosity increased.

Between 50 and 100 vessels were extracted from each AA image, and vessels from all the tumors in each treatment group were grouped together (Figure 3.14). The results indicate that the DM did not provide any significant differences between treated and untreated vessels, and although the SOAM repeatedly produced a significantly ($p < 0.05$) different tortuosity between control and GSI vessels, the results are surprising since GSI was expected to produce more tortuous vasculature.

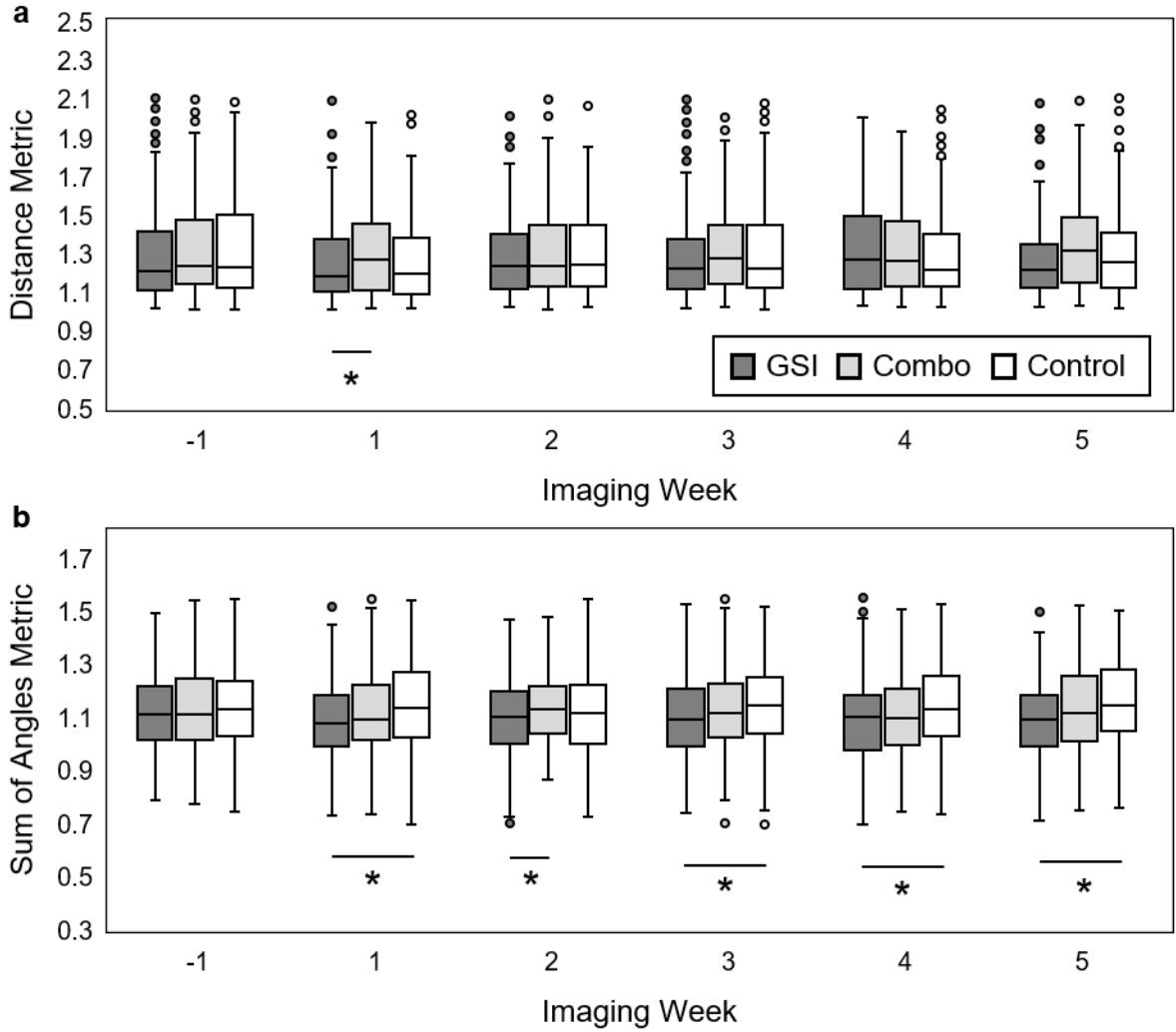


Figure 3.14. Results for the distance metric (a) and sum of angles metric (b). The distance metric for the Combo group was significantly higher than that of the GSI group 1 week after the start of treatment, but there was no difference between groups for the rest of the timepoints. Surprisingly, the sum of angles metric was of the Controls was significantly higher than the GSI group for most timepoints.

3.3.4 AA- Vascular Density

Figure 3.15 shows representative BVD images for each treatment group before the start of treatment and at the end of the study. At the pretreatment time-point, all tumors were well perfused (blue line indicates boundary, yellow indicates MCA). Over the duration of the study, untreated tumors in the control group (top row) exhibited continued growth without significant vascular changes, while the SU and Combo treated tumors (middle and bottom row, respectively) saw stunted growth and a marked decrease in MCA signal density and intensity, indicating vascular disruption.

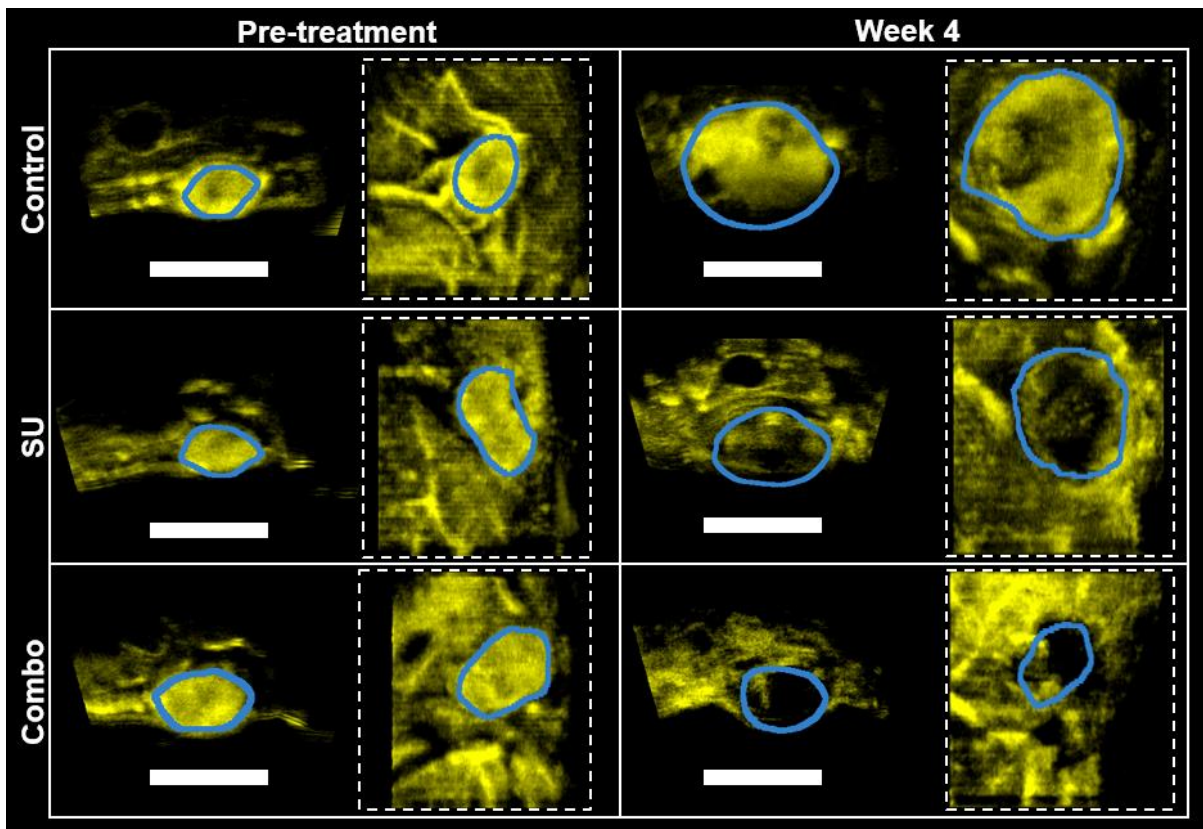


Figure 3.15. Representative vessel density images from the different treatment groups. Representative images are displayed at the beginning (left) and end (right) of the study. In each panel, the image on the left is a cross-section of the tumors while the image on the right (dashed square) is a coronal view. The scale bar represents 1 cm. Yellow indicates microvasculature acquired in AA mode. The blue outlines the tumor region of interest, and was derived via registered anatomical B-mode images (not shown).

Due to unknown health issues, tumor size limitations, and inability to insert the catheter into the tail vein for contrast administration, the different imaging weeks had varying numbers of mice (Table 3.2).

	Imaging Week				
	-1	1	2	3	4
Control	7	8	7	6	4
SU	11	12	11	12	8
Combo	6	7	5	6	4

Table 3.2. Number of animals imaged for each treatment week.

Quantitative assessment of tumor response to therapy is depicted in Figure 3.16. The BVD for the Combo and SU groups were significantly lower ($p < 0.05$) from the Control after only a week of treatment, while it took 2 weeks for the volumes to become significantly different between the groups (Figure 3.16). The BVD for the Combo group remained significantly lower from that of the Controls for the remainder of the study, and although the SU group had a lower median BVD value than the Control group, the difference was not statistically significant after the first week of treatment.

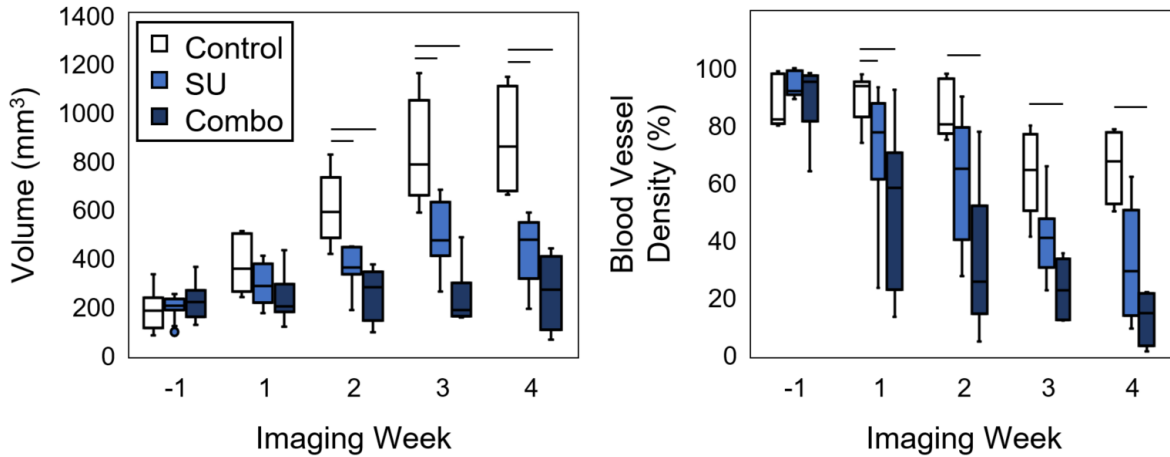


Figure 3.16. Tumor volume and blood vessel density for the different imaging weeks. The vessel density (right) of the SU and Combo groups became significant ($p < 0.05$) from the Controls 1 week after the start of treatment, while it took 2 weeks for a significant difference in volume (left) to emerge. Significance is denoted by the horizontal bars.

The volume measurements of all mice at every imaging time point after the start of treatment were plotted against the corresponding BVD values (Figure 3.17), and a line with a fixed y-intercept was used to classify the data points as treated (under line) or untreated (above line). Using the slope as a classifier, the sensitivity and specificity for a range of slopes were calculated. Setting the slope at $-0.06 \text{ \%}/\text{mm}^3$ (shown in Figure 3.17), the sensitivity and specificity were 89% and 92%, respectively, at classifying the control group from the treated groups. Moreover, when the same slope was used to classify the Control group from the SU and Combo groups individually, the sensitivity was 84% and 100% for SU and Combo, respectively.

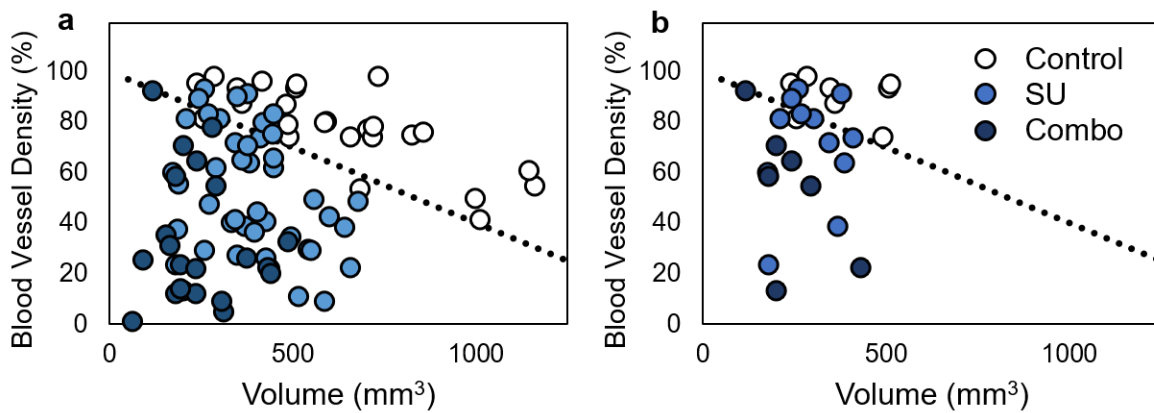


Figure 3.17. Plot of blood vessel density (BVD) vs volume for all datapoints. The two plots display the points after the start of treatment (a) and only those at week 1 (b). A line with a y-intercept set at 100% BVD (black dotted line) can be used to separate the data between treated (under the line) and untreated (above the line).

When only the data from week 1 was used for the analysis (Figure 3.17b), the sensitivity and specificity were 84% and 88% when classifying between treated and untreated, and the sensitivity was 75% and 100% for the SU and Combo, respectively, when the Controls were classified against each group individually.

The histological results collected after 4 weeks of treatment demonstrate that the amount of CD31 neovasculature via staining in the tumors for the SU and Combo groups was significantly lower ($p < 0.05$) than that of the Controls (Figure 3.18). The stained area was quantified and compared to the BVD results, and a strong correlation was demonstrated (Figure 3.19). Furthermore, the correlation

coefficient ρ was similar between the users ($\rho = 0.77 \pm 0.03$). These results confirm that vascular density measurements acquired through AA imaging correlate with histological vascular density measurements.

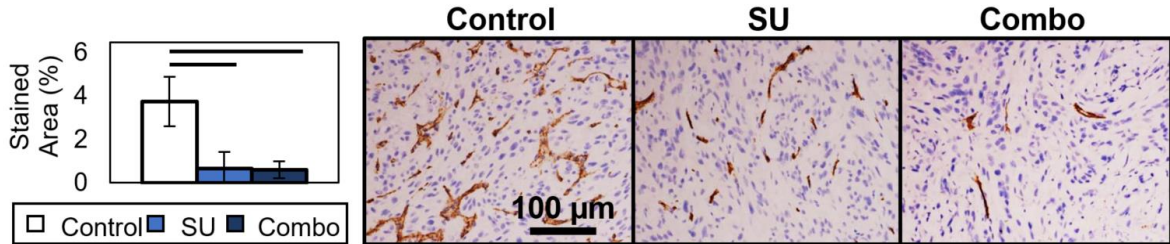


Figure 3.18. Representative CD31 staining images of the different treatment groups and Stained Area results. The SU and Combo groups had significant values ($p < 0.05$) from the Control group. SU and Combo groups were not statistically significantly different from each other.

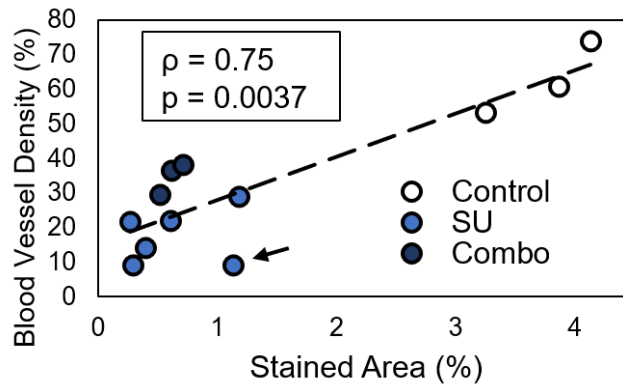


Figure 3.19. Correlation plot of image derived blood vessel density (BVD) vs CD31 stained neovasculature. The results show strong correlation ($\rho = 0.75$) between imaging and histology. Dotted line indicates the linear regression line. The black arrow is pointing towards an outlier measurement in the plots that reduces the strength of the correlation.

The relationship between BVD around day 7 versus tumor volume around day 21 had a significant correlation ($p < 0.001$) and a spearman coefficient of 0.82 (Figure 3.20). An ROC curve was plotted using different PTV thresholds found using the equation of the linear fit model (Figure 3.20a) and the BVD values from around 7 days after the start of treatment (Figure 3.20b), and the curve indicates that a maximum sensitivity and specificity of 94% and 86%, respectively, can be obtained when using a PVT threshold value of 705 mm³. Therefore, the results show that BVD can be used to differentiate between treated and untreated tumors for individual mice with strong confidence.

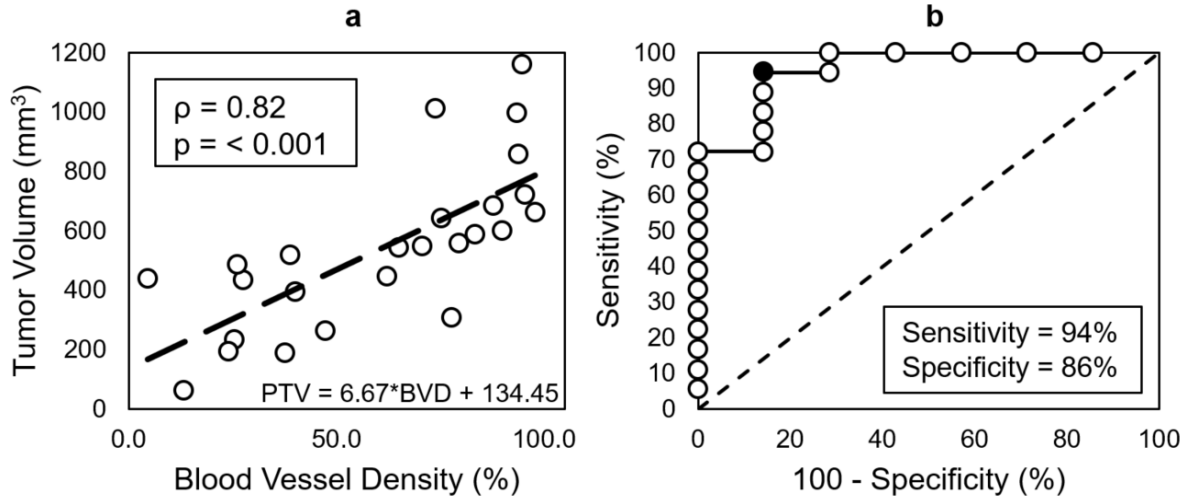


Figure 3.20. Linear regression model used to calculate predicted tumor volume (PTV) and ROC curve for PTV as a classifier. Plot (a) shows the linear regression model (dashed black line) of BVD vs tumor volume used to calculate PTV, and plot (b) shows the ROC curve for PTV as a classifier of treated and untreated tumors. The black filled in circle in the ROC curve represents the PTV threshold with the highest sensitivity (94%) and specificity (86%) and corresponds to a value of 705 mm³. The dashed line in (b) represents a random chance (50%) of correctly classifying the data.

3.4 Discussion

Resistance to therapy is the major limitation of disease control in most cancer types. Thus, it is important to track disease response to adjust treatment for enhanced efficacy. Furthermore, it is also important to accurately and closely track response to therapy of tumors to minimize undesirable side effects of chemo or radiotherapy if treatment begins to fail. Moreover, the array of available therapies for ccRCC is expanding rapidly, creating a scenario where selecting therapy for an individual patient will be more relevant than ever. Conventional methods for evaluating response to therapy typically rely on changes of tumor volume, typically at an interval of 3 months, but tracking volume has been shown to be inaccurate and often underreports the effect of therapy. Imaging techniques such as dynamic contrast-enhanced MRI and metabolic PET imaging have been shown to be effective at tracking and predicting response to therapy by providing functional insights rather than simple changes in tumor volume. These modalities are associated with challenges such as lack of bedside support, cost, contrast contraindications (MRI), and requirements for access to short-lived isotopes (PET). In contrast, CEUS

is inexpensive, portable, and has been shown to outperform volume measurements for disease assessment.

Attaching targeting ligands to MCAs allows for molecular imaging of biomarkers expressed in different diseases. Here, it is shown that the response of ccRCC tumors to VEGFR-2 antiangiogenic and Notch inhibition therapeutics in mice can be accurately tracked throughout the course of therapy using USMI of VEGFR-2 and AA, and the imaging results agree with histological data. Furthermore, we show that USMI and AA can detect statistically significant molecular and functional changes weeks before measurable differences in tumor volume between the treatment groups and the Control group, which indicates that CEUS can be a powerful diagnostic tool for the assessment of disease. The results of this work are consistent with findings from previous work [74,80–82,84–86], but we have also shown here that CEUS can detect response to therapy in individual cases before changes are detectable in tumor volume with high sensitivity and specificity.

3.4.1 USMI

Antiangiogenic drugs, such as SU, enzymatically inhibit and down-regulate VEGFR-2 to inhibit angiogenesis [154,155]. We were able to observe changes in TI corresponding to changes in expression of VEGFR-2. The results show that the anti-VEGF therapy was effective at arresting development of new vasculature, which may have led to anechoic areas, and more importantly, that CEUS can track the tumor response to the treatment more accurately than volume measurements. Additionally, the results showed that a significant difference in TI can be found only 2 days after the start of treatment (Figure 3.5). This is consistent with recent findings indicating that a change in VEGFR-2 expression 24 h after treatment can be detected with USMI using microbubbles targeted to VEGFR-2 before there are detectable changes in tumor growth [86]. Furthermore, the effect of SU can easily be seen in the tumors as an increase in anechoic areas and quantified in the PA metric, which provides another example of the ability of CEUS to detect tumor response to treatment faster and more accurately than tumor growth (Figure 3.7). Moreover, PA calculations can be accomplished with non-

targeted contrast, which could facilitate translation into the clinic since non-targeted contrast agents, such as Definity (Lantheus Medical Imaging, N. Billerica, MA, USA), are already FDA approved for certain applications.

TI and PA results showed that CEUS can detect response of populations to therapy, which can be important for designing new treatment regimens for combating cancer. However, detecting response in individuals is more significant for clinical translation since physicians use individual patient information to tailor the treatment. Here, we show that CEUS was able to detect the individual response (sensitivity) to therapy of most of the mice in the SU and Switch groups by the second week of treatment, while the chance of detecting response with the tumor volume by that time was slightly higher than a coin toss (Figure 3.10). Moreover, the specificity was higher for the imaging metrics than the volume for the first 2 weeks. The tumors used here grow rapidly and their vasculature becomes inefficient over time without any treatment, which is likely the cause of the specificity for the imaging metrics decreasing after the second week. Nevertheless, CEUS was very sensitive to changes in the tumor as a result of therapy and thus, it has great potential as a personalized theranostic tool.

Taken together, these results demonstrate that CEUS has the potential to be a valuable clinical tool for assessing response to treatment without having to biopsy the tissue or wait for delayed changes in tumor size and may allow doctors to tailor treatment to individuals for better efficacy. Furthermore, early identification of ineffective treatments may reduce side effects.

The PI did not significantly vary between treatment groups, which is surprising, given that the GSI and Control groups seemed to have better perfusion and smaller anechoic areas (Figure 3.6). A possible explanation of why PI remained similar among the groups is that there is significant bubble binding by 1 min and therefore, the intensity might be a result of the perfusion of the tissue in addition to VEGFR-2 expression. Thus, PI might not be suitable for the assessment of disease progression. A better technique might be to track the intensity for the first few minutes after injection in order to find

the true peak intensity, as is done by Wang et. al [86], which showed that peak intensity can measure changes in response to therapy.

The results of the staining demonstrate that USMI of VEGFR-2 demonstrates real physiological characteristics of disease. As expected, levels of patent vasculature in the SU group were the lowest among all of the groups, while those of GSI and Control were about the same (Figure 3.9). Furthermore, the Switch group had significantly higher SA than all other groups, most likely caused by the switch to GSI. Additionally, the Pre-Switch SA was significantly lower than the Switch group, confirming that the increase in patent vasculature in the Switch group was caused by the change in treatment. Staining for VEGFR-2 was also performed, but the results showed expression in regions where patent vasculature was not present. Most likely, this is a result of extravascular VEGFR-2 expression or endothelial receptors of non-patent vessels. Since the contrast agents used in this study can only bind to intravascular VEGFR-2 receptors, VEGFR-2 staining results were not included. Nevertheless, we believe that USMI can be a valuable tool for disease monitoring, since it provides information about molecular biomarkers of disease that can be used to closely track disease state and response to therapy without the need for multiple biopsies or exposure to ionizing radiation.

The Notch signaling pathway regulates proper development of new vasculature, and it has been reported that inhibition leads to excessive sprouting, immature vessels, and a reduction in tumor growth [163–165]. Notch inhibition promotes expression of VEGFR-2, so it is not surprising that the TI of the GSI group remained high throughout the experiment (Figure 3.5). Moreover, it is not surprising that the Control and GSI groups had similar levels of TI, since ccRCC is characterized by increased levels of angiogenesis and upregulation of angiogenic growth factors. Previous work suggests that the excessive sprouting resulting from Notch inhibition leads to inefficient perfusion and a reduction in tumor growth [163–166]; however, the results of treatment with this drug as a single agent in a ccRCC xenograft model demonstrate efficient vasculature in the GSI group with PA and PI values similar to the controls and an enhancement in tumor growth. This somewhat surprising result, however, must be

considered in context. In the study reporting on GSI Compound X causing regression in a renal cancer model, Kalen et al. [175] were utilizing the mouse RENCA model. This model system differs from ours in important ways. First, while this is a spontaneously arising kidney tumor from a Balb/C mouse, it lacks the common feature of human renal cell carcinoma, which is inactivation of VHL gene. VHL loss causes a high level of tumor microvasculature and upregulation of glycolysis, driving a unique dependency on oxygen and nutrient delivery. It is this dependency that renders VHL mutant renal cell carcinoma sensitive to the wide variety of anti-VEGF pathway agents currently in clinical use. However, this dependency may make the extra sprouting produced in response to GSI treatment an advantage to the specific physiology of this tumor type. Our model has a well-characterized VHL mutation and is known to demonstrate customary features of human clear cell renal cell carcinoma. The interaction between VEGF pathway targeted therapy and the vascular effects of GSI, however, highlights an intriguing alternate set of targeting strategies to alter vascular properties in tumors, the combination of which may be effective in renal cell carcinoma and potentially in a wider array of cancer settings. As discussed above, finding the PI may not be the best technique for approximating perfusion measurements, so further work is required to assess changes in perfusion efficiency as a result of Notch inhibition.

When the tumors in the Switch group were treated with GSI, the treatment appeared to normalize features of the vasculature, promoting angiogenesis so that the PA was reduced to levels similar to those of the controls. Higher TI suggests greater expression of VEGFR-2 (Figure 3.5). This reversal in the state of the vasculature is only detectable by using CEUS, since the tumor volume of the Switch group remains non-significant from the Control group. However, the volume of the Switch group did become significant from that of the SU group 1 week after the change in treatment to GSI.

Normalization of tumor vasculature has been shown to enhance therapeutic effect in different types of cancer [176–178]. Tumor vasculature is leaky, which produces increased interstitial pressure, and in turn inhibits delivery of therapy into the tissue [179,180]. By normalizing the vasculature and

making it less permeable, the interstitial pressure can be reduced, allowing for drugs to extravasate in larger concentrations for better efficacy [179–181]. We have shown that GSI produced normalization in the vasculature in ccRCC tumors that were first treated with SU. Additionally, it is possible that by renormalizing the vasculature of tumors that stop responding to antiangiogenic therapy, resistance can be overcome. Moreover, we show here that ultrasound can be used to track the progression of the disease and even though we did not conclusively detect the emergence of resistance to SU in the time frame of the study, CEUS can be used to monitor the disease and make the switch to GSI when the tumors start showing signs of resistance.

The mice were imaged on set days of the week, when the tumor reached 200 mm³ (caliper measurement). Since not all of the tumors reached the size threshold at the same time, some mice were treated for different durations before their first imaging session after the start of treatment. Therefore, the effect measured by the different metrics on week 1 (the week after the start of treatment) might have been reduced and may be more drastic than the data show. Furthermore, the small number of mice in each group may have affected at which time point response was detected with the different metrics. For example, the volume of the SU and Control groups does not become significant until 5 weeks after treatment, but the p-values for week 3 and 4 are 0.066 and 0.069, respectively (Figure 3.8). Larger sample sizes would be required to validate this effect. An additional limitation of the study was that all analysis was performed on log compressed data, and while data compression did not allow calculation of absolute differences in intensity between the different treatment groups for PI and TI, relative differences are still valid, so the overall trends and results hold.

Since statistical analysis was performed on all mice at each time point, even if they did not survive the entire study, the results might be biased and indicate a better treatment efficacy for the SU group; presumably, if the health of the mouse was poor, the tumor could progress more aggressively than in a healthy mouse. However, most of the morbidity was due to tumor size limitations, so we do

not expect that the overall results of the study would be significantly changed if statistical analysis were only performed on the animals that survived the entire study.

While the different treatments slowed the tumor growth, no regression or stagnation was observed in this study. In the case of SU, the dose was chosen based on previous work [64,65], and absence of regression is likely due to the early emergence of resistance. The chosen dose of GSI, 90 mg/kg, was shown to be effective against a breast cancer model [66], but it was not optimized for this work, so it is possible that the mice were under-dosed. However, we observed vascular effects that were histologically consistent with the enhanced sprouting expected with Notch inhibition. In addition, mice suffered from weight loss in pilot studies where a dose of 150 mg/kg was used.

Since most of the mice were sacrificed because their tumors grew beyond the size limit, it is difficult to evaluate survival outcome. Therefore, even though USMI can be used to track disease progression, more work is required to assess the ability of this technique to predict eventual survival outcomes.

3.4.2 DCE-US

The results show that DCE-US is a promising diagnostic tool for evaluating the response of cancer to Notch and antiangiogenic therapy. The perfusion of the combination treatment became significantly ($p < 0.1$) slower from that of the untreated animals a week before there were any significant changes in tumor volume (Figure 3.12), illustrating that functional changes can occur before measurable changes in size so CEUS can be a better strategy for tracking the response of cancer to different treatments.

It is difficult to make any conclusions from this data since this experiment was a pilot with very few animals, but the results are encouraging. It is likely that a larger sample size would yield significant differences between the SU and Control groups since the median VPT was consistently higher for the SU animals after the start of treatment, since there is proof that DCE-US is capable of separating treated

and untreated animals after 24 hours of antiangiogenic treatment [86]. Moreover, larger sample sizes might produce significant VPT values for the Combo group earlier than after 3 weeks of treatment.

3.4.3 AA- Morphology

The results indicate that AA might not be sensitive enough to track morphological changes in tumors with a VHL mutation being treated with SU or GSI. The extraction of vessels is a very complex process that is highly dependent on image quality. Therefore, vessels might not be extracted as single long unit with a high tortuosity, but multiple shorter vessels with lower tortuosity values.

The reason for the inability of AA to accurately track morphological changes most likely lies in the scale of the vessel remodeling. The Notch signaling pathway plays a key role in the regulation of VEGF receptors VEGFR-1 and VEGFR-2 for the proper formation [161,166]. Notch negatively regulates VEGFR-2, and positively regulates of VEGFR-1 which prevents excessive sprouting caused by improper cell migration, so Notch inhibition produces aberrant sprouting and increased microvasculature density [164–166]. This process occurs on the capillary level so AA cannot capture the changes in morphology since its resolution limit is around 100 μm .

To overcome resolution limitations associated with conventional ultrasound, researchers have adapted optical localization microscopy [182,183], which allows for optical imaging with resolutions down to 20 nm, to US in a technique called ultrasound localization microscopy which uses MCAs and is more commonly referred to as super resolution [184,185]. Using super resolution, blood vessels as small as 9 μm were imaged in the brains of rats [185]. Furthermore, this technique has been extended to cancer imaging, and the results demonstrated that vessels down to 25 μm could be resolved. Moreover, it was found that tumor vasculature had significantly different tortuosity than healthy tissue by using the same vessel extraction and tortuosity measurement techniques used in this work [186]. Therefore, super resolution has the potential to be a powerful tool for tracking morphological changes in tumor vasculature for the assessment of response to therapy

3.4.4 AA- Vascular Density

Data illustrates that microvascular assessment in conjunction with volume measurements can classify tumors as treated or untreated with very high sensitivity and specificity (Figure 3.17). The results suggest that a tumor can be correctly classified a responder to therapy regardless of its size or duration of treatment with a high degree of confidence. Sensitive classification can be accomplished within a week of the start of treatment, which cannot be accomplished with tumor volume measurements alone, and can be beneficial for clinical applications. While the sensitivity of classifying the tumors treated with SU is only about 75% at week one, every tumor treated with the combination therapy was correctly classified at the week 1 time point (Figure 3.17). Furthermore, the BVD values from around day 7 can be used to predict treatment response with a high degree of confidence before tumor volume measurements become significantly different (Figure 3.20). Although survival outcomes would need to be tracked in order to relate the observed changes in tumor properties to successful or failed treatment, initial results about our ability to assess a tumor's response to treatment compared to controls based on microvascular density prior to volume measurements were encouraging.

Histological validation demonstrated that the relative correlation between image based vascular density and vascular density from histology was high (Figure 3.19), but the value ranges of the two metrics were vastly different. The explanation for this discrepancy lies in the resolution of the two techniques. While optical microscopy, which was used for the histological analysis, can resolve individual capillaries, AA ultrasound imaging utilized here will blur any vessels smaller than the resolution of 100-150 μm in diameter into the entire image voxel, indicating a higher vascular density than optical histology analysis.

There was a strong correlation between imaging results and histology ($\rho = 0.75$), however, a single data point indicated by the arrow in Figure 3.19 reduces the correlation, and when it is removed from the analysis, ρ is 0.9. This suggests that this point was a substantial outlier, and it is likely that a higher correlation overall may be achieved than reported in this study if a larger data set is utilized.

Surprisingly, only 50% of the mice in the SU and Combo groups survived the entire study (Table 1). There is no work reporting this rate of morbidity as a result of the drugs used here, and the USMI study using the same tumor model, therapeutics, and dosage demonstrated no negative health effects on the animals [187]. It is unclear what effect the health issues of the mice had on the results of the study, but the findings of this work agree with those of previous studies which used similar treatment strategies [83,85,89,187]. In addition to the loss of mice due to health issues, the Control mice grew quickly and were euthanized once the tumors reached the size limit so that only ~50% of mice in that group remained at the week 4 time point. Therefore, the diminishing number of mice in the groups probably contributed to the lack of significance in the BVD between the Control and SU groups after the first week of imaging, even though the values appeared to be different (Figure 3.16). Another reason why the BVD of the SU and Control groups was not significant at the end of the study, unlike the histological results, is that the binning of data into weeks results in mice that have been treated for varying amounts of time to be grouped into the same week (e.g. 14 days and 20 days were binned into week 2 of treatment), which likely introduced additional variability. Furthermore, while the BVD values being compared for each group was small (around 4 per group) at the last time point, 30 histology images for each group were used for analysis.

Lastly, the results of this work, and previous work showing that GSI may not be a good treatment alternative [187], demonstrate that a combination of SU and GSI provides a better strategy for angiogenic suppression than delivering either drug individually. The volume results demonstrate that while the SU group had reduced tumor growth from the Controls, the Combo group alone caused the stagnation of tumor growth, and in some cases produced a reduction in tumor volume (Figure 3.16).

3.5 Conclusions

In this study, mice bearing ccRCC tumors were treated with VEGFR-2 antiangiogenic and Notch inhibition therapy. It was observed that CEUS can be used to monitor the disease progression and its response to the different therapies more accurately than using the conventional methods of

tracking tumor volume, which is the gold standard. CEUS has important merits as a variety of targeted and immunotherapy agents crowd the treatment landscape of ccRCC and cancer in general. Other work in recent years has shown that USMI can track response to antiangiogenic therapy [80–82,84–86] and predict whether tumors will respond to different treatments [83,87,88]; however, this is the first study to show that USMI can differentiate and track response to alternate strategies of vascularity-altering therapies and detect the tissue response of individual animals using CEUS earlier than tracking changes in tumor volume with high sensitivity and specificity. Ultrasound can be a valuable tool because it has the capability to assess response to therapy in cancer and monitor disease progression which might allow doctors to modify patient treatment for enhanced therapeutic effect.

CHAPTER 4

PULSE SEQUENCES FOR THE USE OF LOW BOILING-POINT PHASE-CHANGE CONTRAST AGENTS FOR CONTRAST ENHANCED ULTRASOUND^{3,4,5}

4.1 Introduction

As contrast agents, PCCAs require unique ultrasound pulse sequences to optimize diagnostic information. While other approaches are possible, perhaps the simplest is an image-activate-image sequence where the first imaging state is used to gather a pre-activation measurement and the second used to assess the level of contrast generated from an activation state. In the initial liquid state, pre-activation imaging must occur at pressures low enough to avoid droplet activation. When activation is desired (either at intervals or user-triggered), activation should cover the area of interest (pre-designated or operator-designated) and produce droplet vaporization as quickly as possible in the plane or volume – likely through focused pulses to minimize activation elsewhere. For the final imaging state, the imaging pressures must be low enough to not cause further droplet vaporization, and to not disrupt the bubbles produced (unless this is desirable). This post-activation imaging state must also occur quickly enough after the activation to capture contrast before it leaves the imaging plane, although this timing

³ Copyright © 2015 Word Federation for Ultrasound in Medicine & Biology. Published by Elsevier Inc. Reprinted, with permission, from PS Sheeran, JD Rojas, C Puett, J Hjelmquist, CB Arena, PA Dayton, “Contrast-Enhanced Ultrasound Imaging and In Vivo Circulatory Kinetics with Low Boiling-Point Nanoscale Phase-Change Perfluorocarbon Agents”, *Ultrasound in Med. & Biol.*, 2015; 41(3): 814-831.

⁴ © 2017 IEEE. Reprinted, with permission, from JD Rojas, PA Dayton, “Optimizing Acoustic Activation of Phase Change Contrast Agents with the Activation Pressure Matching Method: A Review”, *IEEE Transactions on Ultrasonics, Ferroelectrics, and Frequency Control*, 2017; 64(1): 264-272.

⁵ Copyright © 2018 Word Federation for Ultrasound in Medicine & Biology. Published by Elsevier Inc. Reprinted, with permission, from JD Rojas, PA Dayton, “Vaporization Detection Imaging: A Novel Technique for Imaging Phase-Change Contrast Agents with Higher Depth of Penetration and Contrast Enhancement than Microbubble Imaging”, *Ultrasound in Med. & Biol.*, 2018. In Review.

may be more flexible for droplets that are stationary (such as targeted droplets or those in tissue rather than vasculature).

Creating uniform contrast throughout the target organ is important for obtaining accurate measurements of targeting or perfusion and can be challenging due to the energy-sensitive activation thresholds of these agents; therefore, optimal activation parameters should be used. However, clinical ultrasound scanners typically do not allow the level of pulse sequence customization required to create ideal PCCA-based contrast imaging without manufacturer research agreements. Commercial systems have been used for droplet vaporization [188], but this approach relies on conventional B-mode pulses for vaporization so there is little spatial control of activation. Furthermore, since multiple frames are acquired to generate maximum intensity projections, generated microbubbles are interrogated multiple times with high intensity pulses which can lead to bubble destruction or cavitation. A new generation of highly-customizable ultrasound research platforms made by companies such as Verasonics (Redmond, WA, USA) and Cephasonics (Santa Clara, CA, USA) have allowed researchers to overcome these technological barriers and explore new imaging and processing techniques.

In this chapter, the process of creating custom pulse sequences for the *in vivo* use of PCCAs and optimizing the ultrasound parameters to produce uniform vaporization is explained. Moreover, a different approach to imaging PCCAs that uses the vaporization signal produced by PCCA activation, which will be referred to as vaporization detection imaging (VDI), instead of the image-activate-image scheme, which will be referred to simply as contrast imaging (CI), is demonstrated. Hence, the different parts of this chapter will have three components: the development of pulse sequences for the use of PCCAs, the optimization of these pulse sequences, and the development of VDI.

4.2 Methods

4.2.1 Phase-Change Contrast Agent Fabrication

PCCAs were made using methods previously described [129]. Precursor microbubbles were created by the agitation a 3 mL vial containing 1.5 mL of a lipid solution and a headspace pressurized with either DFB or OFP. The lipid solution consisted of 1,2-distearoyl-sn-glycero-3-phosphocholine (DSPC) and 1,2-distearoyl-sn-glycerol-3-phosphoethanolamine-N-methoxy(polyethylene-glycol)-2000 (DSPE-PEG2000) in a 9:1 M ratio and a total lipid concentration of 1.0 mg/mL and was dissolved in a solution of phosphate-buffered saline (PBS), propylene glycol, and glycerol (16:3:1). The resulting microbubble solution was cooled to temperatures ranging between -10 °C and -12 °C and condensed by pressurizing the vial with room air. For the VDI portion of the study, the bubbles were allowed to separate into 2 layers by waiting 7.5 minutes, and the supernatant was discarded to eliminate large outliers in the population, prior to condensation.

Microbubble size distributions were obtained by measuring 2 μ L of microbubble emulsion with an Accusizer 780A (Particle Sizing Systems, Santa Barbara, CA, USA), and statistics averaged for 3 independent microbubble vials to obtain a representative distribution and concentration. PCCAs formed from condensed microbubbles were sized by using a NanoSight NS500 (Malvern Instruments Inc., Westborough, MA, USA) capable of measuring both size distribution and concentration of sub-micron particles. The NanoSight was used to capture six 30-second recordings at a temperature of 23.3°C for each sample with all other settings at default values. DFB and OFP droplet samples were diluted 1/200 in PBS prior to sampling. Measurements produced from each of the six recordings were averaged to produce a representative size distribution and concentration for each sample, and the process repeated for a total of 3 samples of both DFB and OFP droplets.

4.2.2 Droplet Imaging and Activation Pulse Sequences

Imaging and droplet activation for the first 2 portions of the study (development of activation sequences, and optimization of those sequences) was performed using a fully customizable Verasonics

V1 research ultrasound platform (Verasonics, Redmond, WA, USA), equipped with an ATL L12-5 38mm 192-element linear array probe (Phillips, Andover, MA, USA) for the first part, and an ATL L11-5 128-element linear array for the second part. For the VDI portion, a Verasonics Vantage 256 was used to control an ATL L11-5. The following section explains the pulse sequences that were used for all experiments. Deviations from the parameters described here will be presented for each section of this chapter.

For each part, the transducer was calibrated in the free-field using a needle hydrophone (Onda HNA-0400, Sunnyvale, CA, USA) in degassed water (the center 128 elements of the L12-5 were used). The Verasonics hardware was controlled by MATLAB (The MathWorks, Natick, MA, USA) scripts, which allows for simple customization of acoustic parameters. Three different sequences were developed: One for B-mode (anatomical) images, another for droplet activation, and a pulse inversion approach [42] for contrast-specific imaging. The output of the transducer in each imaging mode was controlled by adjusting the output voltage of the Verasonics hardware using MATLAB scripts.

For B-mode anatomical imaging, a plane-wave coherent angular compounding approach [189] was implemented by delivering 9 MHz, 1-cycle sinusoidal pulses. The final B-mode images were formed by compounding the envelope detected and beamformed RF signal from 7 transmit-receive frames in which the transmit beam was electronically steered at even angular intervals between the axial and lateral dimensions of the transducer (from -18° to 18°). The beamforming and compounding were performed by Verasonics reconstruction algorithms.

For contrast-specific imaging, a similar coherent angular compounding approach as above was used in which the acquisition at each angle consisted of the RF addition of echoes received from sequential 4.5 MHz, 1-cycle pulses delivered 180° out of phase. The initial positive pulse was followed by a negative pulse after an interval of 105 μs , and each image was constructed from the compounding of all angles. The acquisition time between angles was 205 μs , and the final images were captured at a rate of 10 Hz. The number of compounding angles was reduced to 3 (-18° , 0° , 18°) in order to speed

up the data transfer rate and reduce reconstruction time. The Verasonics was set to receive at 9 MHz nominally, although no secondary filtering was performed to further isolate the 2nd harmonic component.

Droplet activation was achieved by a series of electronically focused and steered 5 MHz, with 1-5 cycle sinusoidal pulses, depending on the experiment. The use of focused pulses allowed activation only within the region of the beam where pressures were highest – limiting unwanted activation elsewhere. The pulses were delivered in a raster-scan style along the rows from left to right, starting with the deepest row in order to prevent shadowing by bubble clouds produced early in the sequence. Inter-pulse delay was set to 50 μ s (near the limit of the Verasonics hardware) in order to activate within the region of interest (ROI) as quickly as possible.

Kidney motion due to breathing could result in droplet activation in a plane not aligned with the imaging plane, and therefore a two-trigger structure was developed to ensure alignment between activation and imaging planes (Figure 4.1). Kidney appearance and motion was monitored during the free imaging state, and upon completion of the previous breathing cycle, the operator triggered the pre-activation imaging state. In this state, 10 frames were collected at a frame rate of 10 Hz and then the system returned to a free imaging state to align with breathing motion prior to activation. Once the animal breathing motion ceased, a second trigger transitioned the machine to the droplet activation sequence. After a 500 μ s delay to switch the Verasonics hardware to the activation voltage, focused activation pulses were delivered as described above, completing the entire activation sequence on a short timescale relative to respiratory motion. Upon completion of the last focused pulse, a delay of 1.2 ms allowed the Verasonics hardware time to return to imaging output levels. After this pause, the machine entered a post-activation imaging state and collected 100 images at a rate of 10 Hz for droplet groups and 10 images at a rate of 10 Hz for microbubble groups. Data were transferred to the PC controlling the Verasonics after both the pre-activation and post-activation captures for offline analysis.

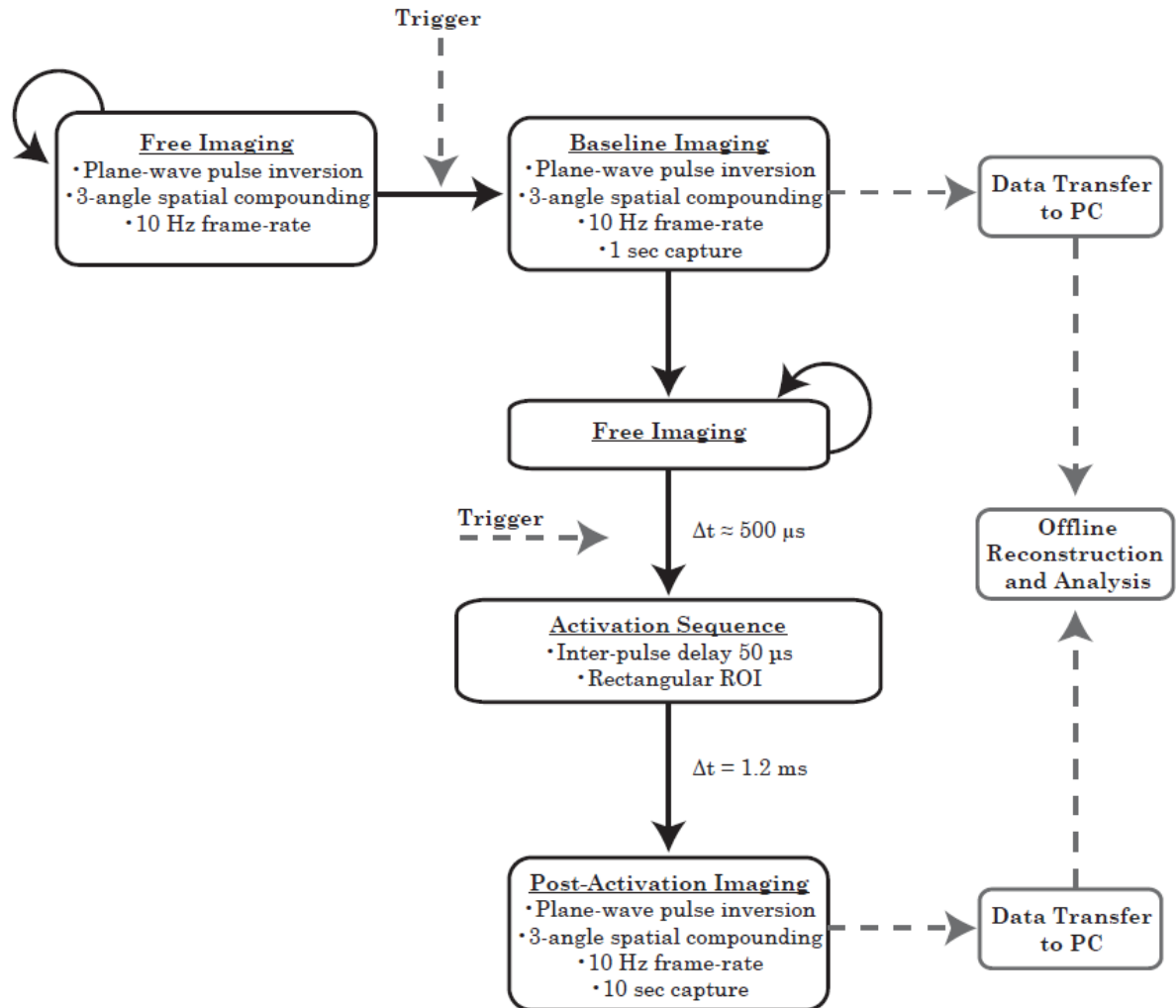


Figure 4.1. Imaging and activation sequence. A free imaging state was used to monitor the breathing cycle prior to a manually triggered transition to the pre-activation imaging state. Pre-activation imaging was followed by a return to the free imaging state. After alignment with the breathing cycle, a transition to the activation sequence was manually triggered. A period of post-activation imaging immediately followed the activation sequence. In these studies, images were reconstructed offline after all imaging and data transfer was complete.

4.2.3 Animal Protocols

The kidneys of Fischer rats (Charles River Laboratories, Morrisville, NC, USA) were imaged using protocols approved by the University of North Carolina School of Medicine’s Institutional Animal Care and Use Committee. All rats were selected based on similar size (~150 g) and age to reduce experimental variation. The rats were anesthetized with 2.5% isoflurane, placed on a heated pad, and the flank was shaved to remove fur.

4.2.4 Development of Pulse Sequences for the Use of PCCAs

In this section, the area of activation was set to a rectangular ROI within the lateral width of the transducer. Focused pulses were delivered uniformly within this region by setting the lateral and axial spacing between each pulse to cover the ROI. Once the kidney was positioned in the desired location, B-mode images of the final kidney placement were captured and stored offline before switching to pulse inversion and droplet activation modes. The final design choices for the imaging and activation states both *in vitro* and *in vivo* are reflected in Table 4.1.

In vitro verification of the droplet activation sequence was performed in an acrylic-walled water bath at 37°C. DFB droplets were dispersed in the water to a concentration of approximately 10^7 droplets/mL, and the water was stirred between experimental runs to redistribute the agents.

Based on preliminary studies, the Verasonics output voltage was set to 18V for all imaging sequences (Table 4.1). Hydrophone measurements of the spatial pressure distribution resulting from the focused pulses were gathered to correlate with images of microbubble clouds generated. The hydrophone was stepped through the transducer's lateral-axial plane at 0.1 mm intervals using a three-axis motion stage (Newport XPS-RC, Irvine, CA, USA). The maximum peak negative pressures were recorded, and the pressure distributions (beam profiles) were analyzed in MATLAB and combined to form a composite beam map.

At a nominal output voltage of 18V peak-to-peak, the maximum peak-negative pressures (PNP) were 482 kPa and 649 kPa for B-mode and pulse-inversion imaging, respectively. These pressures occurred at a depth of 1.5 cm for B-mode and 1.15 cm for pulse-inversion. As both imaging states were implemented with plane wave transmits, the pressure field was relatively uniform compared to a focused-wave approach. During focused activation pulses, the peak negative pressure was 3.0 MPa at a focal depth of 0.5 cm. Due to the elevational lens, pressure increased with increasing depth to a maximum peak negative pressure of 4.8 MPa at 1.4 cm.

Table 4.1. Summary of imaging and activation design parameters. PNP- peak-negative pressure.

State	Center Freq (MHz)	Pulse Cycles	Compound Angles	Tx volts	Free-field Max PNP Axial Location (cm)	Free-field Max PNP Value (MPa)	Lateral ROI Limits	Axial ROI Limits	Lateral Pulse Separation (mm)	Axial Pulse Separation (mm)
B-mode	9.0	1	7	18	1.50	0.48	-	-	-	-
Pulse Inversion	4.5	1	3	18	1.15	0.65	-	-	-	-
Activation (<i>in vitro</i>)	5.0	2	-	18	1.40	4.80	-6mm to 6mm	5mm to 14mm	Various	Various
Activation (<i>in vivo</i>)	5.0	2	-	30	1.10	8.30	-6mm to 6mm	3mm to 12mm	0.85	1.50

Pulses were delivered at even spacing (user specified) within a rectangular region of interest extending laterally from -6 mm to 6 mm relative to the center of the transducer face and axially from 5 to mm 14 mm. The multi-angle coherent plane-wave compounding with pulse inversion script described above was used to image the microbubble clouds generated *in vitro* by droplet activation following the application of focused ultrasound (2 cycles at 5 MHz) in the presence of DFB. Results from these tests were used to set the axial and lateral activation pulse spacing for *in vivo* studies based on the assumption that pulse pressures and spacing adequate to activate DFB *in vivo* would produce even greater activation of OFP droplets – ensuring the ability to measure both agents.

Three groups were included in this section: DFB droplets (N = 7), OFP droplets (N = 6), and microbubbles (N = 6). Animals in the microbubbles group were administered DFB microbubbles (the same precursors used to form DFB droplets).

B-mode imaging was first used as an anatomical reference to locate and align the kidney with the activation ROI. Prior to the injection of contrast agents, the imaging/activation program was used to capture agent-free baseline images.

Contrast agents were delivered as single 120 μL bolus doses injected manually followed by a flush of sterile saline, similar to a previous study in mice with DFB droplets [190]. Based on the contrast agent size distribution and concentration measurements (see Results section), each bolus consisted of 60 μL of contrast agents diluted in 60 μL of saline for an approximate initial blood plasma concentration of 3.99×10^7 #/mL, 8.42×10^8 #/mL, and 1.86×10^9 #/mL for control microbubbles, DFB droplets, and OFP droplets, respectively. Next, the pre-activation and post-activation frames were captured using the imaging/activation sequence every 3 minutes for 19 minutes, starting at 1 minute after the injection for the DFB and OFP groups, and every 2 minutes for 15 minutes, starting 1 minute after the injection for the microbubble group. Animal breathing was monitored closely after the injection and for the remainder of the experiment. The dose of isoflurane was adjusted depending on the breathing rate of the animal.

Based on the results of the *in vitro* verification experiments, a lateral spacing between pulses of 0.85 mm, around 50% of the measured lateral full-width half maximum (FWHM), and axial spacing of 1.5 mm (500% of the approximate axial FWHM). The area of activation was set to a rectangular region spanning 3 mm to 12 mm axially and from -6 mm to 6 mm laterally relative to the center of the transducer. The change in the axial window between *in vitro* and *in vivo* studies was made in order to ensure the region covered the entire kidney region in this imaging orientation. This combination of ROI and pulse spacing resulted in 90 focused pulses spaced evenly across the region delivered at a rate of 20,000 pulses/s. Transducer output voltage was set to 18V for all imaging sequences, but increased to 30V during the activation sequence to counteract the effects of tissue attenuation. This translated to a free-field peak negative pressure (not accounting for tissue attenuation) of 482.3 kPa and 648.8 kPa during B-mode and pulse-inversion imaging, respectively (Table 4.1). The increase in activation voltage resulted in a free-field peak negative pressure of 8.3 MPa (at an axial depth of 1.1 cm).

4.2.4.1 Data Analysis

Custom MATLAB scripts were used to analyze the pulse inversion data captured with the Verasonics. The output image data (envelope-detected and beam formed) was square root-compressed, so the pixel values in all the frames were squared to obtain the linear beam formed voltage data. In order to analyze the contrast properties within the kidney, reference images were normalized and converted to the decibel scale for visualization. ROIs were placed manually in the reference image and applied to all frames of the underlying (linear) data set. In cases where shadowing in the images was present, ROIs were drawn to avoid inclusion of the affected pixels. The average pixel value and standard deviation inside the ROI were calculated on each frame of the voltage data.

The degree of contrast enhancement (CE) was measured by comparing the contrast images with the agent-free baseline in the following sequence. An ROI was drawn around the region of highest activation within the kidney in the first post-activation frame (or post-injection, in the case of microbubbles). The mean pixel value was computed for each frame of the entire data set (agent-free

baseline, pre-activation, post-activation). For groups that were administered microbubbles, the data set consisted of only the agent-free baseline images and the post-injection images. The agent-free baseline value for each animal was calculated by averaging the ROI values from the 10 agent-free baseline images. The mean pixel value of each frame after administration of the contrast agents was normalized to the agent-free baseline value and converted to decibel scale to arrive at a dB increase in contrast relative to agent-free baseline.

Using the CE measurements described above, the decrease in the contrast captured with each sequential data set was analyzed to obtain contrast half-lives and quantitatively compare the longevity of agent circulation. The CE values of each data set were normalized to the maximum value obtained at the 1 minute time point, and the normalized data for each animal was fitted with an exponential of the form

$$e^{-\beta_h(t-1)} \quad (4.1)$$

where t is the time in minutes after injection, and β_h is the rate of decay. In this fit, any time points were excluded where the mean CE captured by the post-activation imaging was not significantly increased compared to the pre-activation imaging. These were excluded due to the fact that the mean contrast should return to zero for the exponential. The contrast measurements capture the maximum signal due to contrast agent enhancement, but once contrast is no longer being produced, this measure will capture the variation in the noise and produce a non-zero value at late time points.

To measure the rate of contrast clearance from the imaging plane post-activation, the CE measurements were clipped to the maximum value (with breathing noise removed) and fit with an exponential curve of the form

$$dB_{max} * e^{-\beta_w(t-t_{max})} \quad (4.2)$$

where β_w is the wash-out rate, t_{max} is the time at which the maximum contrast occurred, and dB_{max} is the maximum CE produced.

4.2.5 Optimization of Activation Parameters

A technique called activation pressure matching (APM) was developed in this work to produce uniform activation of PCCAs. Since the L11-5 has an elevational lens, the free-field pressure for a single applied voltage greatly varies with depth, increasing as the elevational focus is approached (Figure 4.2a). As a result, the amount of vaporization, or the number of droplets that are activated, varies with depth in a water bath, as can be seen in the size difference of the generated bubble clouds (Figure 4.2b). Furthermore, diffraction of focused pulses and a changing F-number, since the aperture size is being kept constant, can cause pressure variations in the field of view and may be additional factors that contribute to the change of vaporization levels with respect to depth. Puett et al. described a method for obtaining uniform contrast generation by optimizing the spacing between the activation pulses so that individual bubble clouds form a larger region that is full of contrast [191]. Although this method accomplishes the goal of uniform droplet vaporization in an ROI, it results in over-activation in the deeper regions of the field of view since the pressure distribution is non-uniform through depth. Consequently, the ROI is insonified with more energy than is necessary which may be undesirable for diagnostic purposes.

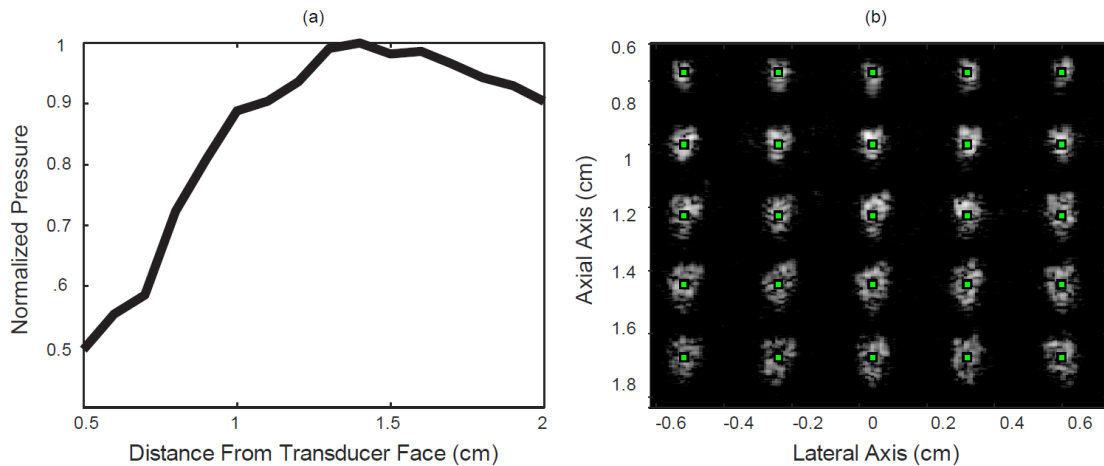


Figure 4.2. Transducer output pressure and activation clouds at different depths. Several activation pulses were delivered to the locations indicated by the green markers in order to activate OFP droplets in a water bath. Output pressure varies with depth in a water bath for a single voltage as a result of the elevational lens on the L11-5 (a). This change in pressure leads to different levels of droplet activation (b). The pressure increases as the 1.4 cm elevational focus is approached, causing the bubble clouds produced by vaporization to be larger.

The rationale for Activation Pressure Matching (APM) is to deliver pulses with the same rarefactional pressure to all activation locations in order to limit the delivered energy. This technique not only overcomes the changes in pressure due to the elevational lens, but also due to diffraction, a changing F-number, and attenuation in tissue. By varying the output voltage, the appropriate acoustic pressure can be delivered at different depths. However, the Verasonics system requires hundreds of microseconds to switch between voltages, thus a complete activation sequence may take several milliseconds. All of the activation pulses should be delivered as quickly as possible to ensure uniform vaporization within a single plane, as respiratory motion may alter the imaging plane during *in vivo* imaging. The generated contrast must also be imaged quickly to ensure accurate measurement since the bubbles produced by the early activation pulses will begin to be cleared from the imaging plane.

Fortunately, the Verasonics offers a tool for modulating the amplitude of the output waveform: pulse-width modulation (PWM). The system uses a tri-state pulser to generate a large variety of waveforms (Figure 4.3a-b), so in addition to changing the voltage, the amplitude of the generated waveform can be adjusted by modifying the number of clock cycles the output is at +volts, ground, and -volts. As can be seen in Figure 4.3a-b, the square wave for a PWM value of 0.6 maintains the high or low voltage value for less time compared to the wave for a value of 1 which produces an output pulse having a lower pressure amplitude. Therefore, a consistent pressure through depth can be achieved by selecting an appropriate voltage and adjusting the PWM parameter.

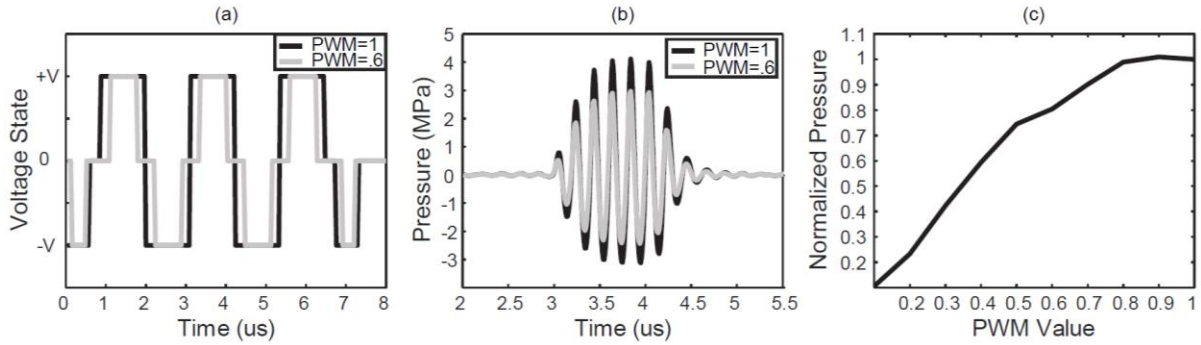


Figure 4.3. Example PWM pulse code and generated pulse. The Verasonics system uses PWM to modulate the amplitude of the output waveform by changing the time the output is at each of the three voltage states (+V, -V, ground). As can be seen in (a), the width of each square cycle is narrower for the PWM of 0.6 (gray line) than for the PWM value of 1 (black line), and this difference produces waveforms of different amplitudes (b). (c) demonstrates that decreasing the PWM value from 1 (no PWM) produces a waveform with a lower peak negative pressure. Therefore, a range in pressures can be achieved using only 1 peak-to-peak voltage.

Because this approach does not require multiple voltage changes, different pressures can be quickly delivered. An example of the relationship between output pressure and PWM value for a given voltage is illustrated in Figure 4.3c; the output pressure increases as the PWM value increases, with a value of 1 signifying no PWM.

In order to determine the correct voltage and PWM values for the desired activation pressures at a specific depth, the system was calibrated with a hydrophone. A needle hydrophone (HNA-0400, Onda, Sunnyvale, CA, USA) was used to calibrate the L11-5 transducer for a range of PWM values at various voltages and depths, for a 5 MHz sinusoid with 5 cycles. Peak rarefactional pressures of 3.75 MPa and 1.5 MPa were chosen because they are above the activation thresholds for DFB and OFP [129,134,192,193], respectively. MATLAB (MathWorks, Natick, MA, USA) can then be readily used to calculate an appropriate voltage-PWM combination that resulted in the desired pressure for each activation depth. An example of this process is shown in Figure 4.4. The target pressure is set to 1.5 MPa, and by using 6V and the PWM values shown in the solid gray line, the output pressure can be set to within the target $\pm 10\%$ to account for measurement error from the hydrophone. Furthermore, as

shown in Figure 4.4, the output pressure at 6V without PWM is enough to cause vaporization at 0.9 cm but is too high in deeper regions and would result in over-activation.

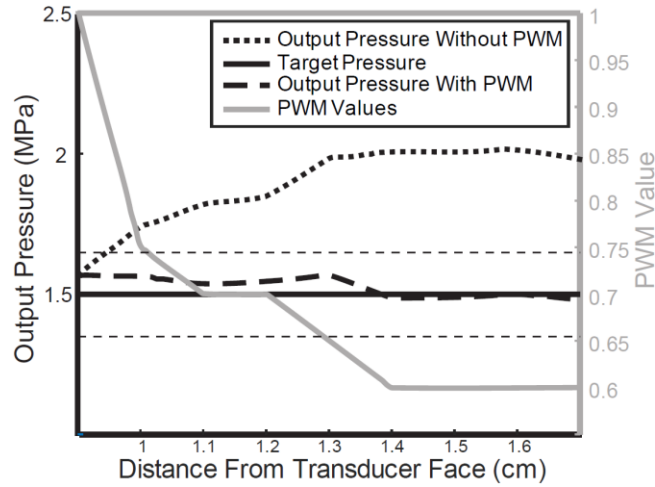


Figure 4.4. Example APM parameters for *in-vitro* activation. In this example, a target activation pressure of 1.5 MPa (solid black) is chosen, and the PWM values (solid gray) are applied to 6V to obtain an output pressure (dashed black) that is within $\pm 10\%$ (light dashed) of the target pressure for depths ranging from 0.9 to 1.7 cm.

4.2.5.1 *In Vitro* Protocols

APM was first tested *in vitro*. For all *in vitro* experiments, a 300 μL volume of the stock droplet solution was injected into a water bath at room temperature (22 $^{\circ}\text{C}$), and a series of focused activation pulses were delivered to produce vaporization.

In order to produce a uniform area of activation in the ROI, the spacing between the activation pulses was adjusted. Puett et al. described a procedure for optimizing the spacing that consisted of activating a group of vertical and horizontal lines, and varying the spacing between them until FWHM of the intensity profiles overlapped [191]. Since APM was not used, the size of the bubble clouds produced by droplet vaporization varied with depth. Therefore, individual lateral and axial spacings had to be derived for different regions in the field of view. In this work, the same procedure described by Puett et al. is used, but since APM produces same-sized bubble clouds regardless of depth, only one set of lateral and axial spacing needed to be calculated. Contrast lines separated by different distances were created by activating droplets in a water bath and intensity profiles were generated by averaging

the uncompressed image data along either the lateral dimension, for calculating the optimal axial spacing, or axially, for calculating the optimal lateral spacing. As discussed above, the optimal spacing is defined by the overlap of the FWHM of the intensity profiles. However, too much overlap is not desirable since any interaction that may cause cavitation or bubble destruction between an activation pulse and a pre-existing bubble cloud. Therefore, the distance between the right FWHM point on the left activation line intensity profile, and the left FWHM point on the right intensity profile should be as close as possible to zero, so the spacing that has the lowest distance value between these two points is the optimal spacing.

4.2.5.2 *In Vivo* Imaging

APM was translated into *in vivo* imaging. The previously described procedure can be applied *in vivo* with attenuation compensation. Here, we demonstrate the effectiveness of APM in rat kidneys. As with *in vitro* activation, an appropriate PWM value must be selected for each depth for a specific voltage. However, the target pressure will not be flat through depth but rather, it will increase so that the same pressure is delivered to all the activation locations after it is attenuated by tissue (Figure 4.5). In order to calculate the required initial pressure before attenuation, the free-field pressure at each depth is derated using the following model: 3.5 mm of superficial tissue ($\alpha = 0.6$ dB/MHz/cm) followed by kidney tissue ($\alpha = 1$ dB/MHz/cm), assuming a kidney frequency dependence of 1.1 ($\alpha = \alpha_0 f^{1.1}$) [194,195]. Similar to the *in vitro* case, APM can yield a pressure through depth that is within $\pm 10\%$ of the target pressure by selecting the appropriate attenuation model and PWM values for the different depths while using the same voltage (8V). Additionally, not using APM would result in over-activation in the shallower regions since 8V produces a pressure that is higher than the target without PWM.

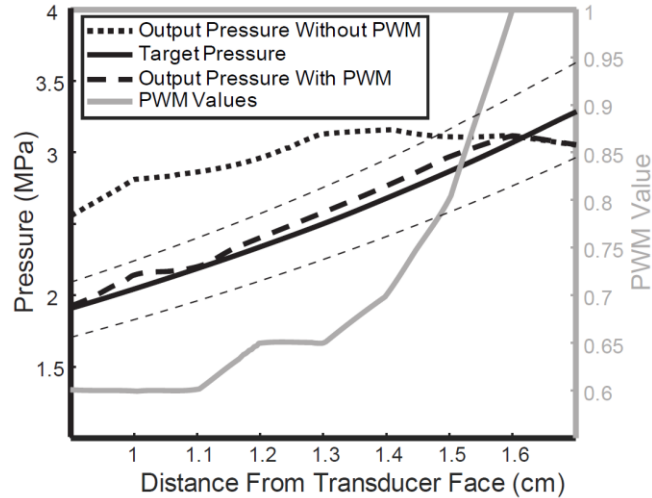


Figure 4.5. Pressure map with distance after accounting for attenuation using a rat kidney attenuation model. The target pressure (solid black) of 1.5 MPa increases with depth since the initial pressure will be derated by the tissue. Using APM with the PWM values shown in the solid gray curve, the pressure delivered to each depth is within $\pm 10\%$ of the target pressure (dashed black line). The output generated without APM (dotted black) is higher than the target and would result in the delivery of higher pressure than is necessary for droplet vaporization.

Using the attenuation-corrected APM method with the optimized activation pulse spacing discussed earlier, OFP droplets were activated in a rat kidney. First, a bolus of 60 μL of OFP droplet was injected and allowed to circulate for 1 minute and was followed by the image-activate-image sequence described previously. In this part of the experiment, optimized spacing was used to produce uniform vaporization *in vivo*.

Furthermore, the same procedure as in the previous section (Development of Pulse Sequences for The Use of PCCAs) was used to, except that APM was used for vaporization at the DFB threshold (3.5 MPa), to explore the effect of optimized activation parameters on the CE kinetics. Briefly, a bolus consisting of 60 μL droplets (around 1×10^9 droplets) diluted in 60 μL of saline was injected and a series of activation pulses was delivered every 3 minutes for 19 minutes, starting 1 minute after injection. Optimized spacing was not used in order to reduce over-activation of OFP, as it is much more volatile than DFB.

For all *in vivo* imaging, a custom MATLAB script was used to manually segment the kidney (found using the B-mode pulse sequence) and calculate the locations of the activation pulses and their appropriate PWM values. Activation locations start with the deepest lines first in order to avoid attenuation of the subsequent pulses by the generated contrast, as indicated by the red dashed lines.

The CE and half-life were calculated using the same methods described in the previous section. The CE was found by dividing the mean intensity inside the ROI for the post-activation images by that of the pre-activation images of the baseline case (before injection of PCCAs). The data was fit to a decaying exponential to calculate the half-life.

4.2.6 Vaporization Detection Imaging

4.2.6.1 Activation Signal Detection

The activation signal resulting from droplet activation was captured *in vitro* to evaluate the effects of pulse length and concentration. DFB and OFP droplets were continuously flowed through a 200 μm microcellulose tube using a syringe pump (PHD2000, Harvard Apparatus, Holliston, MA, USA) set to infuse at 80 $\mu\text{L}/\text{min}$. The tube was submerged in a water bath that was kept at 35 $^{\circ}\text{C}$ to simulate temperatures close to body temperature.

PCCAs were vaporized using an ATL L11-5 linear array controlled by a Verasonics Vantage ultrasound system (Verasonics, Kirkland, WA, USA), using 5 MHz pulses with a pulse length of 1, 3, or 5 cycles. 5 MHz is lower than that used in other studies for imaging droplet vaporization signals [138,139], but it was chosen to reduce tissue attenuation and because it has been previously used in *in vivo* imaging of droplets [127,196]. The activation pulses were delivered at a rate of 1.25 Hz, and a range of pressures (peak-negative) were used for vaporization: 0.5, 0.75, 1, 1.25 MPa for OFP, and 1, 1.5, 2, 2.5 MPa for DFB. The activation signals were captured using a 2.25 MHz piston transducer (Olympus Panametrics V305, Center Valley, PA), amplified with an RF amplifier (BR-640A, RITEC Inc., Warwick, RI, USA), digitized using a 200 MHz sampling rate (CSE1222, Gage, Lachine, QC, Canada), and stored using LabView (National Instruments, Austin, TX, USA). The combination of

flow rate and pulsing rate was chosen to allow fresh droplets to replenish the region of activation between each of the 30 acquisitions captured for each pulse length/pressure/dilution combination.

Three different dilutions were used: 0.01% to study the activation signature of individual droplets or droplets that are far enough away to not affect each other's response, 0.1% because similar dilutions have been used *in vivo* [127,196], and 1% to explore the effect of activating PCCAs in close proximity. Data were collected using all pulse lengths and pressures with only water in the tube to obtain a baseline.

Two parameters were calculated from the activation traces: amplitude area under the curve (AUC) and the mean frequency. The AUC was computed to obtain a metric of vaporization signal strength, and mean frequency was measured to evaluate the interaction between the activation pulses and the produced microbubbles. The higher the mean frequency (a shift towards the transmit frequency), the more interaction between the pulse and the bubbles. Both metrics were found using only the traces that contained vaporization. All processing and analysis was performed using custom MATLAB (The MathWorks, Inc., Natick, MA, USA) scripts.

The AUC was calculated by envelope-detecting the time-domain traces and finding the area under the curve using trapezoidal approximation (Figure 4.6). First, the voltage traces of the non-droplet (water) cases, which is the signal from the microtube, were filtered with low-pass filters (100 order finite impulse response filter) of different corner frequencies, and the AUC was calculated. Next, the filter that produced the lowest AUC (tube signal) was used to filter the time-domain traces of all the droplet data, and the AUC was calculated. Furthermore, the mean AUC of the water measurements was subtracted from each droplet trace.

To find the mean frequency, a fast Fourier transform was first calculated for each unfiltered voltage trace, and the frequency spectrum from the water measurements was subtracted from the droplet data to eliminate the frequency components of tube and droplet scattering (Figure 4.6). Lastly, the mean

frequency of the unfiltered data was calculated from the water-subtracted spectra by summing the product of each frequency (x-axis) by its corresponding amplitude (y-axis), and dividing the result by the summation of all amplitude values.

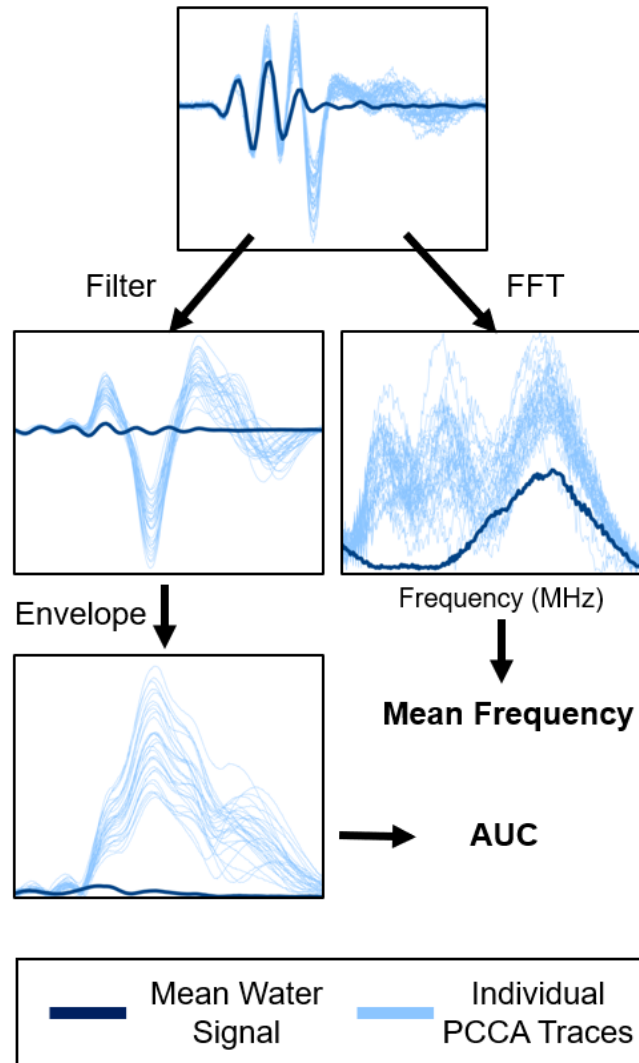


Figure 4.6. Illustration of the analysis for the activation signal detection section. The data was filtered and envelope detected, the AUC was found (left), and the mean frequency was calculated from the frequency spectra (right).

4.2.6.2 Imaging of Phase-Change Contrast Agents

A Vantage system was used to control an L11-5 linear array for all imaging and vaporization. In this work, the conventional image-activate-image method of imaging, CI, was compared to the new

approach of making images from the vaporization signals, VDI. For CI, the pulse inversion technique described previously was used to capture a frame before and after activation, and APM was used to account for attenuation and deliver pulses with similar peak-negative pressures regardless of depth. In order to make VDI images, the signals produced by the activation pulses in the CI protocol were captured.

ADV is an event that produces momentary low frequency signals that last for less than $10\ \mu\text{sec}$ [137]. Therefore, unlike CI, where images are captured after the vaporization pulses have been delivered, VDI requires that RF data be stored for each transmission, and that small reconstruction regions around each activation location be combined to form an image (Figure 4.7), similar to conventional focused imaging. Verasonics reconstruction algorithms, which employed a delay and sum protocol with dynamic electronic receive focusing, were used to form the VDI images from the different activation locations.

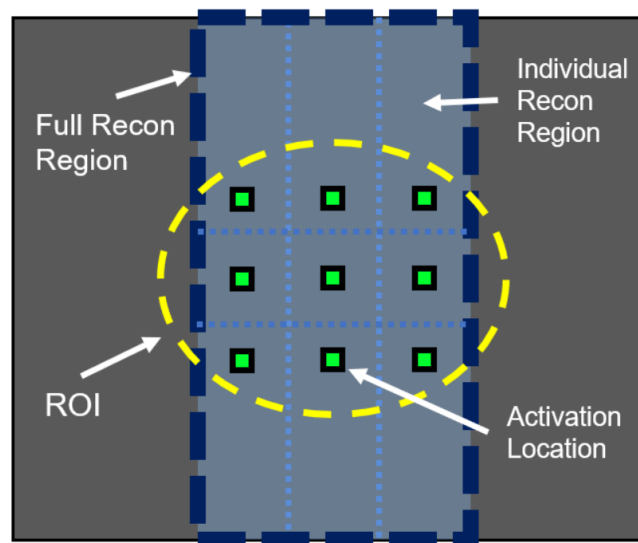


Figure 4.7. Reconstruction technique for making VDI images. There is one reconstruction region (light blue, dotted rectangles) for each activation location (green squares) in the ROI (yellow dashed line). The multiple reconstruction regions are combined to form the image. Since the entire field of view is not insonified, only part of the field of view is reconstruction (dotted, dark blue line).

4.2.6.3 *In Vivo* Imaging

The kidney was found using the B-mode sequence on the Vantage, and a region of interest ROI was drawn around the kidney to select the location of the activation pulses (Figure 4.8). A catheter was inserted into the tail-vein for PCCA administration, which consisted of a continuous infusion of DFB or OFP droplets at a rate of 1.5×10^8 #/min. PCCAs were activated with rarefactional pressures of 3, 3.5, 4, and 4.5 MPa for DFB and 0.75, 1, 1.25, and 1.5 MPa for OFP, using a pulse-length of 1 cycle. Three trials were conducted for each pressure.

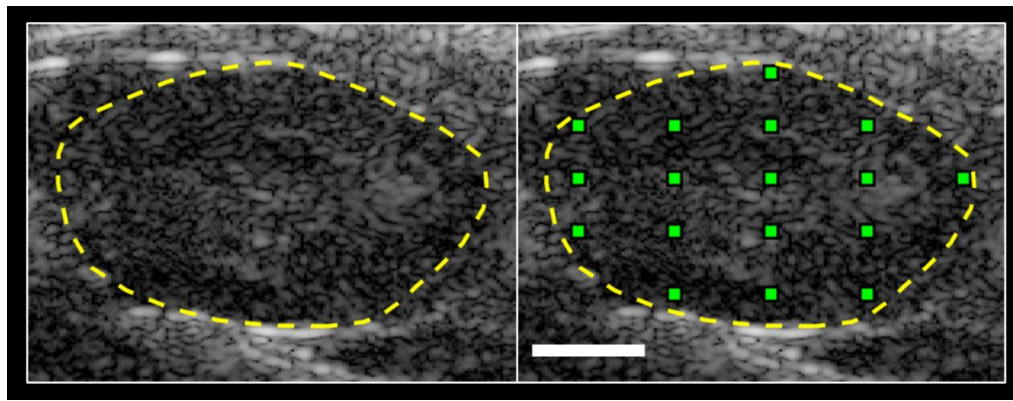


Figure 4.8. ROI (yellow dashed line) drawn on b-mode image (left) and activation locations (right). The scale bar represents 3 mm.

First, the RF data of VDI at the highest pressure for each perfluorocarbon (4.5 and 1.5 MPa for DFB and OFP, respectively) was filtered using filters having different corner frequencies. Next, the filter that provided the best CE was used to filter the data from all pressures, and VDI images were reconstructed using Verasonics reconstruction algorithms. CE was defined as the ratio between the uncompressed mean intensity inside the ROI of the activation images and baseline images taken before the introduction of PCCAs at all the pressures tested. No additional post-processing was performed for the CI images.

CI and VDI were compared by evaluating the CE of each technique. However, the spacing between activation locations was not optimized because it was observed from preliminary work that CI and VDI required different spacing to produce a uniform region of activation. Therefore, simply taking

the mean intensity inside the ROI for the CE calculation would bias the results in favor of VDI because CI requires smaller spacing. Instead, a ROI image mask was created that isolated areas where activation was present so that the CE calculation did not depend on the spatial characteristics of the vaporization (Figure 4.9). Two image masks were created for each rat, one for DFB and one for OFP, using the images of the highest pressure for each PFC. Out of all pixels inside the ROI, only those with intensity values higher than the mean intensity of the no-droplet case plus 3 standard deviations were kept for analysis. Since speckle produces random regions of low and high intensity, a Gaussian filter was applied to smooth the images used for making the masks so that low-intensity pixels produced by speckle were not excluded. Each of the two masks were used for all the data of the same PFC.

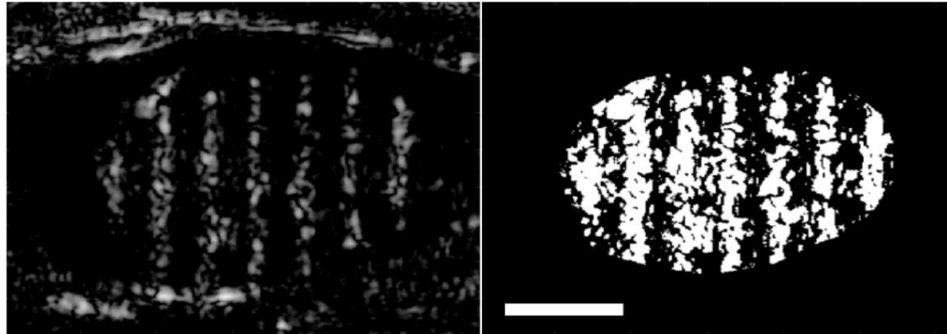


Figure 4.9. Example CI image (left), and mask for analysis (right). Only white pixels were included in the CE calculation. The scale bar represents 3 mm.

4.2.6.4 Imaging at Depth

To test the hypothesis that VDI has better depth of penetration than conventional contrast imaging due to the low frequency of the vaporization signals, PCCAs were activated in microtubes (320 μm inner diameter) that were embedded in a tissue-mimicking phantom with a measured attenuation coefficient of 0.61 dB/cm/MHz, which is in the range of normal tissues, such as liver and fat [194]. The tubes were positioned around 2 and 3 cm from the surface of the phantom, and APM was used to ensure that a 1 cycle, 5 MHz, 1.5 MPa peak-negative pressure was delivered to each activation location and that the imaging pressure for CI was the same at each of these depths. Before a stock droplet solution of OFP was diluted to 1%, the saline in the syringe was heated to 35 °C, and the diluted

solution was immediately infused into the tubes after the droplets were added. VDI and CI images were captured following the infusion of PCCAs, and the same procedure that was described in the previous section was employed to calculate the CE. A higher value is expected for VDI, since there should be less attenuation due to the low frequency of the activation signals.

4.2.6.5 Statistical Analysis

For the activation detection experiment, ANOVA was used to determine significance between any pulse lengths or PFCs, and a Tukey range test was used to find significance between each of the parameters. For the rest of the experiments, where the number of measurements consisted of a dozen or less values, Kruskal-Wallis analysis was performed instead of ANOVA, followed by a Tukey range test. Significance was set at $p < 0.05$.

4.3 Results

4.3.1 Contrast Agent Sizing and Concentration

The averaged distribution of DFB microbubbles, which were used as control agents throughout this study, had a mean diameter and variation of distribution of $1.00 \pm 0.89 \mu\text{m}$, with a mode size of $0.62 \mu\text{m}$, and a total concentration of $6.57 \times 10^9 \pm 0.84 \times 10^9$ bubbles/mL ($N = 3$) (Figure 4.10a). Reproducibility between samples was high, with the standard deviation in the mean of $0.06 \mu\text{m}$, and standard deviation in the mode of $0.01 \mu\text{m}$ ($N = 3$). Similarly, the precursor microbubbles used to make OFP particles had a mean diameter and variation of distribution of $1.03 \pm 0.66 \mu\text{m}$, with a mode size of $0.61 \mu\text{m}$. OFP microbubbles had a higher mean concentration of $8.50 \times 10^9 \pm 1.4 \times 10^9$ bubbles/mL ($N = 3$) compared to DFB microbubbles, but not significantly so ($p = 0.16$, Student's two-sided t-test).

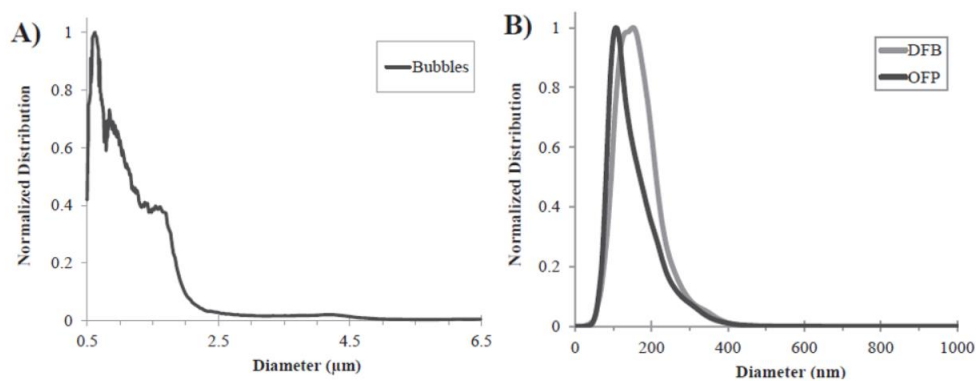


Figure 4.10. Representative distributions of contrast agents used in this study. A) DFB microbubbles had a mean diameter of $1.00 \pm 0.89 \mu\text{m}$ and a mode size of $0.62 \mu\text{m}$. B) Droplets created by condensing DFB and OFP microbubbles produced sub-micron distributions. DFB droplets had a mean diameter of $166 \pm 59 \text{ nm}$ and a mode of 141 nm , while OFP droplets had a smaller mean diameter of $154 \pm 64 \text{ nm}$ and a mode of 110 nm .

The representative distributions obtained by averaging all 3 samples of each type of droplet (Figure 4.10b) produced a mean diameter and distribution variation of $166 \pm 59 \text{ nm}$ for DFB, with a mode size of 141 nm , and a total concentration of $13.88 \times 10^{10} \pm 6.58 \times 10^{10}$ droplets/mL, while OFP produced a mean diameter and distribution variation of $154 \pm 64 \text{ nm}$, with a mode size of 110 nm , and a total concentration of $30.61 \times 10^{10} \pm 9.65 \times 10^{10}$ droplets/mL. Reproducibility between samples was high, with the standard deviation in the mean less than 3 nm for both OFP ($N = 3$) and DFB ($N = 3$). Similarly, mode size of the 3 samples for each droplet type had standard deviations less than 12 nm . A Kolmogorov-Smirnov test showed that the smaller size distribution of OFP droplets was statistically significant compared to DFB ($p < 0.001$), which agreed with Student's two-tailed t-test evaluation of the measured mean ($p = 0.03$) and mode ($p < 0.01$) values for the two droplet types. OFP droplets had a nearly significant increase in concentration compared to DFB ($p = 0.07$), similar to the microbubble concentration results. The smaller mode and mean diameters of the OFP samples can be expected based on ideal gas laws, which predict a greater size-dependent factor of conversion for OFP than DFB [128,137,197]. Given that the peak in the DFB microbubble distribution occurred at $0.62 \mu\text{m}$ and at $0.61 \mu\text{m}$ for OFP, an assumption of ideal conversion between the gas and liquid states suggests a conversion factor of 5.57 ± 0.33 for OFP and 4.41 ± 0.37 for DFB.

4.3.2 Development of Pulse Sequences for the Use of PCCAs

4.3.2.1 *In Vitro* Verification

Testing within an imaging field measuring 1 cm^2 at a depth of 1 cm demonstrated a correlation between the focal pressures and the sizes of individual microbubble clouds generated by droplet activation (Figure 4.11). At the *in vitro* imaging and activation output settings, vaporization of DFB droplets was not observed prior to triggering the focused activation pulses, indicating pressures were low enough to eliminate unintended vaporization. This matches previous *in vitro* measurements showing that efficient DFB activation at frequencies near 5 MHz requires pressures on the order of 2 MPa or greater [130].

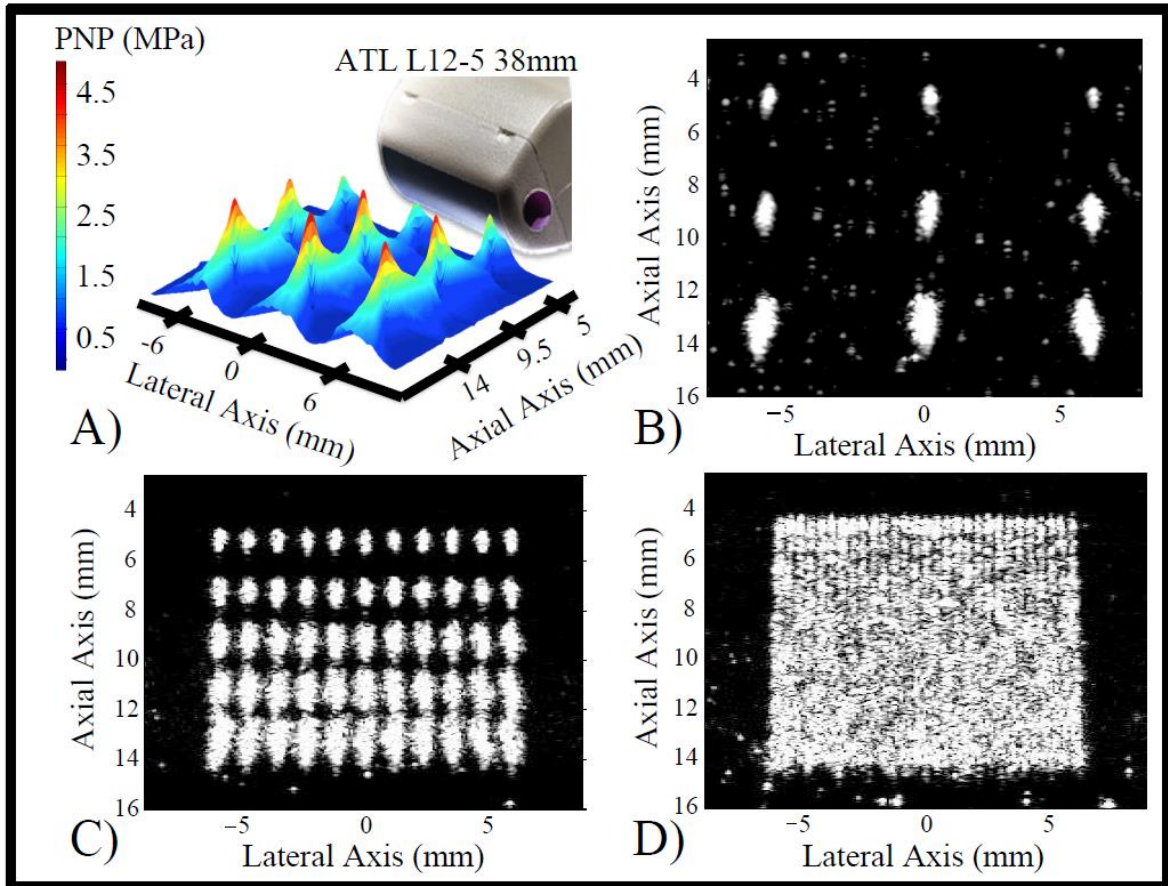


Figure 4.11. *In vitro* activation of DFB droplets. Changes in the magnitude and geometry of the pressure focal zones (A) and corresponding microbubble clouds (B) at nine focal locations occur as a result of electronically steering the activation pulses. A region of interest can be filled with bubbles by the accumulation of discrete microbubble clouds (C). Spacing the focal locations closer results in a more uniform field of bubbles (D).

During focused activation pulses, the focal zones as well as the maximum peak negative pressures achieved within these zones differed depending on the focal depth (Figure 4.11a) as a result of the elevational lens of the L12-5. Accordingly, the sizes of the microbubble clouds differed as a function of the focal depth (Figure 4.11b). Converting the output peak negative pressures to Mechanical Index (MI, defined as the PNP in MPa divided by the square root of the center frequency in MHz [198]), the maximum MI in the imaging state was 0.3, and the maximum MI in the activation state was 2.1. It is important to note that a mechanical index of 2.1 is higher than the current regulatory limits of diagnostic ultrasound output (MI = 1.9). In this study, it is evident that DFB droplets can be activated at ultrasound pressures lower than MI = 1.9. For example, in Figure 4.11b at a focal depth of 0.5 cm, bubble clouds are produced at MI = 1.3, although they are much smaller than those produced using higher pressures.

When focused pulses are placed sparsely, such as a lateral separation of 6 mm and axial separation of 4.5 mm, contrast can be generated in isolated regions with no overlap (Figure 4.11a-b). The accumulation of many individual microbubble clouds can fill a region of interest with bubbles (Figure 4.11c-d). Differences in the individual microbubble cloud shapes and sizes as a function of their location in the acoustic field can be appreciated if the activating foci are spaced at 1.2 mm laterally (70% of the measured lateral full-width-half-max) and 2.1 mm axially (700% of the approximate axial full-width-half-max) (Figure 4.11c). However, a more uniform vaporization field of bubbles can be generated if the activating foci are spaced closer at 0.43 mm laterally (25% of the full-width-half-max) and 0.75 mm axially (250% of the approximate axial full-width-half-max) (Figure 4.11d). Although this results in a visually confluent region of contrast, it also indicates that the vaporization pulses may be interacting with the bubbles produced from previous pulses.

4.3.2.2 *In Vivo* Acoustic Parameters

To transition to *in vivo* verification, a lateral spacing between pulses of 0.85 mm (50% of the measured lateral FWHM) and axial spacing of 1.5 mm (500% of the approximate axial FWHM) was

chosen within the 1.08 cm² activation region (see Methods section) in order to ensure bubble clouds generated from DFB droplets did not overlap significantly and minimizing exposure of existing bubbles to the higher energy activation pulses. These represent distances in between the spacing presented in Figure 4.11c-d. In our setup using a linear array transducer with an elevational lens, the pulse pressures increased with depth up to the elevational focus. However, this will not necessarily be the case *in vivo*, as frequency-dependent attenuation diminishes the pulse pressure as a function of depth and frequency.

Initial *in vivo* investigations at the same pulse parameters used for *in vitro* verification were not capable of producing contrast from DFB droplets, although they proved sufficient to generate contrast from OFP droplets. In order to counteract tissue attenuation and aberration, transducer voltage was increased to 30V for the focused-wave activation state, but the plane-wave imaging states remained at 18V. In order to estimate the actual *in vivo* pressures at this output voltage, the free-field pressures (see Methods section) were derated by a model assuming 3 mm of superficial soft tissue (attenuation coefficient of 0.6 dB/cm at 1 MHz) followed by kidney tissue (attenuation coefficient of 1.0 dB/cm at 1 MHz). The attenuation coefficients were scaled assuming a frequency dependence of 1.1 ($\alpha = \alpha_0 f^{1.1}$) [199–201]. With this model, the highest *in vivo* PNPs during the B-mode and pulse-inversion imaging states were 273.7 kPa (MI = 0.09) and 433.1 kPa (MI = 0.14), respectively (Table 4.2). During the focused-wave activation state the PNP was 3.7 MPa (MI = 1.65) at a depth of 3 mm (the shallowest pulses near the start of the kidney region). At 10 mm, where the kidney region of most of the test rodents ended, the PNP was 4.2 MPa (MI = 1.89). The highest PNP was 4.5 MPa (MI = 2.01), occurring at a depth of 8.5 mm. The deepest focused pulses in the activation ROI, occurring at 12 mm, produced a PNP of 3.8 MPa (MI = 1.70). Thus, the majority of the focused pulses occurred at mechanical indices below the regulatory limit of 1.9, although the pulses central to the kidney occurred at output levels slightly above MI = 1.9 as a result of the elevational focusing lens.

Estimated <i>In Vivo</i> Imaging Pressures			
	Max PNP		
State	Axial Location (cm)	Maximum PNP Value (MPa)	Mechanical Index
B-mode	0.50	0.27	0.09
Pulse Inversion	0.50	0.43	0.14

Estimated <i>In Vivo</i> Activation Pressures			
	Axial Location (cm)	PNP Value (MPa)	Mechanical Index
Start of Kidney	0.30	3.70	1.65
Maximum PNP	0.85	4.50	2.01
End of Kidney	1.00	4.20	1.89
End of Activation ROI	1.20	3.80	1.70

Table 4.2. *In vivo* pressure estimations based on a simple tissue attenuation model.

4.3.2.3 Contrast Enhancement Measurements

For tests involving bubbles (no activation pulse), very little contrast signal (due to artifact) was present prior to injection (Figure 4.12). After injection, the relatively high dose of bubbles created a strong contrast signal that diminished at each time point until no contrast enhancement was observed (typically between minutes 11 and 15). Similar to the microbubble tests, very little signal was present within the kidneys prior to PCCA injection (Figure 4.12). After injection of DFB droplets the kidneys produced similar contrast to the agent-free baseline, indicating agents were still in the liquid state and that few, if any, bubbles were present due to spontaneously vaporized droplets. OFP droplets, however, produced some ‘flashing’ contrast after injection during the pre-activation imaging sequences, indicating either spontaneous vaporization to bubbles while in circulation or activation of OFP droplets by imaging pulse pressures (see further discussion below). After the vaporization sequence was triggered at 1 minute post-injection, a high degree of contrast was present in the kidney for both DFB and OFP (Figure 4.12). DFB droplets created a distinct spatial pattern due to the spacing between the individual vaporization pulses. Subsequent imaging/activation sequences for DFB every 3 minutes up to the final time point at 19 minutes showed a similar spatial pattern with a gradual decrease in the

amount of contrast produced. For tests with OFP droplets, a high degree of uniform contrast was present throughout the kidney after the activation pulse was delivered. No spatial patterning was present, indicating a much higher degree of activation and bubble formation. In fact, at early time points, the contrast present within the kidney was high enough to cause shadowing deep within the kidney that brightened as contrast washed out of the upper imaging plane.

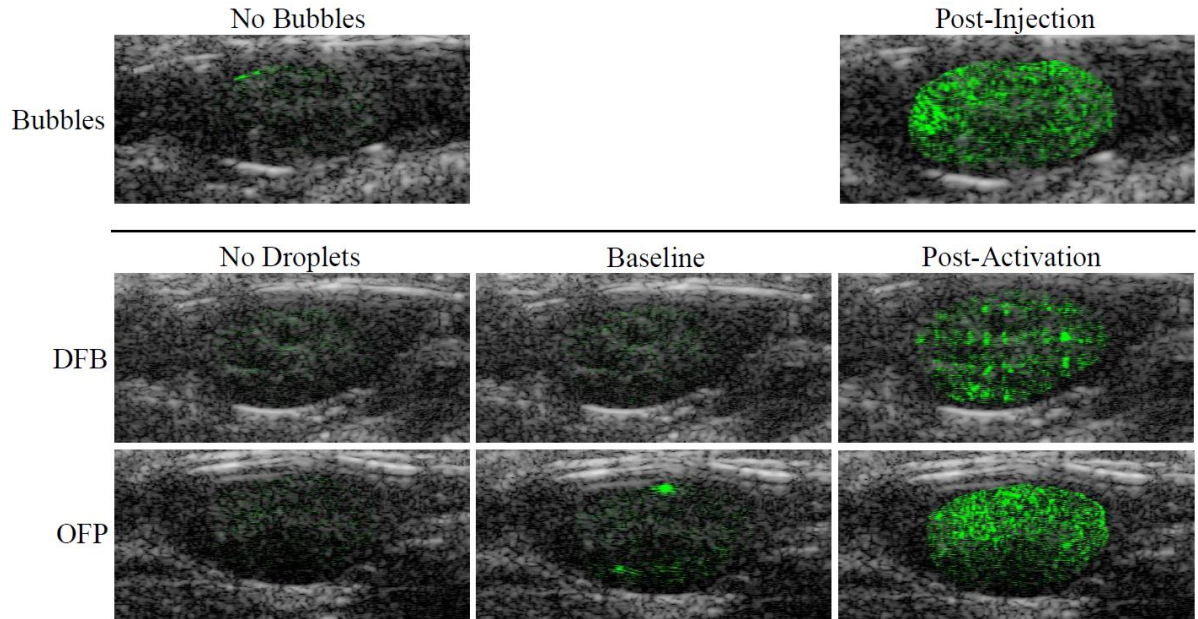


Figure 4.12. Example overlays of B-mode (grey scale) ultrasound scans and contrast-specific pulse-inversion scans (green scale) for each contrast agent tested. In all images, the pulse-inversion scans have been manually cropped to the borders of the kidney region to illustrate differences in signal within the kidney. The first column displays the agent-free case (pre-injection), and the second column corresponds to the pre-activation imaging (after injection but before activation). DFB droplets produced no significant increase in contrast after injection, but once activated exhibited a ‘patterned’ contrast appearance with lower mean contrast compared to microbubbles. OFP droplets, in comparison, exhibited some ‘flashing’ in the pre-activation state as a result of unwanted activation, and generated uniform contrast with a higher mean value than microbubbles after the activation sequence. The level of OFP activation was high enough to produce shadowing deep within the kidney at early time points.

Due to the low vaporization thresholds of OFP and relative thermal instability, contrast is produced even during the pre-activation imaging, manifesting as bright, temporary ‘flashes’ in the videos (Figure 4.12). This may be due to a combination of spontaneously vaporized droplets as well as droplet vaporization due to the pressure of the imaging pulses. In previous *in vitro* studies, the vaporization threshold of microscale OFP droplets exposed to 8 MHz, 2 cycle pulses proved to be at

peak negative pressures on the order of 0.5 MPa [134]. Here, the imaging state reached estimated peak negative pressures in the tissue of 424.2 kPa, and so we hypothesize that this effect is primarily due to imaging pulses that exceed the vaporization threshold of large outlier droplets still in circulation at early time points. This is consistent with preliminary studies using lower imaging pressures, where OFP ‘flashing’ was not observed.

Measuring contrast produced by the microbubble injections inside the ROI produced a steady level of CE in the 1 second captures at each time point. Droplets, on the other hand, produced a distinct wash-out phase as the newly generated contrast diffused out of the imaging plane and into the rest of the kidney and circulatory system over the 10 to 20 seconds following the activation sequence. Characterizing the CE relative to the agent-free baseline for all frames of the video capture produced a contrast wash-out curve at each major time point (Figure 4.13). Repeating this measurement at each major time point allows assessment of the change in the level of activation over time, which is directly related to the decay and clearance of the non-activated agents remaining in circulation. In these contrast wash-out curves, breathing motion manifests as dramatic drops in the measured value, as breathing causes translation into a neighboring imaging plane where fewer bubbles exist. In Figure 4.13, breathing motion artifacts have been manually removed to increase clarity.

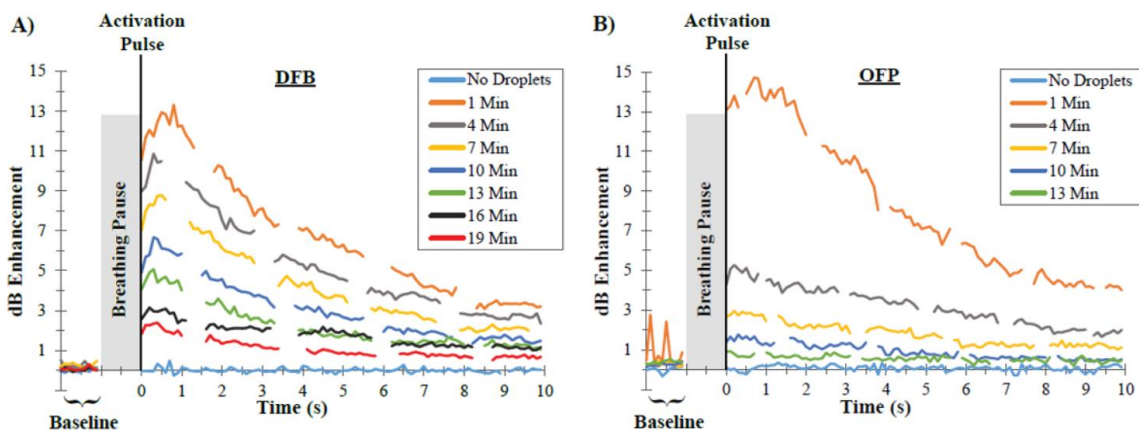


Figure 4.13. Examples of contrast measurements taken for individual animals administered A) DFB and B) OFP droplets. The mean value of the contrast enhancement increased over a short period following the vaporization pulse and then decreased as agents washed out of the kidney imaging plane. For OFP droplets, spikes in the 1 minute pre-activation capture are visible caused by unwanted vaporization.

Grouping the CE results for each animal by agent type allows for further analysis illustrating the fundamental difference in the behavior of the agents. The maximum contrast present in animals prior to microbubble injection (N = 6) (representing the ‘noisiest’ frame in the agent-free video capture) was 0.19 ± 0.10 dB. After injection, microbubbles produced a high degree of initial contrast, with a mean value of 12.63 ± 3.64 dB at the 1 minute time point (Figure 4.14a). Over the next 10 minutes, the contrast decayed quickly and returned to baseline levels by the 13 to 15 minute time points.

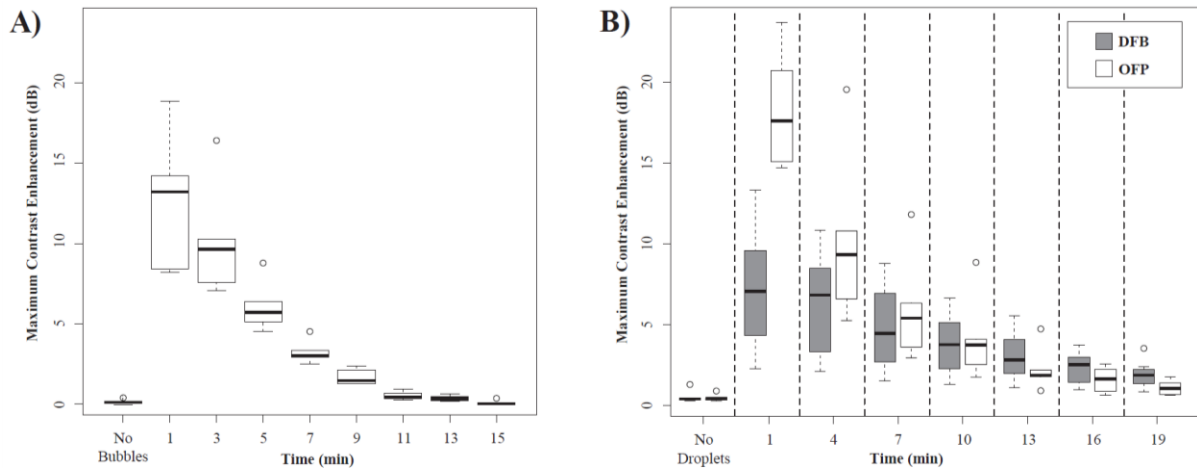


Figure 4.14. Maximum dB enhancement relative to the mean of the agent-free baseline for A) microbubbles after injection and B) droplets after application of a vaporization sequence. The mean signal within the ROI showed that microbubbles produced a high degree of contrast initially that cleared by the 15 minute mark. Contrast generated by activation of OFP was initially greater than DFB and microbubbles, but decayed more rapidly than DFB due to droplet instability.

For the droplet groups, the pre-injection measurements were similar to the microbubble test group, with noise in the measurement on the order of less than 1 dB (Figure 4.14b). After the activation sequence, animals in the DFB test group (N = 7) produced a mean CE at 1 minute post-injection of 7.29 ± 3.65 dB over the agent-free baseline. At each sequential time point, the ‘on-demand’ contrast from the activation sequence gradually decreased in magnitude, producing a mean CE of 2.27 ± 0.92 dB at the 19 minute mark that could be easily observed in the video sequence. In comparison to DFB droplets and microbubbles, activated OFP droplets produced a high initial CE, with a mean value of 18.24 ± 3.14 dB at 1 minute post-injection. Similar to microbubbles, OFP contrast generated from each activation sequence decayed rapidly over the course of 19 minutes. At the 13 minute post-injection time

point, contrast produced by OFP had a lower mean value (2.24 ± 1.19 dB) than DFB (3.49 ± 1.78 dB), suggesting the concentration in the bloodstream diminished much more rapidly than DFB. This matches prior *in vitro* experiments demonstrating relatively poor thermal stability of OFP droplets at 37°C [134]. The results highlight the difference in stability between choices of PFC: at the last time point tested, new contrast was being generated in all animals given DFB droplets, while OFP droplets had cleared from circulation in the majority of animals.

To arrive at the CE values in Figure 4.14, measurements were normalized to the mean value of the agent-free baseline images rather than the pre-activation images collected just before application of the vaporization sequence. This choice was based on preliminary studies showing that the pre-activation measurement of OFP agents was influenced by droplet vaporization (Figure 4.12 and Figure 4.13b). Thus, normalizing to the pre-activation mean value would have the effect of under-reporting the actual contrast generated by OFP particles at early time points.

4.3.2.4 Half-life Measurements

By normalizing the CE data to the maximum value, the circulation half-life can be calculated with a mono-exponential fit described in (Figure 4.15). Using this analysis, microbubbles had a mean decay rate of 0.22 ± 0.02 min⁻¹, producing a mean circulation half-life of 3.26 ± 0.37 min. The minimum and maximum half-lives in the group were 2.77 min and 3.83 min, respectively. OFP droplets produced similar measurements as microbubbles, with a mean decay rate of 0.20 ± 0.06 min⁻¹. The mean half-life of the group was 3.67 ± 0.37 min, with minimum and maximum half-lives in the group of 2.43 min and 5.51 min, respectively. OFP half-lives were not statistically significantly different compared to the half-lives of the microbubble group ($p = 0.4$, student's two-tailed t-test). DFB droplets, while initially showing lower contrast than the other two types of particles at the 1 minute time point, produced a significantly slower mean decay rate of 0.07 ± 0.01 min⁻¹. The mean half-life of the group was 10.84 ± 1.63 min, with minimum and maximum half-lives in the group of 8.07 min and 13.02 min, respectively.

DFB half-lives were statistically significantly different compared to both microbubbles and OFP droplets ($p << 0.01$).

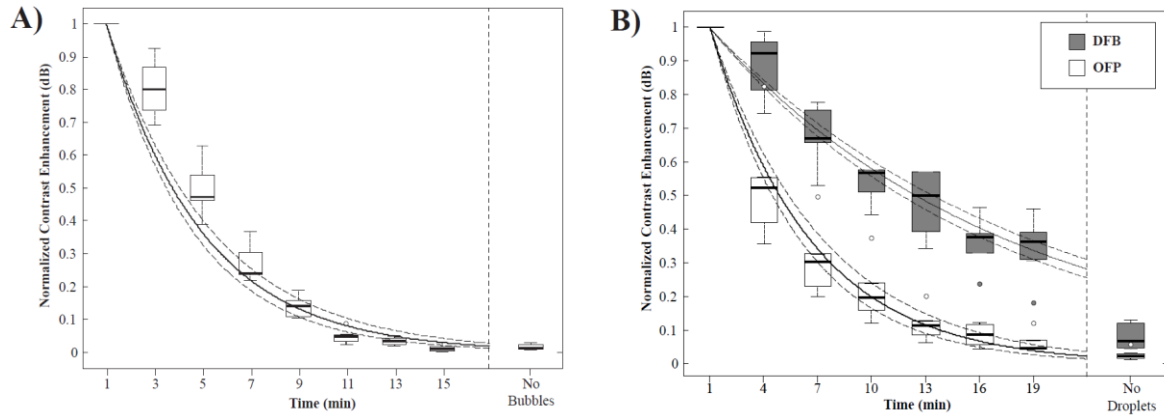


Figure 4.15. Maximum contrast enhancement (CE) over the mean of the agent-free baseline normalized to the maximum value produced by each animal for A) microbubbles and B) droplets. DFB decayed at a significantly slower rate than OFP and microbubbles, resulting in contrast production half-lives on the order of 3-fold longer than microbubbles and OFP droplets. Shown in solid lines are the exponential curve fits to the grouped data, with 95% confidence intervals in dashed lines.

4.3.3 Optimization of Activation Parameters

When APM was used, the bubble clouds produced by the activation pulses are of similar size as a result of the consistent activation pressure throughout the field of view (Figure 4.16a). Conversely, when a single voltage was used without PWM, the bubble clouds were vastly different in size, indicating that the activation pressure for the deeper regions was excessive since vaporization was achieved with a smaller pressure in shallower areas (Figure 4.16b). The size of the bubble clouds produced by the activation pulses was calculated using a method described previously by Puett et al. [191], where the number of pixels with an intensity higher than 1% of the cloud's brightest pixel were counted, and this number was multiplied by the pixel size to get an area measurement (Figure 4.16c-d). Each box in the box plot represents the area for the 5 bubble clouds at the different depths (rows). The size of the bubble clouds is very similar between the different depths when APM was used (Figure 4.16c); cloud size between the different depths is not significant for any two depths. In contrast, when a single voltage is used for activation, there was a clear positive trend as the elevational focus was

approached, and the area of the bubble clouds was significant between rows in all but 3 cases (Figure 4.16d).

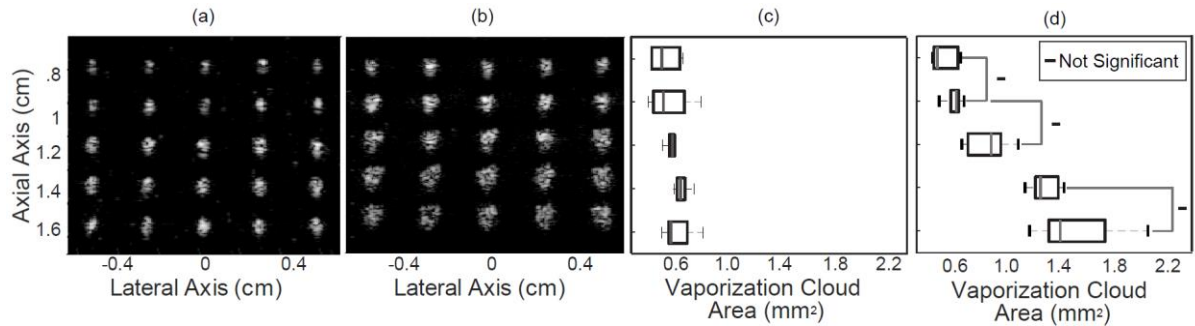


Figure 4.16. Difference between using APM (a) and a single voltage without PWM (b) on bubble cloud size. The bubble clouds on (a) are similar in size, indicating that the vaporization pressure was uniform for all activation areas. Not using PWM results in a range of activation pressures that vary with depth, which increases contrast generation as the pulses approach the elevational focus. The area of the activation clouds was measured for each depth (rows) and APM produced bubble clouds of the same size (c), while the size of the clouds increased with depth when a single voltage was used (d).

Figure 4.17 shows the results of the activation pulse spacing experiments. When the 2 intensity profiles could not be differentiated, or the FWHM points are not visible, because the spacing is too small, the distance value was calculated by subtracting twice the mean FWHM of the largest spacing (1 mm and 0.75 mm for the axial and lateral cases, respectively) from the FWHM of the intensity profile. For example, the FWHM distance value for 0.5 mm in Figure 4.17 a was twice the mean FWHM of the intensity profiles for the 1mm spacing (0.95 mm), subtracted from the FWHM of the 0.5 mm intensity profile (0.475 mm), which produced value -0.475 mm. Three trials were averaged for each spacing, and the FWHM distances for the axial spacings 1, 0.75, and 0.5 mm were 0.515 ± 0.13 , 0.16 ± 0.034 , and -0.475 ± 0.11 mm, respectively, and the values for the lateral spacings 0.75, 0.5, 0.25 mm were 0.4 ± 0.089 , 0.22 ± 0.056 , and -0.36 ± 0.08 mm, respectively. Therefore, the optimal spacing for the L11-5 was around 0.75 mm and 0.5 mm in the axial and lateral directions, respectively.

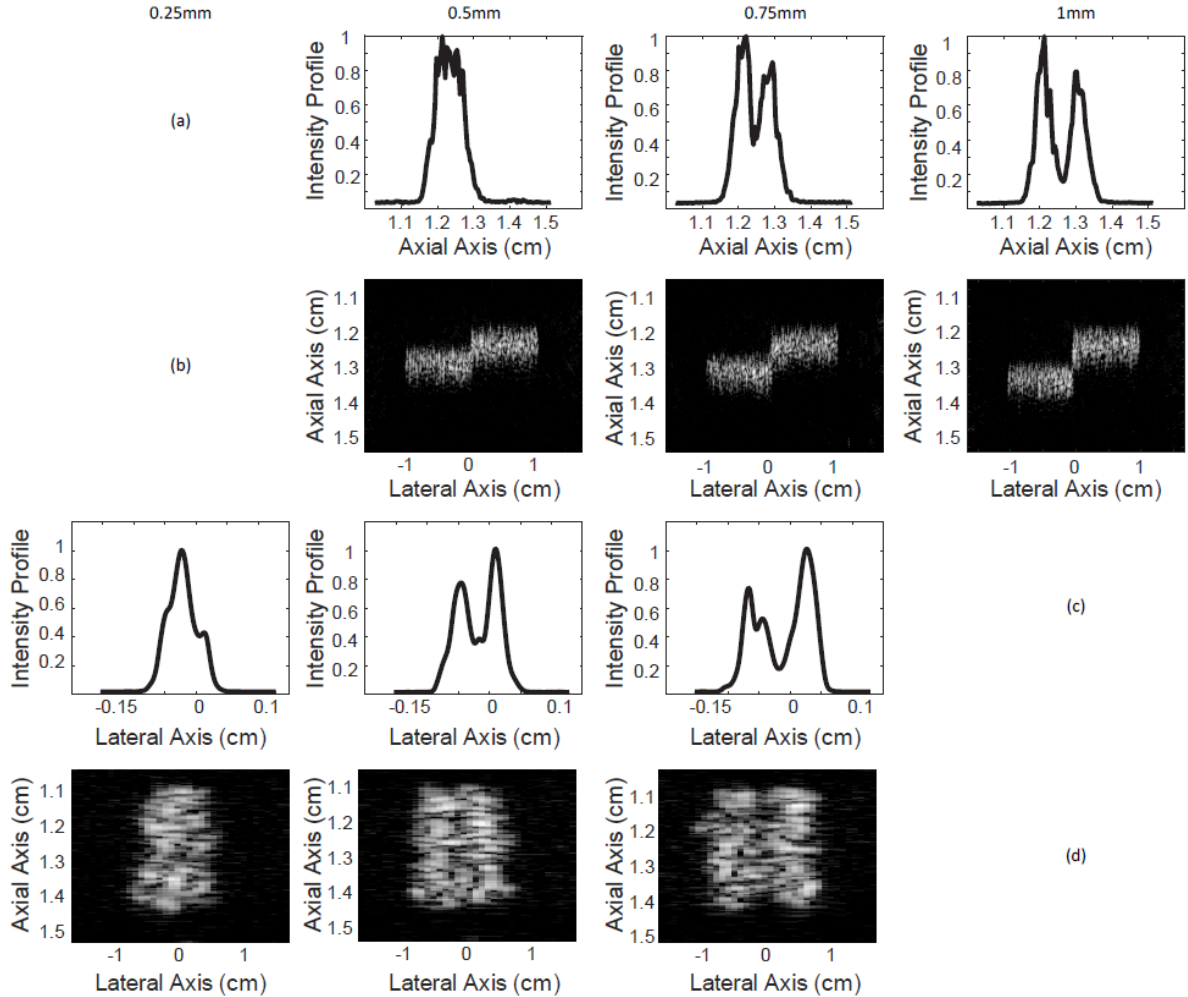


Figure 4.17. Intensity profiles (rows a and c) were generated by averaging imaged data from activation lines (rows b and d) separated by a range of distances between 0.25 and 1 mm. The optimal spacing between activation lines is characterized by the overlap of the FWHM of the intensity profiles of adjacent lines and so 0.75 mm and 0.5 mm are the best axial and lateral spacing.

Using APM along with the optimized spacing, a uniform region of vaporization can be generated (Figure 4.18). As previously discussed, uniform activation is possible without APM using the methods described by Puett et al. [191]. However, that approach requires over-activation of droplets around the elevational focus in order to vaporize regions located further away from the transducer. APM creates uniform vaporization without excessive vaporization or energy delivery in the near-field.

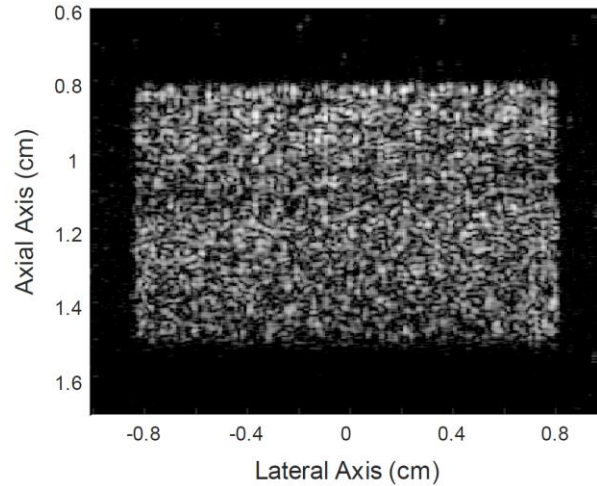


Figure 4.18. APM and optimized spacing creates a region of uniform contrast.

When APM was used in the kidneys of rats, APM generated uniform vaporization inside the kidney, indicating that the pressure delivered to each activation location was similar, and the spacing between locations was appropriate (Figure 4.19).

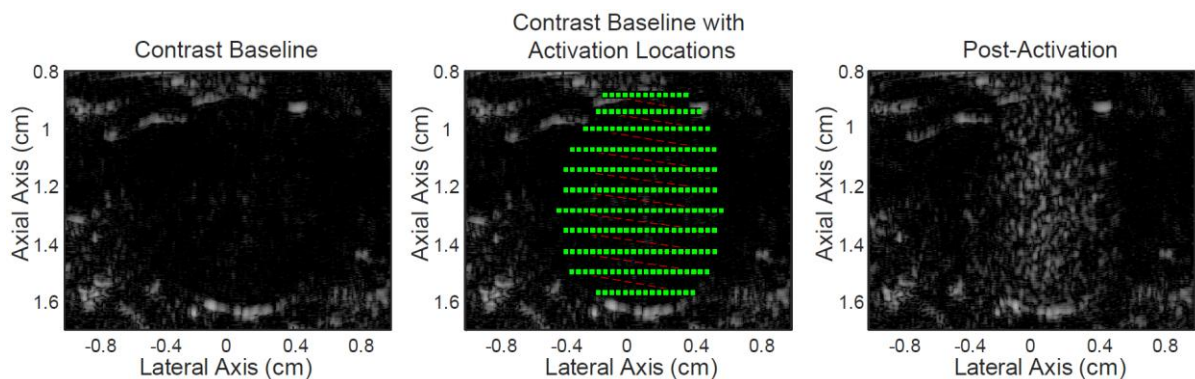


Figure 4.19. OFP droplet activation in a rat kidney using APM and optimized spacing. The left image shows the contrast image of the kidney before droplet vaporization, and the image on the right is an image of the post-activation contrast that was generated by the activation pulses (center). The green dots on the center image represent the activation locations. Consistent activation throughout the kidney was achieved by sending activation pulses with the same peak rarefactional pressure regardless of depth.

The results from the circulation study show that, as expected, OFP yielded a higher contrast enhancement with more droplets activated for a given pulse (Figure 4.20). However, the decreased stability of OFP led to spontaneous vaporization which reduced the concentration of agents in droplet form and decreased the circulation time, as was seen in the previous section. It should be clarified that

what is being referred to as “circulation time” in this study is the time for which detectable contrast can be generated, not the time the droplets remain in the vasculature. Figure 4.20 shows that the CE, in dB, relative to a baseline image taken prior to the injection of PCCAs. The CE for OFP was almost three times that of DFB (a) at the one-minute time point, and OFP was cleared much faster than DFB (b). The CE at each time-point was normalized to the one-minute time point and fitted to a mono-exponential decay model in order to calculate the circulation half-life. The half-life for DFB and OFP was 15.97 ± 3.0 and 6.92 ± 0.7 min, respectively. In both cases, the resulting value obtained by using APM was substantially higher than the previous section when unoptimized activation parameters were used. The droplets were circulating the same amount of time but using APM makes the vaporization at all depths more efficient enabling the use of the injected droplets for a much longer time. This part of the study demonstrates the benefit of using optimized activation parameters for *in vivo* applications.

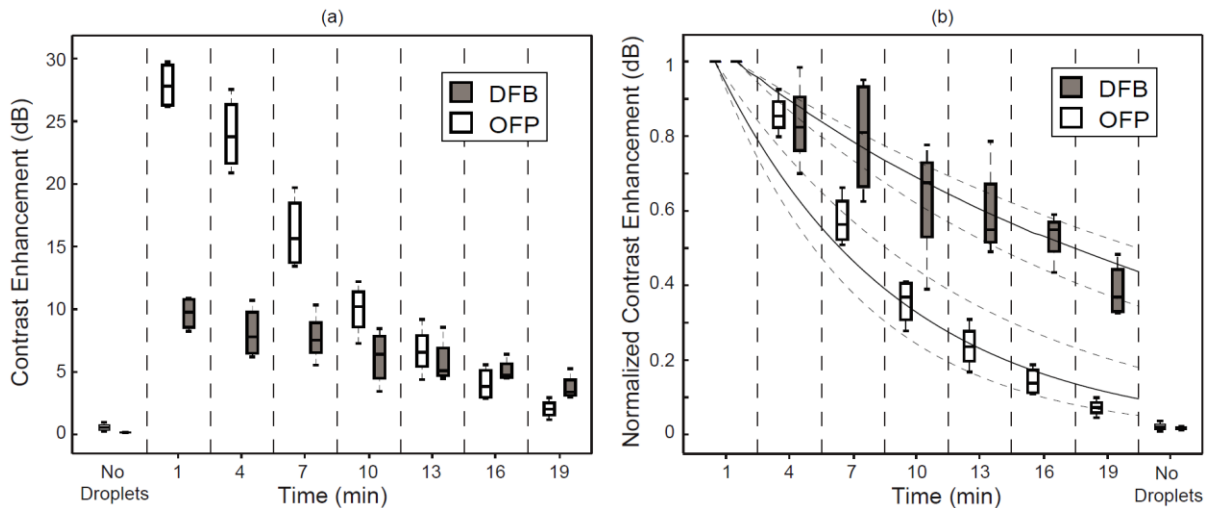


Figure 4.20. Contrast enhancement over the baseline case for each time point (a), and normalized to the one-minute time-point (b). The plot on the left shows that the contrast generated when OFP droplets were activated using APM is much greater than that of DFB at the one-minute time point. Conversely, OFP has a circulation time that is less than that of DFB, as can be seen on the right plot. A mono-exponential (Ae^{-bt}) was fit to the normalized contrast enhancement data (solid line) and used to compute the circulation half-life for each type of droplet. The dashed lines represent the 95% confidence intervals of the fit. The half-life was 15.97 ± 2.96 min for DFB and 6.92 ± 0.65 min for OFP. Both values are much higher than previously reported.

4.3.4 Vaporization Detection Imaging

4.3.4.1 Activation Signal Detection

Example voltage traces can be seen in Figure 4.21. It can be seen that the onset of activation shifts left, earlier in the pulse, as the vaporization pressure increases for 3 and 5 cycles. It is worth noting that the transmitted pulses, closely resembled the water signals in Figure 5 (dark blue), were longer than specified (1, 3, or 5 cycles) due to the ramp up and ring down of the L11-5.

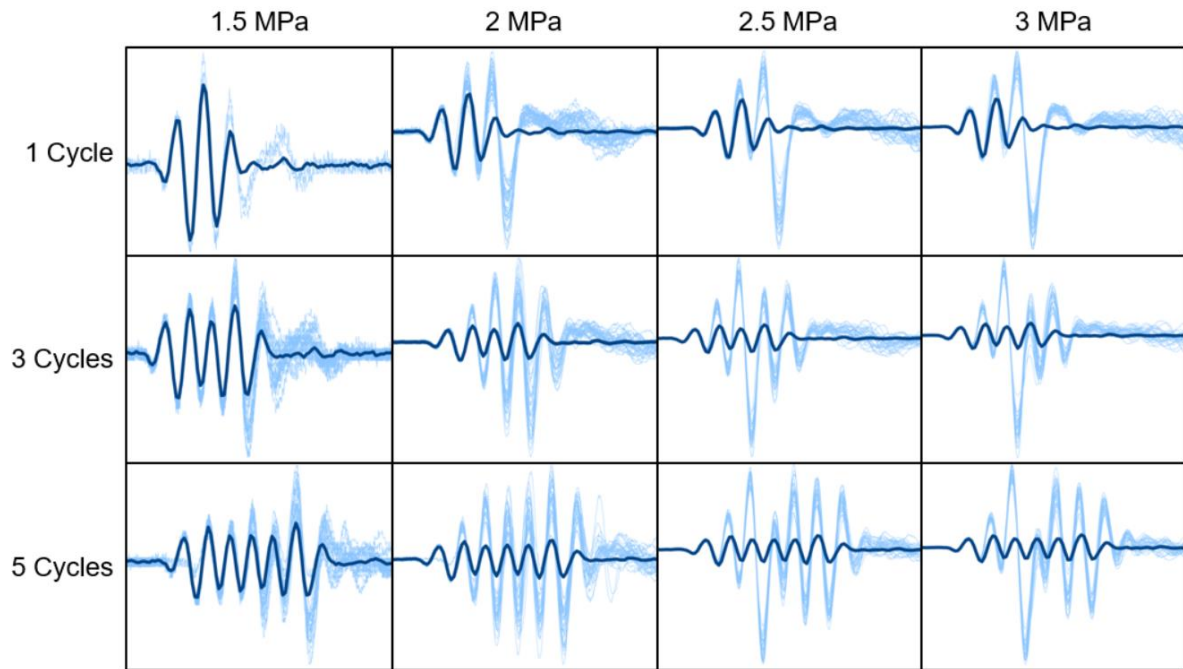


Figure 4.21. Example voltage traces from droplet vaporization detection. Dark blue is the mean voltage trace of the no-droplet case (only water), and the light blue are individual recordings of PCCA activation signals.

After the received signals were filtered, the AUC of the no-droplet case, essentially the signal from the microtube, could not be significantly reduced with filters with corner frequencies below 2 MHz (Figure 4.22). Therefore, all data was filtered with a 2 MHz low-pass filter for the AUC analysis. Filtering the data ensured that the scattered signal from the droplets and microtube were eliminated, so that the spectrum only contained frequency content from vaporization signals.

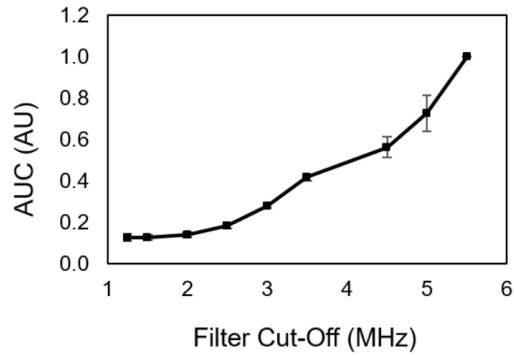


Figure 4.22. AUC of tube signals after different filters.

The effect of pulse length was explored to test the hypothesis that short pulses can achieve efficient activation with large enough amplitudes to make high CTR images, and will limit interactions with the produced bubbles. Therefore, the effect of pulse length on vaporization efficiency, amplitude, and frequency was evaluated.

To investigate the vaporization efficiency of different pulse lengths, a threshold defined as the first pressure at which 25% of acquisitions contained activation was found. The results can be seen in Table 4.3. The vaporization threshold at the 0.1% dilution was higher for the 1 cycle pulses for both DFB and OFP, and it was higher for 1 cycle for OFP at the 0.01% dilution. The lower thresholds for 3 and 5 cycles indicate that longer pulse lengths are more efficient at vaporizing droplets. However, the AUC results showed that using 1 cycle produces signals that were not significantly lower ($p > 0.05$) than 3 and 5 cycles for most pressures and dilutions (Figure 4.23). Therefore, long pulses are not required for effective vaporization and signal detection.

	DFB			OFP		
	0.01%	0.10%	1%	0.01%	0.10%	1%
1	1.5	1.5	1	1	0.75	0.5
3	1.5	1	1	0.75	0.5	0.5
5	1.5	1	1	0.75	0.5	0.5

Table 4.3. Vaporization Threshold (MPa) for the different pulse lengths and dilutions.

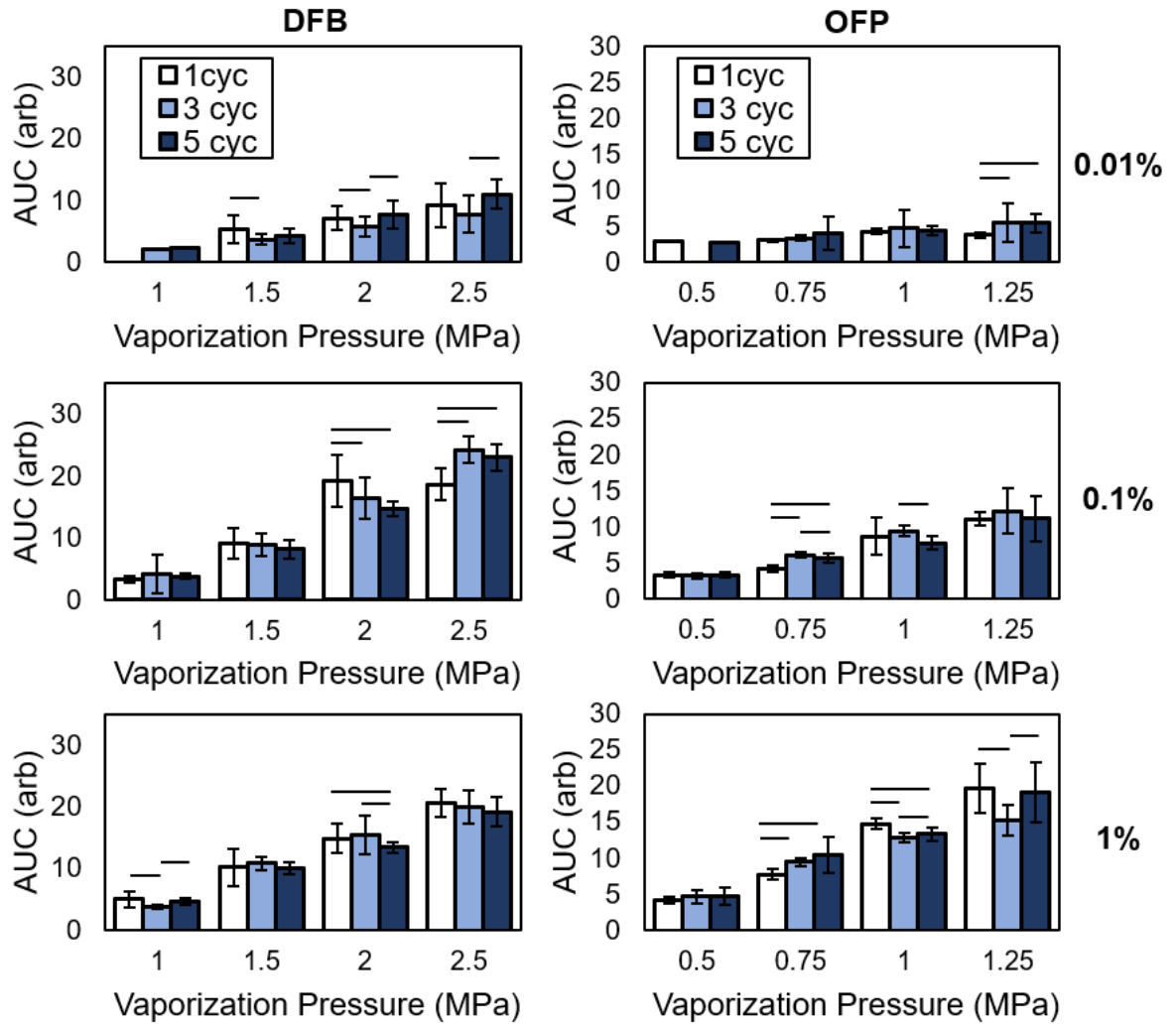


Figure 4.23. AUC results of DFB (left column) and OFP (right column) for the different dilutions (rows). Significance ($p < 0.05$) is denoted by the black bars. 1 cycle (white) activation pulses produce values similar to those produced by 3 (light blue) and 5 (dark blue) cycle pulses in most cases.

The results for the mean frequency analysis are shown in Figure 4.24 and indicate that longer pulses produce a higher mean frequency, especially for the lower dilutions and higher pressures. Furthermore, 1 cycle pulses have a significantly lower ($p < 0.05$) mean frequency than 3 and 5 cycles in most cases. These findings agree with the hypothesis that longer pulses interact with the produced microbubbles, since the mean frequency shifts toward the transmit frequency.

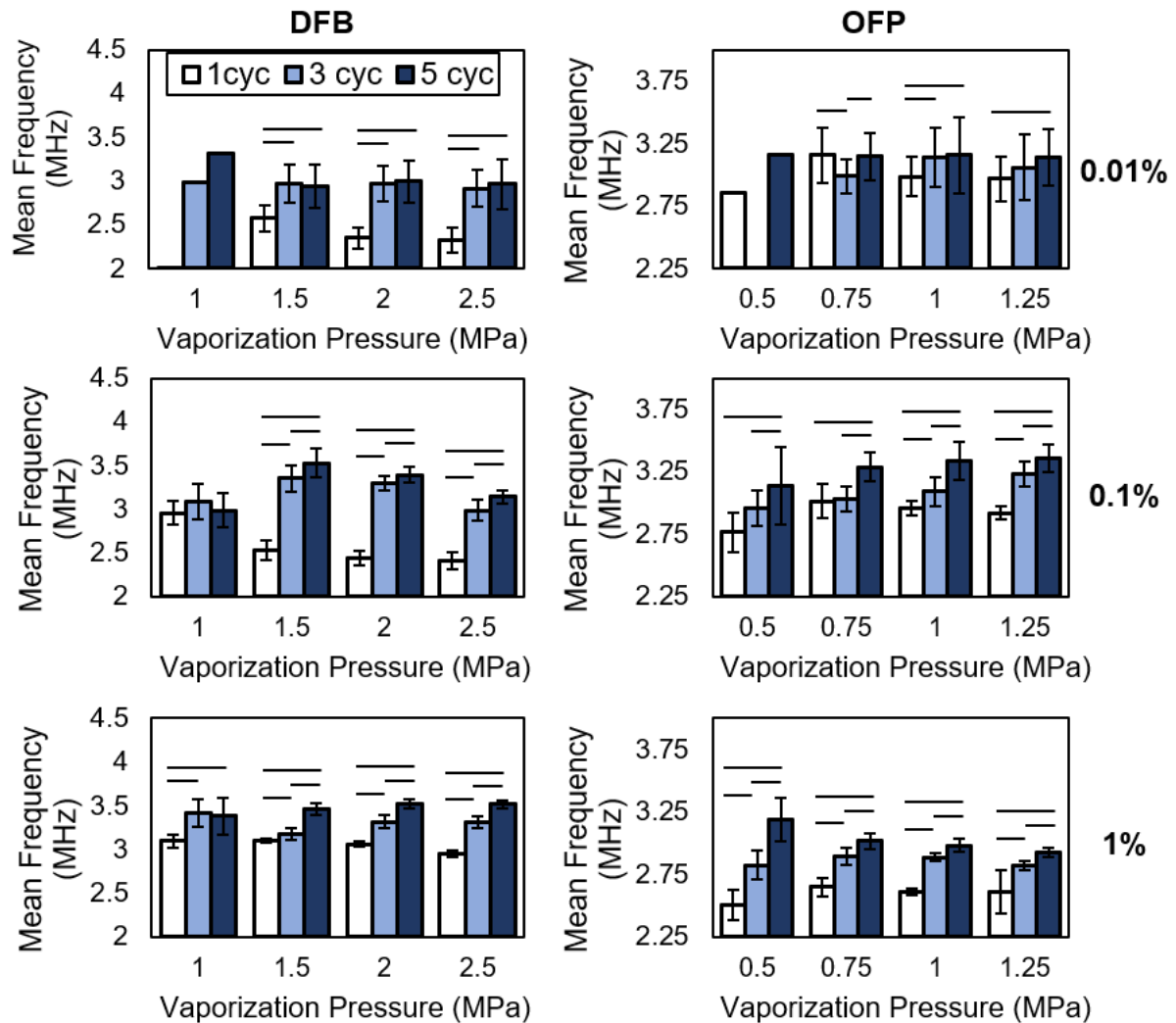


Figure 4.24. Mean Frequency results of DFB (left column) and OFP (right column) for the different dilutions (rows). Significance ($p < 0.05$) is denoted by the black bars. The mean frequency increases with pulse-length for most pressure-concentration combinations for OFP and DFB.

Lastly, the effect of the PFC core was explored. In order to compare DFB and OFP, a threshold where all the pulse lengths produced activation in 25% of trials was calculated (Table 4.4). DFB had a significantly lower ($p < 0.05$) AUC from OFP in only a single instance (Figure 4.25 **Error! Reference source not found.**). Therefore, the results suggest that DFB produces vaporization signals that are as strong or stronger than OFP.

DFB			OFP		
0.01%	0.10%	1%	0.01%	0.10%	1%
1.5	1.5	1	0.75	0.75	0.5

Table 4.4. Vaporization Threshold (MPa) used for comparing DFB and OFP. Defined as the first pressure at which all pulse lengths produced activation in 25% of experiments.

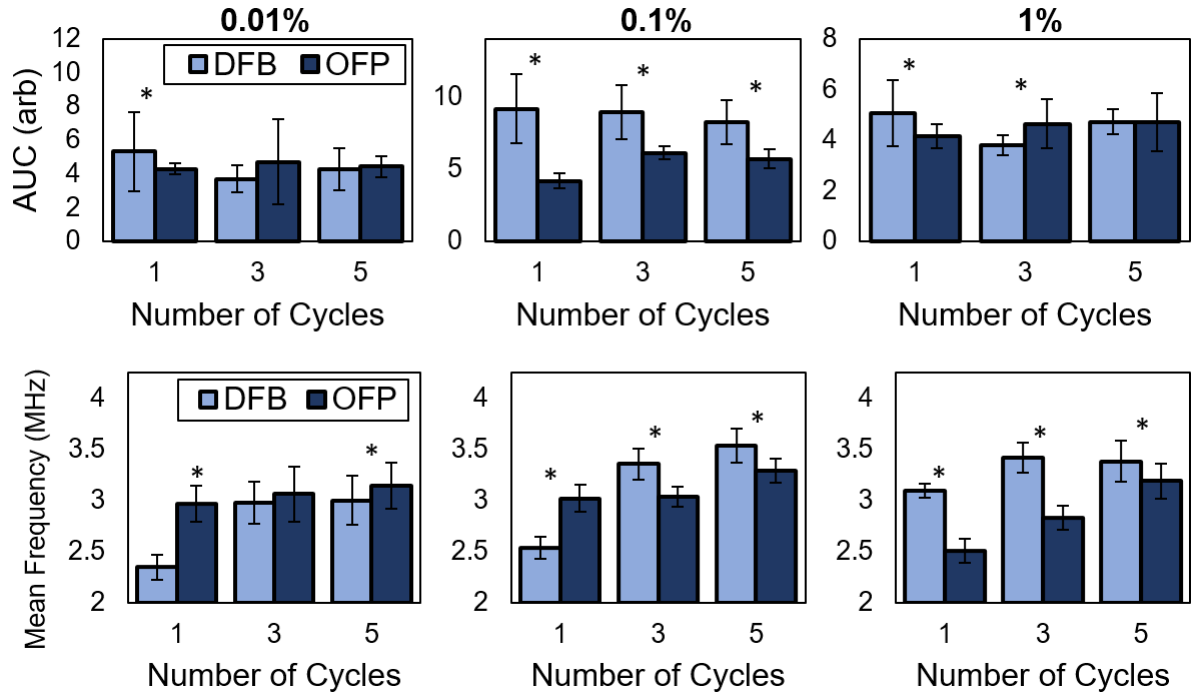


Figure 4.25. AUC comparison between DFB (light blue) and OFP (dark blue) for the different dilutions (columns) using the 25% threshold (top row). Mean Frequency results of DFB vs OFP at the 80% threshold for the different dilutions (bottom row). The AUC for DFB is as high or higher than OFP in most cases, and no clear relationship was found for the mean frequency results. Significance ($p < 0.05$) is denoted by (*).

The thresholds described before represent the onset of activation and are appropriate for exploring the amplitude of the activation signals, since the pressure is the minimum that is required and will not affect the response unnecessarily. However, a threshold where activation is produced most of the time (at least 80% of trials) is more suitable for imaging and was also calculated (Table 4.5). When this 80% threshold was used to calculate the mean frequency, no clear relationship was found between

the mean frequency of DFB and OFP, except that DFB had a significantly higher ($p < 0.05$) mean frequency at the 1% dilution for all cycles (Figure 4.25).

DFB			OFP		
0.01%	0.10%	1%	0.01%	0.10%	1%
2	1.5	1	1.25	0.75	0.5

Table 4.5. 80% vaporization threshold.

4.3.4.2 *In vivo* Imaging

The CE of the VDI images using the different filters is shown in Figure 4.26. The 1.5 MHz filter was chosen even though its CE was not significant from the 2 MHz filter for either DFB or OFP, because its CE was significantly higher from the 1 MHz filter for OFP and has the highest average CE.

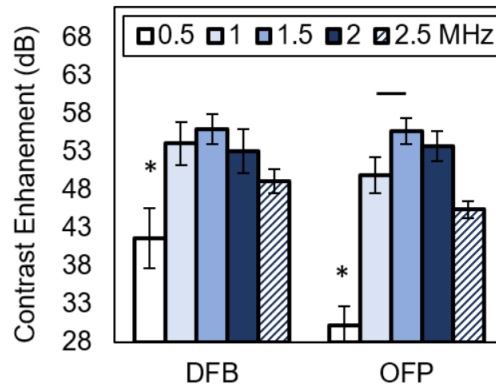


Figure 4.26. CE of *in vivo* data using different filters for both DFB (left) and OFP (right). Significance ($p < 0.05$) is denoted by the black bars, and the (*) represents significance from all other filters. The 1.5 MHz has the highest mean CE and was chosen to filter the rest of the data.

Figure 4.27 shows example images of VDI filtered with the 1.5 MHz filter, and Figure 4.28 shows example CI images. The CE analysis shows that VDI has significantly higher values from CI for all DFB pressures and the three highest OFP pressures (Figure 4.29).

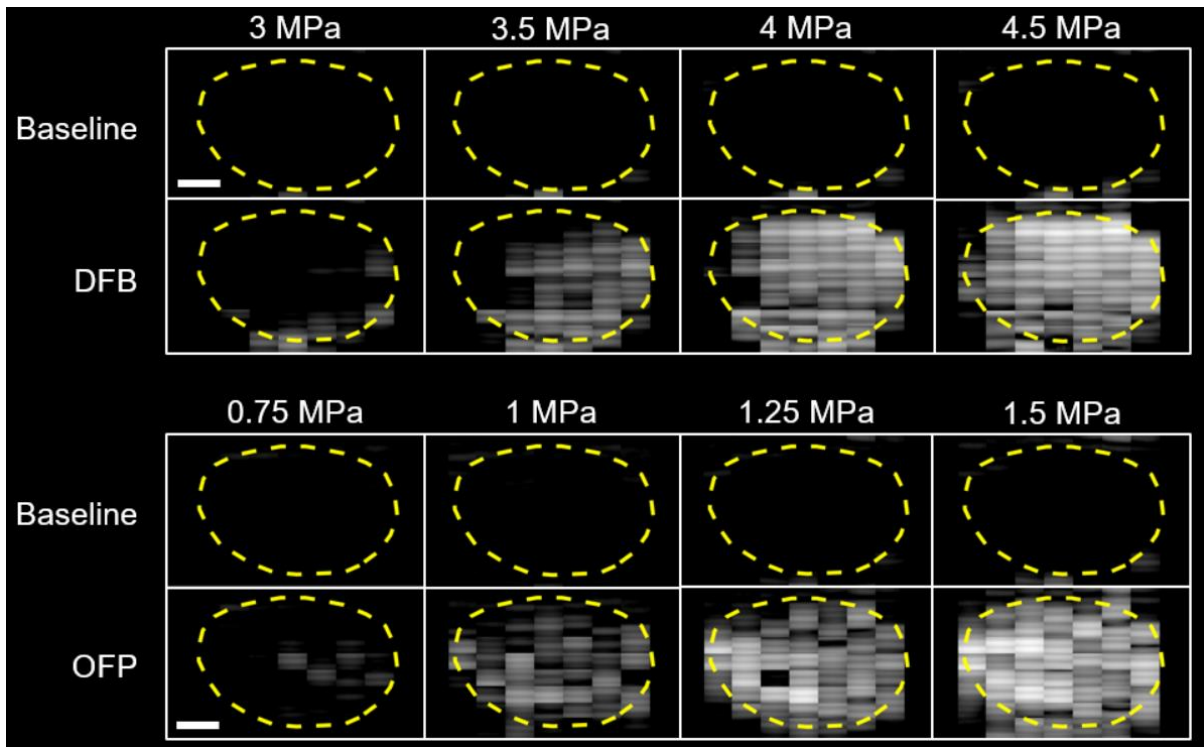


Figure 4.27. Example *in vivo* VDI images from DFB (top panel) and OFP (bottom panel). The baseline images are shown on the top row of each panel for each of the different pressures (columns), and the activation images are shown on the bottom row. The scale bars represent 2 mm.

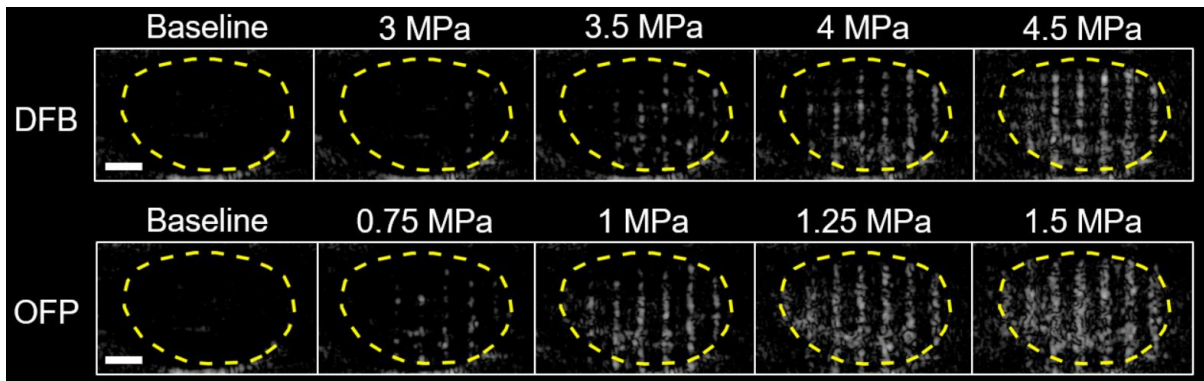


Figure 4.28. Example *in vivo* CI images of DFB (top row) and OFP (bottom row) before PCCA injection (left-most column) and at each activation pressure (column). The scale bars represent 2 mm.

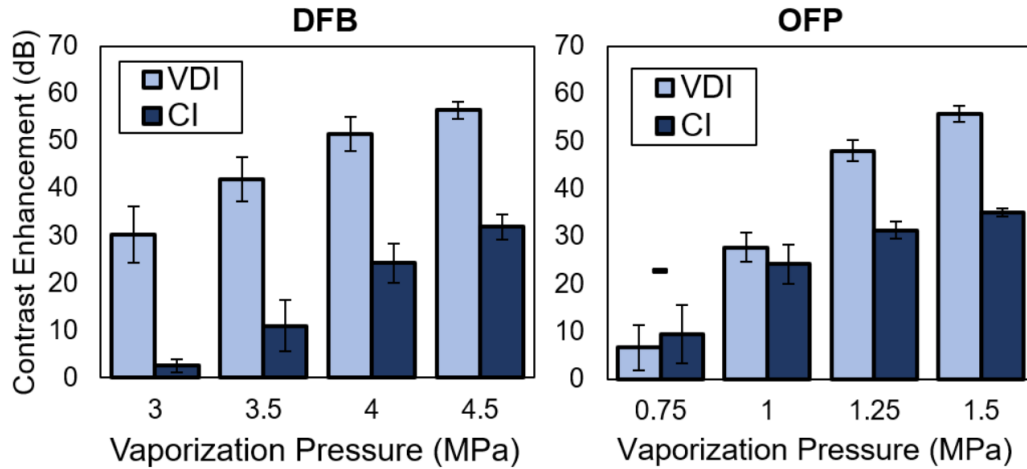


Figure 4.29. CE of VDI vs CI images for DFB (left) and OFP (right). VDI is significant ($p < 0.05$) from CI for all cases except for OFP at 0.75 MPa, denoted by (-).

4.3.4.3 Activation at Depth

Figure 4.30 shows example images of VDI and CI of the two microtubes in the tissue-mimicking phantom. Similar to the *in vivo* imaging, the CE is significantly higher for VDI over CI (Figure 16). These results are expected and confirm the hypothesis that VDI has better depth of penetration, since the vaporization signals have a low frequency, and produces higher CE values.

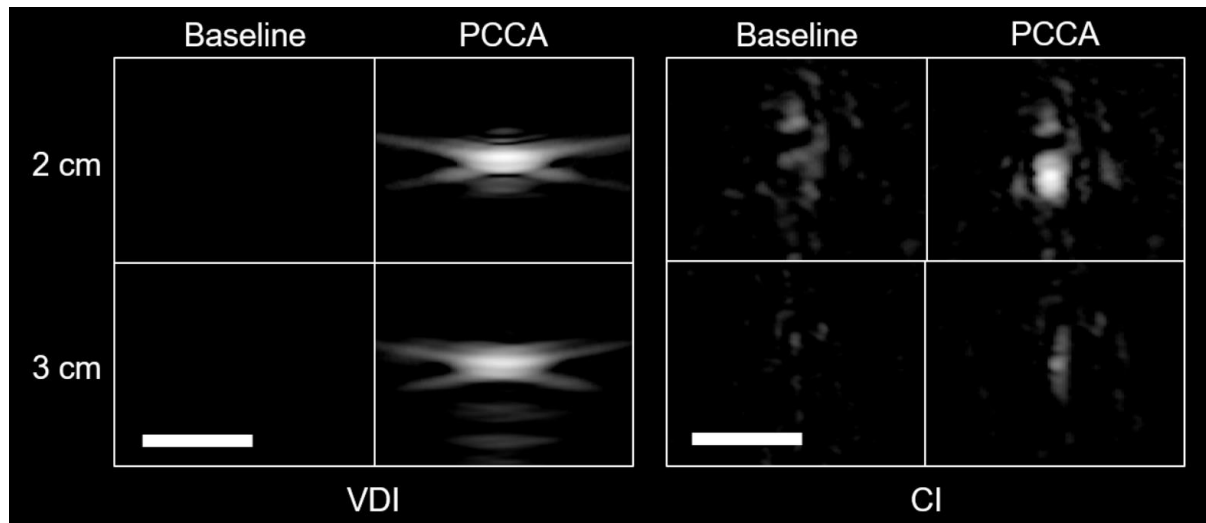


Figure 4.30. CE of VDI (left panel) and CI (right panel) images of activation at depth in the 2 and 3 cm tubes before (left column) and after (right column) the introduction of droplets. The scale bars represent 3mm.

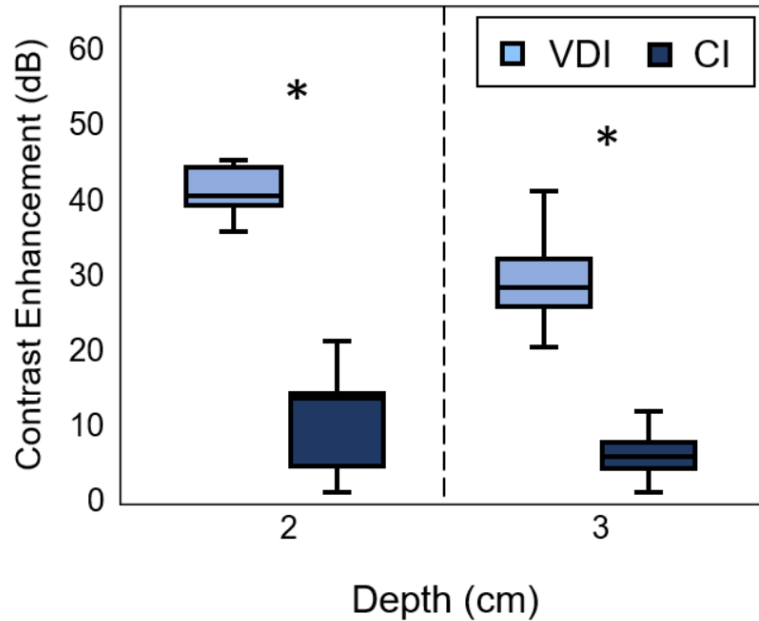


Figure 4.31. CE of VDI (light blue) and CI (dark blue) images from droplet activation in the microtubes at 2 and 3 cm.

4.4 Discussion

4.4.1 Development of Pulse Sequences for the Use of PCCAs

One unexpected aspect of the wash-out curves captured in this study (Figure 4.13) is the appearance of two distinct phases. In the first phase, typically occurring in the first second following the vaporization sequence, the contrast within the ROI increases until it reaches a maximal value within 1 to 2 dB of the initial value. This increase may be partly due to contrast spreading from the spatial location of the peak pressures into neighboring regions. It may also be a result of bubble growth shortly after vaporization due to intake of ambient gases dissolved in the bloodstream [101,128,129,202]. In the second phase, the contrast decays exponentially as it washes out of the imaging plane and into the rest of the bloodstream. The mechanisms that create this two-phase behavior require further investigation.

The exponential decay portion of these contrast curves affords a unique possibility to measure a wash-out rate of the vascular network in the imaging plane. Because contrast can be generated ‘on-

demand' with PCCAs and monitored in real-time, the clearance rate can be captured and used as an indication of perfusion. This is similar in concept to the destruction-replenishment curves gathered in microbubble-enhanced ultrasound that have been utilized to measure tissue perfusion [203,204]. In destruction-replenishment, pressures near the current upper limit of diagnostic ultrasound are used to destroy the microbubbles in the imaging plane, followed by lower imaging pressures to capture contrast reperfusion. Conversely, with a PCCA sequence, high pressures are used to generate contrast in the imaging plane rather than destroy it, and lower pressures used to capture wash-out rather than reperfusion.

Although the wash-out characteristics here were captured after a single activation sequence spanning the entire region of interest and with similar droplet size distributions, there are many implementations that could be explored in future studies. Beyond measuring differences in perfusion as a function of droplet size, one could create sparse pockets (i.e. from single pulses) at desired locations and measure the dissipation as an indication of the underlying vasculature. This differs fundamentally from MCA DCE-US, where microbubbles in the entire imaging volume are destroyed and the measurement depends on the re-perfusion from all neighboring vascularized tissue. It may be much simpler to apply PCCA wash-out measurements to 3D imaging than destruction-replenishment, since a single bolus could be created in the center of the volume of interest and then be tracked as it dissipates. In larger vessels, PCCAs could be vaporized upstream using electronic steering and the microbubble bolus tracked as it passes a target site - allowing measurement of both flow velocity and flow dynamics. This may be a very desirable approach to theranostic applications, such as targeted clot break-up, where a site is evaluated using PCCA perfusion and then treated.

The results demonstrate that PCCAs generally have longer circulation properties than microbubbles Figure 4.15. Even the most volatile PCCA explored in literature to date - OFP droplets (PFC boiling point of -36.7°C) - exhibited a virtually identical clearance rate to microbubbles, while DFB droplets had more than three times the measured contrast half-life that microbubbles exhibited.

This study also demonstrates that PCCAs at relatively similar doses can produce similar contrast properties as clinical microbubble formulations, which matches previous studies exploring the acoustic properties of bubbles produced from PCCAs [205].

The performance of the two different PCCA formulations was compared with set imaging and activation parameters in order to evaluate relative differences when the same acoustic settings are chosen. In reality, the pulse sequence should be designed around formulation and intended use (therapeutic vs. diagnostic) of the PCCA. Some of these considerations are highlighted in a recently published investigation performed in parallel to this one [206]. Here, the acoustic choices resulted in over-activation and unintended vaporization during imaging for OFP droplets, and under-activation of DFB droplets as a result of the drastic differences in droplet boiling point. Because of elevational focusing from the transducer used, the peak negative pressures varied highly with depth. This resulted in activation pulses that were lower than the regulatory limits ($MI = 1.9$) as well as some that exceeded these limits, highlighting the need for optimized activation parameters. It is evident from the images both *in vitro* (Figure 4.11) and *in vivo* (Figure 4.12) that activation of DFB and OFP can be accomplished at PNPs below these limits – as contrast is produced at superficial locations where the measured pressures do not exceed these limits. This is consistent with previous *in vitro* studies showing that DFB droplets can be activated optimally with short pulses that do not exceed $MI = 1.9$ [130].

4.4.2 Optimization of Activation Parameters

Activation Pressure Matching, the method described in this study, relies on using PWM to regulate the output pressure so that all activation locations are insonified with the same amount of pressure. The use of this approach allows for efficient droplet vaporization and the generation of uniform contrast in a region of interest without delivery of excessive pressure. In addition to modulating the output pressure for different depths, optimal spacing between activation points can be found in order to consistently vaporize droplets in the target. APM can be applied *in vivo* by using an appropriate attenuation model. In this study a rat kidney model was used to demonstrate that by modulating the

initial output pressure, uniform vaporization is achieved in the tissue after attenuation compensation Figure 4.19. When APM was used to activate OFP and DFB droplets over time, it was found that the circulation time of both compounds was much longer than indicated by previous experiments that used un-optimized activation parameters because higher amounts of detectable contrast are generated Figure 4.20.

This experiment presented a new method for activating droplets that can be a valuable tool for PCCA applications for the treatment and assessment of disease. For example, if droplets are targeted to a disease marker, as in USMI, it is imperative that the vaporization pressure is consistent throughout the tissue since variations in activation pressure will cause spatial inhomogeneities in vaporization. This is an issue because it would be challenging to determine if differences in contrast are a result of inconsistent pressures or different levels of targeting throughout the tissue.

Inconsistent activation pressure would also be a problem for a perfusion imaging approach using PCCAs. Instead of measuring the wash-in of contrast into an imaging plane, as is done in microbubble destruction reperfusion techniques, the contrast generated by droplet activation can be monitored as it washes out of the imaging plane to obtain a measure of perfusion. Because droplets provide excellent temporal and spatial control of contrast generation, different regions of a target can be activated at different times in order to see any differences in perfusion in different tissues. A previous study found that the perfusion rate in kidneys depends on the concentration of microbubbles that is used [58]. Therefore, if different vaporization pressures are used, the perfusion rates might be different due to a disparity in droplet activation and not due to any physiological factors.

Additionally, when investigating bio-effects caused by droplet vaporization, it is essential to produce uniform vaporization in order to reliably correlate droplet vaporization with therapeutic effects or tissue damage. Also, it is reasonable to assume that limiting the amount of energy delivered into the tissue to the minimum needed to achieve the desired result will induce the least amount of bioeffects.

These needs suggest that APM will be a desirable tool in not only imaging but also therapeutic applications.

APM can vaporize droplets efficiently to produce uniform contrast generation in rat kidneys. However, APM does not take into account phenomena such as aberration which is a significant factor in human ultrasound imaging. As a result of aberration, pulses become de-focused by changes in density and speed of sound between different tissues. De-focusing of activation pulses can result in uneven vaporization of PCCAs and may require the tissue to be insonified with increased energy to overcome the loss of pressure due to weaker focusing. Therefore, a simple attenuation model may not be appropriate for use in humans where the volume of tissue that is interrogated is much larger than in a rat or mouse. Interestingly, using droplets for aberration correction has been proposed [94], so it is possible that preliminary pulses can be delivered to form microbubbles and monitor vaporization differences in order to evaluate aberration effects and further calibrate APM for efficient activation. Additionally, APM depends heavily on using the correct attenuation model and therefore, a different derating scheme must be used for each type of tissue (various types of tumors and body organs) in order to efficiently obtain uniform droplet activation.

APM is a novel approach to PCCA activation that has various advantages over using unoptimized activation parameters; mainly, the ability to deliver the same amount of pressure to all activation sites in order to minimize the energy that is delivered and produce uniform activation throughout the target. Furthermore, APM can serve as an important tool for the accurate assessment of disease progression and response to therapy.

4.4.3 Vaporization Detection Imaging

The *in vitro* examination of the vaporization signals showed that even though pulses with 3 and 5 cycles were more efficient at vaporizing DFB and OFP droplets, the signal produced by the 1 cycle pulses was equally as strong (Figure 4.23). Furthermore, using longer pulses produces signals with higher mean frequencies (Figure 4.24), suggesting that the pulse may be interacting with the

microbubbles that are being created. The interaction of the high-pressure activation pulses with microbubbles might generate cavitation and lead to unwanted bioeffects. Additionally, using long pulses for vaporization might introduce error to the image reconstruction of VDI, since the onset of vaporization can occur at different parts of the pulse, depending on pressure (Figure 4.21). The reconstruction regions for each activation location should be positioned around the maximum amplitude of the signal, but this point may be at different depths depending on which cycle of the pulse triggers vaporization, so individual reconstruction regions may not be centered with the maximum of the vaporization signals. Therefore, short pulses should be used for making images from PCCA vaporization signals.

Interestingly, it was found that DFB produced similar or higher AUC values than OFP when compared at the 25% threshold (Figure 4.25). This contradicts the findings of a previous study, which showed that OFP produces significantly higher signals than DFB [137]. A possible explanation is that Sheeran et al. used the same vaporization pressures for both types of agents, even though OFP is much more volatile, so more OFP droplets may have been activated than DFB when the same pressure was used. It is expected for OFP to produce higher amplitude signals because of its higher volatility [137]. However, in this work, DFB, which requires higher pressures for activation than OFP, has higher AUC values, especially at the 0.1% dilution, suggesting that the amplitude of the activation pulses may have an effect on the amplitude of the vaporization signal.

Surprisingly, there was no apparent relationship in the mean frequency between DFB and OFP, except that DFB has a higher value at the 1% dilution. The two PFCs behave differently at the same temperature because of their difference in volatility, so it might be expected that one type of PCCAs would consistently have a higher or lower frequency, but this is not the case here. Further investigation is required to determine whether or not there is a difference in the frequency of vaporization signals of OFP and DFB droplets.

In vivo results show that VDI produces significantly higher CE than CI for all DFB pressures and all OFP pressures except 0.75 MPa (Figure 4.29). Specifically, CI for DFB has a very small CE value at 3 MPa, while VDI has a value that is more than an order of magnitude higher, suggesting that VDI may be able to detect signals from a small number of droplets that are undetectable using CI. This is not the case, however, with OFP at 0.75 MPa, where the CE is not significant between VDI and CI. As previously discussed, the amplitude of the vaporization pulses may affect the amplitude of the activation signals, so a possible explanation is that the vaporization signal is weak due to the small amplitude of the activation pulse.

The pressures used for OFP vaporization are much lower than those used for DFB so the OFP baseline should contain less tissue signal. Therefore, the CE for OFP should theoretically be higher. However, the intensity obtained from the baseline and vaporization images of VDI is almost 2 orders of magnitude larger for DFB, and the maximum CE is similar. This difference in intensity is much more drastic than the difference in AUC from the *in vitro* experiment. *In vivo*, the difference in activation pressures was much larger than *in vitro*, so the large difference in intensity between DFB and OFP supports the hypothesis that the amplitude of the activation pulses affects the amplitude of vaporization signals. Since DFB and OFP have different acoustic vaporization thresholds, it is difficult to test this theory, so a protocol involving thermal activation [131,135] may be more appropriate. However, there is evidence that temperature plays a large role in microbubble behavior and response to ultrasound [207,208], so differences in activation may be caused by the ambient temperature and not the composition of the droplet core.

One of the main limitations of this work is the inability to objectively compare DFB and OFP, as mentioned previously, because of differences in the acoustic vaporization threshold. Since different pressures were used to activate either OFP or DFB, it is unclear if the amplitude of the vaporization signals is only a product of the core and shell composition. Even though 1 MPa was used to activate both OFP and DFB *in vitro*, it is difficult to determine if the comparison is valid, since this pressure is

hardly enough to activate DFB. Furthermore, the L11-5 was used to enable the comparison of VDI and CI but using a transducer with a more appropriate bandwidth may provide better results. Additionally, the L11-5 has a lens that focuses the beam elevationally at around 1.25 cm, so the output pressure is greatly reduced for deeper regions. Therefore, a more suitable transducer could allow exploration of droplet activation at depths of 5 cm or more. Droplet activation at depth could be explored at depths of 5 cm or more with a more suitable transducer.

The conventional imaging technique used here was pulse inversion, which involves capturing the second harmonic components of the bubbles produced by PCCA activation. However, using other techniques such as CPS, which has been shown to be more sensitive to MCAs than pulse inversion [43], might make the difference in CE between conventional imaging and VDI smaller. Furthermore, contrast imaging techniques such as subharmonic imaging, which captures the frequency components at half of the excitation frequency, might allow for higher depth of penetration due to the lower frequency [209–212], and might be better for imaging deep targets than pulse inversion.

We have demonstrated that a single ultrasound transducer can be used to capture the vaporization signals of low boiling-point PCCAs and make images that have significantly higher CE values than traditional methods. Because droplet activation signals have characteristic frequencies below 1 MHz, they provide better depth of penetration, but the resolution is poor. Therefore, with the current approach, VDI cannot be used to produce high resolution vascular maps as with Acoustic Angiography [69,186]. However, because VDI has a very high sensitivity to PCCAs, it could be used in applications that do not require high spatial resolution, such as molecular imaging, where being able to detect small changes in biomarker expression is desirable.

4.5 Conclusions

In work, it was demonstrated that custom imaging and activation sequences can be developed to produce and capture contrast from perfluorocarbon phase-change contrast agents *in vivo*. Moreover, the bubbles produced by these pulse sequences can circulate much longer than MCAs *in vivo*,

depending on the formulation, and have similar levels of contrast generation. Furthermore, it was shown that activation pressure matching can be used to produce uniform activation of PCCAs *in vitro* and *in vivo* and extend the time for which PCCAs can generate usable contrast. Lastly, a new technique for imaging PCCAs was developed, which is highly sensitive to droplets and can produce significantly higher contrast-to-tissue ratios than the conventional image-activate-image pulse sequences.

CHAPTER 5

THE EFFECT OF HYDROSTATIC PRESSURE, BOUNDARY CONSTRAINTS, AND VISCOSITY ON THE VAPORIZATION THRESHOLD OF LOW BOILING- POINT PHASE-CHANGE CONTRAST AGENTS⁶

5.1 Introduction

Low boiling-point PCCAs have been proposed for diagnostic applications such as molecular and perfusion imaging [126,127], and the feasibility of using them for diagnosis *in vivo* has been demonstrated [127,143,196]. However, activation thresholds using clinical frequencies (< 10 MHz) *in vivo* have been reported to be higher than *in vitro* [127,196]. In this work, hydrostatic pressure, viscosity, and boundary constraints imposed by vessel walls are explored as possible contributors to this discrepancy.

It has been shown that hydrostatic pressure affects the response of microbubbles so that subharmonic content can be used to estimate microvascular and interstitial fluid pressure in a technique called SHAPE [213,214]. Additionally, the Borden group has performed extensive work on the characterization of droplet condensation and vaporization using changes in temperature [131,215,216].

⁶ Copyright © 2018 Word Federation for Ultrasound in Medicine & Biology. Published by Elsevier Inc. Reprinted, with permission, from JD Rojas, MA Borden, PA Dayton, "Effect of Hydrostatic Pressure, Boundary Constraints, and Viscosity on the Vaporization Threshold of Low Boiling-Point Phase-Change Contrast Agents", *Ultrasound in Med. & Biol.*, 2018. In Review.

Pressure is also a parameter in the governing equations for superheat stability, which suggests that hydrostatic pressure may influence the vaporization threshold of PCCAs.

The effect of boundary constraints on microbubble oscillations has been explored in tubes and chambers with rigid boundaries [217–219] and compliant microvessels [220], and the results from these studies show that the response of the microbubbles is dampened when near or at a boundary. Furthermore, Caskey et al. showed that expansion of microbubbles resulting from an ultrasound pulse is reduced with decreasing tube diameter even in tubes that are an order of magnitude larger than the initial bubble diameter [217]. This result suggest that boundaries affect the response of the oscillating bubble even if the bubble does not come in contact with the wall, probably due to the increased resistance displacing fluid in a small diameter tube. When low-boiling point PCCAs are activated, the sudden transition of the core from liquid to gas causes the agent to over-expand past, and oscillate down to, its final diameter in an event that takes less than 10 μ s and produces a unique acoustic signal [137,215] and thus, the activation threshold might be affected if the vessel walls reduce the over-expansion of the droplet.

Many studies have modeled the effect of viscosity on microbubble response and suggested that a more viscous surrounding media dampens bubble oscillations [221–223]. More recently, work involving contemporary contrast agents has experimentally shown that viscosities close to that of blood reduce oscillation amplitude and fragmentation [224,225]. Furthermore, the threshold for inertial cavitation was increased, and the harmonic content was reduced and exhibited non-linear resonance characteristics [226]. Increased viscosity dampens microbubble response, so it may play a role on the vaporization threshold of PCCAs.

In this study, the hypotheses that hydrostatic pressure, boundary constraints, and viscosity increase the threshold for PCCA activation were tested using microtubes with sizes down to 12.5 μ m, and a pressurized chamber. Using different activation measurement techniques, we demonstrate that the activation threshold increases when droplets are vaporized in conditions simulating vasculature,

namely the boundary constraints and increased viscosity *in-vivo*. Furthermore, we confirm that the *in vitro* results translate to *in vivo* imaging in a rat kidney.

5.2 Materials and Methods

The *in vitro* components of the study consisted of 3 parts: the effect of boundary constraints (1), hydrostatic pressure (2), and viscosity (3) on the threshold for droplet activation. In all parts, droplets were vaporized using a range of pressures and the level of activation was measured to find the pressure threshold required for activation. In part 1, levels of activation were measured in tubes of different diameters using ultrasound (US) imaging, optical microscopy, and detection of the vaporization signal produced by droplet activation. In part 2, activation inside of a chamber was measured using US imaging only while the chamber was pressurized with pressures ranging between 0 (no added pressure) and 17.24 kPa. For part 3, droplets in a microtube were vaporized when mixed with phosphate-buffered saline (PBS), viscosity of 1 cP, and a blood-mimicking fluid with a viscosity of 5.4 cP. Activation was measured using ultrasound imaging.

In each experiment, droplets were introduced into the tube or chamber, and activation measurements were taken after droplets were interrogated with pulses having peak negative pressures (PNP) between 1 and 4 MPa were delivered. New droplets were introduced between US exposures with flow to wash away the bubbles produced by activation and replenish the activation area. The delivered pressure (peak rarefactional) started at 1 MPa and was increased by 500 kPa steps after each activation, and the whole process was repeated for a total of 3 trials. All *in vitro* experiments were performed in a temperature-controlled water bath at 37°C. The final component of the study consisted of using US imaging to find the activation threshold of droplets *in vivo*.

5.2.1 Phase-Change Contrast Agent Fabrication

The phase-change contrast agents were made using established procedures [129,192] where conventional lipid-shelled microbubbles with a perfluorocarbon gas core were cooled to temperatures between -10°C and -12°C and pressurized with room air until the gas core condensed into a liquid. The

precursor microbubbles consisted of a decafluorobutane (DFB) core and a shell consisting of the following formulation: the lipids 1,2-distearoyl-sn-glycero-3-phosphocholine (DSPC) and 1,2-distearoyl-sn-glycerol-3-phosphoethanolamine-N-methoxy(polyethylene-glycol)-2000 (DSPE-PEG2000) in a 9:1 M ratio and a total lipid concentration of 1.0 mg/mL were dissolved in a solution of PBS, propylene glycol, and glycerol (16:3:1). Precursor microbubbles were produced by adding 1.5 mL of the lipid solution into a 3 mL vial, gas-exchanging the head space with DFB, and rapidly agitating the vial. Before condensation, an additional step was taken to remove outliers from the bubble population using a decantation method similar to that used in other work [143,227]. Briefly, bubbles were allowed to separate for 10 minutes so that 2 separate layers emerged and the infranatant was taken and used. This size-selection process eliminates outliers in the distribution that can throw off bulk activation threshold measurements. The final droplet size is between 100 and 400 nm.

5.2.2 Microtubes

A range of tubes of varying diameters were tested to explore the effect of a boundary on droplet activation. Three tubes of identical wall material and similar wall thickness were utilized, as well as a fourth very small tube, which unfortunately was made of a different material with walls that were approximately twice as thick. Three tubes consisted of fluorinated ethylene propylene (FEP), with lumen sizes of 50, 108, and 160 μm , and wall thicknesses of 8.5, 8.5, and 10 μm , respectively (Paradigm, Incom Inc, Charlton, MA, USA). The fourth tube, which was a different material the others but provided the smallest available lumen, was an acrylic tube with a 12.5 lumen and 18.75 μm wall thickness (Paradigm, Incom Inc, Charlton, MA, USA). For all experiments where tubes were used, a diluted solution consisting of 1-part stock droplet suspension ($5.0 \times 10^{10} \pm 4.5 \times 10^9$ #/mL) and 10 parts PBS was manually pumped through the tubes.

5.2.3 Pressurized Chamber

The chamber used for this experiment was a Slide-A-Lyzer 3.5K Dialysis Cassette (ThermoFisher Scientific, Waltham, MA, USA), because air or fluids could be easily injected into this

cassette, and prior tests have demonstrated the cassette wall membranes are acoustically translucent at the parameters tested (data not shown). The chamber was filled with a droplet solution with the same concentration used for the microtube experiments ($5.0 \times 10^{10} \pm 4.5 \times 10^9 \text{ \#/mL}$), and air was used to increase the hydrostatic pressure inside of the chamber. A syringe was used to inject air into port 1 of the chamber (Figure 5.1), and the hydrostatic pressure was monitored using redundant gauges at both port 1 and 2. The solution of droplets was refreshed between activations by injecting 1 mL of fresh solution using ports 3 and 4. The hydrostatic pressures used were 0, 3.45, 6.89, and 17.24 kPa. A maximum hydrostatic pressure of 17.24 kPa was chosen because it corresponds to a normal systolic pressure (129 mmHg).

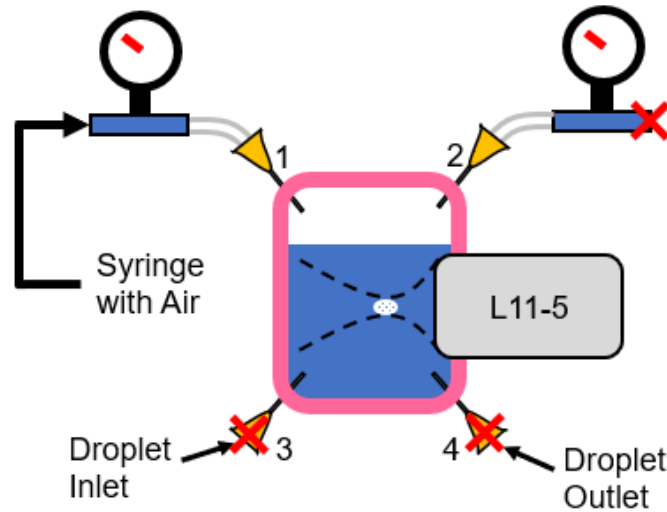


Figure 5.1. Schematic of the pressurized chamber system used for part 2 of the *in vitro* experiments; testing the effect of hydrostatic pressure on droplet activation. In the configuration shown in this figure, all ports are closed (marked with the red X's) except for port 1, which is being used to pump in air, so the chamber is being pressurized.

5.2.4 Blood-Mimicking Fluid

The 160 μm tube was used for the viscosity experiment. The same droplet concentration was used as described in the previous two sections, but the droplets were mixed with PBS (1 cP) or a blood-mimicking fluid (5.4 cP) which consisted of 56% (w/w) glycerol, and 1.3% (w/w) sodium chloride in PBS [228]. This fluid has the same viscosity as blood [229,230].

5.2.5 Phase-Change Contrast Agent Activation

All activation was performed using a 128-element ATL L11-5 linear array driven by a Verasonics V1 Research Ultrasound System (Verasonics, Kirkland, WA, USA). Activation pulses consisted of 5 MHz, 5 cycle, sinusoid focused at a depth of 1.3 cm (f-number of 0.4). The transducer was calibrated using a needle hydrophone (HNA-0400, Onda, Sunnyvale, CA, USA).

5.2.6 Measurement of Activation- Ultrasound Imaging

Ultrasound was used to monitor the level of activation by imaging the microbubbles that were created by the vaporization pulses. A pulse inversion scheme was used to capture bubble signal and reduce the signal from the tubes. Pulse inversion consists of delivering two consecutive pulses that are 180° out of phase and adding the radiofrequency signal received from each pulse in order to cancel the fundamental component of tissue signal and only keep the second harmonic content of microbubbles [42]. Here, we delivered the duo of pulses at 3 different angles (-18°, 0°, 18°) and an image was produced by the compounding of all the angles. The pulses were 4.5 MHz, 1 cycle, sinusoids with a mechanical index (MI, given by the PNP in MPa, derated by 0.3 dB/cm/MHz, divided by the square root of the frequency in MHz) of 0.17 at 1.3 cm. One image was captured before and after the vaporization pulse(s) was delivered. For experiments where the activation measurement method was US imaging, 5 activation pulses that were separated laterally by 1.5 mm and temporally by 150 μs were delivered in a line at a depth of 1.3 cm (Figure 5.2a). This was done to increase the level of activation signal in order to distinguish small differences in vaporization. 1.5 mm was chosen as the spacing between the activation pulses because it's large enough (30 dB beam separation) so that pulses didn't interact with the contrast created by the previous pulse.

5.2.7 Measurement of Activation- Optical Microscopy

An inverted microscope (Olympus IX71, Center Valley, PA) was used to observe droplet activation in each of the microtubes for the full range of vaporization pressures. The microtubes were positioned in the optical focus of the microscope, and droplets that were manually pumped through

were activated using the L11-5, which was aligned with the optical focus using the same needle hydrophone that was used for calibration. The 100x (NA = 1.0) water immersion objective was interfaced with a high-speed camera (FastCam SA1.1, Photron USA, Inc., San Diego, CA) to capture images before and after the delivery of the activation pulse at a rate of 125 frames per second. A framerate of millions of Hertz is required to capture the vaporization event, so the bubbles are evaluated once they have reached their final size. The activation event Droplet activation was confirmed using US imaging.

5.2.8 Measurement of Activation- Vaporization signal detection

When droplets are activated they over-expand and oscillate down to their final size, producing a very unique acoustic signature. The frequency content of this signal has been reported to range between a few hundred kHz and around 2 MHz, regardless of the vaporization pulse frequency [137]. Detecting vaporization of small numbers of droplets, as is the case in microtubes with small diameters (< 100 μm), may be difficult. However, droplet vaporization signals are larger than those resulting from microbubble excitation at vaporization pressures [137], and therefore, listening for these signals might be the most sensitive method for detecting activation. Here, a piston transducer with a center frequency of 1 MHz (Olympus Panametrics V314, Center Valley, PA) was used to receive the acoustic signature from droplets vaporized in the different microtubes, which were activated using the L11-5. First, the piston and the L11-5 were aligned using the needle hydrophone. For alignment of the piston, the transducer was driven with a 1 cycle sinusoid that was produced by an arbitrary function generator (AFG3021C, Tektronix, Inc., Beaverton, OR) and amplified by a 60 dB RF amplifier (A500, ENI, Rochester, NY). Once the transducers were aligned, the piston was connected to an RF receiver amplifier (BR-640A, RITEC, Inc., Warwick, RI, USA) set to pass signals above 50 kHz with a gain of 28 dB. The amplified signal from the piston were digitized at a sampling rate of 100 MHz (PDA14, Signatec, IL, USA) and captured with LabView (National Instruments, Austin, TX, USA) for offline analysis. Next, the microtube was aligned with the transducers by transmitting with the L11-5 and

moving the tube until the received signal from the piston was maximized. Before droplets were activated, the tubes were filled with water to obtain a baseline for each pressure.

5.2.9 *In Vivo* Droplet Activation

Droplet activation was performed in the right kidneys of 4 Fischer rats and vaporization was measured using the ultrasound imaging approach discussed above, following animal protocols approved by the University of North Carolina Institutional Animal Care and Use Committee. The animals were anesthetized using 2.5 % isoflurane and the right abdominal region was cleared of fur using an electric razor and chemical hair remover. The transducer was coupled to the skin using water-based ultrasound gel, and the droplets were administered through a 24-gauge catheter inserted into the tail vein. A continuous infusion of equal parts droplets-sterile saline (2.5×10^{10} #/mL) at a rate of 30 μ L/min was used. The droplets were allowed to circulate for 2 minutes before the first activation to allow the concentration to reach a steady state in the vasculature. As in the *in vitro* experiments, Activation Pressure Matching (APM) was used to deliver the same pressure to a series of vaporization locations to create a region of uniform activation inside the kidney [196]. The pulses were separated by 0.5 and 0.75 mm laterally and axially, respectively, and were delivered at a pulse repetition frequency of 6.67 kHz. APM accounts for tissue attenuation and modulates the transducer output so that every pulse has approximately the same pressure regardless of depth. For each animal, a range of pressures from 2.5 and 4.5 MPa was used and a contrast image was captured before and after the vaporization sequence (Figure 5.2b).

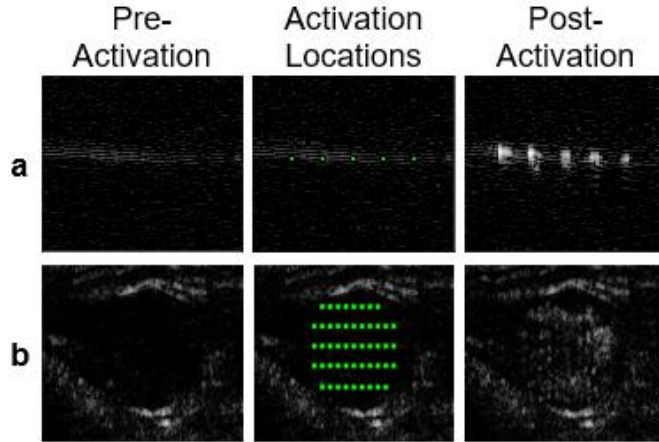


Figure 5.2. Example of activation scheme for US imaging measurement of activation in the 50 μm microtube (row a) and in a rat kidney (row b). The images on the left column show an example PI image of the kidney before vaporization, which was used for CE computations, and the images on the right column shown the contrast produced by the activation pulses represented in the center column by green squares. For the microtubes, 5 pulses were delivered at a depth of 1.3 cm. For activation in the kidney, a varying number of pulses were delivered to produce an area of uniform activation.

5.2.10 Data Analysis

All analysis was performed using custom MATLAB (The MathWorks, Natick, MA, USA) scripts. From the US imaging data, the contrast enhancement (CE) was found; CE was calculated by drawing a region of interest (ROI) around the activation locations and dividing the mean intensity inside the ROI of the post-activation frame by that of the pre-activation frame and turning the result into dB using the equation $\text{dB}=20\log_{10}(x)$.

The microscope data was viewed using ImageJ [174] software and the number of activate droplets was counted manually. The frames captured before vaporization were used to eliminate droplets or bubbles that were already present from the total count.

For the droplet activation detection technique, the frequency content of the received signals was explored rather than the amplitude. A fast Fourier transform was calculated for each receive line, and the result from the baseline measurements was subtracted from that of the droplet transforms. In order to quantify the results, the area under the curve (AUC) was found by integration using trapezoidal approximation (Figure 5.3). Frequency components around the transmit frequency, 5 ± 1.5 MHz, were

assumed to originate from the tubes, or from the excitation of microbubbles created by droplet vaporization, and thus were excluded from the analysis.

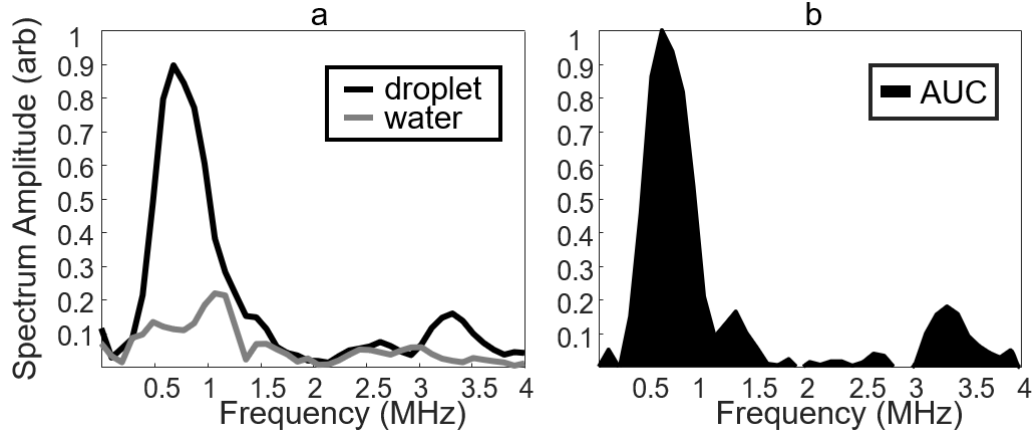


Figure 5.3. Example fast Fourier transform of the received signal from the 1 MHz piston transducer (a). The plot on the right shows the baseline-subtracted frequency spectrum and the AUC (b).

The activation threshold was found using each of the activation metrics (CE, number of bubbles, AUC) for the various microtubes, and was set as the first pressure at which the metric became higher than 10% of its maximum. The thresholds for the 3 different trials were averaged to find one threshold for each tube.

5.2.11 Statistical Analysis

Kruskal-Wallis analysis was performed for the vaporization threshold values of each tube found by each of the activation measurement metrics in order to determine if there was a significant difference between any of the microtubes, and a Tukey range test was used to find significance between each of the tubes. The same procedure was used between the thresholds for the hydrostatic pressures and viscosities for part 2 and 3, respectively.

5.3 Results

5.3.1 Effect of Boundary Constraints on Droplet Activation Threshold

Measurable contrast was obtained from all tubes except for the 12.5 μm tube. Figure 5.4 shows ultrasound images depicting the amount of activation for each tube for the pressure range of 1.5-4 MPa.

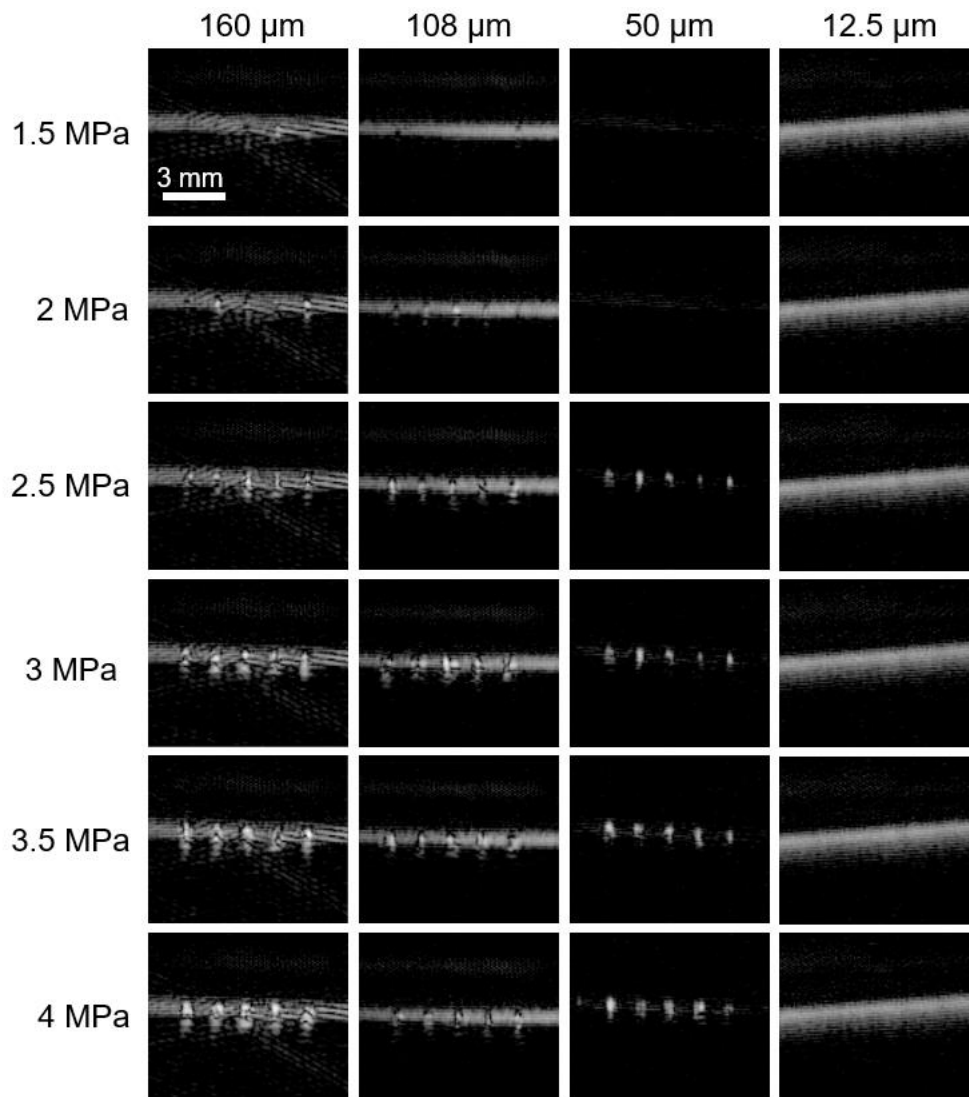


Figure 5.4. Post-activation images of the different tubes (columns) and pressures (rows).

As was expected, the amount of contrast generated by the activation pulses increased with rarefactional pressure. The CE of each of the 3 trials for the different pressure-tube size combinations was calculated and the activation threshold for each microtube was found (Figure 5.5a-b). CE increased with pressure but surprisingly, the maximum CE was the highest for the 50 μm tube. A smaller tube has a smaller volume for a given length, so fewer droplets should be in the tube for that length, given the same concentration. Therefore, less droplets should be activated in smaller diameter tubes which would produce a smaller signal. The vaporization threshold was 2 MPa for all trials in the 160 μm tube, 2, 2, and 1.5 MPa for the 108 μm tube, and 2.5 MPa for all trials in the 50 μm tube. The threshold for

the 50 μm was significantly higher ($p < .05$) from that of both the 108 and 160 μm tubes, and activation was not detected in the 12.5 μm tube, so the results show that the activation threshold increased once the tube diameter decreased below 108 μm for the tube sizes tested.

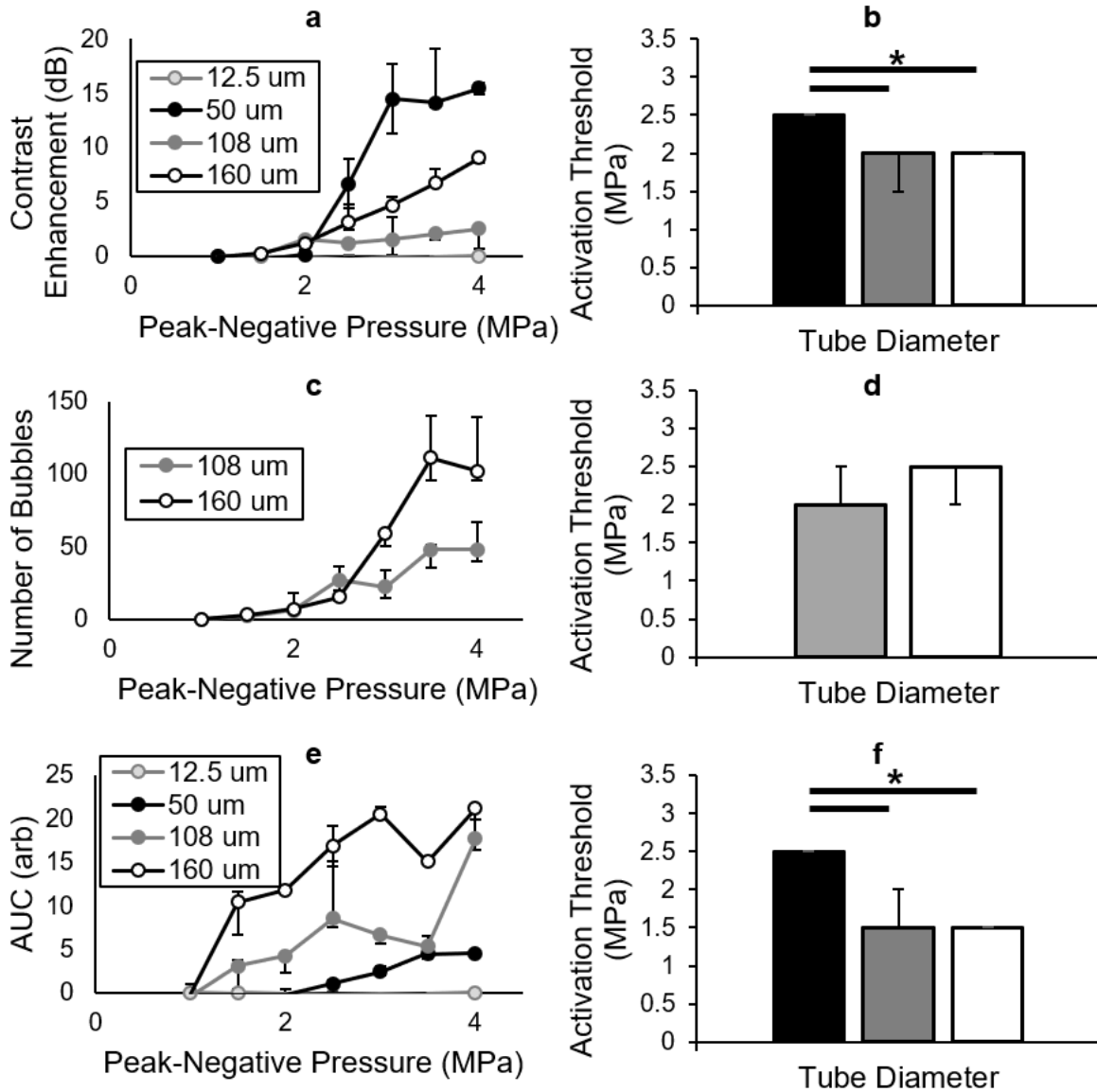


Figure 5.5. Results from the 3 different techniques for measuring droplet vaporization in microtubes of different diameters: US imaging (a, b), optical microscopy (c, d), and droplet activation detection (e, f). The metrics of the 3 measurement techniques- contrast enhancement (a), number of bubbles (c), area under the curve (d)- increased with rarefactional pressure. The plots show the median value from the 3 trials and the error bars correspond to the minimum and maximum values. The vaporization threshold, set as the lowest pressure to produce 10 % of the maximum of each metric, increased with decreasing tube diameter (b, d, f). Activation was not achieved in the 12.5 μm tube so the threshold is not shown. Vaporization was not observed using optical microscopy, even though it was detected using US, in the 50 μm tube.

Microscope images of droplet activation for the different tubes over the range of pressures are shown in Figure 5.6. Bubbles resulting from activation were not visually observed in the 12.5 and 50 μm tubes. US images confirmed that activation was taking place, so the experiment was repeated to ensure the L115 was aligned correctly to the optical focus, but the results remained unchanged. More bubbles were observed in the 160 μm tube than the 108 μm tube due to the larger diameter (Figure 5c-d). The number of activated droplets increased with the delivered pressure, and the vaporization thresholds were 2.5, 2, and 2.5 MPa, and 2, 2.5, and 2 MPa for the 160 and 108 μm tubes, respectively.

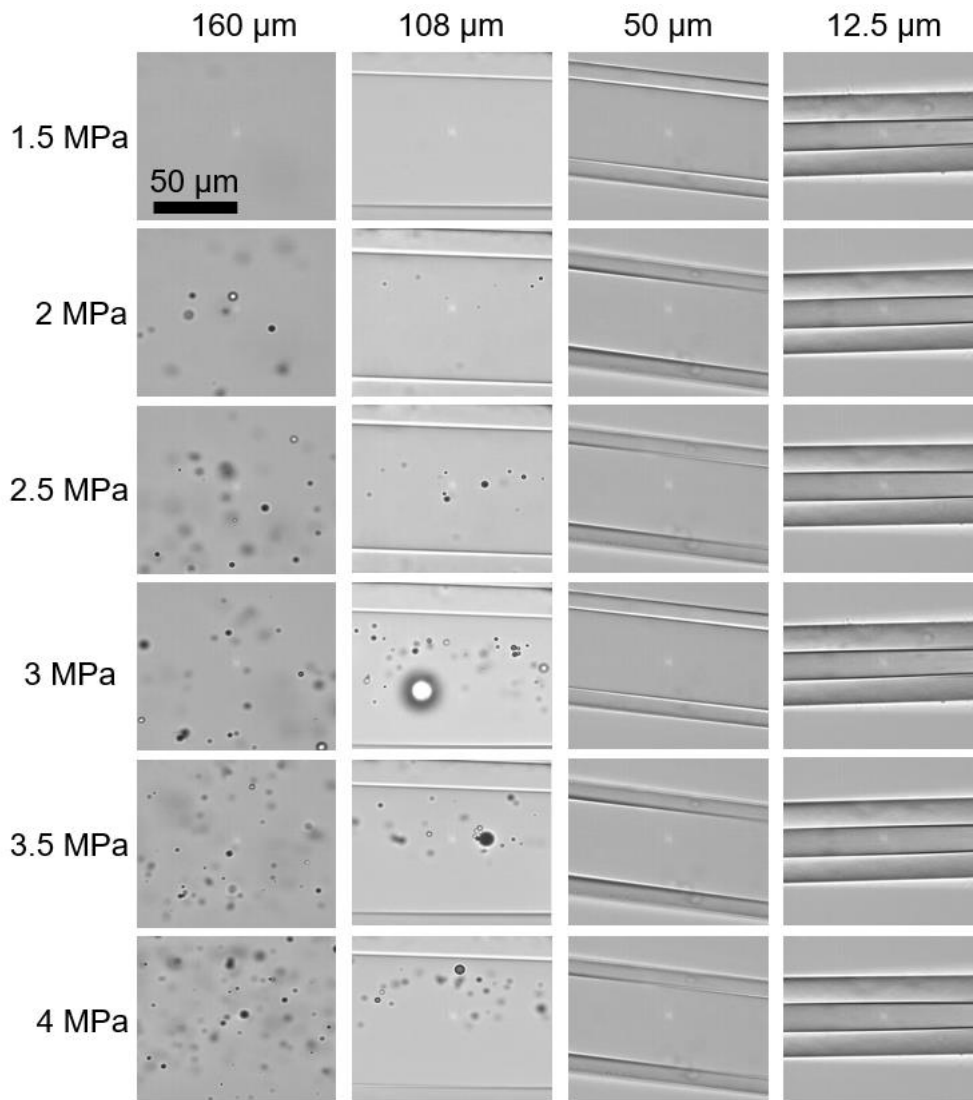


Figure 5.6. Microscope images of droplet activation. Activation was confirmed using US imaging, but no bubbles were observed in the 12.5 and 50 μm tubes after the activation pulses were delivered.

AUC measurements obtained from the vaporization signature from phase-changing droplets show that the activation threshold increases as the tube size decreases (Figure 5.5e-f), and no measurable signal was measured in the 12.5 μm tube. The activation thresholds were 2.5 MPa for all trials in the 50 μm tube and 1.5 MPa for all trials in the 160 μm tube, and 1.5, 1.5, and 2 MPa for the 108 μm tube.

5.3.2 Effect of Hydrostatic Pressure on Droplet Activation Threshold

The results show that the contrast enhancement generated by droplet activation inside of the chamber increases with increasing interrogation pressure, as expected, but the activation threshold does not change under different hydrostatic pressures (Figure 5.7). The activation threshold was 1.5 MPa in all trials for all hydrostatic pressures, except for the 0 and 6.89 kPa pressures which had one trial with a threshold of 2 MPa.

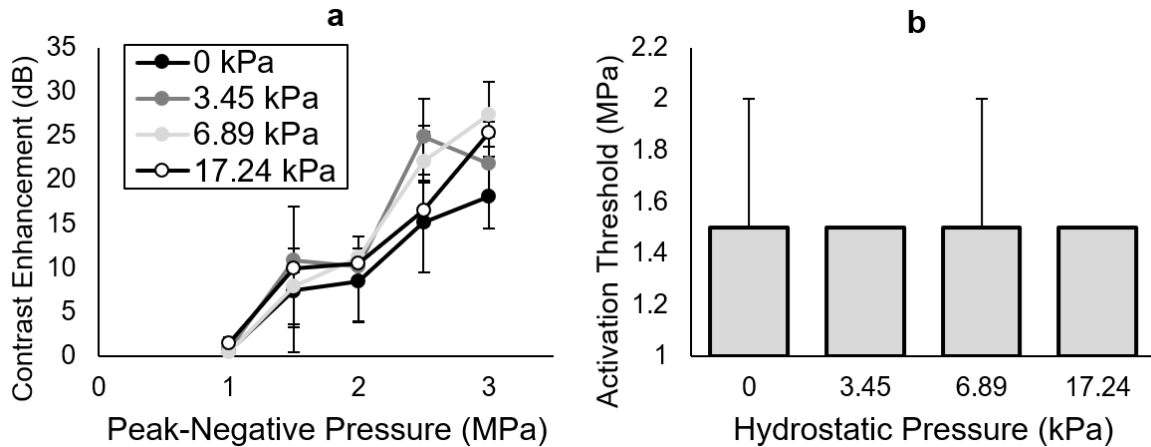


Figure 5.7. Contrast enhancement generated by droplet activation inside the pressure chamber increased with peak-negative pressure under different hydrostatic pressures (a). Droplet activation threshold does not significantly change with different hydrostatic pressures (b). The plots show the median value from the 3 trials and the error bars correspond to the minimum and maximum values.

5.3.3 Effect of Viscosity on Droplet Activation Threshold

When the viscosity of the fluid in which droplets were activated matched that of blood, the activation threshold was significantly higher ($p < 0.05$) than when the droplets were activated in PBS

(Figure 5.8). The threshold was 1.5 MPa for all trials in PBS, and 1.75 MPa for all the trials in the blood-mimicking fluid.

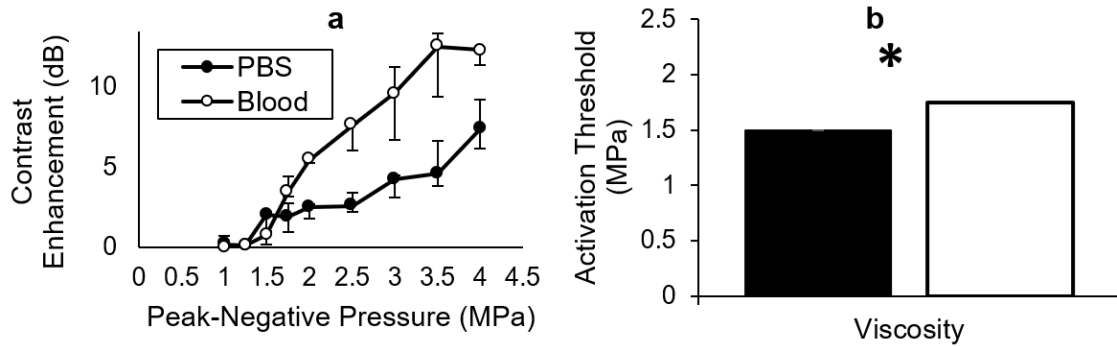


Figure 5.8. Contrast enhancement generated by droplet activation increased with pressure (a). The vaporization threshold is significantly higher for the blood-mimicking fluid (b). The plots show the median value from the 3 trials and the error bars correspond to the minimum and maximum values. Significance ($p < 0.05$) is represented by the asterisk. The label for the blood-mimicking fluid was shortened to “blood” for clarity inside figure.

5.3.4 *In Vivo* Droplet Activation

The CE inside of the kidney was measured for the range of pressures that was used (Figure 5.9). The activation threshold was determined to be the pressure that first exceeded 10% of the maximum CE, and that was found to be 3.5 MPa for all trials on each of the rats.

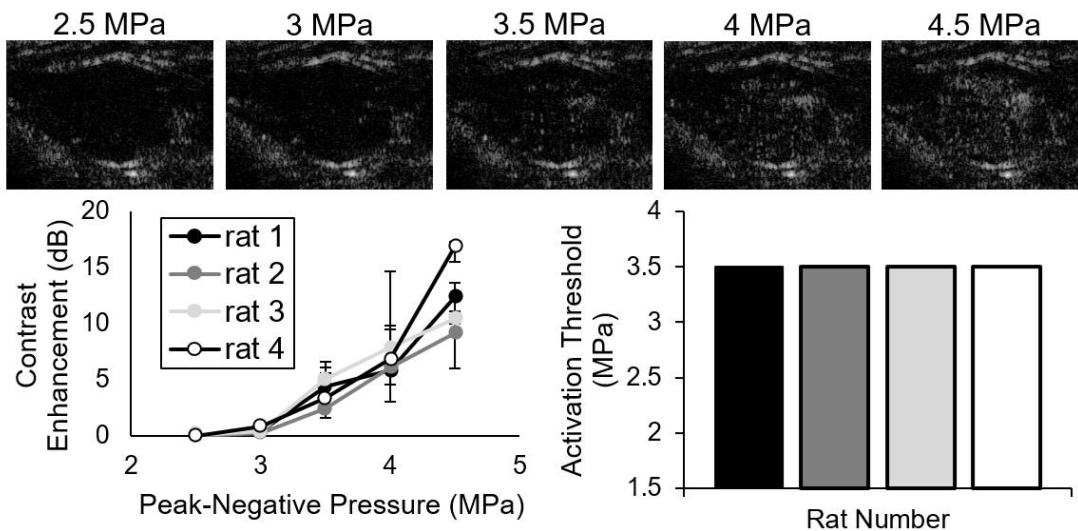


Figure 5.9. Example images of droplet vaporization in a rat kidney resulting from activation pulses of different pressures (top row). CE enhancement inside of the kidney for all the rats is shown on the bottom left, and the vaporization threshold (10% of maximum CE) is shown on the bottom right. The plots show the median value from the 3 trials and the error bars correspond to the minimum and maximum values.

5.4 Discussion

5.4.1 Effect of Boundary Constraints on Droplet Activation Threshold

Intriguingly, activation was not seen in the 50 μm tube with microscopy, even though US imaging confirmed vaporization. The simplest explanation is that the bubbles produced by the vaporization pulse are getting destroyed in the area around the optical field of view so that no bubbles are visible on the microscope, but the bubbles in areas away from the optical focus are not destroyed and can be detected by US imaging. To test this hypothesis, a 32x objective was used to observe vaporization in a larger region, and the resulting images show small groups of bubbles away from the center. This suggests that the peak pressure at the center of the US beam is destructive to the resulting microbubbles, but it decreases laterally until it no longer destroys bubbles (Figure 5.10). This phenomenon only occurred in the 50 μm tube so the size tube must play a role. One possible explanation is that the presence of a boundary induced non-spherical oscillations on the produced microbubbles, which greatly contribute to cavitation and fragmentation [231–234]. Non-spherical oscillations may also occur away from the focus but may not be destructive since bubbles are visible away from the center of the field of view (Figure 5.10). Sheeran et al. showed that the probability of vaporization increases with pulse length, and that longer pulses can lead to bubble fragmentation and coalescence during the later cycles of the pulse [130]. Therefore, it is possible that droplets were activated with the first few cycles of the vaporization pulse, and the resulting bubbles were destroyed by the last few cycles due to non-spherical oscillations caused by the presence of a boundary. Droplets were activated in the 50 μm tube using pulses with 1 and 2 cycles instead of 5 in a follow-up experiment, and vaporization can be seen throughout the field of view (Figure 5.10), suggesting that activation is occurring within the first couple of cycles. It is worth noting that using 1 or 2 cycles is less efficient at vaporizing droplets so the optimal pulse length for activation, without destruction of the produced bubbles, might be 3 or 4 cycles. Also, the 1 cycle pulse refers to the signal used to excite the transducer, but the actual pressure wave has 1.5 cycles due to transducer ring-down.

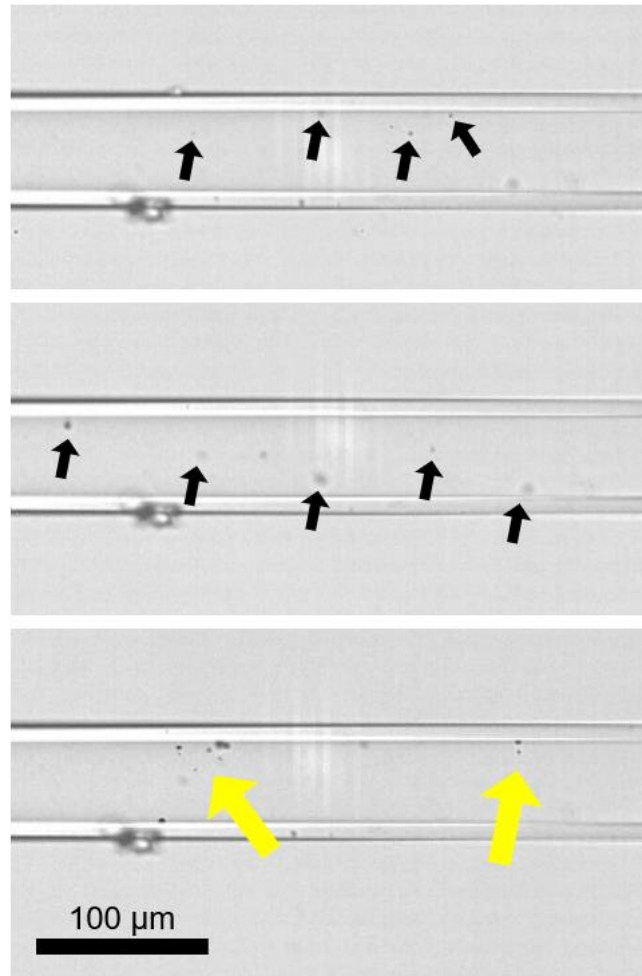


Figure 5.10. Example microscope image of droplet activation in 50 μm tube at 32X magnification. Bubbles are present on either side of the center of the tube (yellow arrows) when 5 cycles are used for vaporization (bottom). Activation is present throughout the field of view when 1 cycle (top) and 2 cycles (middle) are used for vaporization, as marked by the black arrows.

The biggest question brought up by the results is whether the measuring techniques employed were not sensitive enough to detect vaporization in the 12.5 μm tube, or if it was not possible to activate droplets in a tube that small. To answer this, the number of droplets in the 12.5 μm tube was calculated, and that number of droplets was used for vaporization in an acrylic 105/140 μm (inner/outer diameter) and an FEP (320/360) μm microtubes. The acrylic tube was chosen to match the material and thickness of the 12.5 μm , and the FEP tube was chosen to match the thickness and to explore the role of material on droplet activation since acrylic, 6.4 dB/cm @ 5 MHz [235], is more attenuating than FEP, 3.9 dB/cm @ 5MHz [236]. The difference in the number of droplets between different tubes for any given length,

assuming equal concentration, is a factor of the tube radius squared. Therefore, to match the number of droplets at a 1:10 concentration in the 12.5 μm tube for a given length, droplet solutions with concentrations of 1:770 and 1:6500 for the 105 and 320 μm tubes, respectively, were used for vaporization. The droplet activation detection method was used, and the results show that vaporization can be detected over a range of exposure pressures (Figure 5.11), suggesting that the activation detection method is sensitive enough to detect vaporization of small numbers of droplets, as is the case in the 12.5 μm tube. Therefore, these results suggest that the pressures used for activation in this study are not capable of activating droplets in a 12.5 μm tube, which supports the hypothesis that vaporization is harder to achieve in smaller tubes due to boundary constraints.

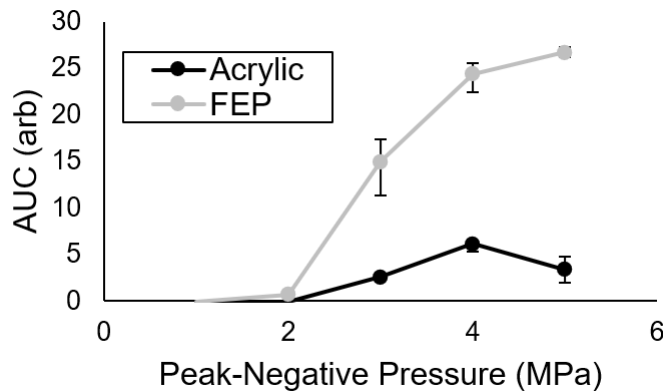


Figure 5.11. AUC measurements from the 105 μm acrylic and 320 μm FEP tubes with a concentration of droplets matching the number of droplets in the 12.5 μm tube.

Having established that activation from a number of droplets equivalent to the that contained within a 12.5 μm tube can be detected in a much larger tube (tube diameter at least 105 μm), the results suggests that the activation threshold increases as the tube size decreases. From both US imaging and activation detection, the threshold for the 50 μm tube was significantly higher than that of the 108 μm and 160 μm tubes, and activation could not be achieved in the 12.5 μm tube. As the droplet is vaporized it over expands and displaces the fluid around it. When activation occurs in an unconstrained environment, or when the boundaries are far enough away, the created bubble is able to displace the fluid around, but the overexpansion may be dampened when the boundaries are further constrained.

This behavior was seen by Zheng et. al in oscillating microbubbles, where the amplitude of bubble oscillations was nearly twice as large in a 200 μm tube than in a 12 μm tube, and bubbles translated more than 5 times farther in the larger tube [237]. Therefore, even though the 50 μm tube is an order of magnitude larger than the diameter of the resulting microbubbles, the boundary constraints had a significant effect on the vaporization threshold.

It is interesting to point out that the measurements for the dilute concentrations (1:770 and 1:6500) produced much larger maximum AUC values than the other activation detection experiments. It has been reported that bubble oscillations are significantly reduced when in close proximity to other bubbles [218], so the 1:10 concentration of droplets used for the experiments might have been too high, and the resulting droplets attenuated each other's activation signal. This has important implications for droplet-specific imaging techniques that have been proposed [138,139]. Furthermore, the frequency content of the activation signal has been reported to range between a few hundred kHz and around 2.5 MHz, but it was measured to extend past 3 MHz in this study.

The AUC for the FEP tube was much higher than that of the acrylic tube even though the same number of droplets were activated and the tube thickness was about the same, which is reasonable since acrylic is a harder material.

5.4.2 Effect of Hydrostatic Pressure on Droplet Activation Threshold

The activation threshold of droplets did not change by varying the hydrostatic pressure between 0 and 17.24 kPa (Figure 5.7). The body of work discussed in the introduction suggests that hydrostatic pressure influences the behavior of microbubbles, but the results here show that this is not the case with liquid droplets. Previous work has shown that vaporization of DFB droplets occurs at a reduced temperature ($\frac{T}{T_c}$) of around 88% [132], where T is the temperature of the system and T_c is the critical temperature, which is the maximum temperature at which a gas be condensed by applying pressure.

The embryo formation flux, which is the rate at which the gas nuclei are formed, is estimated to be [238]:

$$J = \rho_L \left(\frac{2\sigma}{\pi m} \right)^{1/2} \exp \left[\frac{-16\pi\sigma^3}{3kT \left[\exp\left(\frac{P-P_{sat}}{\rho_L RT}\right) P_{sat} - P \right]^2} \right] \quad (5.1)$$

where ρ_L is the density of DFB in the liquid phase ($1.45 \times 10^3 \text{ kg/m}^3$ at 37°C), σ is the surface tension of a DFB vapor embryo ($6.06 \times 10^{-3} \text{ N/m}$ at 37°C), m is the molecular mass ($3.12 \times 10^{-25} \text{ kg}$), k is Boltzmann's constant, T is absolute temperature, P_{sat} is the saturation pressure ($3.83 \times 10^5 \text{ Pa}$ at 37°C), R is the mass-weighted gas constant (44.2 J/kg) and P is the pressure inside the droplet. Using equation (1) and the results from Mountford [132], the critical flux for vaporization is estimated to be $\log_{10} J = -92.6$. The corresponding acoustic PNP to achieve this flux increases from 1.64 MPa to 1.66 MPa as the hydrostatic pressure increases from 0 to 17.24 kPa . Note that these values are within the range of values observed experimentally, but the effect of hydrostatic pressure is negligible compared to the experimental error.

Kripfgans et. al first showed that bubbles created by droplet vaporization increase inside due to dissolved gasses in the surrounding liquid diffusing into the agent [101]. Pressurizing the chamber with air may have increased the amount of dissolved air into the solution, which could have led to bigger bubbles and higher CE values. However, a greater concentration of air in the solution would not affect the vaporization threshold of the droplets.

5.4.3 Effect of Viscosity on Droplet Activation Threshold

The results showed that viscosity increases the vaporization threshold of low-boiling point PCCAs (Figure 5.8). It has been shown that increased viscosity reduces fragmentation and limits cavitation [224,225], so it is possible that a similar mechanism can enhance the droplet's metastability to homogeneous nucleation or slow the embryo formation flux required for complete vaporization of the core.

5.4.4 *In Vivo* Droplet Activation

As shown in previous work, the vaporization threshold for *in vivo* activation of droplets was higher, even when attenuation was accounted for, than *in vitro* (Figure 5.9). Interestingly, the activation threshold was much more consistent in the *in vivo* results rather than the more controlled *in vitro* setup. The threshold for *in vitro* experiments inside of the chamber without any added hydrostatic pressure or boundary constraints, or free conditions, and was as low as 1.5 MPa, and as high as 2.5 MPa in the smallest tube where vaporization was still detected. The vaporization threshold *in vivo* was 3.5 MPa, so even though boundary constraints account for some of the difference between the threshold of the free conditions state and *in vivo*, other factors not explored here must be playing a role in increasing the activation threshold.

5.4.5 Limitations

The main limitation of this work is that the increment (500 kPa) of the pressure delivered to activate droplets in the *in vitro* experiments was too large, which could confound some of the conclusions of this work. For example, a finer increment in pressure could have produced activation in the 50 μm that was detectable using optical microscopy before bubble destruction was induced by the pulse. The reason that such a coarse increment was chosen was that the range of pressures required to vaporize droplets *in vivo* and *in vitro* span between 1.5 and 4 MPa, so we expected hydrostatic pressure and boundary constraints to have a larger effect on the activation threshold than what was found in this work. A finer pressure increment may have yielded smaller differences in vaporization threshold between the microtubes, but the conclusion that tube size affects the threshold would not change.

Another factor that must be discussed is the vaso-activity of the isoflurane used to anesthetize the animals. It has been shown that isoflurane use increases heart rate and decreases blood pressure [239–241], which would not affect the results in this work since it has been demonstrated that hydrostatic pressure does not influence PCCA vaporization threshold, but there is evidence that isoflurane causes vasoconstriction and vasodilation depending on the size of the vessel [242], or part

of the body [243,244]. Therefore, isoflurane may play a role on the *in vivo* vaporization threshold since the vessel size (tube size in this work) has been shown to affect it, and it likely depends on the dose of isoflurane used and the imaging target.

5.4.6 Implications for *In Vivo* Imaging

The largest advantage of PCCAs over conventional microbubble contrast agents is that they can be manufactured to be small enough to extravasate (100-400 μm). In cancer, blood vessels grow very quickly to keep up with the demand for nutrients from the growing tumor and are often disorganized, immature, and “leaky”. As a result, large particles that would not be able to escape the vascular space in healthy tissue extravasate and accumulate in the interstitial space in what is referred to as the enhanced permeability and retention effect (EPR) [120,121]. Therefore, PCCAs that extravasate can have the potential to be used for drug delivery or extravascular diagnostic imaging.

The extravascular environment consists of the extracellular matrix (ECM), which is mainly composed of connective proteins such as collagen that provide structure and support to cells [245–247], and the interstitial fluid, which consists of mainly proteins [248]. In cancer, the ECM is characterized by excess deposition of connective proteins, which make tumors stiffer than healthy tissue [245–247]. Increased amounts of connective tissue and cancer cells themselves might impose additional boundary constraints on vaporizing droplets, likely increasing the vaporization threshold as was demonstrated here. Although, stiffness of boundary constraints was not explored in this work, the added stiffness of cancerous tissues might also affect the activation threshold of droplets. As discussed above, leaky vasculature in cancer leads to fluid and particles leaking out of circulation, which can increase the interstitial fluid pressure in the tumors [177,249]. The results from this work indicate, however, that increased fluid pressure does not affect droplet vaporization thresholds. Lastly, the viscosity of the interstitial fluid may have an effect of activation threshold. It is difficult to extract interstitial fluid to measure its characteristics [248] so there is few studies exploring its viscosity [250]. However, it has been shown that the viscosity of the interstitial fluid is similar to that of lymph [251], so an estimation

can be obtained. Experiments have measured the viscosity of lymph to be higher than that of plasma and water [250,252], so the vaporization threshold of droplets activating in the extravascular space may be increased, according to the results from this work.

The data from this study suggests that boundary constraints and increased viscosity may influence the vaporization of droplets when used to extravascular drug delivery or diagnosis and should be taken into consideration when designing vaporization protocols.

5.5 Conclusions

This work explored the effect of boundary constraints, increased hydrostatic pressure, and viscosity on the vaporization threshold of sub-micron PCCAs. Using different methods to detect activation, it was demonstrated that the vaporization threshold increases as tube diameter decreases until it was no longer possible to detect vaporization, and that viscosity of the surrounding media also increases the activation threshold. Surprisingly, we found that increased hydrostatic pressure did not have any effect on the activation threshold. Finally, we showed that higher pressures are required to activate droplets *in vivo*, and that boundary constraints and viscosity account for part of this difference but more work is required to find all the factors that affect the vaporization threshold of droplets in the vasculature.

CHAPTER 6

**MOLECULAR IMAGING USING LOW BOILING-POINT PHASE-CHANGE
CONTRAST AGENTS⁷**

6.1 Introduction

Molecular imaging generally refers to the evaluation and quantification of cellular and molecular processes. For example, positron emission tomography (PET), the most commonly used imaging technique in oncology, can use ¹⁸F-fluorodeoxyglucose to image metabolic activity of tumors and assess malignancy, response to therapy, and recurrence [253–255]. Furthermore, PET can also be used to image angiogenesis using agents targeted to the $\alpha_v\beta_3$ integrin [256,257], which plays a key role in tumor development [258,259]. However, as previously discussed, PET is expensive, cannot provide anatomical information, requires cyclotron-produced radioisotopes, and involves radiation exposure to the patient and hospital staff, which limits its application.

In comparison, contrast-enhanced ultrasound (CEUS) imaging is inexpensive, portable for bedside diagnostics, widely available, and does not involve any ionizing radiation. Since low boiling-point PCCAs are manufactured from MCAs, creation of targeted PCCAs can be achieved using the same methods already employed for conjugating targeting ligands to MCAs for USMI.

The enhanced circulation time of PCCAs may provide more opportunities for endothelial binding, allowing the use of smaller contrast doses and a reduction in imaging time. Furthermore, PCCAs are only detectable with US after they have been converted to microbubbles, so there is no need

⁷ Copyright © 2018 by Elsevier. Parts used from JD Rojas, PA Dayton, “In-Vivo Molecular Imaging Using Low-Boiling-Point Phase-Change Contrast Agents: A Proof of Concept Study”, *Ultrasound in Med. & Biol.*, 2018. In Review.

to wait until most of the free-flowing agents are cleared from circulation; vaporization pulses can theoretically be delivered at any point after injection, and after the free-flowing agents wash out of the plane of imaging following activation, the only remaining signal should be that of bound agents.

USMI using PCCAs has been demonstrated *in vitro* by targeting $\alpha_v\beta_3$ expressed by human umbilical vein endothelial cells, but to our knowledge, no other work has demonstrated USMI with droplets *in vivo*. In this work, the feasibility of using PCCAs as intravascular USMI agents is demonstrated. As a first step towards extravascular USMI, we provide proof of principle for targeting $\alpha_v\beta_3$ *in vivo* using PCCAs.

6.2 Methods

6.2.1 Agent Formulation

Both MCAs and PCCAs were used in this work. Droplets were formed from prepared MCAs, so both agents were composed of the same lipid formulation. The lipid solution used for control (untargeted) agents consisted of 1,2-distearoyl-sn-glycero-3-phosphocholine (DSPC) and 1,2-distearoyl-sn-glycerol-3-phosphoethanolamine-N-methoxy(polyethylene-glycol)-2000 (DSPE-PEG2000) in a 9:1 molar ratio with a total lipid concentration of 1.0 mM and was dissolved in a solution of propylene glycol (15% v/v), and glycerol (5% v/v) in phosphate-buffered saline (PBS). The lipid solution for agents targeting $\alpha_v\beta_3$ integrin consisted of the same formulation as the control solution with a cyclic RGD peptide (Cyclo-Arg-Gly-Asp-D-Tyr-Cys) cross-linked to DSPE-MAL-PEG2000 (0.4 mol%) replacing an equivalent portion of DSPE-PEG2000 [260]. The headspace of a 3 mL vial containing 1.5 mL of the lipid solution was filled with OFP and, the vial was mechanically agitated to form microbubbles.

6.2.2 Size Selection

It has been shown that selecting for large bubbles greater than 1 μm significantly improves USMI sensitivity *in vivo* [260], so a size selection protocol was employed in this work. Additionally,

selecting larger bubbles allows the formation of droplets greater than 400 nm in diameter, which will prevent extravasation. Since the focus of this work is intravascular USMI, unintentional extravasation would confound the results.

After agitation, the microbubbles were centrifuged inside the vial for 1 minute at 230 g, and the infranatant containing the smaller bubbles was replaced with 1 mL of the PBS, propylene glycol, and glycerol solution described in the previous section. This process was performed a total of three times for all agents.

6.2.3 Condensation

Size-selected microbubbles were condensed into droplets using methods previously described by Sheeran and colleagues [129]. The microbubble suspension was cooled to -10°C and pressurized with air until the bubbles condensed.

6.2.4 Agent Sizing

After the size selection process, the size distribution and concentration of the bubbles were measured using an Accusizer 780 (Particle Sizing Systems, Santa Barbara, CA, USA) that is capable of measuring particles down to 0.5 μm . Samples from five targeted and five control vials were averaged. After the microbubbles were condensed, the resulting droplets were sized using the Accusizer (three vials per group) and a NanoSight NS500 (Malvern Instruments, Westborough, MA, USA), which can measure particles between 20 and 2000 nm. For the NanoSight measurements, the droplets were diluted 300-fold in HPLC-grade, 20 nm filtered water, and five 30 s videos were captured to calculate the average distribution and concentration for each sample. Three control and three targeted samples from different vials were used to find average values for each group.

6.2.5 Tumor Model and Animal Protocols

Fischer 344 rats (Charles River Laboratories, Morrisville, NC, USA) were implanted with fibrosarcoma (FSA) tissue provided by the Dewhirst lab at Duke University in the right flank using

protocols approved by the University of North Carolina Institutional Animal Care and Use Committee (IACUC). FSA was chosen because USMI has successfully been demonstrated in this model using the targeting strategy used in this work [260].

During imaging experiments, animals were anesthetized using 2.5% isoflurane and placed on a heated platform to conserve body temperature. The flank area was cleared of hair, and a 24G catheter was inserted into the tail vein for contrast agent administration. The animals were euthanized at the end of each imaging session using protocols approved by the UNC IACUC.

6.2.6 Pulse Sequences

All imaging and activation was performed using an ATL L11-5 linear array transducer controlled by a Verasonics Vantage ultrasound research system (Verasonics, Kirkland, WA, USA) using custom pulse sequences.

The vaporization pulse sequence consisted of delivering a series of 1 cycle, 5 MHz pulses to a predetermined region of interest (ROI). The pulses were separated by 1.2 mm laterally and 0.72 mm axially and were delivered serially at a pulse repetition frequency of 6.67 kHz. Activation Pressure Matching (APM) was used to account for tissue attenuation and deliver activation pulses with a peak-negative pressure of 2.5 MPa to each vaporization location regardless of depth [196]. An attenuation model consisting of a 1 mm layer of fat (attenuation coefficient $\alpha = 0.6$ dB/MHz/cm) followed by the tumor tissue ($\alpha = 1$ dB/MHz/cm [194]) was used for the APM calculation.

Three different types of imaging pulse sequences were implemented: B-mode, contrast-specific imaging, and vaporization detection imaging (VDI). The B-mode sequence consisted of conventional focused imaging, where a series of focused pulses (focused at 1.3 cm) were delivered across the field of view (FOV), the received echoes from each pulse were used to reconstruct an A-line, and an image was formed by compiling all A-lines. 128 pulses were delivered by sweeping a sub-aperture (25% of

entire aperture) in steps equal to the element spacing and receiving echoes with the full aperture at each lateral location. The transmit frequency was 9 MHz, and the maximum pressure was 673.5 kPa.

The contrast-specific pulse sequence (CSS) used here was similar to CPS (Cadence™ contrast pulse sequencing, Siemens Medical Solutions, Inc., Issaquah, WA, USA), an approach where a full-amplitude pulse was followed by two half-amplitude and inverted pulses. The received echoes from the transmissions were summed, and the process was repeated for each A-line to form a focused CSS image. This approach has been found to be more sensitive to MCAs than other contrast-specific approaches, such as pulse inversion and amplitude modulation [41–43]. Transmit pulses consisted of 4 MHz, 1 cycle sinusoids at a mechanical index (MI) of 0.18, where MI is defined as the peak-negative pressure (derated using an attenuation coefficient of 0.3 dB/MHz/cm) divided by the square root of the frequency. This MI was chosen because it has been shown to be non-destructive to MCAs [260].

VDI is a PCCA-specific imaging technique that uses the vaporization signals produced by droplets to make images that are highly sensitive to PCCAs and have higher CTR values than conventional contrast imaging [261]. The received signals from droplet activation were captured and filtered using a low-pass filter with a corner frequency of 1.25 MHz to reduce signal from tissue. The signals from individual vaporization pulses were used to reconstruct regions around the location of each pulse, and the different reconstruction regions were combined to form an image.

6.2.7 Imaging Protocol

The imaging protocol consisted of several steps, as illustrated in Figure 6.1. The B-mode sequence was used to locate the largest cross-section of the tumor, and an ROI was drawn to select the vaporization locations. Next, droplets were injected, and five baseline frames were captured at a rate of 5 Hz using the CSS sequence. Vaporization pulses were then delivered to the activation locations, and a VDI image was formed from the received echoes. Lastly, post-activation frames were collected at 5 Hz for 8 s to capture the contrast generated by droplet activation and monitor the wash-out of the bubbles from the FOV. Steps 2 through 4 were repeated throughout the experiment and will be referred

to as the droplet imaging sequence. For imaging microbubbles, the sequence will be referred to as the bubble imaging sequence, which consisted of capturing 5 CSS frames at a rate of 5 Hz and clearing the FOV from both bound and freely-flowing bubbles by increasing the imaging pressure to maximum MI of 1.25.

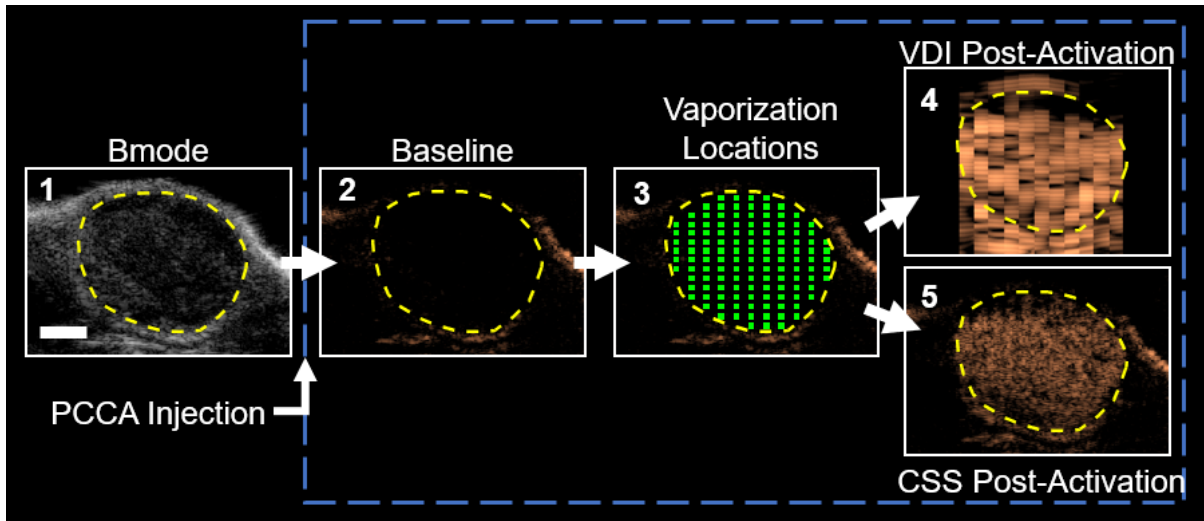


Figure 6.1. Summary of imaging protocol. B-mode was used to find tumor and draw ROI, yellow dotted line (1). Baseline CSS Images were captured after droplet injection (2). Vaporization pulses (green squares) were delivered inside of the ROI (3). Post-activation VDI images (4) and CSS images of the produced contrast (5) were captured. The blue dotted box includes the steps that are repeated in the droplet imaging sequence. The scale bar represents 3 mm.

In USMI experiments, the bubbles are typically injected and allowed to circulate for several minutes and bind to their targets before any imaging is performed. In this work, the agents were allowed to circulate for three different time periods to explore the optimal wait time for PCCAs: 3 min (short), 6 min (moderate), 9 min (long).

Dosing is an important parameter in USMI. A high dose enhances binding but requires long wait times to allow the free-flowing bubbles to be cleared from circulation, while a low dose requires shorter wait times but produces worse targeting. Since droplets cannot be detected with US, it is expected that once the droplets are activated into bubbles, the unbound bubbles will wash out of the FOV, and the remaining signal will contain only bound agents. Therefore, long wait times should not be required regardless of the dose. To test this hypothesis, two different doses of droplets were explored:

a low dose of 2×10^7 droplets and a high dose of 2×10^8 droplets. The dose was calculated using the concentration measurements of the bubbles before condensation.

To test whether the droplets are targeting $\alpha_v\beta_3$ or passively accumulating in the tumor, both targeted and control droplets were injected at the high dose. Additionally, both targeted bubbles and targeted droplets were injected at the low dose in order to compare USMI with the different agents. Lastly, the wash-in of the low dose of bubbles was captured using CSS at 2 Hz for 1 minute after injection.

Figure 6.2 summarizes the experimental parameters tested. A total of 13 contrast doses were administered to each animal. Streeter and Dayton showed that microbubbles can be administered repeatedly without affecting the amount of targeting with each subsequent injection [262], so we did not expect any bias in the results from repeated administrations of the agents. Additionally, a recent study demonstrated that exposure to contrast agents containing polyethylene glycol (PEG) produces an immune response that accelerates the clearance from circulation [263]. However, an effect was not seen until 2 days after the initial exposure, so we do not expect any changes in circulation between the different doses since all the imaging for each animal took place during the same session.

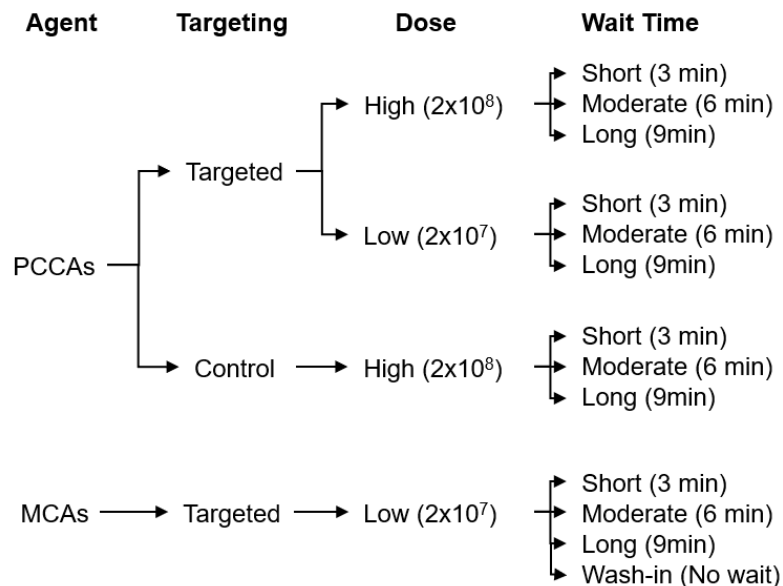


Figure 6.2. Summary of all experimental trials performed in each animal. 13 injections were administered to each rat.

The droplet imaging or bubble imaging sequences were performed for each trial at the designated wait time, 30 s after wait time, and every 1 min until 12 min after the injection. For example, for a wait time of 9 min, the droplet or bubble imaging sequence would be repeated at 9, 9.5, 10, 11, and 12 min after injection. It was found in preliminary studies that 12 min is enough time for the agents to be cleared from circulation.

6.2.8 Data Analysis

To quantify the amount of biomarker targeting inside the sample volume, a previously described protocol for USMI was used [49]; droplets or bubbles were allowed to reperfuse the tissue after the first activation or imaging/destruction, respectively, so that the level of free-flowing agents could be captured by the 30 s acquisition. The mean intensity inside of the ROI of the post-activation frames (CSS and VDI, for droplet imaging sequence) and the CSS frames (bubble imaging sequence) was calculated for each time-point. Next, the targeting intensity (TI) was then calculated by dividing the maximum mean intensity of the first time-point (3, 6, or 9 min) by that of the 30 s time-point, which is the level of freely-flowing contrast. Furthermore, in the case of droplet imaging, the mean intensity of the baseline CSS frames was used to monitor any bubbles that remained bound from the activation in the previous time-point.

Perfusion in tumors is highly heterogeneous, so different regions will become fully perfused at different times. As such, 30 s or 1 min might not be sufficient for some regions to properly perfuse, so using the entire area inside the ROI might bias the results when calculating TI. Therefore, two masks including all the regions that became perfused in 30 s or 60 s were applied to the data of the second time-point or the third and later time-points, respectively, when calculating TI. The wash-in CSS frames were blurred, as described previously [187], and the pixels above a predetermined threshold 30 and 60 s after the appearance of contrast in the FOV were added to the 30 and 60 s masks, respectively (Figure 6.3).

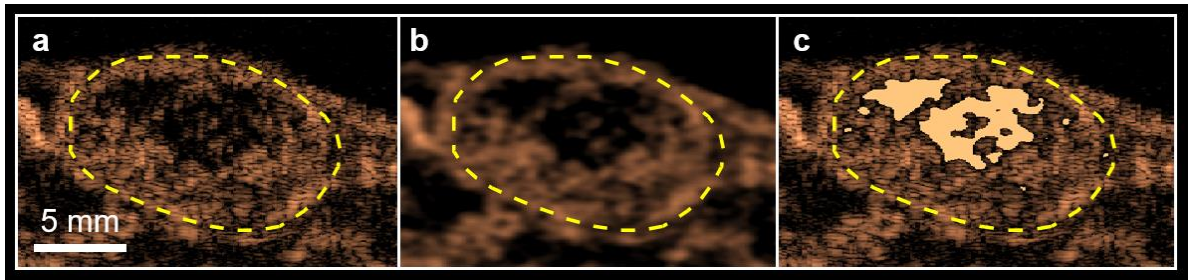


Figure 6.3. Illustration of the mask making process. The frames at either 30 or 60 s (a) are blurred using a Gaussian filter (b), and the areas that are not perfused (filled in regions) were excluded from analysis (c).

Each acquisition destroyed the bound bubbles either with the destructive pulses for the bubble imaging sequence or the vaporization pulses for the droplet imaging sequence, so the different time-points were used to make a circulation curve. For each agent/targeting/dose combination, the data for the three wait times, excluding the first time-point in each, was combined to find a circulation clearance curve by fitting the data to a mono-exponential (Eq. 6.1) where b is the clearance rate and t is time (Figure 6.4a).

$$y = Ae^{-bt} \quad (6.1)$$

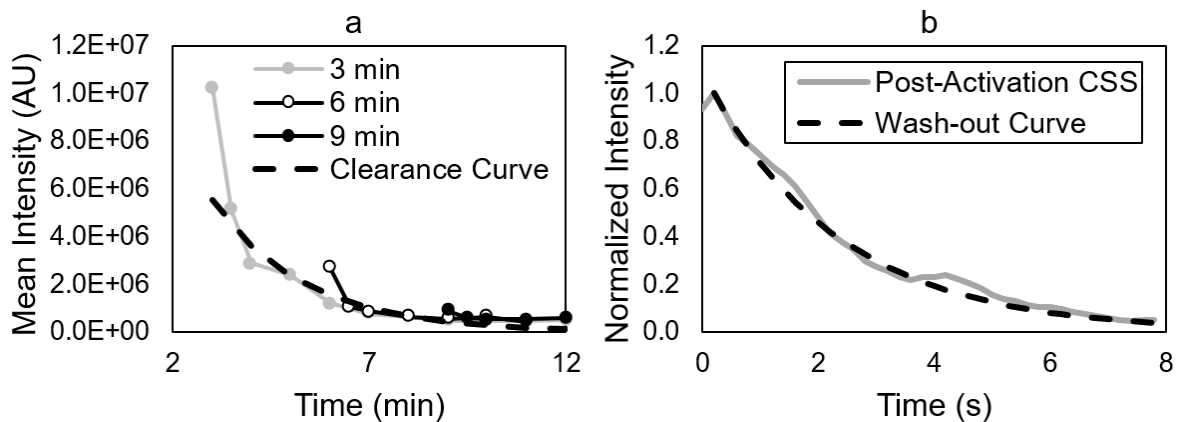


Figure 6.4. Example of data acquired by imaging protocol at the three different timepoints with example clearance curve (a) and example wash-out curve with mean intensity data captured with CSS imaging after droplet vaporization (b). Note: the clearance curve in (a) was calculated without using the first time-points of each wait time, and both curves in (a) and (b) were found using Equation 1.

When droplets are activated, the unbound bubbles that are generated should wash out and leave only the targeted agents. Therefore, the wash-out bubbles generated by the activation of targeted

droplets should be different from that of bubbles generated by the activation of control droplets, so the wash-out was also explored. Equation 1 was used to fit the mean intensity of the post-activation CSS frames (first time-point in the 3, 6, and 9 min wait times), starting with the frame that had the maximum mean intensity, to find a wash-out curve and calculate the wash-out rate, b_{wo} (Figure 6.4b).

6.2.9 Statistical Analysis

Kruskal-Wallis analysis was performed to determine significance in any groups being tested (agents, wait times, detection methods), and a Tukey range test was used to find significance between each of the parameters. Significance was set as $p < 0.05$.

6.3 Results

Size distributions of MCAs and PCCAs can be seen in Figure 6.5. MCAs had a mean size of $2.7 \pm 0.2 \mu\text{m}$ and $2.6 \pm 0.4 \mu\text{m}$ and a concentration of $1.6 \times 10^9 \pm 0.4 \times 10^9 \text{ \#/mL}$ and $2.1 \times 10^9 \pm 0.4 \times 10^9 \text{ \#/mL}$ for the control and targeted agents, respectively. After condensation, the Accusizer measured sizes of $675 \pm 5 \text{ nm}$ for controls and $675 \pm 15 \text{ nm}$ for targeted droplets. NanoSight results contained PCCA sizes of $198 \pm 18 \text{ nm}$ and $169.6 \pm 28 \text{ nm}$ for control and targeted droplets, respectively.

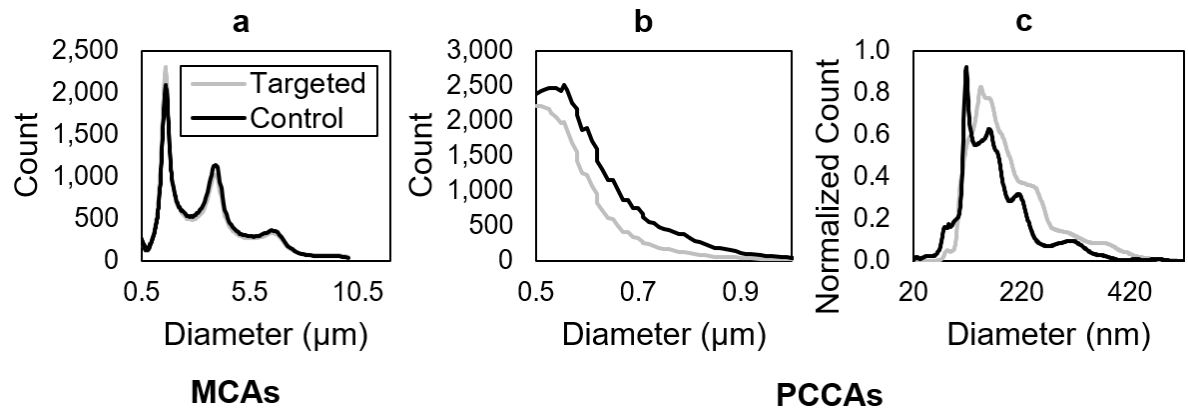


Figure 6.5. Size distributions of MCAs (a) and PCCAs using the Accusizer (b) and NanoSight (c).

Figure 6.6 shows example images of post-activation CSS, VDI, and CSS of MCAs, respectively, at the different wait times and at the 30 s acquisition.

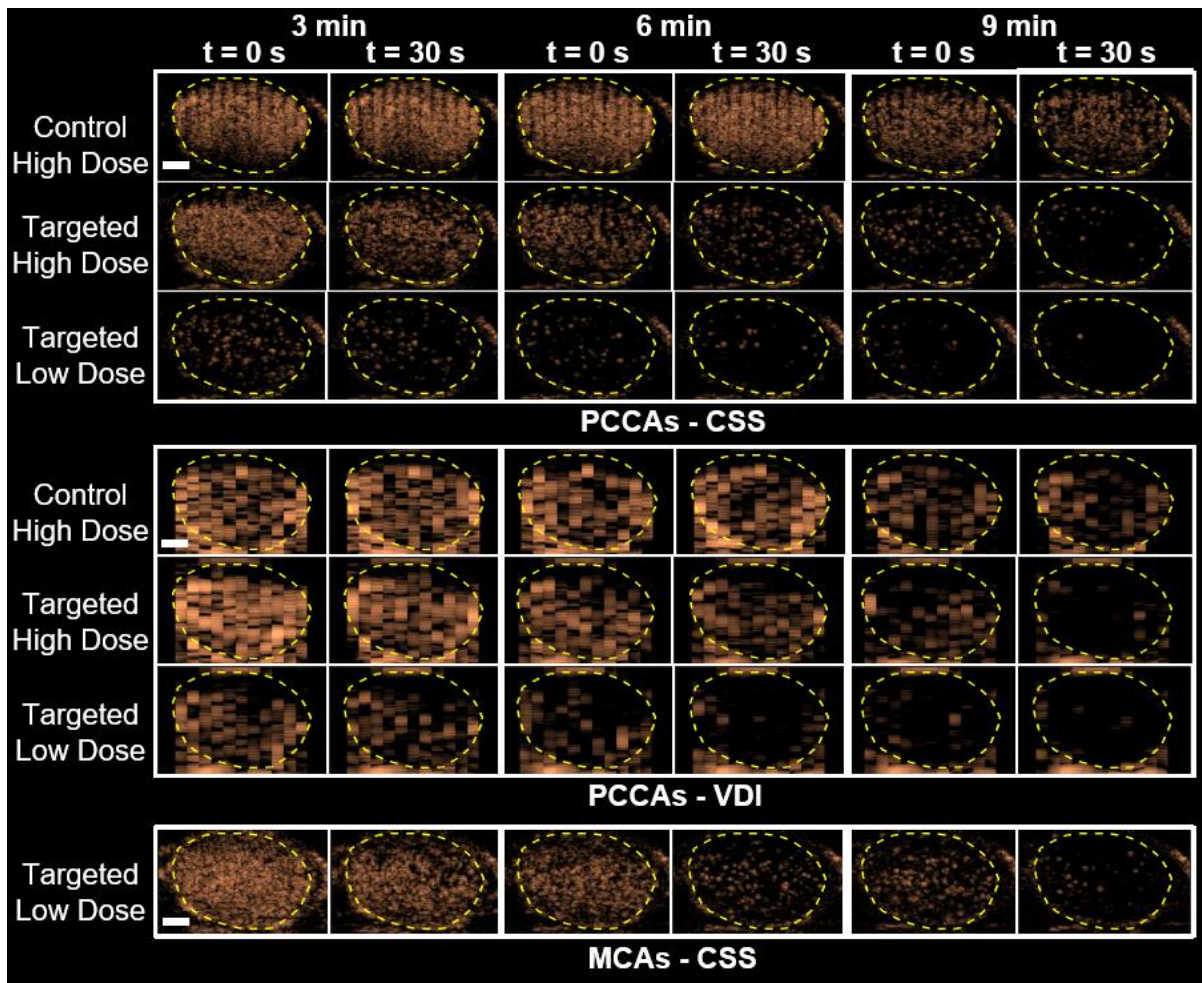


Figure 6.6. Example post-activation CSS (top), VDI (middle), and MCA CSS (bottom) images. The odd and even columns show the activation at the different wait times and the acquisition at the 30 s time-point, respectively. Images from control and targeted PCCAs at the doses tested are shown in the different rows of the top and middle panels, while the bottom panel shows images of MCAs at the low dose. The scale bar represents 3 mm, and the tumor tissue ROI is depicted by the dashed yellow line.

Firstly, the TI results from the targeted PCCAs were compared with those from the control agents for the high dose. As can be seen in Figure 6.7, both post-activation CSS and VDI produced significantly higher ($p < 0.05$) TI values for the targeted droplets over the control agents at the 3 and 6 min wait times.

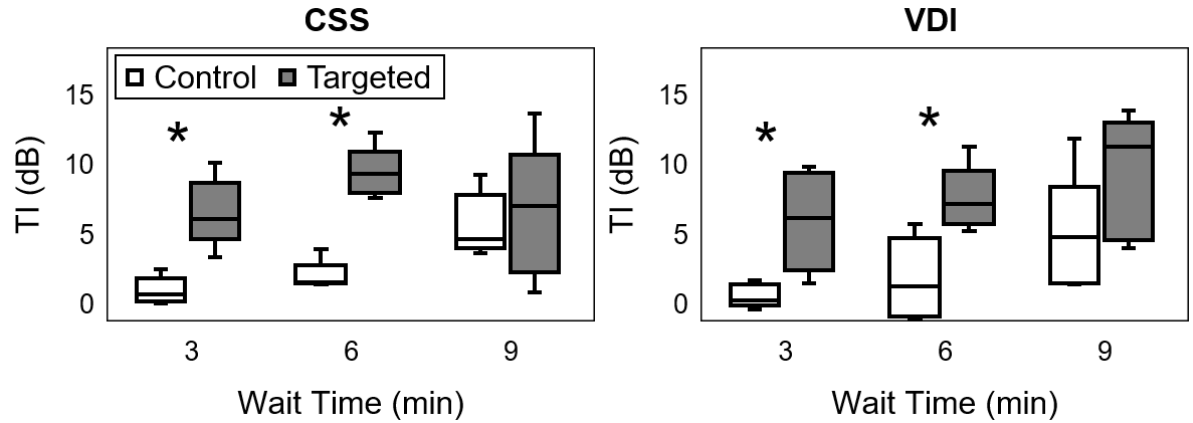


Figure 6.7. Targeting intensity (TI) for post-activation CSS and VDI at the different wait times. Both CSS and VDI had significantly higher ($p < 0.05$) TI for the 3 and 6 min wait times. Significance is denoted with an asterisk.

Circulation time is an important parameter in USMI, so the clearance rate b was compared between targeted and control PCCAs using post-activation CSS data. It was found that targeted PCCAs had a significantly higher ($P < 0.05$) clearance rate than control droplets, which circulated nearly twice as long (Figure 6.8).

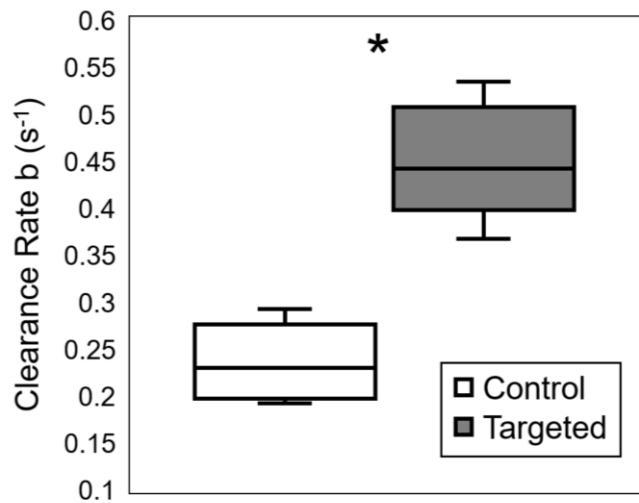


Figure 6.8. Clearance rate b of control and targeted PCCAs. Control droplets had a significantly lower ($p < 0.05$) rate than targeted agents. Significance is denoted with an asterisk.

Next, the TI of VDI and post-activation CSS for USMI with targeted droplets was compared for all wait times and doses tested in this work. While there was no statistical difference between CSS

and VDI for the high dose, VDI had a significantly higher TI for the 6 and 9 min wait times for the low dose (Figure 6.9).

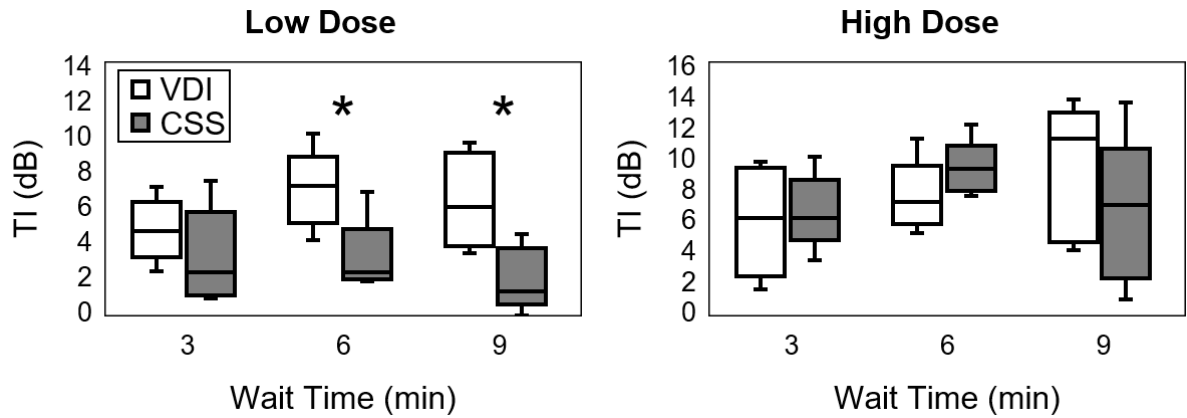


Figure 6.9. Comparison of VDI and post-activation CSS for all wait times and doses. VDI had a significantly higher ($p < 0.05$) targeting intensity (TI) for the 6 and 9 min time-points of the low dose.

The efficacy of droplets (VDI) as intravascular USMI contrast agents was compared against that of MCAs. As can be seen in Figure 6.10, MCAs produced superior TI than PCCAs for all wait times when the low dose was used.

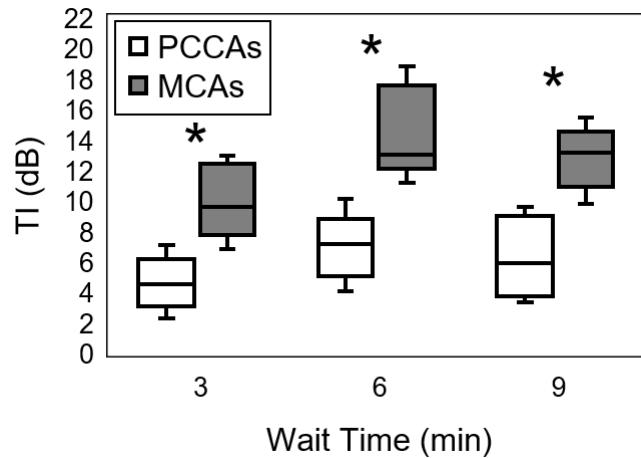


Figure 6.10. Comparison of PCCAs and MCAs. Microbubbles had a significantly higher ($p < 0.05$) targeting intensity (TI) than PCCAs (VDI) for all wait times.

Furthermore, the TI values for the different wait times was compared for all targeted agents and doses tested. It was found that even though the 3 min wait time has a higher median value in most

cases, the wait times did not produce significantly higher TI values for any agent/dose combination (Figure 6.11). However, it is worth pointing out that for the MCA case, 6 min was nearly significant ($p = .051$) from the 3 min wait time, suggesting that a larger sample size may have produced significant results.

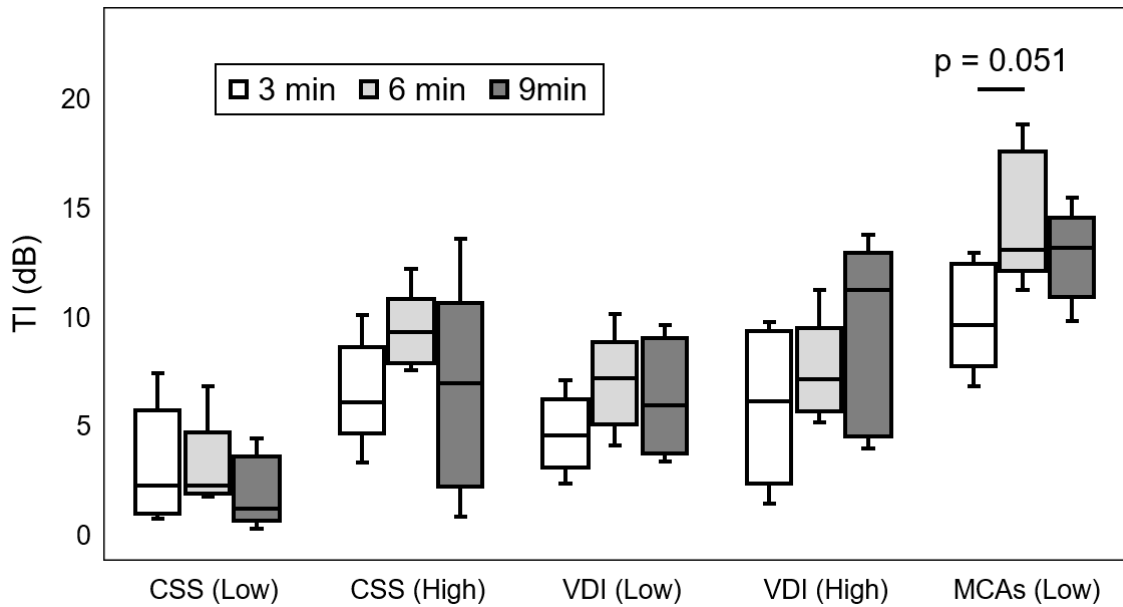


Figure 6.11. Targeting intensity (TI) for the different wait times. Wait times were not significant ($p < 0.05$) for any dose or contrast agent. The 6 min time-point for the MCA case was nearly significantly higher from the 3 min time-point ($p = 0.051$).

As previously discussed, the bubbles produced by the vaporization of targeted PCCAs that were unbound should wash out of the FOV over several seconds and leave only the bubbles produced by activation of bound PCCAs. Hence, the wash-out between targeted and control droplets should be different since all control bubbles should wash out, theoretically. The wash-out rate, b_{wo} , of control and targeted PCCAs was compared using post-activation CSS data, and it was found that b_{wo} was not significant between the two types of agents for any of the wait times (Figure 6.12).

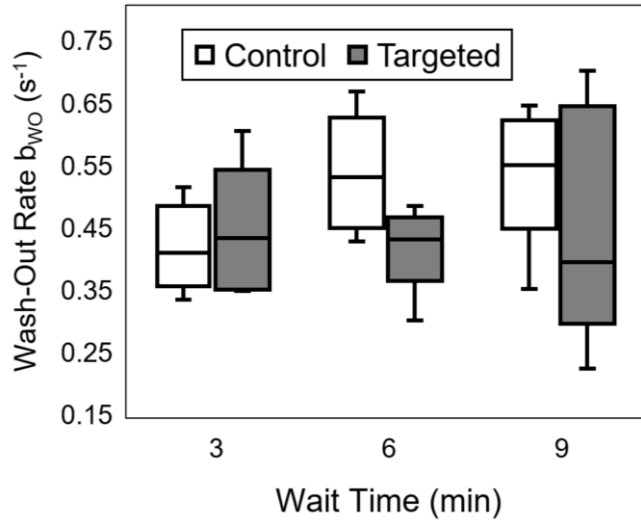


Figure 6.12. Wash-out rate, b_{wo} , for control and targeted PCCAs at all wait times. Wash-out rates were statistically equal for all cases ($p > 0.05$).

Furthermore, the CSS baseline frames of the 30 s time-point should contain any remaining bubbles from the first time-point activation. However, no remaining contrast was detected on any of the baseline frames. Additionally, in both the targeted and control cases, the intensity decreased to values similar to the baseline, so very few bound bubbles produced by droplet activation remained in the FOV after 8 s (Figure 6.4b).

6.4 Discussion

The purpose of this work was to assess the capabilities of low boiling-point PCCAs as intravascular USMI contrast agents, as a first step towards an extravascular USMI platform. In theory, the enhanced circulation time of PCCAs might provide more chances for targeting and produce better binding than MCAs. Additionally, unbound bubbles produced by droplet activation should be washed out from the FOV by blood flow so that only bound bubbles remain, allowing USMI to be performed much faster than conventional techniques using MCAs, which require a waiting period for the freely-flowing agents to be cleared from circulation. In order to test these theories, two types of droplet imaging techniques were used to compare control and targeted PCCAs and MCAs using different doses and wait times. The results show that even though PCCAs do not perform as well as MCAs, they are

viable USMI contrast agents. Furthermore, it was shown that VDI is a more sensitive method for detecting smaller numbers of bound PCCAs than conventional contrast imaging techniques, such as CSS.

The size distributions of PCCAs produced by the Accusizer and NanoSight did not agree (Figure 6.5). While the Accusizer distribution contained a large number of PCCAs larger than 500 nm, the Nanosight distribution did not show a significant number of agents in this range. Theoretically, droplets should be 5-10 times smaller than the precursor microbubbles [101,128]. Therefore, there should be large numbers of droplets between 500 and 1000 nm since the MCA distribution extends past 5 μm . This theory agrees with the Accusizer measurements and suggests that the NanoSight system might not be sensitive to PCCAs larger than 500 nm.

The results show that the targeted PCCAs actively bind to their target ($\alpha_v\beta_3$), since their TI is significantly higher than the controls for the 3 and 6 min wait times (Figure 6.7). At the 9 min wait time, there was no significant difference between TI with the control and targeted PCCAs. This is likely due to the longer circulation time of control droplets, which provides more opportunity for unspecific binding and accumulation in the tumor. It is likely that using a control with similar kinetics to the targeted PCCAs would produce a lower TI at the 9 min wait-time, and the TI for the cRGD agents would be significant. For example, control agents with cRAD (Arg-Ala-Asp), which should not bind to $\alpha_v\beta_3$, have been used previously [264], may be cleared from circulation at similar rates as the cRGD and would be a more appropriate control. Furthermore, it is possible that the longer circulation time of control PCCAs allowed the agents to extravasate and accumulate in the tumor tissue, which would make the TI at the 9 min wait-time artificially high. The imaging techniques used here cannot differentiate between targeting and extravasation, so more work is required to separate these two phenomena.

Control PCCAs circulated for nearly twice as long as the targeted droplets (Figure 6.8). The explanation for this phenomenon lies in the shell composition of the agent. Adding polyethylene glycol

(PEG) to the shell of nanoparticles has been common practice for decades, as the PEG provides a steric shield that prevents immune cell recognition and dramatically decreases particle clearance by the mononuclear phagocytic system, also known as the reticuloendothelial system [33–35]. Hence, PEGylated lipids are ubiquitous in US contrast agent shells [36,37]. However, there is evidence demonstrating that PEGylated agents with targeting ligands can be cleared from circulation faster than untargeted PEGylated agents [265–268], and studies have found that the concentration of the targeting ligand heavily contributes to the increase in clearance by the immune system [269–271]. Furthermore, it has been shown that microbubbles conjugated with cRGD produce a much larger immune response than untargeted PEGylated bubbles [36], so it is likely that the accelerated clearance of the targeted PCCAs seen here was a result of an enhanced immune response. A possible strategy to overcome the accelerated clearance is using agents with ‘buried’ targeting ligands. This approach consists of having contrast agents with a shell that has an overbrush, where the PEG chains not containing the targeting ligands are much longer, thereby hiding the ‘buried’ targeting ligands to reduce immune recognition [264].

The detection of small numbers of targeted agents is important for accurately tracking disease progression with USMI. The results indicate that while at the high dose, VDI and CSS did not produce significantly different TI values, VDI is superior to CSS when the low dose was used (Figure 6.9). The caveat to this conclusion is that neither VDI nor CSS produced significantly different TI compared to the controls for the high dose. However, a low dose of the control PCCAs was not tested, so the low dose of targeted agents might produce a TI that is significantly higher from that of a low control dose. This hypothesis is supported by the fact that the 9 min wait time produced TI that was not significantly lower from the 3 or 6 min wait times for either dose of the targeted PCCAs (Figure 6.11).

USMI with MCAs did, however, produce a TI that was nearly significantly higher for the 6 min wait time, and this result probably would have been significant with a larger animal number. This result suggests that large numbers of freely-flowing bubbles can negatively impact USMI results, so it

is better to wait for unbound bubbles to be cleared. However, the 9 min wait time has a lower distribution of TI values, although not significant from the 6 min wait time, so wait time that is too long might be disadvantageous due to agent detachment caused by blood flow shear stress [272,273].

One of the hypotheses for PCCAs enhancing USMI was that the increased circulation time of droplets compared to microbubbles would provide more opportunities for binding, leading to greater accumulation of droplets in the tumor. However, results of this work demonstrate that MCAs are still better USMI agents, despite the faster clearance from circulation (Figure 6.10). The difference in targeting might be attributed to the size of agents. Studies have shown that the amount of binding and detachment is highly dependent on the site density of the target biomarker [39,272]; more attachment points (ligand-marker attachments) will lead to greater and stronger bubble binding. Therefore, since PCCAs are around 5 times smaller than MCAs, the surface area is lower by a factor of 25, and the number of targeting ligands presented is much lower per unit area. As a result, PCCAs form fewer links to the endothelial markers, making them more likely to not bind at all or detach from shear stress caused by blood flow.

Since PCCAs cannot be detected using US unless they are vaporized into echogenic microbubbles, USMI could be performed faster because there would be no need to wait for the freely-flowing agents to be cleared from circulation. Theoretically, both bound and unbound droplets would be activated, but only the unbound bubbles produced by the vaporization pulses would be washed out of the FOV. Hence, the targeted and control agents should have different wash-out characteristics, since all the produced control bubbles should wash out. However, the results showed that this is not the case, and in fact, the targeted agents almost completely washed out of the imaging plane (Figure 6.12). In order to further elucidate the wash-out process, the perfusion was explored spatially for both the microbubble wash-in and the wash-out of bubbles generated by PCCA vaporization (3 min wait time, first time-point) by making parametric perfusion maps, like those previously described by Feingold and colleagues [58]. These maps allow for the visualization of perfusion on a pixel-by-pixel basis by color-

coding perfusion times of each pixel. Example maps can be seen in Figure 6.13. Green and red pixels denote fast and slow perfusion, respectively, from 0 s to the maximum perfusion time, which was 40 s for the bubble wash-in and 8 s for the droplet (bubbles generated by droplet vaporization) wash-out. Surprisingly, the perfusion maps look completely different, with the slow perfusion areas in the bubble wash-in at the top (Figure 6.13a) and at the bottom of the tumor for the control PCCA wash-out (Figure 6.13b).

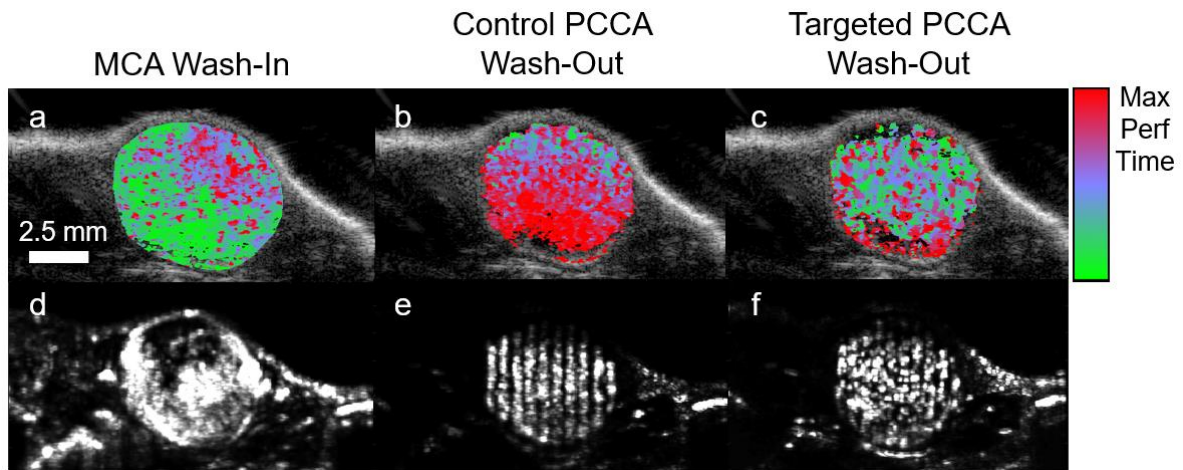


Figure 6.13. Perfusion maps of MCA wash-in (a), control (b) and targeted (c) PCCA wash-out, overlaid over Bmode images. The color range is normalized to the maximum perfusion time for each case (40 s for wash in and 8 s for wash-out). Standard deviation (STD) maps of wash-in (d), control (e) and targeted (f) wash-out. Color and STD maps shown here are from different animals.

Furthermore, when the standard deviation (STD) of each pixel is taken through time (all frames in wash-in or wash-out), maps depicting the change in intensity can be created, where bright areas represent large changes in perfusion (Figure 6.13d-f). Similar to the perfusion color maps, the STD maps between the bubble wash-in and droplet wash-out look completely different, with the largest changes in perfusion appearing in different areas of the tumor. Once PCCAs are activated, the produced bubbles should disperse throughout the tissue, but the majority remain in the location where they were activated. This is illustrated by the STD maps, where the columns of activation seen in Figure 6.6 correspond to the areas of largest perfusion in Figure 6.13e-f.

The fact that the perfusion maps look completely different between bubble wash-in and control droplet wash-out suggest that the clearance of PCCAs from the FOV is not solely dependent on blood flow. The bubbles seem ‘stuck’ in the regions of activation, which should not happen with control agents. Even for targeted agents that should be stationary after activation, they almost completely disappear from the FOV by 8 s, but it doesn’t appear that they are washing out, since they don’t have the same perfusion characteristics as MCAs washing-in. The violent oscillation of the vaporization process may be detaching the produced bubbles that were bound, which explains why the mean intensity in the tumor nearly disappears, but this theory does not explain the spatial perfusion inconsistencies illustrated by the maps in Figure 6.13. Although in-vitro studies have shown that targeted droplets retain adherent after vaporization, these in-vitro studies did not involve flow [126]. Further studies will need to be performed to further elucidate what is responsible for signal loss. Another possible explanation for the inconsistencies in these perfusion patterns is that the droplets are in fact extravasating, and this is the reason they appear stationary after activation. While this is a reasonable explanation, it is unlikely that extravasation plays a major role, since the droplets only circulated for 3 min before activation, and previous studies have found that significant extravasation occurs over several hours [121,266,267,274]. Moreover, the same pattern of perfusion was seen in the 30 s time-points, and in many control cases, the mean intensity of the first and second time-points was equal, which would imply that the same number of droplets extravasated in only 30 seconds.

It has been reported that bubbles produced by droplet vaporization can grow to several times their initial size within the first 200 ms after activation and can coalesce to form large bubbles [104,136,141,275]. Therefore, a possible explanation is that the bubbles produced by activation of PCCAs quickly coalesce to form very large bubbles that become lodged in the tumor vasculature and slowly dissolve over time. Few studies have explored the stability of PCCAs more than 400 ms after vaporization, but preliminary studies in our lab have found that vaporized PCCAs are less resistant to dissolution and fragmentation caused by imaging pulses than conventional MCAs, which has been

corroborated by a recent study [276]. These observations suggest that the wash-out rate might, in part, be driven by the dissolution of bubbles or destruction by imaging pulses and not solely by blood-flow. More work is required to determine the mechanism of vaporized PCCA clearance after activation.

A different type ultrasound contrast agents that has potential for extravascular USMI are nanobubbles, which are nano-scale bubbles that have been reported to passively accumulate in the tissue and provide high contrast levels *in vivo* [277,278]. However, the smaller diameter of these agents reduces their stability *in vivo*, and the echogenicity at clinical frequencies (1-10 MHz), compared to conventional MCAs [278–280]. Therefore, more work is required for nanobubbles to become viable contrast agents for USMI. Moreover, echogenic liposomes [281] and biogenic gas vesicles [282] are nanoscale agents that have been used for USMI *in vivo*, but due to their small cross-section, they are significantly less echogenic than vaporized PCCAs.

This work has found that PCCAs are inferior to MCAs for intravascular USMI. However, because they can be manufactured with sizes smaller than 400 μm , there is potential for using targeted droplets for extravascular USMI. Much like this work, droplets would be injected and allowed to circulate, but instead of binding to endothelial markers, PCCAs would extravasate due to the enhanced permeability and retention (EPR) effect and bind to markers expressed by cancer cells. The unbound PCCAs would then be cleared by the lymphatic system, leaving only bound droplets which could be vaporized to obtain USMI signal. However, many aspects of this process need to be explored, such as the circulation time required for sufficient accumulation of droplets in the tumor tissue and the amount of time the droplets would have to remain stable while the lymphatic system clears unbound agents.

6.5 Conclusion

PCCAs have advantages over MCAs that might enhance USMI. Droplets have longer circulation times *in vivo*, which might produce better targeting through increased opportunities to bind. USMI with PCCAs might be able to be performed before faster than current methods by simply measuring the wash-out of the bubbles produced by activation or the remaining signal of bound bubbles

after wash-out, eliminating the need to wait for the unbound agents to be cleared from circulation. However, this work has shown that the increased circulation of PCCAs is offset by lower targeting due to their small size, and that the wash-out information after vaporization cannot be used to quantify targeting without long wait times, making droplets perform worse than MCAs for USMI. Nevertheless, PCCAs were able to bind their target and provide significant molecular signal. Even though they are not efficient intravascular USMI agents, PCCAs have the potential to be used to target extravascular markers.

CHAPTER 7

PROTOCOLS FOR PERFUSION IMAGING USING PCCAS

7.1 Introduction

As was shown in the previous chapter, the bubbles produced by PCCA activation seem to coalesce and form very large bubbles that become lodged in the vasculature. Although, the contrast “washes” out of the imaging plane, the clearance is most likely destruction and dissolution caused by the imaging pulses. As a result, reliable measures of perfusion cannot be obtained. In this chapter, several factors are explored in an effort to reduce coalescence and dissolution. Namely, the effect of size, concentration, vaporization pressure, pulse length, and the shell formulation on coalescence and formation of large bubbles was explored.

The MCAs used for this dissertation often have a polydisperse distribution, and since PCCAs are made from these bubbles, there will be large droplets that may occlude vessels once converted back microbubbles. Therefore, the effect of removing large outliers was explored. Furthermore, it has been reported that bubbles produced by PCCA vaporization coalesce to form larger bubbles [104,105], so the role of concentration, vaporization pressure, and activation pulse length were also evaluated.

Lastly, the lipid shell formulation was altered to enhance stability and prevent coalescence and dissolution. There are 2 main shell components on conventional MCAs: the main lipid making up most of the shell and the PEGylated lipid used to prevent coalescence and immune recognition. There is evidence that bubbles produced by vaporization that have a longer PEG chain on the shell can traverse the vasculature and do not become lodged [143], so different PEG lengths were compared. Furthermore,

shells with longer lipid acyl chains (more carbons on the chain) have been shown to decrease dissolution [283,284] and make more stable PCCAs [131] so different chain lengths were assessed.

7.2 Methods

7.2.1 Animal Protocol

The kidneys of Fischer 344 rats (Charles River Laboratories, Morrisville, NC, USA) were used as targets because there should be no extravasation, unlike tumors. The rats were anesthetized with 2.5% isoflurane, placed on a heated pad, and the flank was shaved to remove fur. A catheter was inserted into the tail-vein for PCCA administration in a bolus or continuous infusion. All animal and imaging protocols were approved by the University of North Carolina School of Medicine's Institutional Animal Care and Use Committee.

7.2.2 PCCA and MCA Formulations

Both MCAs and PCCAs were used in this work. Droplets were formed from prepared MCAs, so both agents were composed of the same lipid formulation. The lipid solution consisted of 1,2-distearoyl-sn-glycero-3-phosphocholine (DSPC) and 1,2-distearoyl-sn-glycerol-3-phosphoethanolamine-N-methoxy(polyethylene-glycol)-2000 (DSPE-PEG2000) in a 9:1 M ratio and a total lipid concentration of 1.0 mg/mL and was dissolved in a solution of phosphate-buffered saline (PBS), propylene glycol, and glycerol (16:3:1). This is the formulation conventional formulation used in the experiments not exploring the role of PEG chain length or acyl chain length.

To test the effect of different PEG chain lengths, DSPE-PEG5000 was compared to DSPE-PEG2000, and 1,2-diarachidoyl-sn-glycero-3-phosphocholine (DBPC, C:20, 20 carbons on the acyl chain) was compared to the conventional DSPC (C:18) to evaluate the effect of acyl chain length.

The headspace of a 3 mL vial containing 1.5 mL of the different lipid solution was filled with OFP or DFB and the vial was mechanically agitated to form microbubbles with a distribution that will be referred to as native. In order to eliminate the large outliers from the native distribution, the bubbles

were allowed to separate into 2 layers by waiting 7.5 minutes, and the supernatant was discarded. This distribution will be referred to as size-selected.

Finally, the different MCA formulations were condensed into PCCAs using previously described methods [129].

7.2.3 MCA Sizing

The size distribution and concentration of the bubbles were measured using an Accusizer 780 (Particle Sizing Systems, Santa Barbara, CA, USA) that is capable of measuring particles down to 0.5 μm .

7.2.4 Imaging Protocols

Two types of imaging pulse sequences were implemented: B-mode and contrast imaging. Both sequences consisted of plane-wave imaging with angular compounding, as is described in Chapter 4. The kidney was found using a conventional B-mode script on a Verasonics V1, and a region of interest (ROI) was drawn around the kidney to select the location of activation pulses. The vaporization pulses were focused, delivered serially and were separated by 0.75 mm and 0.5 mm axially and laterally, respectively. APM was used to account for tissue attenuation and deliver the same pressure to all locations, and the vaporization pulses consisted of 5-cycle sinusoids at 5 MHz. As described in Chapter 4, baseline contrast frames were first captured, the vaporization pulses were delivered, and post-activation contrast frames were captured to monitor the wash-out of the produced microbubbles.

7.2.5 Data Analysis

The amount of activation was quantified as the contrast enhancement (CE), which was calculated by dividing the linearized mean intensity inside of the ROI of the post-activation frames by the average mean intensity of the baseline frames. To quantify the wash-out of PCCAs or wash-in of MCAs, the CE was normalized to the maximum value and fitted to a mono-exponential. Equations 7.1 and 7.2 were used for PCCA wash-out and MCA wash-in, respectively,

$$y(t) = e^{-b_{wo}t} \quad (7.1)$$

$$y(t) = 1 - e^{-b_{wi}t} \quad (7.2)$$

Where b_{wo} is the wash-out rate, b_{wi} is the wash-in rate, and t is time.

7.2.6 MCA Perfusion Imaging

DCE-US with MCAs was performed to quantify perfusion in the kidneys and compare it to that obtained using PCCAs. The pulse sequence used was similar to the PCCAs activation sequence: baseline contrast frames were captured, destructive (focused) pulses (MI=1.3) were delivered to clear bubbles from the imaging plane, and post-destruction contrast frames were captured to monitor the bubbles flowing back into the kidney.

To assess whether or not the imaging pulse sequence was sensitive to changes in perfusion, dopamine was used to increase perfusion rate, as described previously [58]. Size-selected MCAs were continuously infused at a rate of 1.5×10^8 bubbles/min and allowed to circulate for 2 minutes before imaging to allow the concentration in the blood to reach a steady state and a pre-drug scan was acquired. Next dopamine was added to a fresh solution of microbubbles and infused at a rate of $2 \mu\text{g/kg/min}$ while keeping the bubble infusion rate at 1.5×10^8 bubbles/min. The bubbles and drug were allowed to circulate for the drug to take effect, and 3 post-drug scans were taken at 3, 5, and 7 min after the start of drug infusion.

7.2.7 Effect of PCCA Size

Bolus injections of 6×10^8 size-selected DFB and OFP droplets were administered and allowed to circulate for 1 min before activation. The resulting contrast and wash-out was captured by the post-activation contrast frames at a rate of 10 Hz for 10 s. Droplets were activated using pulses with peak-negative pressures of 4.25 and 1 MPa for DFB and OFP, respectively.

7.2.8 Effect of Concentration and Vaporization Pressure

Size-selected OFP PCCAs were continuously infused at 4 different rates: 1.2×10^7 , 2×10^7 , 2.8×10^7 , and 3.6×10^7 #/min. Droplets were activated using 1.25 MPa activation pulses to explore the effect of concentration of PCCAs in the blood with a set vaporization pressure. In a separate experiment, droplets were activated using 0.75, 1, 1.25, and 1.5 MPa for all infusion rates.

7.2.9 Effect of Pulse Length

The effect of activation pulse length was explored by monitoring the generated bubbles from size-selected OFP activation using optical microscopy. PCCAs at a concentration of 5×10^9 #/mL were manually infused through a 200 μm cellulose tube submerged in a water bath at room temperature. A 100x (NA = 1.0) water immersion objective on an inverted microscope (Olympus IX71, Center Valley, PA) was interfaced with a high-speed camera (FastCam SA1.1, Photron USA, Inc., San Diego, CA) to capture images before and after activation at a rate of 125 frames per second. A framerate of millions of Hertz is required to capture the vaporization event, so the bubbles were evaluated once they have reached their final size. Vaporization pulses with 1, 2, 5, 10, and 15 cycles and a peak-negative pressure of 1.5 MPa were used. The generated bubbles were localized and sized using a custom MATLAB (The Mathworks, Inc., Natick, MA) script employing the Hough Transform [285,286].

7.2.10 Effect of PEG Chain Length

In order to isolate the PEG length as the only variable, size-selected DFB and OFP droplets were activated in their vials using temperature. The precursor MCAs were sized using the Accusizer, the vials were opened to relieve pressure and partially submerged in a heated water bath (40°C and 65°C for DFB and OFP, respectively) for 1 min, and the solution was sized again. This protocol was implemented to explore shifts in the distribution of the bubbles before condensation and after vaporization. It has been reported that bubbles produced by droplet vaporization can grow to several times their initial size within the first 200 ms after activation due to dissolved gasses in the environment diffusing in [104,136,141,275], which would confound the results here. The lipid solution was placed

under vacuum to remove all of the dissolved gasses before the gas-exchange and agitation process. Therefore, there should not be any dissolved gasses in the MCA/PCCA solution inside the vial, which will limit the shift in size distribution due to gas diffusion after vaporization.

7.2.11 Effect of Acyl Chain Length

Size-selected OFP PCCAs with both C:18 and C:20 acyl chains were injected in rats. Bolus doses of either 2.25×10^8 or 1×10^9 droplets were injected and allowed to circulate for 1 min before activation. Vaporization pulses with peak-negative pressures of 1.25 MPa were used, and the contrast wash-out was captured using contrast imaging frames at 10 Hz. Furthermore, droplets were also activated using pulses that were spatially separated by 2.5 mm both axially and laterally to explore the effect of pulse proximity on coalescence.

7.2.12 PCCA Perfusion imaging

Changes in perfusion using PCCAs were explored using a similar dopamine experiment described previously. Size-selected OFP droplets (PEG2000, C:18) were continuously infused at a rate of 2.8×10^7 droplets/min and activations were captured at 3, 4, and 5 min after the start of infusion. Dopamine ($2 \mu\text{g}/\text{kg}/\text{min}$) was then added to a fresh droplet solution and activations were captured 3, 4, 5, and 6 min after the start of the drug/droplet infusion.

7.2.13 Statistical Analysis

Kruskal-Wallis analysis was performed to determine significance between any groups being tested (wash-in or wash-out rates, distributions, doses), and a Tukey range test was used to find significance between each of the parameters. ANOVA was used for determining significance between the number of cycles for the effect of pulse length. Significance was set as $p < 0.05$.

7.3 Results

7.3.1 MCA Perfusion Imaging

The wash-in rate for all rats was grouped, and it was found that the rate was significantly higher before the infusion of dopamine (Figure 7.1). It is worth pointing out that complete reperfusion inside the kidney happens in the order of hundreds of milliseconds and not seconds, as in the wash-out curves shown in Chapter 4.

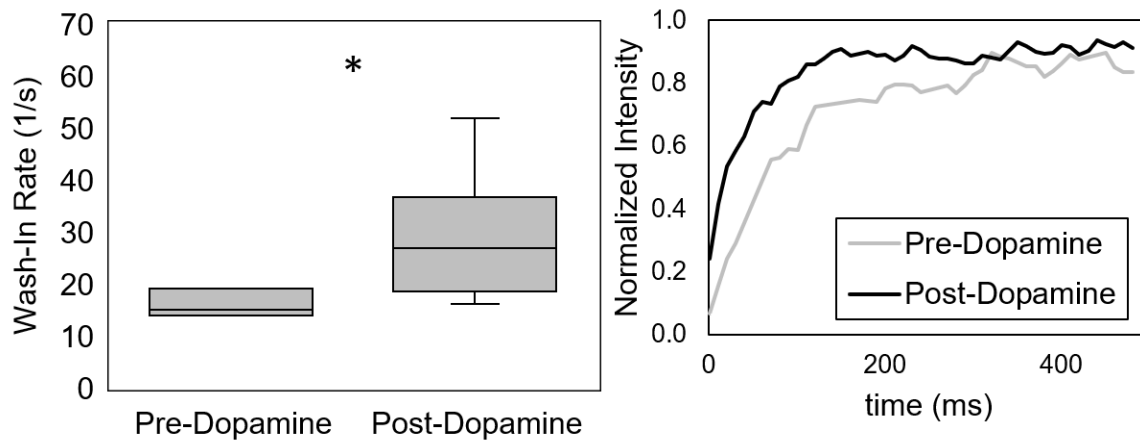


Figure 7.1. Plots of MCA wash-in rate (left) and curves (right) in rate kidneys before and after administration of dopamine. The wash-in rate was significantly ($p < 0.05$) faster after the infusion of dopamine.

7.3.2 Effect of PCCA Size

Accusizer results are shown in Figure 7.2. The size-selection process reduces the number of bubbles larger than $1.5 \mu\text{m}$ and eliminates most of the outliers. The distribution shifts from a mean of $1.05 \pm 0.09 \mu\text{m}$ to $0.87 \pm 0.01 \mu\text{m}$ from the native to the size selected distributions, respectively. The mean diameter values of the two types of PCCAs is significant. However, when the droplets were activated *in vivo*, both OFP and DFB wash-out of the imaging plane in time scales that were an order of magnitude longer than the reperfusion of MCAs (Figure 7.2). The CE of DFB only decreased by about 50% in 10 s and OFP completely washed-out in around 5 s.

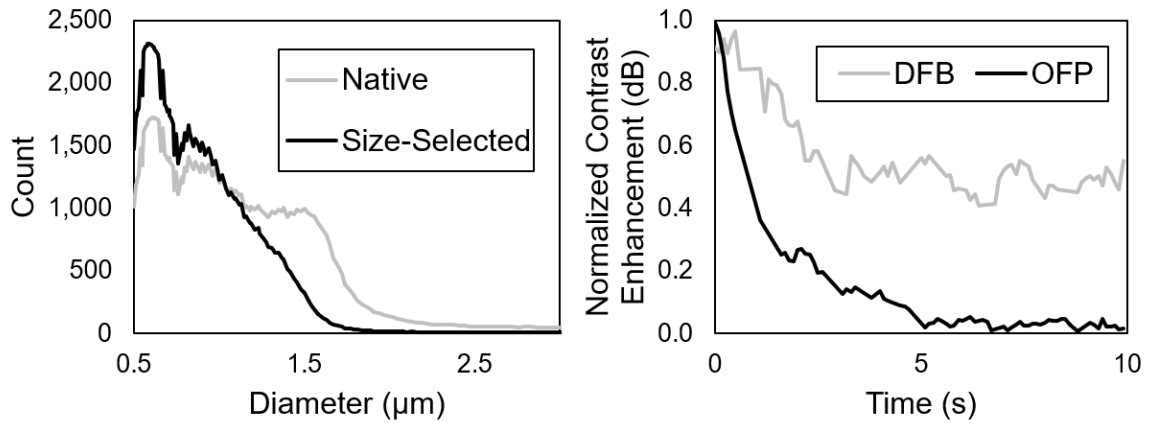


Figure 7.2. Size distributions for native and size-selected MCAs (left) and the averaged wash-out curves for size-selected PCCAs. The size-selection process eliminated outliers and majority of bubbles greater than 1.5 µm. The wash-out of size selected vaporized droplets was still an order of magnitude larger than MCA wash-in.

7.3.3 Effect of Concentration and Vaporization Pressure

The wash-out rates increased, and the maximum CE decreased with decreasing PCCA dose (Figure 7.3). There was a significant negative spearman correlation ($\rho = 0.79$, $p = 2 \times 10^{-11}$) between wash-out rate and dose. Furthermore, the wash-out rate was generally higher for the lower activation pressures, although only significant between 1 and 1.5 MPa for the 2 highest doses. 0.75 MPa produced inconsistent vaporization so it was excluded from the wash-out analysis. Concentration of PCCAs in the blood and the activation pressure were found to have an effect on the wash-out rate, but the rate was still an order of magnitude higher than bubble reperfusion even at the lowest pressure and dose.

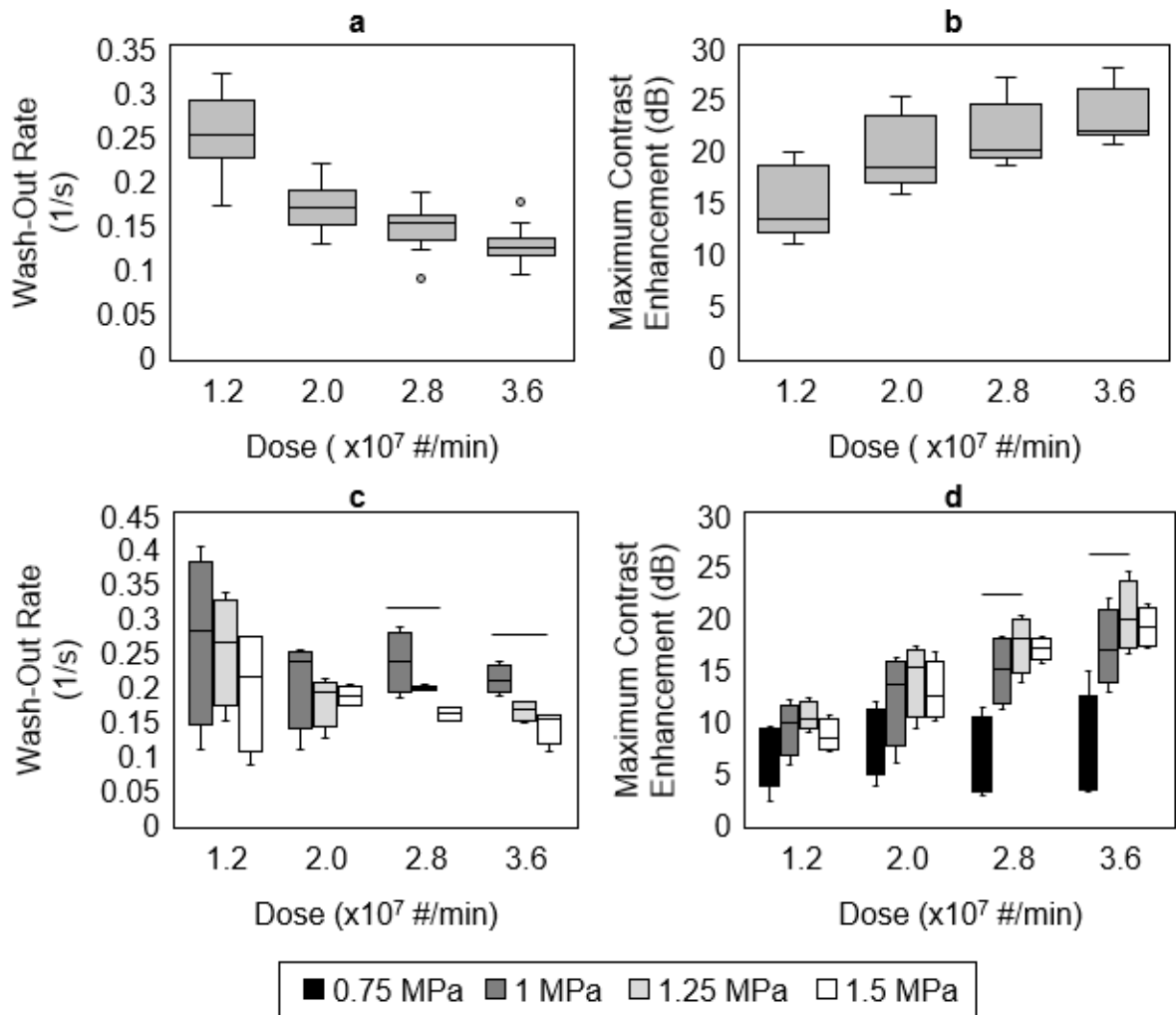


Figure 7.3. Plots of wash-out rate and maximum contrast enhancement for different size-selected OFP PCCAs doses and vaporization pressures. The wash-out rate became slower as dose increased (a), and the reverse was true for contrast enhancement (b). The wash-out rate generally decreased with increasing vaporization pressure (c) and 1.25 MPa produced higher median contrast enhancement (d).

7.3.4 Effect of Pulse Length

Figure 7.4 illustrates an example image of the bubbles produced by vaporization, and the algorithm localizing a sizing the bubbles. The results indicate that the 1 cycle group was significant from all other groups, but the distributions from the other groups were not significant from each other. The number of activated droplets increased with pulse length, which agrees with previous findings about vaporization thresholds [134,287], so it is likely that the 1 cycle pulses produced a larger distribution of bubbles because they could only activate larger droplets, which are easier to vaporize.

Therefore, the results suggest that pulse length does not heavily influence final diameter of bubbles produced by PCCA activation.

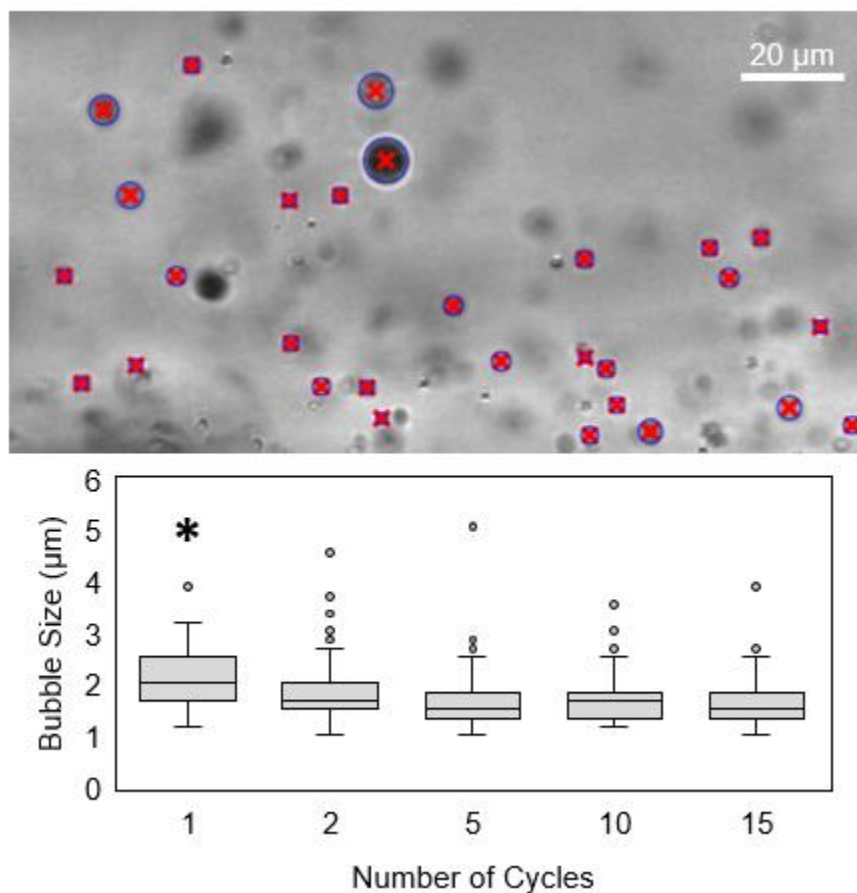


Figure 7.4. Example microscopy image (top) of vaporized PCCAs and plot of bubble sizes for each number of cycles group (bottom). The localization of bubbles using the Hough transform is displayed by the red x's (bubble center) and blue circles (bubble outline). The bubble size for the 1 cycle group was significant ($p < 0.05$) from all other groups (denoted with a *), but none of the other groups were significant from each other.

7.3.5 Effect of PEG Chain Length

The size distributions of pre-condensation and post-vaporization OFP and DFB bubbles with PEG2000 and PEG5000 are shown in Figure 7.5. In both lengths of PEG, the distribution shifts towards larger bubbles after vaporization, suggesting coalescence. For DFB, the distribution shifted from $0.825 \pm 0.005 \mu\text{m}$ to $1.55 \pm 0.43 \mu\text{m}$, and from $0.945 \pm 0.005 \mu\text{m}$ to $1.275 \pm 0.025 \mu\text{m}$, for PEG2000 and PEG5000, respectively. For OFP, the distribution shifted from $0.82 \pm 0.01 \mu\text{m}$ to $0.945 \pm 0.05 \mu\text{m}$, and

from $1.02 \pm 0.02 \mu\text{m}$ to $1.125 \pm 0.035 \mu\text{m}$, for PEG2000 and PEG5000, respectively. None of the pre-condensation and post-vaporization values were significant, likely due to the small number of samples per group (3), but the distribution curves clearly show a shift in size. Therefore, PEG5000 did not prevent more coalescence than PEG2000.

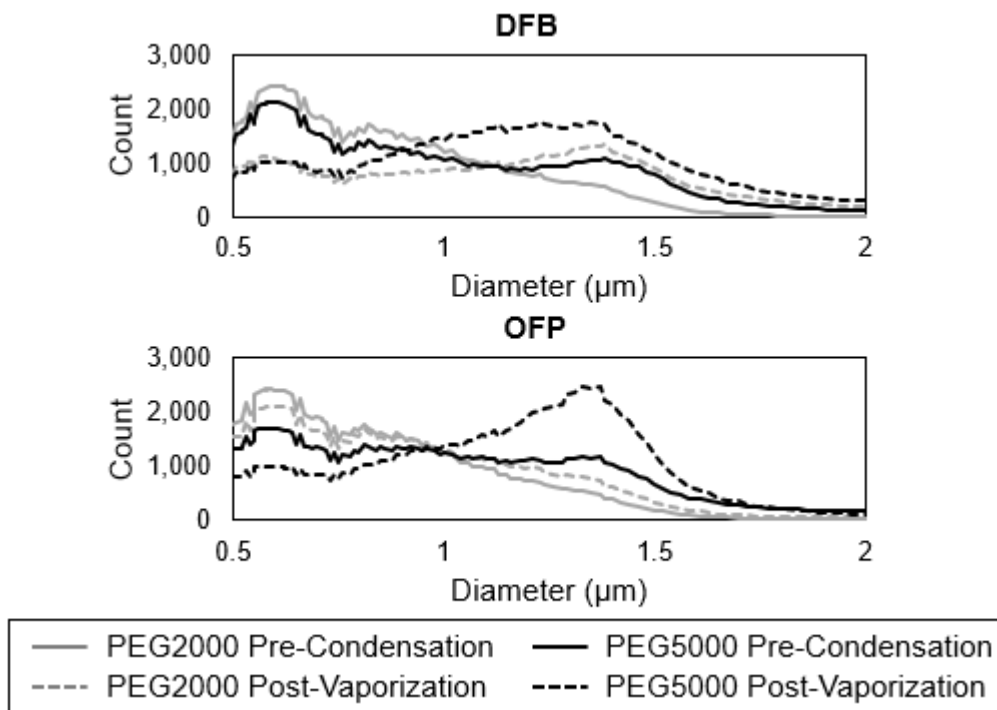


Figure 7.5. Size distributions of size-selected DFB and OFB bubbles before condensation and after vaporization for PEG2000 and PEG5000. The distributions of both types of PEG shifts right (larger) after vaporization.

7.3.6 Effect of Acyl Chain Length

Representative curves for the different conditions are displayed in Figure 7.6. At both the low (2.25×10^8 droplets) and high (1×10^9 droplets) dose, the C:20 bubbles produced by droplet vaporization were cleared from the imaging plane much slower than for C:18. Furthermore, using a larger spacing produced a faster wash-out rate, suggesting that activation pulse proximity has an effect of coalescence and bubble lodging in the vasculature. The bubbles produced by the activation of both C:20 and C:18 PCCAs appeared to be stuck in the blood vessels, but the C:20 bubbles seemed to be more resistant to dissolution or destruction caused by the imaging pulses, which contributed to the slower wash-out.

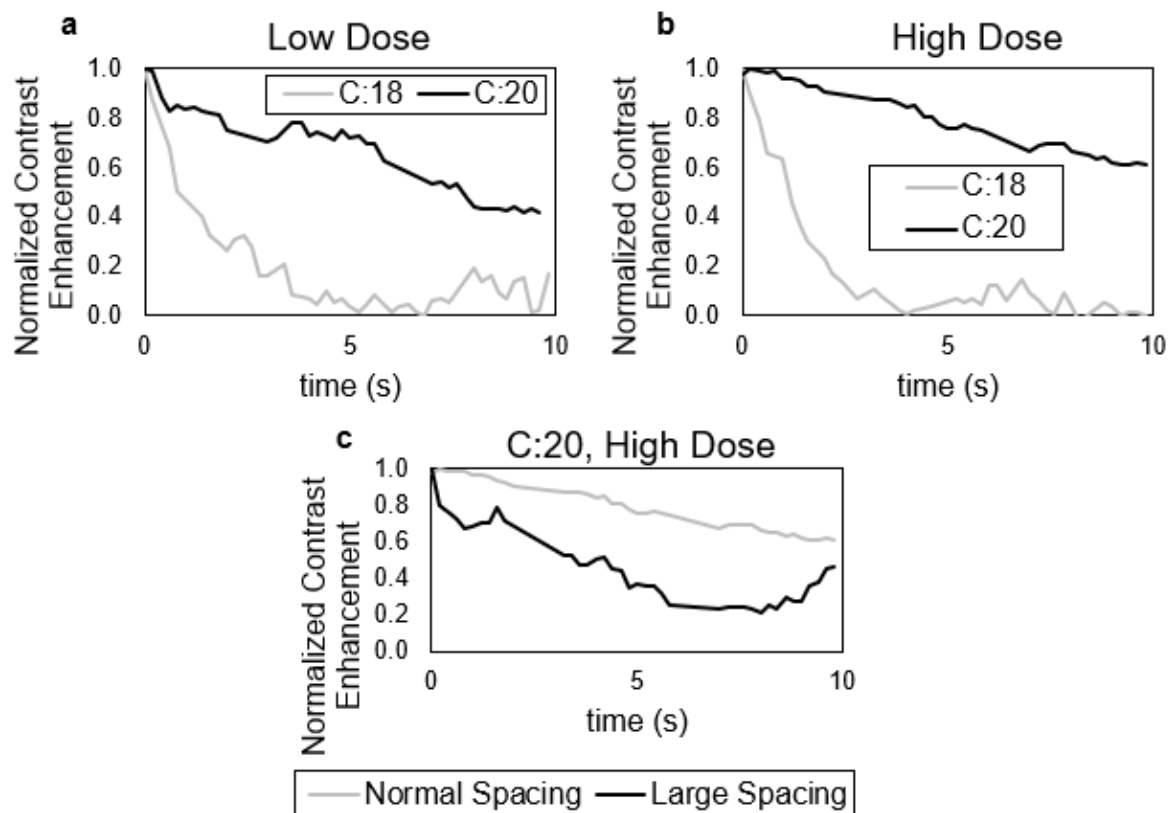


Figure 7.6. Example wash-out curves for size-selected OFP droplets with C:18 and C:20 acyl chain lengths. At both the low (a) and high doses (b), the vaporized C:18 droplets were cleared from the imaging plane much faster than vaporized C:20 droplets. Vaporized droplets were washed out faster when a large spacing between activation pulses was used (c).

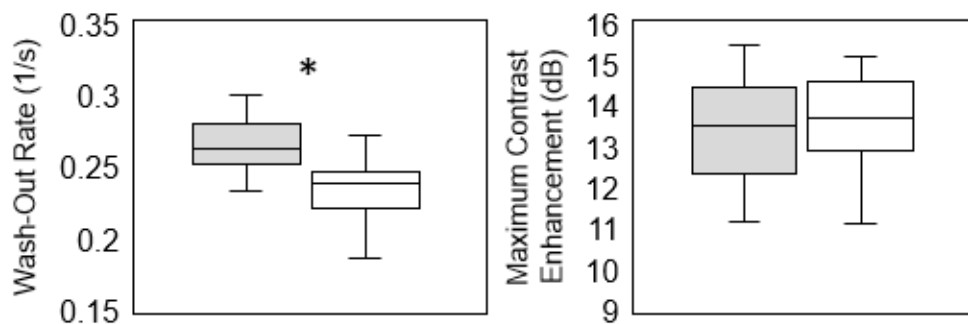


Figure 7.7 Wash-out rate (left) and maximum contrast enhancement (right) of vaporized size-selected OFP droplets in the kidneys of rats before and after the administration of dopamine. The contrast enhancement was not significant, but the wash-out rate was significantly lower ($p < 0.05$) after the administration of dopamine.

7.3.7 PCCA Perfusion Imaging

The wash-out rates for all the pre-drug trials for all rats were combined, and it was found that the pre-drug wash-out rate was significantly higher than that of combined post-drug wash-out rate (Figure 7.7). The maximum CE was not significant between the two groups, so it is not clear why the dopamine had the opposite effect than what was seen in MCA perfusion imaging.

7.4 Discussion

The results indicate that vaporized droplets still coalesce and form large bubbles that become lodged in the vasculature regardless of modifications to the vaporization parameters or shell formulation. The effect of dopamine to the wash-out dynamics of bubbles produced by droplet activation was opposite of what it was with MCAs and it was an order of magnitude longer. Therefore, the wash-out of vaporized PCCAs does not seem to depend heavily on blood flow but on dissolution and fragmentation by imaging pulses.

Figure 7.8 shows colormaps of the wash-in of MCAs into the kidney, like those from DCE-US in Chapter 3, and the wash-out of vaporized PCCAs. The MCAs map shows that the perfusion in the kidney is slow in the center and fast in the periphery. However, perfusion maps for PCCA wash-out do not follow this pattern, but rather, seem to have random areas of fast and slow perfusion. Furthermore, when standard deviation maps, like those from the previous chapter, are made, it can be seen that large changes in intensity (flow, dissolution, fragmentation) are only seen in the areas where vaporization occurred, and not on the periphery where there should be faster perfusion.

Lastly, a longer acyl chain produces bubbles that were more stable and resistant to dissolution and fragmentation by imaging pulses, which lead to a slower wash-out, supporting the hypothesis that bubbles produced by droplet activation become lodged in the vasculature and the apparent wash-out is more heavily driven by dissolution and destruction than by blood flow.

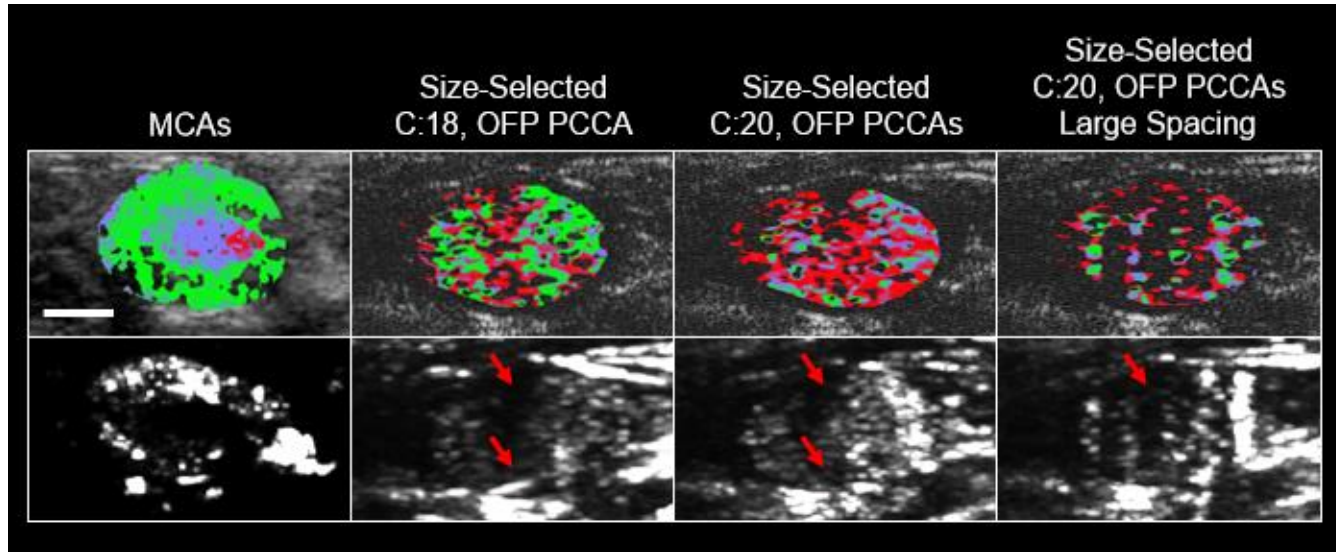


Figure 7.8. Perfusion (top) and standard deviation (bottom) maps. The MCA wash-in maps show that most of the perfusion in the kidney occur on the periphery, while the perfusion maps for PCCA wash-out show that the perfusion happens randomly throughout the kidney. Areas that are dark did not reach the threshold (above 80% of baseline for MCA wash-in, and below 20% of maximum for PCCA wash-out), so the perfusion map for the large spacing indicates that the generated contrast does not spread out but remains in the location at which it was generated. This is specially highlighted in the standard deviation maps, since the dark regions (slow perfusion) exist where there is the faster perfusion (red arrows). The scale bar represents 5 mm.

7.5 Conclusion

The clearance of vaporized low boiling-point PCCAs from the imaging plane is governed by bubble dissolution and destruction due to imaging pulses rather than blood flow. Therefore, accurate measurements of perfusion cannot be obtained with PCCAs with the current formulation.

CHAPTER 8

DISCUSSION AND CONCLUSIONS

8.1 Assessment of Response to Therapy Using Microbubble Contrast Agents

The first hypothesis of this thesis was that CEUS can assess response to therapy more accurately and earlier than changes in tumor volume. The results in Chapter 3 demonstrate USMI of VEGFR-2 and vascular density measurements using AA can accurately track the response of ccRCC tumors in mice to antiangiogenic and Notch inhibition therapies and detect the response of the tumors before changes in tumor volume, which is the clinical gold standard. Furthermore, the results from the small pilot study of DCE-US are encouraging and a larger study with higher numbers of animals per group would likely produce significant results, as those from recent studies using DCE-US for assess response to therapy in tumors [86,87].

The work described in this thesis, along with other experiments in the last decade, demonstrate the value of CEUS for cancer diagnosis and evaluation of response to therapy. The next step is to translate these techniques into the clinic. CEUS is already used to characterize and classify liver [288,289], thyroid [290], and breast [291] lesions in patients, as well as diagnosing different gallbladder cancers [292] and characterizing between renal cancer subtypes [29]. Moreover, there has been work on early assessment of renal and gastrointestinal tumors to antiangiogenic therapy, that illustrate the benefits of CEUS and its potential to become a crucial tool for cancer diagnosis [20,90–93]. Therefore, the tools are already in place to explore the capabilities of CEUS in different types of cancers and therapies.

All the experiments described in the previous paragraph used DCE-US. However, the results of this work and others over the last five years suggest that USMI might be a more sensitive technique than DCE-US for the assessment of response to antiangiogenic therapies. VEGFR-2 targeted agents have recently been approved for human use, and a few studies have demonstrated the feasibility of USMI with these agents in human patients [30,31], so it is now up to the field to explore the capabilities of USMI for the evaluating response to therapy in patients.

8.2 Phase-Change Contrast Agents for the Assessment of Response to Therapy

The second hypothesis of this thesis was that CEUS can be performed using PCCAs. The results of this work demonstrate that pulse sequences can be created to activate PCCAs and generate uniform vaporization within a target, kidney or tumor, and produce contrast enhancement levels similar to those of conventional MCAs. Moreover, the activation signal of PCCAs can be captured to produce images with significantly higher contrast-to-tissue ratios than conventional microbubble specific pulse sequences. It was also discovered that the bubbles produced by droplet activation wash out of the imaging plane, so capturing this clearance might provide measures of blood perfusion. However, the results of the previous two chapters demonstrate the wash-out rate of vaporized PCCAs might be governed by destruction and dissolution of bubbles that coalesce and become lodged in the vasculature, and not blood flow. Therefore, meaningful perfusion measurements cannot be obtained with the current formulation of PCCAs.

Changes to the major components of the shell, PEG and acyl chains, were modified without significant improvements in perfusion, so it is likely that a lipid shell is not the best option for this application. A stiffer shell is likely to prevent dissolution or coalescence, but like shells with long lipid (C:22 and above), would make the agent harder to condense and vaporize, and would return smaller ultrasound signals [131,140].

The results of Chapter 6 demonstrated that PCCAs can be used as intravascular USMI agents, which is encouraging for the goal of extravascular USMI. However, there are limitations that have to

be overcome before PCCAs can be used to image extravascular markers. The premise of extravascular USMI is that the droplets extravasate in to the interstitial space and the unbound agents are cleared by the lymphatic system, which is a network of vessels that clear waste from cell metabolism out of the interstitium. The remaining droplets can be assumed to be targeted to the desired marker, and can be activated and imaged. However, much like the blood vessels, lymphatic vessels in cancer are disorganized, inefficient, or non-existent [248,293,294]. For this reason, nanoparticles accumulate in the tumor tissue for hours to days. Therefore, PCCAs would have to be manufactured to be stable at body temperature for far longer periods than low-boiling point PCCAs can be. Thus, a higher boiling point liquid core would be needed, which could increase the vaporization threshold past the diagnostic limit.

The results indicate that CEUS can be performed using low boiling-point PCCAs, and that these agents have the potential to be valuable contrast agents for cancer diagnosis and assessment of response to therapy, but substantial modifications to the formulation are required for effective *in vivo* use.

BIBLIOGRAPHY

1. American Cancer Society. Cancer Facts and Figures 2017. American Cancer Society. 2017.
2. Vasudev NS, Goh V, Juttla JK, Thompson VL, Larkin JMG, Gore M, et al. Changes in tumour vessel density upon treatment with anti-angiogenic agents: Relationship with response and resistance to therapy. *Br J Cancer*. 2013;109:1230–42.
3. Smith AD, Shah SN, Rini BI, Lieber ML, Remer EM. Morphology, Attenuation, Size, and Structure (MASS) criteria: Assessing response and predicting clinical outcome in metastatic renal cell carcinoma on antiangiogenic targeted therapy. *Am J Roentgenol*. 2010;194:1470–8.
4. Therasse P, Arbuck SG, Eisenhauer EA, Wanders J, Kaplan RS, Rubinstein L, et al. New Guidelines to Evaluate the Response to Treatment. *J Natl Cancer Inst*. 2000;92(3):205–16.
5. Mazumdar M, Smith A, Schwartz LH. A statistical simulation study finds discordance between WHO criteria and RECIST guideline. *J Clin Epidemiol*. 2004;57:358–65.
6. Prior JO, Montemurro M, Orcurto M-V, Michielin O, Luthi F, Benhattar J, et al. Early Prediction of Response to Sunitinib After Imatinib Failure by 18F-Fluorodeoxyglucose Positron Emission Tomography in Patients With Gastrointestinal Stromal Tumor. *J Clin Oncol*. 2009;27(3):439–45.
7. Benjamin RS, Choi H, Macapinlac HA, Burgess MA, Patel SR, Chen LL, et al. We should desist using RECIST, at least in GIST. *J Clin Oncol*. 2007;25(13):1760–4.
8. Yang JC, Haworth L, Sherry RM, Hwu P, Schwartzentruber DJ, Topalian SL, et al. A Randomized Trial of Bevacizumab, an Anti-Vasucular Endothelial Growth Factor Antibody, for Metastatic Renal Cancer. *N Engl J Med*. 2003;349(5):427–34.
9. Escudier B, Eisen T, Stadler WM, Szczylik C, Oudard S, Siebels M, et al. Sorafenib in Advanced Clear-Cell Renal-Cell Carcinoma. *N Engl J Med*. 2007;356(2):125–34.
10. Choi H, Charnsangavej C, Faria SC, Macapinlac HA, Burgess MA, Patel SR, et al. Correlation of Computed Tomography and Positron Emission Tomography in Patients With Metastatic Gastrointestinal Stromal Tumor Treated at a Single Institution With Imatinib Mesylate : Proposal of New Computed Tomography Response Criteria. *J Clin Oncol*. 2007;25(13):1753–9.
11. Lamuraglia M, Escudier B, Chami L, Schwartz B, Leclere J, Roche A, et al. To predict progression-free survival and overall survival in metastatic renal cancer treated with sorafenib: Pilot study using dynamic contrast-enhanced Doppler ultrasound. *Eur J Cancer*. 2006;42(15):2472–9.
12. Smith AD, Lieber ML, Shah SN. Assessing tumor response and detecting recurrence in metastatic renal cell carcinoma on targeted therapy: Importance of size and attenuation on contrast-enhanced CT. *Am J Roentgenol*. 2010;194:157–65.
13. Yu JL, Rak JW, Coomber BL, Hicklin DJ, Kerbel RS. Effect of p53 status on tumor response to antiangiogenic therapy. *Science (80-)*. 2002;295(5559):1526–8.

14. Hlatky L, Hahnfeldt P, Folkman J. Clinical application of antiangiogenic therapy: Microvessel density, what it does and doesn't tell us. *J Natl Cancer Inst.* 2002;94(12):883–93.
15. Morgan B, Thomas AL, Dreves J, Henning J, Buchert M, Jivan A, et al. Dynamic Contrast-Enhanced Magnetic Resonance Imaging As a Biomarker for the Pharmacological Response of PTK787/ZK 222584, an Inhibitor of the Vascular Endothelial Growth Factor Receptor Tyrosine Kinases, in Patients With Advanced Colorectal Cancer and Liv. *J Clin Oncol.* 2003;21:3955–64.
16. Wieder HA, Brucher BLDM, Zimmermann F, Becker K, Lordick F, Beer A, et al. Time course of tumor metabolic activity during chemoradiotherapy of esophageal squamous cell carcinoma and response of treatment. *J Clin Oncol.* 2004;22(5):900–8.
17. Nathan PD, Vinayan A, Stott D, Juttla J, Goh V. CT response assessment combining reduction in both size and arterial phase density correlates with time to progression in metastatic renal cancer patients treated with targeted therapies. *Cancer Biol Ther.* 2010;9(1):14–9.
18. Stroobants S, Goeminne J, Seegers M, Dimitrijevic S, Dupont P, Nuyts J, et al. 18FDG-Positron emission tomography for the early prediction of response in advanced soft tissue sarcoma treated with imatinib mesylate (Gleevec®). *Eur J Cancer.* 2003;39(14):2012–20.
19. Zerizer I, Al-Nahhas A, Towey D, Tait P, Ariff B, Wasan H, et al. The role of early 18F-FDG PET/CT in prediction of progression-free survival after 90Y radioembolization: Comparison with RECIST and tumour density criteria. *Eur J Nucl Med Mol Imaging.* 2012;39:1391–9.
20. Frampas E, Lassau N, Zappa M, Vullierme M-P, Koscielny S, Vilgrain V. Advanced Hepatocellular Carcinoma: Early evaluation of response to targeted therapy and prognostic value of Perfusion CT and Dynamic Contrast Enhanced-Ultrasound. Preliminary results. *Eur J Radiol.* 2013;82:205–11.
21. Sodickson A, Baeyens PF, Andriole KP, Prevedello LM, Nawfel RD, Hanson R, et al. Recurrent CT, Cumulative Radiation Exposure, and Associated Radiation-induced Cancer Risks from CT of Adults. *Radiology.* 2009;251(1):175–84.
22. Husband JE, Schwartz LH, Spencer J, Ollivier L, King DM, Johnson R, et al. Evaluation of the response to treatment of solid tumours - a consensus statement of the International Cancer Imaging Society. *Br J Cancer.* 2004;90(12):2256–60.
23. Thomsen HS, Morcos SK. Risk of contrast-medium-induced nephropathy in high-risk patients undergoing MDCT - A pooled analysis of two randomized trials. *Eur Radiol.* 2009;19(4):891–7.
24. Marckmann P, Skov L, Rossen K, Dupont A, Damholt MB, Heaf JG, et al. Nephrogenic Systemic Fibrosis: Suspected Causative Role of Gadodiamide Used for Contrast-Enhanced Magnetic Resonance Imaging. *J Am Soc Nephrol.* 2006;17:2359–62.
25. Hasebroock KM, Serkova NJ. Toxicity of MRI and CT contrast agents. *Expert Opin Drug Metab Toxicol.* 2009;5(4):403–16.
26. Abdelmoneim SS, Bernier M, Scott CG, Dhoble A, Ness SAC, Hagen ME, et al. Safety of Contrast Agent Use During Stress Echocardiography. A 4-Year Experience From a Single-

- Center Cohort Study of 26,774 Patients. *JACC Cardiovasc Imaging*. 2009;2(9):1048–56.
27. Dolan MS, Gala SS, Dodla S, Abdelmoneim SS, Xie F, Cloutier D, et al. Safety and Efficacy of Commercially Available Ultrasound Contrast Agents for Rest and Stress Echocardiography. A Multicenter Experience. *J Am Coll Cardiol*. 2009;53(1):32–8.
 28. Cox K, Weeks J, Mills P, Chalmers R, Devalia H, Fish D, et al. Contrast-Enhanced Ultrasound Biopsy of Sentinel Lymph Nodes in Patients with Breast Cancer: Implications for Axillary Metastases and Conservation. *Ann Surg Oncol*. 2016;23(1):58–64.
 29. Kasoji SK, Chang EH, Mullin LB, Chong WK, Rathmell WK, Dayton PA. A Pilot Clinical Study in Characterization of Malignant Renal Cell Carcinoma Subtype with Contrast-Enhanced Ultrasound. *Ultrason Imaging*. 2016;39(2):126–36.
 30. Willmann JK, Bonomo L, Carla Testa A, Rinaldi P, Rindi G, Valluru KS, et al. Ultrasound Molecular Imaging With BR55 in Patients With Breast and Ovarian Lesions: First-in-Human Results. *J Clin Oncol*. 2017;35(19):2133–40.
 31. Smeenge M, Tranquart F, Mannaerts CK, de Reijke TM, van de Vijver MJ, Laguna MP, et al. First-in-Human Ultrasound Molecular Imaging With a VEGFR2-Specific Ultrasound Molecular Contrast Agent (BR55) in Prostate Cancer. *Invest Radiol*. 2017;52(7):419–27.
 32. Borden MA, Kruse DE, Caskey CF, Zhao S, Dayton PA, Ferrara KW. Influence of lipid shell physicochemical properties on ultrasound-induced microbubble destruction. *IEEE Trans Ultrason Ferroelectr Freq Control*. 2005;52(11):1992–2002.
 33. Hoarau D, Delmas P, David S, Roux E, Leroux JC. Novel long-circulating lipid nanocapsules. *Pharm Res*. 2004;21(10):1783–9.
 34. Dobrovolskaia M a, Aggarwal P, Hall JB, Mcneil SE. Preclinical studies to understand NP interaction with the immune system and its potential effects on NP biodistribution. *Mol Pharm*. 2009;5(4):487–95.
 35. Vonarbourg A, Passirani C, Saulnier P, Simard P, Leroux JC, Benoit JP. Evaluation of pegylated lipid nanocapsules versus complement system activation and macrophage uptake. *J Biomed Mater Res*. 2006;78(3):620–8.
 36. Chen CC, Borden MA. The role of poly(ethylene glycol) brush architecture in complement activation on targeted microbubble surfaces. *Biomaterials*. 2011;32(27):6579–87.
 37. Borden MA, Pu G, Runner GJ, Longo ML. Surface phase behavior and microstructure of lipid/PEG-emulsifier monolayer-coated microbubbles. *Colloids Surfaces B Biointerfaces*. 2004;35(3–4):209–23.
 38. Klibanov AL. Ligand-carrying gas-filled microbubbles: Ultrasound contrast agents for targeted molecular imaging. *Bioconjug Chem*. 2005;16(1):9–17.
 39. Rychak JJ, Lindner JR, Ley K, Klibanov AL. Deformable gas-filled microbubbles targeted to P-selectin. *J Control Release*. 2006;114(3):288–99.
 40. Gessner RC, Aylward SR, Dayton PA. Mapping Microvasculature with Acoustic Angiography

- Yields Quantifiable Differences between Healthy and in a Rodent Model. *Radiology*. 2012;264(3):733–40.
41. Whittingham TA. Contrast-Specific Imaging Techniques: Technical Perspective. *Contrast Media Ultrason*. 2005;43–70.
 42. Simpson DH, Chin CT, Burns PN. Pulse inversion Doppler: a new method for detecting nonlinear echoes from microbubble contrast agents. *IEEE Trans Ultrason Ferroelectr Freq Control*. 1999 Jan;46(2):372–82.
 43. Eckersley RJ, Chin CT, Burns PN. Optimizing phase and amplitude modulation schemes for imaging microbubble contrast agents at low acoustic power. *Ultrasound Med Biol*. 2005 Feb [cited 2014 Jul 18];31(2):213–9.
 44. Lindner JR. Molecular imaging of cardiovascular disease with contrast-enhanced ultrasonography. *Nat Rev Cardiol*. 2009 Jul [cited 2014 Jul 18];6(7):475–81.
 45. Christiansen JP, Leong-Poi H, Klibanov AL, Kaul S, Lindner JR. Noninvasive imaging of myocardial reperfusion injury using leukocyte-targeted contrast echocardiography. *Circulation*. 2002;105(15):1764–7.
 46. Kaufmann BA, Sanders JM, Davis C, Xie A, Aldred P, Sarembock IJ, et al. Molecular imaging of inflammation in atherosclerosis with targeted ultrasound detection of vascular cell adhesion molecule-1. *Circulation*. 2007;116(3):276–84.
 47. Bachmann C, Klibanov AL, Olson TS, Sonnenschein JR, Rivera-Nieves J, Cominelli F, et al. Targeting mucosal addressin cellular adhesion molecule (MAdCAM)-1 to noninvasively image experimental Crohn's disease. *Gastroenterology*. 2006;130(1):8–16.
 48. Tlaxca JL, Rychak JJ, Ernst PB, Konkalmatt PR, Shevchenko TI, Pizzaro TT, et al. Ultrasound-based molecular imaging and specific gene delivery to mesenteric vasculature by endothelial adhesion molecule targeted microbubbles in a mouse model of Crohn's disease. *J Control Release*. 2013;165(3):216–25.
 49. Rychak JJ, Graba J, Cheung AMY, Mystry BS, Lindner JR, Kerbel RS, et al. Microultrasound molecular imaging of vascular endothelial growth factor receptor 2 in a mouse model of tumor angiogenesis. *Mol Imaging*. 2007;6(5):289–96.
 50. Bzyl J, Lederle W, Rix A, Grouls C, Tardy I, Pochon S, et al. Molecular and functional ultrasound imaging in differently aggressive breast cancer xenografts using two novel ultrasound contrast agents (BR55 and BR38). *Eur Radiol*. 2011;21(9):1988–95.
 51. Leguerney I, Scoazec J-Y, Gadot N, Robin N, Pénault-Llorca F, Victorin S, et al. Molecular ultrasound imaging using contrast agents targeting endoglin, vascular endothelial growth factor receptor 2 and integrin. *Ultrasound Med Biol*. 2015;41(1):197–207.
 52. Stieger SM, Dayton PA, Borden MA, Caskey CF, Griffey SM, Wisner ER, et al. Imaging of angiogenesis using Cadence contrast pulse sequencing and targeted contrast agents. *Contrast Media Mol Imaging*. [cited 2014 Jul 18];3(1):9–18.
 53. Beer AJ, Schwaiger M. Imaging of integrin $\alpha V\beta 3$ expression. *Cancer Metastasis Rev*. 2008 Dec

[cited 2014 Jul 18];27(4):631–44.

54. Anderson CR, Hu X, Tlaxca J, Houghtaling R, Sharma K, Lawrence M, et al. Ultrasound Molecular Imaging of Tumor Angiogenesis with an Integrin Targeted Microbubble Contrast Agent. *Invest Radiol.* 2011;46(4):215–24.
55. Anderson CR, Rychak J, Backer M, Backer J, Ley K, Klibanov A. scVEGF Microbubble Ultrasound Contrast Agents: A Novel Probe for Ultrasound Molecular Imaging of Tumor Angiogenesis. *Invest Radial.* 2010;45(10):579–85.
56. Kogan P, Johnson KA, Feingold S, Garrett N, Guracar I, Arendshorst WJ, et al. Validation of dynamic contrast-enhanced ultrasound in rodent kidneys as an absolute quantitative method for measuring blood perfusion. *Ultrasound Med Biol.* 2011 Jun;37(6):900–8.
57. Roberts VHJ, Lo JO, Salati JA, Ba KSL, Lindner JR, Morgan TK, et al. Quantitative assessment of placental perfusion by contrast-enhanced ultrasound in macaques and human subjects. *Am J Obstet Gynecol.* 2016;214(3):214–369.
58. Feingold S, Gessner R, Guracar IM, Dayton PA. Quantitative Volumetric Perfusion Mapping of The Microvasculature Using Contrast Ultrasound. *Invest Radiol.* 2010;45(10).
59. Senior R, Monaghan M, Main ML, Zamorano JL, Tiemann K, Agati L, et al. Detection of coronary artery disease with perfusion stress echocardiography using a novel ultrasound imaging agent: Two Phase 3 international trials in comparison with radionuclide perfusion imaging. *Eur J Echocardiogr.* 2009;10(1):26–35.
60. Porter TR, Xie F. Myocardial Perfusion Imaging With Contrast Ultrasound. *JACC Cardiovasc Imaging.* 2010;3(2):176–87.
61. Martina AD. Ultrasound Contrast Agents for Brain Perfusion Imaging and Ischemic Stroke Therapy. *J Neuroimaging.* 2005;15(3):217–32.
62. Meyer-Wiethe K, Cangür H, Schindler A, Koch C, Seidel G. Ultrasound Perfusion Imaging: Determination of Thresholds for the Identification of Critically Disturbed Perfusion in Acute Ischemic Stroke-A Pilot Study. *Ultrasound Med Biol.* 2007;33(6):851–6.
63. Wiesmann M, Meyer K, Albers T, Seidel G. Parametric Perfusion Imaging with Contrast-Enhanced Ultrasound in Acute Ischemic Stroke. *Stroke.* 2004;35(2):508–13.
64. Chang EH, Chong WK, Kasoji SK, Dayton PA, Rathmell WK. Management of Indeterminate Cystic Kidney Lesions: Review of Contrast-enhanced Ultrasound as a Diagnostic Tool. *Urology.* 2016;87:1–10.
65. Smeenge M, Mischi M, Laguna Pes MP, de la Rosette JJMCH, Wijkstra H. Novel contrast-enhanced ultrasound imaging in prostate cancer. *World J Urol.* 2011;29(5):581–7.
66. Lassau N, Chami L, Benatsou B, Peronneau P, Roche A. Dynamic contrast-enhanced ultrasonography (DCE-US) with quantification of tumor perfusion: A new diagnostic tool to evaluate the early effects of antiangiogenic treatment. *Eur Radiol Suppl.* 2007;17(SUPPL. 6):89–98.

67. Streeter JE, Gessner RC, Tsuruta J, Feingold S, Dayton PA. Assessment of Molecular Imaging of Angiogenesis with Three-Dimensional Ultrasonography. *Mol Imaging*. 2013;10(6):460–8.
68. Chomas JE, Pollard RE, Sadlowski AR, Griffey SM, Wisner ER, Ferrara KW. Contrast-enhanced US of microcirculation of superficially implanted tumors in rats. *Radiology*. 2003;229(2):439–46.
69. Gessner RC, Frederick CB, Foster FS, Dayton PA. Acoustic angiography: A new imaging modality for assessing microvasculature architecture. *Int J Biomed Imaging*. 2013;
70. Bouakaz a., Frigstad S, Ten Cate FJ, de Jong N. Super harmonic imaging: A new imaging technique for improved contrast detection. *Ultrasound Med Biol*. 2002;28(1):59–68.
71. Kruse DE, Ferrara KW. A new imaging strategy using wideband transient response of ultrasound contrast agents. *IEEE Trans Ultrason Ferroelectr Freq Control*. 2005;52(8):1320–9.
72. Shelton SE, Lee YZ, Lee M, Cherin E, Foster FS, Aylward SR, et al. Quantification of Microvascular Tortuosity during Tumor Evolution Using Acoustic Angiography. *Ultrasound Med Biol*. 2015;41(7):1896–904.
73. Rao SR, Shelton SE, Dayton PA. The “fingerprint” of cancer extends beyond solid tumor boundaries: assessment with a novel ultrasound imaging approach. *IEEE Trans Biomed Eng*. 2016;63(5):1082–6.
74. Kasoji SK, Rivera JN, Gessner RC, Chang SX, Dayton PA. Early assessment of tumor response to radiation therapy using high-resolution quantitative microvascular ultrasound imaging. *Theranostics*. 2018;8(1):156–68.
75. Lindsey BD, Shelton SE, Martin KH, Ozgun KA, Rojas JD, Foster FS, et al. High Resolution Ultrasound Superharmonic Perfusion Imaging: In Vivo Feasibility and Quantification of Dynamic Contrast-Enhanced Acoustic Angiography. *Ann Biomed Eng*. 2016;
76. Potente M, Gerhardt H, Carmeliet P. Basic and therapeutic aspects of angiogenesis. *Cell*. 2011;146(6):873–87.
77. Carmeliet P, Jain RK. Molecular mechanisms and clinical applications of angiogenesis. *Nature*. 2011;473:298–307.
78. Jain RK. Normalization of Tumor Vasculature: An Emerging Concept in Antiangiogenic Therapy. *Science* (80-). 2005;307:58–62.
79. Li C, Shan S, Braun RD, Dewhirst MW. Initial Stages of Tumor Cell-Induced Angiogenesis: Evaluation Via Skin Window Chambers in Rodent Models. *J Natl Cancer Inst*. 2000;92(2):143–7.
80. Pysz MA, Machtaler SB, Seeley ES, Lee JJ, Brentnall TA, Rosenberg J, et al. Vascular endothelial growth factor receptor type 2-targeted contrast-enhanced US of pancreatic cancer neovasculature in a genetically engineered mouse model: potential for earlier detection. *Radiology*. 2015;274(3):790–9.
81. Baron Toaldo M, Salvatore V, Marinelli S, Palama C, Milazzo M, Croci L, et al. Use of VEGFR-

- 2 targeted ultrasound contrast agent for the early evaluation of response to sorafenib in a mouse model of hepatocellular carcinoma. *Mol Imaging Biol.* 2015;17(1):29–37.
82. Baetke SC, Rix A, Tranquart F, Schneider R, Lammers T, Kiessling F, et al. Squamous Cell Carcinoma Xenografts: Use of VEGFR2-targeted Microbubbles for Combined Functional and Molecular US to Monitor Antiangiogenic Therapy Effects. *Radiology.* 2016;278(2):430–40.
 83. Zhou J, Wang H, Zhang H, Lutz AM, Tian L, Hristov D, et al. VEGFR2-targeted three-dimensional ultrasound imaging can predict responses to antiangiogenic therapy in preclinical models of colon cancer. *Cancer Res.* 2016;76(14):4081–9.
 84. Wang H, Kaneko OF, Tian L, Hristov D, Willmann JK. Three-dimensional Ultrasound Molecular Imaging of Angiogenesis in Colon Cancer using a Clinical Matrix Array Ultrasound Transducer. *Invest Radiol.* 2015;50(5):322–9.
 85. Eschbach RS, Clevert D-A, Hirner-Eppeneder H, Ingrisch M, Moser M, Schuster J, et al. Contrast-Enhanced Ultrasound with VEGFR2-Targeted Microbubbles for Monitoring Regorafenib Therapy Effects in Experimental Colorectal Adenocarcinomas in Rats with DCE-MRI and Immunohistochemical Validation. *PLoS One.* 2017;12(1):1–22.
 86. Wang H, Lutz AM, Hristov D, Tian L, Willmann JK. Intra-animal Comparison between Three-dimensional Molecularly Targeted US and Three-dimensional Dynamic Contrast-enhanced US for Early Antiangiogenic Treatment Assessment in Colon Cancer. *Radiology.* 2017;(2):443–52.
 87. Streeter. A Comparative Evaluation of Ultrasound Molecular Imaging, Perfusion Imaging, and Volume Measurements in Evaluating Response to Therapy in Patient-Derived Xenografts. *Technol Cancer Res Treat.* 2013;12(4).
 88. Sirsi SR, Flexman ML, Vlachos F, Huang J, Hernandez SL, Kim HK, et al. Contrast Ultrasound Imaging for Identification of Early Responder Tumor Models to Anti-Angiogenic Therapy. *Ultrasound Med Biol.* 2012;38(6):1019–29.
 89. Zhou J, Zhang H, Wang H, Lutz AM, El Kaffas A, Tian L, et al. Early prediction of tumor response to bevacizumab treatment in murine colon cancer models using three-dimensional dynamic contrast-enhanced ultrasound imaging. *Angiogenesis.* 2017;20:547–55.
 90. Lassau N, Koscielny S, Chami L, Chebil M, Benatsou B, Roche A, et al. Advanced Hepatocellular Carcinoma : Early Evaluation of Response to Bevacizumab Therapy at Dynamic Contrast-enhanced US with Quantification-Preliminary Results. *Radiology.* 2011;258(1):291–300.
 91. Lassau N, Koscielny S, Albiges L, Chami L, Benatsou B, Chebil M, et al. Metastatic renal cell carcinoma treated with sunitinib: Early evaluation of treatment response using dynamic contrast-enhanced ultrasonography. *Clin Cancer Res.* 2010;16(4):1216–25.
 92. Lassau N, Chami L, Koscielny S, Chebil M, Massard C, Benatsou B, et al. Quantitative functional imaging by Dynamic Contrast Enhanced Ultrasonography (DCE-US) in GIST patients treated with masatinib. *Invest New Drugs.* 2012;30(2):765–71.
 93. Zocco MA, Garcovich M, Lupascu A, Di Stasio E, Roccarina D, Annicchiarico BE, et al. Early prediction of response to sorafenib in patients with advanced hepatocellular carcinoma: The role

- of dynamic contrast enhanced ultrasound. *J Hepatol.* 2013;59(5):1014–21.
94. Kripfgans OD, Fowlkes JB, Woydt M, Eldevik OP, Carson PL. In vivo droplet vaporization for occlusion therapy and phase aberration correction. *IEEE Trans Ultrason Ferroelectr Freq Control.* 2002;49(6):726–38.
 95. Samuel S, Duprey A, Fabiilli ML, Bull JL, Brian Fowlkes J. In Vivo Microscopy of Targeted Vessel Occlusion Employing Acoustic Droplet Vaporization. *Microcirculation.* 2012;19(6):501–9.
 96. Kripfgans OD, Orifici CM, Carson PL, Ives KA, Eldevik OP, Fowlkes JB. Acoustic droplet vaporization for temporal and spatial control of tissue occlusion: A kidney study. *IEEE Trans Ultrason Ferroelectr Freq Control.* 2005;52(7):1101–8.
 97. Miller DL, Kripfgans OD, Carson PL. Cavitation nucleation agents for nonthermal ultrasound therapy. *J Acoust Soc Am.* 2000;107(6):3480–6.
 98. Kripfgans OD, Zhang M, Fabiilli ML, Carson PL, Padilla F, Swanson SD, et al. Acceleration of ultrasound thermal therapy by patterned acoustic droplet vaporization. *J Acoust Soc Am.* 2014;135(January 2014):537–44.
 99. Zhu M, Jiang L, Fabiilli ML, Zhang A, Fowlkes JB, Xu LX. Treatment of murine tumors using acoustic droplet vaporization-enhanced high intensity focused ultrasound. *Phys Med Biol.* 2013;58(17):6179.
 100. Zhang P, Kopechek JA, Porter TM. The impact of vaporized nanoemulsions on ultrasound-mediated ablation. *J Ther ultrasound.* 2013;1(2):1–13.
 101. Kripfgans OD, Fowlkes JB, Miller DL, Eldevik OP, Carson PL. Acoustic Droplet Vaporization for Therapeutic and Diagnostic Applications. *Ultrasound Med Biol.* 2000;26(7):1177–89.
 102. Haworth KJ, Fowlkes JB, Carson PL, Kripfgans OD. Towards Aberration Correction of Transcranial Ultrasound Using Acoustic Droplet Vaporization. *Ultrasound Med Biol.* 2008;34(3):435–45.
 103. Wong ZZ, Kripfgans OD, Qamar A, Fowlkes JB, Bull JL. Bubble evolution in acoustic droplet vaporization at physiological temperature via ultra-high speed imaging. *Soft Matter.* 2011;7(8):4009.
 104. Reznik N, Shpak O, Gelderblom EC, Williams R, De Jong N, Versluis M, et al. The efficiency and stability of bubble formation by acoustic vaporization of submicron perfluorocarbon droplets. *Ultrasonics.* 2013;53(7):1368–76.
 105. Haworth KJ, Kripfgans OD. Initial growth and coalescence of acoustically vaporized perfluorocarbon microdroplets. *Proc - IEEE Ultrason Symp.* 2008;623–6.
 106. Qamar A, Wong ZZ, Fowlkes JB, Bull JL. Dynamics of acoustic droplet vaporization in gas embolotherapy. *Appl Phys Lett.* 2010;96(14).
 107. Li DS, Kripfgans OD, Fabiilli ML, Brian Fowlkes J, Bull JL. Initial nucleation site formation due to acoustic droplet vaporization. *Appl Phys Lett.* 2014;104(6):1–5.

108. Kripfgans OD, Fabiilli ML, Carson PL, Fowlkes JB. On the acoustic vaporization of micrometer-sized droplets. *J Acoust Soc Am*. 2004;116(1):272–81.
109. Shpak O, Verweij M, Vos HJ, de Jong N, Lohse D, Versluis M. Acoustic droplet vaporization is initiated by superharmonic focusing. *Proc Natl Acad Sci*. 2014;111(5):1697–702.
110. Fabiilli ML, Member S, Haworth KJ, Fakhri NH, Kripfgans OD, Carson PL, et al. The Role of Inertial Cavitation in Acoustic Droplet Vaporization. *IEEE Trans Ultrason Ferroelectr Freq Control*. 2009;56(5):1006–17.
111. Li DS, Kripfgans OD, Fabiilli ML, Brian Fowlkes J, Bull JL. Initial nucleation site formation due to acoustic droplet vaporization. *Appl Phys Lett*. 2014;104(6):6–10.
112. Christopher, Brennen E. Cavitation and bubble dynamics [Internet]. *Annual Review of Fluid Mechanics*. New York: University of Oxford Press, Inc.; 1995.
113. Dewhurst MW, Viglianti BL, Lora-Michiels M, Hanson M, Hoopes PJ. Basic principles of thermal dosimetry and thermal thresholds for tissue damage from hyperthermia. *Int J Hyperth*. 2003;19(3):267–94.
114. ter Haar G, Coussios C. High intensity focused ultrasound: Physical principles and devices. *Int J Hyperth*. 2007;23(2):89–104.
115. Li J-J, Gu M-F, Luo G-Y, Liu L-Z, Zhang R, Xu G-L. Complications of High Intensity Focused Ultrasound for Patients with Hepatocellular Carcinoma. *Technol Cancer Res Treat*. 2009;8(3):217–24.
116. Tung YS, Liu HL, Wu CC, Ju KC, Chen WS, Lin WL. Contrast-agent-enhanced ultrasound thermal ablation. *Ultrasound Med Biol*. 2006;32(7):1103–10.
117. Phillips LC, Puett C, Sheeran PS, Wilson Miller G, Matsunaga TO, Dayton PA. Phase-shift perfluorocarbon agents enhance high intensity focused ultrasound thermal delivery with reduced near-field heating. *J Acoust Soc Am*. 2013;134(2):1473–82.
118. Kopechek J a, Park E-J, Zhang Y-Z, Vykhodtseva NI, McDannold NJ, Porter TM. Cavitation-enhanced MR-guided focused ultrasound ablation of rabbit tumors in vivo using phase shift nanoemulsions. *Phys Med Biol*. 2014;59(13):3465–81.
119. Fix SM, Novell A, Yun Y, Dayton PA, Arena CB. An evaluation of the sonoporation potential of low-boiling point phase-change ultrasound contrast agents in vitro. *J Ther Ultrasound*. 2017;5(1):7.
120. Maeda H, Wu J, Sawa T, Matsumura Y, Hori K. Tumor vascular permeability and the EPR effect in macromolecular therapeutics: a review. *J Control Release*. 2000 Mar 1;65(1–2):271–84.
121. Danhier F, Ansorena E, Silva JM, Coco R, Le Breton A, Préat V. PLGA-based nanoparticles: An overview of biomedical applications. *J Control Release*. 2012;161(2):505–22.
122. Yuan F, Dellian M, Fukumura D, Leunig M, Berk DA, Torchilin VP, et al. Vascular Permeability in a Human Tumor Xenograft: Molecular Size Dependence and Cutoff Size.

Cancer Res. 1995;55:3752–7.

123. Rapoport N, Nam K-H, Gupta R, Gao Z, Mohan P, Payne A, et al. Ultrasound-mediated tumor imaging and nanotherapy using drug loaded, block copolymer stabilized perfluorocarbon nanoemulsions. *J Control Release*. 2011 Jul 15;153(1):4–15.
124. Fabiilli ML, Haworth KJ, Sebastian IE, Kripfgans OD, Carson PL, Fowlkes JB. Delivery of chlorambucil using an acoustically-triggered perfluoropentane emulsion. *Ultrasound Med Biol*. 2010;36(8):1364–75.
125. Rapoport N, Payne A, Dillon C, Shea J, Scaife C, Gupta R. Focused ultrasound-mediated drug delivery to pancreatic cancer in a mouse model. *J Ther ultrasound*. 2013;1:1–12.
126. Sheeran PS, Streeter JE, Mullin LB, Matsunaga TO, Dayton PA. Toward ultrasound molecular imaging with phase-change contrast agents: an in vitro proof of principle. *Ultrasound Med Biol*. 2013 May [cited 2014 Jul 18];39(5):893–902.
127. Sheeran PS, Rojas JD, Puett C, Hjelmquist J, Arena CB, Dayton PA. Contrast-Enhanced Ultrasound Imaging and in Vivo Circulatory Kinetics with Low-Boiling-Point Nanoscale Phase-Change Perfluorocarbon Agents. *Ultrasound Med Biol*. 2015 Mar [cited 2015 Mar 3];41(3):814–31.
128. Sheeran PS, Wong VP, Luois S, McFarland RJ, Ross WD, Feingold S, et al. Decafluorobutane as a phase-change contrast agent for low-energy extravascular ultrasonic imaging. *Ultrasound Med Biol*. 2011 Sep [cited 2014 Jul 16];37(9):1518–30.
129. Sheeran PS, Luois S, Dayton PA, Matsunaga TO. Formulation and acoustic studies of a new phase-shift agent for diagnostic and therapeutic ultrasound. *Langmuir*. 2011 Sep 6;27(17):10412–20.
130. Sheeran PS, Matsunaga TO, Dayton PA. Phase-transition thresholds and vaporization phenomena for ultrasound phase-change nanoemulsions assessed via high-speed optical microscopy. *Phys Med Biol*. 2013 Jul 7 [cited 2014 Aug 30];58(13):4513–34.
131. Mountford PA, Thomas AN, Borden MA. Thermal Activation of Superheated Lipid-Coated Perfluorocarbon Drops. *Langmuir*. 2015;31:4627–34.
132. Mountford PA, Borden MA. On the thermodynamics and kinetics of superheated fluorocarbon phase-change agents. *Adv Colloid Interface Sci*. 2016;237:15–27.
133. Shpak O, Verweij M, Vos HJ, de Jong N, Lohse D, Versluis M. Acoustic droplet vaporization is initiated by superharmonic focusing. *Proc Natl Acad Sci U S A*. 2014;111(5):1697–702.
134. Sheeran PS, Luois SH, Mullin LB, Matsunaga TO, Dayton PA. Design of ultrasonically-activatable nanoparticles using low boiling point perfluorocarbons. *Biomaterials*. 2012 Apr [cited 2014 Jul 18];33(11):3262–9.
135. Mountford PA, Smith WS, Borden MA. Fluorocarbon Nanodrops as Acoustic Temperature Probes. *Langmuir*. 2015;150911170424004.
136. Reznik N, Seo M, Williams R, Bolewska-Pedyczak E, Lee M, Matsuura N, et al. Optical studies

- of vaporization and stability of fluorescently labelled perfluorocarbon droplets. *Phys Med Biol*. 2012;57(21):7205–17.
137. Sheeran PS, Matsunaga TO, Dayton PA. Phase change events of volatile liquid perfluorocarbon contrast agents produce unique acoustic signatures. *Phys Med Biol*. 2014 Jan 20 [cited 2014 Jul 18];59(2):379–401.
 138. Arena CB, Novell a N, Sheeran PS, Puett C, Moyer LC, Dayton PA. Dual Frequency Acoustic Droplet Vaporization Detection for Medical Imaging. *IEEE Trans Ultrason Ferroelectr Freq Control*. 2015;62(9):1623–33.
 139. Novell A, Arena CB, Oralkan O, Dayton PA. Wideband acoustic activation and detection of droplet vaporization events using a capacitive micromachined ultrasonic transducer. *J Acoust Soc Am*. 2016;139(6):3193–8.
 140. Mountford PA, Sirsi SR, Borden MA. Condensation phase diagrams for lipid-coated perfluorobutane microbubbles. *Langmuir*. 2014;30(21):6209–18.
 141. Reznik N, Williams R, Burns PN. Investigation of Vaporized Submicron Perfluorocarbon Droplets as an Ultrasound Contrast Agent. *Ultrasound Med Biol*. 2011;37(8):1271–9.
 142. Lin S, Zhang G, Leow CH, Tang M-X. Effects of microchannel confinement on acoustic vaporisation of ultrasound phase change contrast agents. *Phys Med Biol*. 2017;62:6884–98.
 143. Sheeran PS, Daghighi Y, Yoo K, Williams R, Cherin E, Foster FS, et al. Image-Guided Ultrasound Characterization of Volatile Sub-Micron Phase-Shift Droplets in the 20-40 MHz Frequency Range. *Ultrasound Med Biol*. 2015;42(3):795–807.
 144. Choudhury SA, Xie F, Dayton PA, Porter TR. Acoustic Behavior of a Reactivated, Commercially Available Ultrasound Contrast Agent. *J Am Soc Echocardiogr*. 2017;30:189–97.
 145. Nyankima AG, Rojas JD, Cianciolo R, Johnson KA, Dayton PA. In Vivo Assessment of the Potential for Renal Bio-Effects from the Vaporization of Perfluorocarbon Phase-Change Contrast Agents. *Ultrasound Med Biol*. 2018;44(2):368–76.
 146. Slamon DJ, Leyland-Jones B, Shak S, Fuchs H, Paton V, Bajamonde A, et al. Use of Chemotherapy Plus a Monoclonal Antibody Against HER2 for metastatic breast cancer that overexpresses HER2. *N Engl J Med*. 2001;344(11):783–92.
 147. Weber WA. Assessing Tumor Response to Therapy. *J Nucl Med*. 2009;50(Suppl_1):1S–10S.
 148. Vogel CL, Cobleigh MA, Tripathy D, Gutheil JC, Harris LN, Fehrenbacher L, et al. Efficacy and Safety of Trastuzumab as a Single Agent in First-Line Treatment of *HER2* -Overexpressing Metastatic Breast Cancer. *J Clin Oncol*. 2002;20(3):719–26.
 149. Lewis Phillips GD, Li G, Dugger DL, Crocker LM, Parsons KL, Mai E, et al. Targeting *HER2*-positive breast cancer with trastuzumab-DM1, an antibody-cytotoxic drug conjugate. *Cancer Res*. 2008;68(22):9280–90.
 150. Kim WY, Kaelin WG. Molecular Pathways in Renal Cell Carcinoma-Rationale for Targeted Treatment. *Semin Oncol*. 2006;33(5):588–95.

151. Creighton, Morgan, Gunaratne, Wheeler, Gibbs, Gordon Robertson, et al. Comprehensive molecular characterization of clear cell renal cell carcinoma. *Nature*. 2013;499(7456):43–9.
152. Rini BI, Flaherty K. Clinical effect and future considerations for molecularly-targeted therapy in renal cell carcinoma. *Urol Oncol*. 2008;26(5):543–9.
153. Motzer RJ, Michaelson MD, Redman BG, Hudes GR, Wilding G, Figlin RA, et al. Activity of SU11248, a multitargeted inhibitor of vascular endothelial growth factor receptor and platelet-derived growth factor receptor, in patients with metastatic renal cell carcinoma. *J Clin Oncol*. 2006;24(1):16–24.
154. Cook KM, Figg WD. Angiogenesis inhibitors: current strategies and future prospects. *CA Cancer J Clin*. 2010;60(4):222–243.
155. Gan HK, Seruga B, Knox JJ. Sunitinib in solid tumors. *Expert Opin Investig Drugs*. 2009;18(6):821–34.
156. Bergers G, Hanahan D. Modes of resistance to anti-angiogenic therapy. *Nat Rev Cancer*. 2008 Aug;8(8):592–603.
157. Rini BI, Atkins MB. Resistance to targeted therapy in renal-cell carcinoma. *Lancet Oncol*. 2009;10(10):992–1000.
158. Motzer RJ, Hutson TE, Tomczak P, Michaelson MD, Bukowski RM, Oudard S, et al. Overall survival and updated results for sunitinib compared with interferon alfa in patients with metastatic renal cell carcinoma. *J Clin Oncol*. 2009;27(22):3584–90.
159. Chappell JC, Mouillesseaux KP, Bautch VL. Flt-1 (vascular endothelial growth factor receptor-1) is essential for the vascular endothelial growth factor-notch feedback loop during angiogenesis. *Arterioscler Thromb Vasc Biol*. 2013;33(8):1952–9.
160. Hellström M, Phng L-K, Hofmann JJ, Wallgard E, Coultas L, Lindblom P, et al. Dll4 signalling through Notch1 regulates formation of tip cells during angiogenesis. *Nature*. 2007;445(7129):776–80.
161. Chappell JC, Wiley DM, Bautch VL. Regulation of blood vessel sprouting. *Semin Cell Dev Biol*. 2011;22(9):1005–11.
162. Kushner EJ, Bautch VL. Building blood vessels in development and disease. *Curr Opin Hematol*. 2013;20(3):231–6.
163. Kuhnert F, Kirshner JR, Thurston G. Dll4-Notch signaling as a therapeutic target in tumor angiogenesis. *Vasc Cell*. 2011;3(1):20.
164. Ridgway J, Zhang G, Wu Y, Stawicki S, Liang W-C, Chanthery Y, et al. Inhibition of Dll4 signalling inhibits tumour growth by deregulating angiogenesis. *Nature*. 2006;444:1083–7.
165. Noguera-Troise I, Daly C, Papadopoulos NJ, Coetzee S, Boland P, Gale NW, et al. Blockade of Dll4 inhibits tumour growth by promoting non-productive angiogenesis. *Nature*. 2006;444(7122):1032–7.

166. Miles KM, Seshadri M, Ciamporcero E, Adelaiye R, Gillard B, Sotomayor P, et al. Dll4 Blockade Potentiates the Anti-Tumor Effects of VEGF Inhibition in Renal Cell Carcinoma Patient-Derived Xenografts. *PLoS One*. 2014;9(11):e112371.
167. Yuan B, Rychak J. Tumor functional and molecular imaging utilizing ultrasound and ultrasound-mediated optical techniques. *Am J Pathol*. 2013;182(2):305–11.
168. Wei S, Fu N, Sun Y, Yang Z, Lei L, Huang P, et al. Targeted contrast-enhanced ultrasound imaging of angiogenesis in an orthotopic mouse tumor model of renal carcinoma. *Ultrasound Med Biol*. 2014;40(6):1250–9.
169. Safran M, Kim WY, O'Connell F, Flippin L, Günzler V, Horner JW, et al. Mouse model for noninvasive imaging of HIF prolyl hydroxylase activity: assessment of an oral agent that stimulates erythropoietin production. *Proc Natl Acad Sci U S A*. 2006;103(1):105–10.
170. Rathmell WK, Hickey MM, Bezman NA, Chmielecki CA, Carraway NC, Simon MC. In vitro and in vivo models analyzing von Hippel-Lindau disease-specific mutations. *Cancer Res*. 2004;64:8595–603.
171. Gessner R, Lukacs M, Lee M, Cherin E, Foster FS, Dayton PA. High-Resolution, High-Contrast Ultrasound Imaging Using a Prototype Dual-Frequency Transducer: In Vitro and In Vivo Studies. *IEEE Trans Ultrason Ferroelectr Freq Control*. 2010;57(8):1772–81.
172. Aylward SR, Bullitt E. Initialization, noise, singularities, and scale in height ridge traversal for tubular object centerline extraction. *IEEE Trans Med Imaging*. 2002;21(2):61–75.
173. Bullitt E, Gerig G, Pizer SM, Lin W, Aylward SR. Measuring tortuosity of the intracerebral vasculature from MRA images. *IEEE Trans Med Imaging*. 2003 Sep;22(9):1163–71.
174. Abramoff MD, Magalhães PJ, Ram SJ. Image processing with ImageJ. *Biophotonics Int*. 2004;11(7):36–43.
175. Kalén M, Heikura T, Karvinen H, Nitzsche A, Weber H, Esser N, et al. Gamma-secretase inhibitor treatment promotes VEGF-A-driven blood vessel growth and vascular leakage but disrupts neovascular perfusion. *PLoS One*. 2011;6(4).
176. Chauhan VP, Stylianopoulos T, Martin JD, Popović Z, Chen O, Kamoun WS, et al. Normalization of tumour blood vessels improves the delivery of nanomedicines in a size-dependent manner. *Nat Nanotechnol*. 2012;7(6):383–8.
177. Jain RK. Normalizing tumor microenvironment to treat cancer: bench to bedside to biomarkers. *J Clin Oncol*. 2013;31(17):2205–18.
178. Jain BRK. Taming Vessels to Treat Cancer. *Sci Am*. 2008;18:64–71.
179. Batchelor TT, Gerstner ER, Emblem KE, Duda DG, Kalpathy-Cramer J, Snuderl M, et al. Improved tumor oxygenation and survival in glioblastoma patients who show increased blood perfusion after cediranib and chemoradiation. *Proc Natl Acad Sci U S A*. 2013;110(47):19059–64.
180. Sorensen AG, Emblem KE, Polaskova P, Jennings D, Kim H, Ancukiewicz M, et al. Increased

- survival of glioblastoma patients who respond to antiangiogenic therapy with elevated blood perfusion. *Cancer Res.* 2012;72(2):402–7.
181. Tong RT, Boucher Y, Kozin S V., Winkler F, Hicklin DJ, Jain RK. Vascular normalization by vascular endothelial growth factor receptor 2 blockade induces a pressure gradient across the vasculature and improves drug penetration in tumors. *Cancer Res.* 2004;64(11):3731–6.
 182. Rust MJ, Bates M, Zhuang X. Sub-diffraction-limit imaging by stochastic optical reconstruction microscopy (STORM). *Nat Methods.* 2006;3(10):793–5.
 183. Betzig E, Betzig E, Patterson GH, Sougrat R, Lindwasser OW, Olenych S, et al. Imaging Intracellular Fluorescent Proteins at Nanometer Resolution. *Science* (80-). 2006;313(2006):1642–6.
 184. Desailly Y, Couture O, Fink M, Tanter M. Sono-activated ultrasound localization microscopy. *Appl Phys Lett.* 2013;103(174107).
 185. Errico C, Pierre J, Pezet S, Desailly Y, Lenkei Z, Couture O, et al. Ultrafast ultrasound localization microscopy for deep super-resolution vascular imaging. *Nature.* 2015;527(7579):499–502.
 186. Lin F, Shelton SE, Espíndola D, Rojas JD, Pinton G, Dayton PA. 3-D Ultrasound Localization Microscopy for Identifying Microvascular Morphology Features of Tumor Angiogenesis at a Resolution Beyond the Diffraction Limit of Conventional Ultrasound. *Theranostics.* 2017;7(1):196–204.
 187. Rojas JD, Lin F, Chiang Y-C, Chytil A, Chong DC, Bauth VL, et al. Ultrasound Molecular Imaging of VEGFR-2 in clear-cell Renal Cell Carcinoma Tracks Disease Response to Antiangiogenic and Notch-Inhibition Therapy. *Theranostics.* 2018;8(1):141–55.
 188. Sheeran PS, Yoo K, Williams R, Daghighi Y, Cherin E. Image-guided characterization of phase-shift droplets at pre-clinical frequencies in vitro and in vivo. *IEEE Int Ultrason Symp Proceedings, IUS.* 2015;
 189. Montaldo G, Tanter M, Bercoff J, Benech N, Fink M. Coherent plane-wave compounding for very high frame rate ultrasonography and transient elastography. *IEEE Trans Ultrason Ferroelectr Freq Control.* 2009;56(3):489–506.
 190. Chen CC, Sheeran PS, Wu S-Y, Olumolade OO, Dayton PA, Konofagou EE. Targeted drug delivery with focused ultrasound-induced blood-brain barrier opening using acoustically-activated nanodroplets. *J Control Release.* 2013;172(3):795–804.
 191. Puett C, Sheeran PS, Rojas JD, Dayton PA. Pulse sequences for uniform perfluorocarbon droplet vaporization and ultrasound imaging. *Ultrasonics.* 2014;54(7):2024–33.
 192. Sheeran PS, Dayton PA. Phase-change contrast agents for imaging and therapy. *Curr Pharm Des.* 2012 Jan;18(15):2152–65.
 193. Matsunaga TO, Sheeran PS, Luois S, Streeter JE, Mullin LB, Banerjee B, et al. Phase-change nanoparticles using highly volatile perfluorocarbons: toward a platform for extravascular ultrasound imaging. *Theranostics.* 2012 Jan [cited 2014 Jul 18];2(12):1185–98.

194. Cobbold RSC. *Foundations of Biomedical Ultrasound*. New York: Oxford University Press; 2007. 76,329-380.
195. Hill CR, Bamber J, ter Haar G. *Physical Principles of Medical Ultrasonics*. Second. Hill CR, Bamber J, ter Haar G, editors. Wiley; 2004.
196. Rojas JD, Dayton PA. Optimizing acoustic activation of phase change contrast agents with the activation pressure matching method: A review. *IEEE Trans Ultrason Ferroelectr Freq Control*. 2017;64(1):264–72.
197. Evans DR, Parsons DF, Craig VS. Physical properties of phase-change emulsions. *Langmuir*. 2006/11/01. 2006;22(23):9538–45.
198. Apfel RE, Holland CK. Gauging the likelihood of cavitation from short-pulse, low-duty cycle diagnostic ultrasound. *Ultrasound Med Biol*. 2014 Aug;17(2):179–85.
199. Mast TD. Empirical relationships between acoustic parameters in human soft tissues. *Acoust Res Lett Online*. 2000;1:37.
200. Bamber JC. Ultrasonic Properties of Tissues. In: Duck FA, Baker AC, Starritt HC, editors. *Ultrasound in Medicine*. Boca Raton, FL: CRC Press/Taylor and Francis; 2002. p. 500.
201. Bamber JC. Attenuation and Absorption. In: Hill CR, Bamber JC, ter Haar GR, editors. *Physical Principles of Medical Ultrasonics*. New York, NY: John Wiley & Sons, Inc.; 2005. p. 528.
202. Shpak O, Stricker L, Versluis M, Lohse D. The role of gas in ultrasonically driven vapor bubble growth. *Phys Med Biol*. 2013;58(58):2523–35.
203. Wei K, Jayaweera AR, Firoozan S, Linka A, Skyba DM, Kaul S. Quantification of Myocardial Blood Flow With Ultrasound-Induced Destruction of Microbubbles Administered as a Constant Venous Infusion. *Circulation*. 1998;97(5):473–83.
204. Quaia E. Assessment of tissue perfusion by contrast-enhanced ultrasound. *Eur Radiol*. 2011;21:604–15.
205. Reznik N, Lajoinie G, Shpak O, Gelderblom EC, Williams R, de Jong N, et al. On the acoustic properties of vaporized submicron perfluorocarbon droplets. *Ultrasound Med Biol*. 2014;40(6):1379–84.
206. Puett C, Sheeran PS, Rojas JD, Dayton PA. Pulse sequences for uniform perfluorocarbon droplet vaporization and ultrasound imaging. *Ultrasonics*. 2014 Jun 6 [cited 2014 Jul 18];54:2024–33.
207. Mulvana H, Stride E, Hajnal J V., Eckersley RJ. Temperature dependent behavior of ultrasound contrast agents. *Ultrasound Med Biol*. 2010;36(6):925–34.
208. Mulvana H, Stride E, Tang M, Hajnal J V., Eckersley R. Temperature-Dependent Differences in the Nonlinear Acoustic Behavior of Ultrasound Contrast Agents Revealed by High-Speed Imaging and Bulk Acoustics. *Ultrasound Med Biol*. 2011;37(9):1509–17.
209. Zheng H, Mukdadi O, Shandas R. Physics in Medicine & Biology Related content Subharmonic generation from ultrasonic contrast agents. *Phys Med Biol*. 1999;44:681–94.

210. Chomas J, Dayton P, May D, Ferrara K. Nondestructive subharmonic imaging. *IEEE Trans Ultrason Ferroelectr Freq Control*. 2002;49(7):883–92.
211. Forsberg F, Shi WT, Goldberg BB. Subharmonic imaging of contrast agents. *Ultrasonics*. 2000;38:93–8.
212. Shankar PM, Krishna PD, Newhouse VL. Advantages of subharmonic over second harmonic backscatter for contrast- to-tissue echo enhancement. *Ultrasound Med Biol*. 1998;24(3):395–9.
213. Halldorsdottir VG, Dave JK, Eisenbrey JR, Machado P, Zhao H, Liu JB, et al. Subharmonic aided pressure estimation for monitoring interstitial fluid pressure in tumours - In vitro and in vivo proof of concept. *Ultrasonics*. 2014;54(7):1938–44.
214. Shi WT, Forsberg F, Raichlen JS, Needleman L, Goldberg BB. Pressure dependence of subharmonic signals from contrast microbubbles. *Ultrasound Med Biol*. 1999;25(2):275–83.
215. Dove JD, Mountford PA, Murray TW, Borden M a. Engineering optically triggered droplets for photoacoustic imaging and therapy. *Biomed Opt Express*. 2014;5(12):4417.
216. Mullin L, Gessner R, Kwan J, Kaya M, Borden MA, Dayton PA. Effect of anesthesia carrier gas on in vivo circulation times of ultrasound microbubble contrast agents in rats. *Contrast Media Mol Imaging*. 2011 [cited 2014 Jul 18];6(3):126–31.
217. Caskey CF, Kruse DE, Dayton PA, Kitano TK, Ferrara KW. Microbubble oscillation in tubes with diameters of 12, 25, and 195 microns. *Appl Phys Lett*. 2006;88:1–3.
218. Garbin V, Cojoc D, Ferrari E, Di Fabrizio E, Overvelde MLJ, Van Der Meer SM, et al. Changes in microbubble dynamics near a boundary revealed by combined optical micromanipulation and high-speed imaging. *Appl Phys Lett*. 2007;90(11).
219. Overvelde M, Garbin V, Dollet B, De Jong N, Lohse D, Versluis M. Dynamics of Coated Microbubbles Adherent to a Wall. *Ultrasound Med Biol*. 2011;37(9):1500–8.
220. Caskey CF, Stieger SM, Qin S, Dayton PA, Ferrara KW. Direct observations of ultrasound microbubble contrast agent interaction with the microvessel wall. *J Acoust Soc Am*. 2007;122(2):1191–200.
221. de Jong N, Hoff L, Skotland T, Bom N. Absorption and scatter of encapsulated gas filled microspheres: Theoretical considerations and some measurements. *Ultrasonics*. 1992;30(2):95–103.
222. Medwin H. Counting bubbles acoustically: a review. *Ultrasonics*. 1977;15(1):7–13.
223. Devin C. Survey of Thermal , Radiation , and Viscous Damping of Pulsating Air Bubbles in Water. *J Acoust Soc Am*. 1959;31(12):1654–67.
224. Helfield B, Black JJ, Qin B, Pacella J, Chen X, Villanueva FS. Fluid viscosity affects the fragmentation and inertial cavitation threshold of lipid encapsulated microbubbles. *Ultrasound Med Biol*. 2016;42(3):782–94.
225. Helfield B, Chen X, Qin B, Villanueva FS. Individual lipid encapsulated microbubble radial

- oscillations: Effects of fluid viscosity. *J Acoust Soc Am*. 2016;139(1):204–14.
226. Khismatullin DB. Resonance frequency of microbubbles: effect of viscosity. *J Acoust Soc Am*. 2004;116(3):1463–73.
 227. Goertz DE, de Jong N, van der Steen AFW. Attenuation and Size Distribution Measurements of Definity(TM) and Manipulated Definity(TM) Populations. *Ultrasound Med Biol*. 2007;33(9):1376–88.
 228. Evgenidis SP, Karapantsios TD. Effect of bubble size on void fraction fluctuations in dispersed bubble flows. *Int J Multiph Flow*. 2015;75:163–73.
 229. Baskurt OK, Meiselman HJ. Blood Rheology and Hemodynamics. *Semin Thromb Hemost*. 2003;29(5):435–50.
 230. Cerney LC, Cook FB, C. WC. Rheology of blood. *Am J Physiol*. 1962;202(6):1188–94.
 231. Zhao S, Ferrara KW, Dayton PA. Asymmetric oscillation of adherent targeted ultrasound contrast agents. *Appl Phys Lett*. 2005;87(13):1–3.
 232. Vos HJ, Dollet B, Bosch JG, Versluis M, de Jong N. Nonspherical Vibrations of Microbubbles in Contact with a Wall-A Pilot Study at Low Mechanical Index. *Ultrasound Med Biol*. 2008;34(4):685–8.
 233. Dollet B, van der Meer SM, Garbin V, de Jong N, Lohse D, Versluis M. Nonspherical Oscillations of Ultrasound Contrast Agent Microbubbles. *Ultrasound Med Biol*. 2008;34(9):1465–73.
 234. Vos HJ, Dollet B, Versluis M, De Jong N. Nonspherical Shape Oscillations of Coated Microbubbles in Contact With a Wall. *Ultrasound Med Biol*. 2011;37(6):935–48.
 235. Onda Corporation. *Acoustic Properties of Plastics*. 2003.
 236. Onda Corporation. *Acoustic Properties of Solids*. 2003;
 237. Zheng H, Dayton PA, Caskey CF, Zhao S, Qin S, Ferrara KW. Ultrasound-Driven Microbubble Oscillation and Translation Within Small Phantom Vessels. *Ultrasound Med Biol*. 2007;33(12):1978–87.
 238. Carey VP. *Liquid-vapor phase-change phenomena: an introduction to the thermophysics of vaporization and condensation processes in heat transfer equipment*. New York: Taylor and Francis; 2008.
 239. Constantinides C, Mean R, Janssen BJ. Effects of Isoflurane Anesthesia on the Cardiovascular Function of the C57BL/6 Mouse. *ILAR J*. 2011;52.
 240. Marano G, Grigioni M, Tiburzi F, Vergari A, Zanghi F. Effects of Isoflurane on Cardiovascular System and Sympathovagal Balance in New Zealand White Rabbits. *J Cardiovasc Pharmacol*. 1996;28(4):513–8.
 241. Li CX, Patel S, Auerbach EJ, Zhang X. Dose-dependent effect of isoflurane on regional cerebral blood flow in anesthetized macaque monkeys. *Neurosci Lett*. 2013;541:58–62.

242. Park KW, Dai HB, Lowenstein E, Darvish A, Sellke FW. Heterogeneous vasomotor responses of rabbit coronary microvessels to isoflurane [Internet]. Vol. 81, *Anesthesiology*. 1994. p. 1190–7.
243. Park KW, Dai HB, Lowenstein E, Darvish A, Sellke FW. Oxygen-Derived Free Radicals Mediate Isoflurane-Induced Vasoconstriction of the Rabbit Coronary Resistance Arteries. *Anesth Analg*. 1995;80:1163–7.
244. Matta BF, Heath KJ, Tipping K, Summers C. Direct cerebral vasodilatory effects of sevoflurane and isoflurane. *Anesthesiology*. 1999;91(3):677–80.
245. Butcher DT, Alliston T, Weaver VM. A tense situation: Forcing tumour progression. *Nat Rev*. 2009;9:108–22.
246. Levental KR, Yu H, Kass L, Lakins JN, Egeblad M, Ertel JT, et al. Matrix Crosslinking Forces Tumor Progression by Enhancing Integrin Signaling. *Cell*. 2009;139:891–906.
247. Lu P, Weaver VM, Werb Z. The extracellular matrix: A dynamic niche in cancer progression. *J Cell Biol*. 2012;196(4):395–406.
248. Wiig H, Tenstad O, Iversen P, Kalluri R, Bjerkvig R. Interstitial fluid: the overlooked component of the tumor microenvironment? *Fibrogenesis Tissue Repair*. 2010;3(12):1–11.
249. Boucher Y, Baxter LT, Jain RK. Interstitial pressure gradients in tissue- isolated and subcutaneous tumours: implications for therapy. *Cancer Res*. 1990;50:4478–84.
250. Zurovsky Y, Mitchell G, Hattingh J. Composition and viscosity of interstitial fluid of rabbits. *Exp Physiol*. 1995;80(2):203–7.
251. Aukland K, Reed RK. Interstitial-Lymphatic Mechanisms in the Control of Extracellular Fluid Volume. *Physiol Rev*. 1993;73(1).
252. Bouta EM, Wood RW, Brown EB, Rahimi H, Ritchlin CT, Schwartz E. In vivo quantification of lymph viscosity and pressure in lymphatic vessels and draining lymph nodes of arthritic joints in mice. *J Physiol*. 2013;592(6):1213–23.
253. Swisher SG, Erasmus J, Maish M, Correa AM, Macapinlac H, Ajani JA, et al. 2-Fluoro-2-deoxy-d-glucose positron emission tomography imaging is predictive of pathologic response and survival after preoperative chemoradiation in patients with esophageal carcinoma. *Cancer*. 2004;101(8):1776–85.
254. Haioun C, Itti E, Rahmouni A, Brice P, Rain J, Belhadj K, et al. [18F] fluoro-2-deoxy-D-glucose positron emission tomography (FDG-PET) in aggressive lymphoma: an early prognostic tool for predicting patient outcome. *Blood*. 2005;106(4):1376–81.
255. Mikhaeel NG, Hutchings M, Fields PA, O’Doherty MJ, Timothy AR. FDG-PET after two to three cycles of chemotherapy predicts progression-free and overall survival in high-grade non-Hodgkin lymphoma. *Ann Oncol*. 2005;16(9):1514–23.
256. Beer AJ, Haubner R, Wolf I, Goebel M, Luderschmidt S, Niemeyer M, et al. PET-based human dosimetry of 18F-galacto-RGD, a new radiotracer for imaging alpha v beta3 expression. *J Nucl*

- Med. 2006;47:763–9.
257. Beer AJ, Haubner R, Goebel M, Luderschmidt S, Spilker ME, Wester H-J, et al. Biodistribution and Pharmacokinetics of the avB3 -Selective Tracer 18 F-Galacto-RGD in Cancer Patients. *J Nucl Med.* 2005;41:1333–42.
 258. Ruoslahti E. Specialization of Tumour Vasculature. *Nat Rev Cancer.* 2002;2(2):83–90.
 259. Hood JD, Cheresh DA. Role of Integrins in Cell Invasion and Migration. *Nat Rev Cancer.* 2002;2:91–100.
 260. Streeter JE, Gessner R, Miles I, Dayton PA. Improving the Sensitivity in Ultrasound Molecular Imaging by Tailoring Contrast Agent Size Distribution. *Mol Imaging.* 2011;9(2):87–95.
 261. Rojas JD, Dayton PA. Vaporization Detection Imaging: A Novel Technique for Imaging Phase-Change Contrast Agents with Higher Depth of Penetration and Contrast Enhancement. *Ultrasound Med Biol.* 2018;In Review.
 262. Streeter JE, Dayton PA. An in vivo evaluation of the effect of repeated administration and clearance of targeted contrast agents on molecular imaging signal enhancement. *Theranostics.* 2013;3(2):93–8.
 263. Fix SM, Nyankima AG, McSweeney MD, Tsuruta JK, Lai SK, Dayton PA. Accelerated Clearance of Ultrasound Contrast Agents Containing Polyethylene Glycol is Associated with the Generation of Anti-Polyethylene Glycol Antibodies. *Ultrasound Med Biol.* 2018;
 264. Borden MA, Streeter JE, Sirsi SR, Dayton PA. In Vivo Demonstration of Cancer Molecular Imaging with Ultrasound Radiation Force and Buried-Ligand Microbubbles. *Mol Imaging.* 2013;12(6):357–63.
 265. Cheng Z, Zaki A Al, Hui JZ, Muzykantov VR, Tsourkas A. Multifunctional Nanoparticles : Cost Versus Benefit of Adding Targeting and Imaging Capabilities. *Nature.* 2012;338:903–10.
 266. McNeeley KM, Annapragada A, Bellamkonda R V. Decreased circulation time offsets increased efficacy of PEGylated nanocarriers targeting folate receptors of glioma. *Nanotechnology.* 2007;18.
 267. Gabizon A, Horowitz AT, Goren D, Tzemach D, Shmeeda H, Zalipsky S. In vivo fate of folate-targeted polyethylene-glycol liposomes in tumor-bearing mice. *Clin Cancer Res.* 2003;9:6551–9.
 268. Noble GT, Stefanick JF, Ashley JD, Kiziltepe T, Bilgicer B. Ligand-targeted liposome design: Challenges and fundamental considerations. *Trends Biotechnol.* 2014;32(1):32–45.
 269. Sawant RR, Torchilin VP. Challenges in Development of Targeted Liposomal Therapeutics. *AAPS J.* 2012;14(2):303–15.
 270. Huwyler J, Wu D, Pardridge WM. Brain drug delivery of small molecules using immunoliposomes. *Proc Natl Acad Sci U S A.* 1996;93:14164–9.
 271. Zalipsky S, Hansen CB, Lopes DE, Menezes D, Allen TM. Long-circulating , polyethylene

- glycol-grafted immunoliposomes. *J Control Release*. 1996;39:153–61.
272. Takalkar AM, Klivanov AL, Rychak JJ, Lindner JR, Ley K. Binding and detachment dynamics of microbubbles targeted to P-selectin under controlled shear flow. *J Control Release*. 2004;96(3):473–82.
 273. Gessner R, Dayton PA. Advances in Molecular Imaging with Ultrasound. *Mol Imaging*. 2010;9(3):117–27.
 274. Maeda H. Macromolecular therapeutics in cancer treatment: The EPR effect and beyond. *J Control Release*. 2012;164(2):138–44.
 275. Williams R, Wright C, Cherin E, Reznik N, Lee M, Gorelikov I, et al. Characterization of Submicron Phase-change Perfluorocarbon Droplets for Extravascular Ultrasound Imaging of Cancer. *Ultrasound Med Biol*. 2013;39(3):475–89.
 276. Lin S, Jamburidze A, Chee M, Leow CH, Garbin V, Tang M-X. Imaging of vaporised sub-micron phase change contrast agents with high frame rate ultrasound and optics. *Phys Med Biol*. 2018;
 277. Yin T, Wang P, Zheng R, Zheng B, Cheng D, Zhang X, et al. Nanobubbles for enhanced ultrasound imaging of tumors. *Int J Nanomedicine*. 2012;7:895–904.
 278. Güvener N, Appold L, de Lorenzi F, Golombek SK, Rizzo LY, Lammers T, et al. Recent advances in ultrasound-based diagnosis and therapy with micro- and nanometer-sized formulations. *Methods*. 2017;130:4–13.
 279. Perera RH, Hernandez C, Zhou H, Kota P, Burke A, Exner AA. Ultrasound imaging beyond the vasculature with new generation contrast agents. *Wiley Interdiscip Rev Nanomedicine Nanobiotechnology*. 2015;7(4):593–608.
 280. Zlitni A, Gambhir SS. Molecular imaging agents for ultrasound. *Curr Opin Chem Biol*. 2018;45:113–20.
 281. Herbst SM, Klegerman ME, Kim H, Qi J, Shelat H, Wassler M, et al. Delivery of stem cells to porcine arterial wall with echogenic liposomes conjugated to antibodies against CD34 and intercellular adhesion molecule-1. *Mol Pharm*. 2010;7(1):3–11.
 282. Shapiro MG, Goodwill PW, Neogy A, Yin M, Foster FS, Schaffer D V., et al. Biogenic gas nanostructures as ultrasonic molecular reporters. *Nat Nanotechnol*. 2014;9(4):311–6.
 283. Kwan JJ, Borden MA. Lipid monolayer collapse and microbubble stability. *Adv Colloid Interface Sci*. 2012;183–184:82–99.
 284. Borden MA, Longo ML. Dissolution behavior of lipid monolayer-coated, air-filled microbubbles: Effect of lipid hydrophobic chain length. *Langmuir*. 2002;18:9225–33.
 285. Wu S-Y, Fix SM, Arena CB, Chen CC, Zheng W, Olumolade OO, et al. Focused ultrasound-facilitated brain drug delivery using optimized nanodroplets: vaporization efficiency dictates large molecular delivery. *Phys Med Biol*. 2018;63.

286. Papadopoulou V, Evgenidis S, Eckersley RJ, Mesimeris T, Balestra C, Kostoglou M, et al. Decompression induced bubble dynamics on ex vivo fat and muscle tissue surfaces with a new experimental set up. *Colloids Surfaces B Biointerfaces*. 2015;129:121–9.
287. Lo AH, Kripfgans OD, Carson P, Fowlkes JB. Acoustic droplet vaporization: Effects of Pulse Duration and Contrast Agent Attenuation. *Int Symp Ther Ultrasound*. 2007;54(5):933–46.
288. Von Herbay A, Westendorff J, Gregor M. Contrast-enhanced ultrasound with SonoVue: Differentiation between benign and malignant focal liver lesions in 317 patients. *J Clin Ultrasound*. 2010;38(1):1–9.
289. Claudon M, Dietrich CF, Choi BI, Cosgrove DO, Kudo M, Nolsøe CP, et al. Guidelines and Good Clinical Practice Recommendations for Contrast Enhanced Ultrasound (CEUS) in the Liver - Update 2012. A WFUMB-EFSUMB Initiative in Cooperation with Representatives of AFSUMB, AIUM, ASUM, FLAUS and ICUS. *Ultrasound Med Biol*. 2013;39(2):187–210.
290. Nemeč U, Nemeč SF, Novotný C, Weber M, Czerný C, Krestan CR. Quantitative evaluation of contrast-enhanced ultrasound after intravenous administration of a microbubble contrast agent for differentiation of benign and malignant thyroid nodules: Assessment of diagnostic accuracy. *Eur Radiol*. 2012;22:1357–65.
291. Caproni N, Marchisio F, Pecchi A, Canossi B, Battista R, D'Alimonte P, et al. Contrast-enhanced ultrasound in the characterisation of breast masses: Utility of quantitative analysis in comparison with MRI. *Eur Radiol*. 2010;20:1384–95.
292. Xie XH, Xu HX, Xie XY, Lu M De, Kuang M, Xu ZF, et al. Differential diagnosis between benign and malignant gallbladder diseases with real-time contrast-enhanced ultrasound. *Eur Radiol*. 2010;20(1):239–48.
293. Leu AJ, Berk DA, Lymboussaki A, Alitalo K, Jain RK. Absence of Functional Lymphatics within a Murine Sarcoma : A Molecular and Functional Evaluation. *Cancer Res*. 2000;60:4324–7.
294. Padera TP, Kadambi A, Tomaso E, Carreira CM, Brown EB, Boucher Y, et al. Lymphatic Metastasis in the Absence of Functional Intratumor Lymphatics. *Science (80-)*. 2002;296:1883–6.